DOCTOR OF PHILOSOPHY

Hybrid Group IV Nanophotonics

Abdou, Aly

Award date:
2018

Awarding institution:
Bangor University

Hybrid Group IV Nanophotonics

PRIFYSGOL
BANGOR
UNIVERSITY

Aly Abdou

Supervisor: Dr Maziar Nezhad

School of Electronic Engineering
Bangor University

This thesis is submitted for the degree of
Doctor of Philosophy

March 2018

Acknowledgements

First I would like to acknowledge the financial support provided by the Welsh Government and Higher Education Funding Council for Wales through the Sêr Cymru National Research Network in Advanced Engineering and Materials. And I would like to personally thank ***Prof Huw Summers***, ***Mrs Claudia Rabello Strugnell***, and ***Miss Ruth Thomas*** for all the time and hard-work they put in making my doctorate experience very beneficial. And a special 'thank you' for the good times and laughs we shared.

Most importantly, I would like to thank my supervisor ***Dr Maziar Nezhad*** for guidance and help throughout my doctoral studies. It was very helpful to have a supervisor with the right balance between offering help and advice when needed, and giving me the space to try and fail when appropriate. Thank you very much, your attitude helped me improve remarkably in a short time. Another thank you for being very generous in teaching and sharing your research experience with me. Thank you for being there when I approach you with nonacademic issues; you are the mentor and friend.

Also, I would like to thank my colleague ***Mr Parashara Panduranga*** for his help, advice and the constructive discussions we had about the different aspects of the work conducted in this thesis. I also appreciate sharing his experience and knowledge for teaching me some of the experimental aspects of micro- and nano-fabrication techniques. I did not forget, thank you for driving us to all activities and conferences outside Bangor.

I would like to thank ***Dr Paul Sayers*** for coping with my many requests and questions concerning the use of the cleanroom, materials, and the laboratory facilities in the department. Thank you to ***Dr Colin Watson*** for being very generous with advice and help in the cleanroom.

Last but not least, I would like to thank the people behind the scenes, whose help was very essential for the completion of this thesis. Thanks to ***Mr Ben Assinder***, the research technician; and ***Mr Iwan A Jones***, the workshop technician.

Abstract

Advancements in electronic integrated chip technology are slowing down with transistor sizes approaching their theoretical limit in most equipment and devices. As the data transmission rate has benefited from the telecommunication technology through optical fibers, Photonic Integrated Chips (PICs) are expected to fill the gap in the demand for higher transmission rates and faster computational speeds that the electronic chips would fail to fulfill.

The research into PICs is in the center of attention in the academic and industrial fields, and the way in front of PICs development and improvement is still long. There are many opportunities including the use of new materials, different designs and architectures, and the use of various physical effects on the macro and micro scales.

The main aim of this work is to design a hybrid-multi-layer PIC that allows the integration between an ultra-high-Q micro-resonator made of silica and an optical waveguide of a different material through a MEMS actuated coupler. To date, the ultra-high-Q silica micro-resonators can confine light within for the longest period, which is very beneficial for many applications including revolutionary accurate time measurements, and studying non-linear optical phenomena using modest laser powers. As using silica micro-resonators offers the highest-Q factor, using an optical waveguide of different material can offer the best operation condition based on the required application. For instance, having a silicon waveguide with high refractive index allows the fabrication of dense photonic chips, while using nanocrystalline diamond (NCD) waveguide suits wide-transmission-window applications.

To achieve this goal, several studies were required along the way. For example, the hybrid-chip would include a suspended NCD waveguide structure that has not been demonstrated before. So we took the initiative and designed, fabricated and studied its operation. During fabricating the chips in this work, the ablation of NCD films using CO_2 laser was observed, which was unexpected. As explanations in the literature was unsatisfactory, we hypothesized a new explanation, and confirmed it using numerical and experimental tests.

After designing the hybrid-multi-layer PIC, we took the study a step further and developed the fabrication process. Also, an analytical formula for estimating the scattering loss from asymmetric rough rectangular waveguide surfaces has been formulated to assess the practicality of using specific waveguide designs using certain fabrication techniques. Finally, the design of grating couplers is presented as a starting point for prospective work. The work presented here is believed to be a beneficial milestone in the realisation of practical hybrid multi-layer PICs.

Research Declaration

All theoretical work, analytical analysis and numerical simulations, carried out in this thesis is the product of the author. The author acknowledges the teaching, guidance and help from his supervisor to achieve the presented results.

The practical experiments included are the result of team effort by the author, author's colleague, collaborators and supervisor. The author and the author's colleague work in the Nanophotonic Devices and Systems Laboratory (***NDSL***) at ***Bangor University, UK*** , where the work conducted by them or their supervisor will be referred to as work conducted by NDSL, either it took part at ***NDSL*** or at other facilities. Experimental work by the author's collaborators will be identified to the researcher and the institute where the work was conducted.

All nanocrystalline diamond used in this work has been grown on silicon wafers by the project's collaborator ***Prof. Oliver Williams*** in ***Cardiff Diamond Foundry*** at ***Cardiff University, UK***.

The nanocrystalline diamond platform in **Chapter 5** has been measured using an infrared laser setup by ***Mr Jens Richter*** in the ***Institute of Integrated Photonics*** led by ***Prof Jeremy Witzens*** at ***RWTH Aachen University, Germany***.In addition, the micro-machining of the thin nanocrystalline diamond film in **Chapter 6** was performed by ***Mr Jens Richter*** in the ***Institute of Integrated Photonics*** at ***RWTH Aachen University, Germany***.

The e-beam patterns of the suspended nanocrystalline diamond platform in **Chapter 5** were written in ***Nano3, Qualcomm Institute*** at ***University of California San Diego, USA***.

Some of the preliminary e-beam patterns in **Chapter 8**, as well as dry bonding tests, bonding under vacuum, and chip dicing have been tested by ***NDSL*** with the help of ***Dr Mark Rosamond Richter*** and ***Dr Li Chen*** at ***Leeds University, UK***.

All photo-lithography, RIE dry etching, wet etching, wet bonding, thermal evaporation and sputtering have been conducted by ***NDSL*** at ***Bangor University, UK***. ICP-RIE dry etching and e-beam lithography have been performed by ***NDSL*** in ***The Graphene Institute,*** at ***NDSL*** at ***Manchester University, UK***.

All results processing, optical imaging, SEM and AFM measurement were performed by ***NDSL*** at ***Bangor University, UK***, ***Chester University, UK***, ***Liverpool University, UK***, ***Leeds University, UK Manchester University, UK***.

Table of contents

List of figures **xvii**

List of tables **xxi**

1 Introduction **1**
1.1 Thesis layout and achievements 3

2 Theoretical Foundation & Preliminary Work **5**
2.1 Maxwell's equations 5
2.2 Dielectric optical waveguide 6
2.2.1 Optical materials 6
2.2.1.1 Silicon and silicon oxide 6
2.2.1.2 Synthetic diamond 8
2.2.2 Optical losses 8
2.2.2.1 Scattering loss 8
2.2.2.2 Material loss 9
2.2.2.3 Bend loss 9
2.3 Optical micro-resonators 9
2.3.1 Nonlinear effects in optical micro-resonators 14
2.3.2 Silica micro-toroid resonators 15
2.4 Numerical methods 16
2.4.1 Finite Difference Method (FDM) 16
2.4.2 The Method Of Moments (MOM) 17
2.4.3 Finite Element Method (FEM) 18
2.4.4 Eigenmode Expansion Method 18

3 Grating Coupler Design **19**
3.1 Introduction 19
3.2 Design 21

3.2.1 First principles (symmetric straight grating coupler) 21
3.2.2 Apodised straight grating coupler 27
3.2.3 Curved grating coupler 28
3.3 Summary 30

4 Scattering Loss from Asymmetric Rough Rectangular Waveguides 31
4.1 Loss from symmetric slab waveguide 31
4.2 Loss from asymmetric rectangular waveguide 33
4.3 Results 37
4.4 Summary 38

5 Nanocrystalline Diamond Waveguide 39
5.1 Introduction 39
5.2 Design 40
5.3 Fabrication 43
5.4 Loss measurements 46
5.5 Summary 50

6 CO_2 Laser Micromachining of Diamond Films 51
6.1 Introduction 51
6.2 Infrared optical properties of diamond and silicon at elevated temperatures . 53
6.3 Modelling and simulations 54
6.4 Experimental results 59
6.5 Summary 62

7 Photonic Integrated Chip Design 63
7.1 Device model 63
7.2 Optical design 63
7.2.1 Micro-toroid resonator mode analysis 65
7.2.2 Waveguide design 66
7.2.2.1 Coupler waveguide 68
7.2.2.2 Waveguide dispersion 71
7.2.2.3 Straight waveguide 71
7.2.2.4 Bends 72
7.2.2.5 Input- and output-couplers 74
7.2.2.6 Waveguide transitions 78
7.3 Electromechanical design 82

7.3.1 Material doping . . . 86
7.3.1.1 Silicon doping . . . 87
7.3.1.2 Diamond doping . . . 90
7.3.2 Deflection vs actuation voltage . . . 93
7.4 Mechanical design . . . 94
7.4.1 Vibration analysis . . . 94
7.4.2 Vacuum breaking channels . . . 96

8 Photonic Integrated Chip Fabrication 99
8.1 Theory . . . 103
8.1.1 Sputtering . . . 103
8.1.2 Thermal evaporation . . . 105
8.1.3 Silicon etching . . . 108
8.1.4 Silica dry etching . . . 111
8.1.5 Electron-beam lithography . . . 111
8.2 Bottom chip processing . . . 113
8.2.1 Wet silicon dioxide (silica) etching (steps **2-4** in Fig. 8.1) . . . 115
8.2.2 Lower electrode deposition (step2 **5-8 in** Fig. 8.1) . . . 116
8.2.3 Separation layer (steps **9 and 10 in** Fig. 8.1) . . . 117
8.2.4 Silicon isotropic etching (step **11 in** Fig. 8.1) . . . 120
8.2.5 Silica melting (step **12 in** Fig. 8.1) . . . 121
8.3 Bonding (steps **13 and 14 in** Fig. 8.1) . . . 123
8.4 Top chip processing . . . 124
8.4.1 Deep silicon etching (step **15 in** Fig. 8.1) . . . 124
8.4.2 Silica dry etching (step **15 in** Fig. 8.1) . . . 125
8.4.3 Electron-beam lithography (steps **16 and 17 in** Fig. 8.1) . . . 125
8.4.4 Silicon anisotropic etching (steps **18-21 in** Fig. 8.1) . . . 126
8.4.5 Polymer dry etching (step **22 in** Fig. 8.1) . . . 127
8.5 Summary . . . 128

9 Conclusion 131

References 137

Appendix A Grating coupler simulator 149
A.1 CAMFR script example . . . 152

Appendix B MATLAB® Code for Estimating Scattering Loss **155**
B.1 MATLAB® code 156

Appendix C KOH Etching of Silicon **159**
C.1 Introduction 159
C.2 Experiment 161
C.3 Results 162
C.3.1 Masks against KOH solution 162
C.3.2 Masks against KOH-IPA solution 163
C.3.3 Etching silicon 164
C.4 Conclusion 164

List of figures

2.1 Diagram of SOI chip. 7
2.2 Schematic of resonator waveguide coupler 12
2.3 Coupling coefficient vs separation gap 14
2.4 Parametric oscillation spectrum 15
2.5 Schematic of silica micro-toroid resonator fabrication 16

3.1 Schematic of symmetric grating coupler 20
3.2 Optical fibre's field gaussian profile vs grating coupler's field exponential profile 21
3.3 Sample reflection and transmission plot for grating couplers 23
3.4 Domain materials and boundary conditions for reflection and transmission simulations 23
3.5 Effect of substrate thickness on grating coupler's efficiency 24
3.6 Simulated grating coupler scattered field using CAMFR 26
3.7 Efficiency plots for silicon grating couplers 26
3.8 Gaussian stepwise approximation of grating coupler field 27
3.9 Schematic of curved grating coupler 29

4.1 Asymmetric rough horizontal slab, vertical slab and rectangular waveguides 32
4.2 Assymetric slab waveguide 34
4.3 Complex representation of refractive index 37
4.4 Scattering loss from rough waveguide surfaces vs operation wavelengths . . 38

5.1 Schematic of the proposed suspended NCD structure 41
5.2 Designed waveguide electric field distribution (V/m) with dimensions and effective index 42
5.3 Bend loss in $dB/90^o$bend vs bend radius and etch depth for suspended diamond rib waveguide 43
5.4 SEM image of the fabricated suspended NCD platform 45

5.5 Fabricated waveguide final dimensions with mode electric field distribution (V/m) and effective index 45
5.6 SEM image showing the deflection of the suspended edge 46
5.7 Near Infra-red image at 1550*nm* for the fabricated waveguides 47
5.8 Image of measurement setup 47
5.9 Example of power decay measurements fitting 48

6.1 Calculated optical absorption coefficient of silicon at 10.6μm for different doping levels and temperatures 55
6.2 Simulated laser beam penetration and resulting temperature profiles 57
6.3 Maximum diamond surface temperature for different substrate doping and beam power combinations 58
6.4 Maximum diamond surface temperature for different diamond thickness and beam power combinations 59
6.5 Schematic of CO_2 laser setup 60
6.6 Undercut and patterns in nanocrystalline diamond film on silicon substrate . 61

7.1 Device exploded view 64
7.2 Toroid micro-resonator parameters 65
7.3 Toroid micro-resonator modes 66
7.4 Slab waveguide 66
7.5 Ridge (rib) waveguide 67
7.6 Rectangular waveguide 68
7.7 Rib-waveguide confined mode 69
7.8 Single and multi-mode cut-off dimensions for silicon and diamond waveguides 70
7.9 Mode shape and effective index of silicon and diamond coupler waveguides 70
7.10 Coupler waveguides and resonator wavelength dispersion 71
7.11 Mode shape and effective index of the rib-waveguide 72
7.12 Twisted and bent waveguide structure 73
7.13 Mode shape and location for bent waveguides of different bend radii 75
7.14 Input and output coupling mechanisms 76
7.15 Example of TE_0 mode input merging with higher order modes 80
7.16 Refractive indices of first 6 modes of rib waveguides 80
7.17 Rib-to-rectangular waveguide transition 81
7.18 Adiabatic transition from rib to rectangular waveguides 81
7.19 Adiabatic rectangular taper transition 82
7.20 Smooth supported-to-hanging transitions 83

7.21 Coupler structure 84
7.22 Carrier refraction in crystalline-Si as a function of free carrier concentration 88
7.23 Optical absorption spectra of crystalline-Si 89
7.24 Absorption curves for n- and p-Si samples at 294^o K 90
7.25 Effect of boron doping on electrical conductivity of diamond 91
7.26 Absorption coefficient α calculated for NCD samples 91
7.27 Absorption coefficient for undoped diamond samples 92
7.28 Exaggerated visual representation of coupler deflection 93
7.29 Deflection vs voltage for silicon and diamond couplers 94
7.30 The first 6 natural frequencies of silicon and diamond couplers 96

8.1 Flow diagram of fabrication steps. 102
8.1 Flow diagram of fabrication steps (cont.). 103
8.2 Representation of physical sputtering. 104
8.3 Schematic of a standard sputtering system. 104
8.4 Sputtered atom scattering angle vs bombardment particle energy 105
8.5 Schematic diagram of resistive thermal evaporator system. 106
8.6 Schematic of ebeam thermal evaporator. 107
8.7 Main crystal orientations in silicon lattice. 108
8.8 Isotropic vs anisotropic etching. 108
8.9 Scalloping effect in anisotropic dry etching 110
8.10 Block diagram of the major components of ebeam lithography system. . . . 112
8.11 $1cm \times 1cm$ chip layout 113
8.12 SEM image of the fabricated bottom chip. 114
8.13 Oxide etch mask. 115
8.14 Patterned photoresist and silica rings. 116
8.15 Lower electrode etch mask. 117
8.16 Patterning Molybdenum 117
8.17 Voids and vacuum breaking channels mask. 118
8.18 Optical image showing the cracks in the PMMA layer after chromium deposition. 118
8.19 Edge beads and wavy surface due to void presence in spin-coated films. . . 119
8.20 Patterning SU-8. 120
8.21 SEM images of silicon isotropic etching. 120
8.22 SEM images showing the vertical and lateral silicon undercut. 121
8.23 SEM image of silicon isotropic etch using SU-8 mask. 121
8.24 Schematic showing toroid microresonator fabrication steps. 122

8.25 SEM image of melted silica ring resonator. 123
8.26 SEM image showing epoxy thickness. 124
8.27 ebeam pattern with inverse-taper coupler magnified in the inset. 125
8.28 SEM image of partially etched waveguide. 126
8.29 Mask for fully etched waveguide. 127
8.30 SEM image of dry-etched PMMA 128

A.1 Operation parameters window 149
A.2 Operation variables window 150
A.3 Parametric sweeps window 150
A.4 Adveanced settings window 150
A.5 Output files window 151
A.6 Sample plot output 151
A.7 Sample field output 152

B.1 Schematic of refractive index distribution for the effective index method . . 155

C.1 Molybdenum surface after KOH etching. 162
C.2 Isotropic and anisotropic etching behaviour of KOH-IPA solutions. 163

List of tables

2.1 Maxwell's equations and the wave equation 6

6.1 Silicon physical parameters used in the COMSOL® modelling steps. 56
6.2 Diamond physical parameters used in the COMSOL® modelling steps. . . 56

7.1 Silicon coupler efficiency vs coupler width 78
7.2 Diamond coupler efficiency vs coupler width 79
7.3 Silicon doping requirements 90
7.4 Calculated and simulated natural frequencies 95
7.5 Flow velocity and Reynold's number in venting ducts 97

8.1 Outline of fabrication steps. 101
8.2 Chromium resistive thermal evaporation parameters. 119

C.1 Brief experimental procedures of masking materials for KOH etching. . . . 160

Chapter 1

Introduction

Photonic Integrated Chips (PICs) have gained a lot of interest for decades [1, 2]. After the remarkable success of optical communication through optical fibres, the need to move from electronics towards photonics was a logical decision. Using photonics at both the sender and receiver ends would increase operational speed and efficiency. In addition to optical communication, PICs are used for bio-medical applications, optical sensing, and metrology.

Advances in photonics and micro- and nano-fabrication techniques made PICs an ideal candidate for pursuing quantum computing. Quantum computers depending on photonic chips have been demonstrated [3]. IBM® has released a roadmap for commercial quantum computers [4], and Google™ is planning to release quantum technologies in five years [5]; which show that research in PICs is essential and in high demand.

Three of group IV materials that have caught the attention of researchers are silicon, silicon dioxide, and synthetic diamond. Silicon is an interesting candidate for PICs due to its high transparency in the near infrared range (communication wavelengths), the advances in silicon electronics, and the complementary metal-oxide semiconductor (CMOS) technology. Therefore, all the advances made with the electronics silicon technology can be used for photonic chips. Also, silicon allows for easy integration of photonic and electronic circuits on one chip. Silicon dioxide attracts attention since it can work as a core material, as well as a cladding material. Different doping concentrations of silicon dioxide allows for its use as core and cladding materials in the same structure, as in the case of optical fibres. Synthetic semiconducting diamond has been in the centre of research for decades [6]. Diamond has attracted attention due to its transparency over a broad spectrum of optical wavelengths [7].

One of the important components of PICs are microresonators, which is an optical cavity that resonates at certain wavelengths. Microresonators are extremely useful due to their compact size and high performance. They can perform several tasks including optical signal sensing, switching, amplification, and multiplexing/demultiplexing. Microresonators have

been fabricated in silicon [8] and have showed high quality factors[1] (Q-factor). Microresonators in diamond have also been simulated and showed similar Q-factors as the silicon ones [9], and when demonstrated in practice, they showed an order of magnitude increase in Q-factors [10]. The so-called surface-tension-induced microresonators possess the highest possible Q-factors to date. Such microresonators are demonstrated mainly by melting silicon oxide into spherical or toroidal shapes [11].

Most of the demonstrated PICs with microresonators are static chips [12] with no moving parts. Such static chips do not allow for fabrication intolerances, and cannot be mechanically tuned. As will be shown in **Chapter 2**, coupling light waves into/out from microresonators is a function of the separation gap between the resonator and the waveguide. Therefore, having a movable platform acting as an on/off switch for coupling light, or as a controller of the amount of energy being coupled in/out of the resonator is essential for full control over PIC operation. Such controllability can be achieved using MEMS (Micro-Electro-Mechanical-systems) integration [13, 14].

Some MEMS actuated PICs have been demonstrated [15, 16]. These works that represent dynamic PICs are considered single substrate chips, and all the chip components are fabricated on a single layer. The drawback in single substrate chips is the limitation in the chosen material properties, where compromises are necessary to achieve final chip operation; which comes at the price of reduced functionality and/or efficiency. Multi-substrate (hybrid) PICs overcome such a limitation, where more than one chip with several layers of different properties are combined together, and used to fabricate the required device on multiple layers, for example the work demonstrated in [17].

In the presented work, we improve on the work done previously on multi-layer PICs, where we lay the groundwork for achieving higher controllability over optical couplers' performance with our improved design on the MEMS actuator. Along this path we report a study of suspended nanocrystalline diamond (NCD) waveguide, a new photonic platform. Also a new explanation of patterning NCD films grown on highly doped silicon substrates using CO_2 laser is presented with experimental demonstration. An analytical formula for calculating the scattering loss from rough waveguide surfaces is derived to confirm the practicality of waveguides' designs and fabrication techniques. Finally, we present SOI (Silicon-On-Insulator) grating coupler design, and the required performance calculation codes are presented. The grating coupler was chosen as a modification to the coupling mechanism of the suspended NCD platform, as it can provide a more robust structure than the inverse nano-taper edge coupler used in the platform.

[1] Quality factor can be simply explained as a measure of the time the cavity can confine the wave within.

1.1 Thesis layout and achievements

In this work we target the use of one of the new materials in the field of photonics, nano-crystalline diamond (NCD), in a new suspended photonic platform. Also, patterning NCD films using CO_2 laser has been studied. Then a large portion of the work is devoted to the design of a new multi-layer PIC for the integration between MEMS and photonic chips.

The new suspended NCD platform has been designed, fabricated, and optically tested to confirm its practicality. The results presented show the simplicity of fabrication and the acceptable loss coefficient of such platform. This platform is very beneficial for many application, e.g. sensing. The design of grating couplers is also presented as an improvement for the suspended NCD platform.

The second study is concerned with the micro-machining of thin NCD films using CO_2 laser. The presented method offers an affordable and fast patterning technique for NCD. Patterning NCD films using CO_2 laser is not a novel topic, but we have provided a better insight on the ablation mechanism. In previous works, the role of the substrate that the NCD is grown on has been totally ignored. And in this work we have shed the light on this role through simulation and experimental demonstration.

The last and biggest part of this work is concerned with the design and fabrication of a MEMS actuated micro-toroid resonator coupler. Micro-resonators attract a lot of attention due to the potential of their use in several applications depending on nonlinear optical properties. As micro-resonators confine light energy for long periods, the build-up effect allows for exciting the nonlinear effects. As of the time of writing this thesis, surface-tension-induced micro-resonators confine light for the longest period. This long confinement period allows for the excitation of nonlinear effects with very low laser powers, which opens up the possibility in front of several applications without the increased hazard of using high-power lasers. Among the many applications of micro-resonators are frequency combs, that can be used in high precision measurements and sensing.

To improve the practicality of using micro-resonators on PICs, dynamic couplers are required. To address this issue we have designed a multi-layer PIC, which adds the freedom of using different materials for the resonator and the waveguide coupler. The designed PIC comprises of a micro-toroid-resonator and a MEMS actuated coupler that offers total controllability over the PIC operation. The fabrication process has been designed and reported here, but the finalized PIC has not been fully fabricated and is still an ongoing work.

Also, an analytical treatment of scattering loss from asymmetric rectangular dielectric waveguides with rough surfaces is being conducted. A mathematical formula has been produced that relates the scattering loss to the waveguide and operational parameters (waveguide dimensions and materials, roughness characteristics, and operation wavelength).

The thesis layout starts with a general background in **Chapter 2**, which is aimed towards building the basic literature review for the work conducted in later chapters. Then the results achieved in this work are presented in the following order:

1. First, the design of an SOI grating coupler (GC) is presented in **Chapter 3**. It is organised in sequential order to provide systematic design steps for GCs. The resultant designs are presented for symmetric straight and curved CGs. The work on apodised GCs is an ongoing work, where more efficient genetic algorithm codes are being studied and developed.

2. **Chapter 4** presents the analytical study of scattering loss from rough asymmetric rectangular waveguides.

3. Then the design, fabrication and measurement of the suspended NCD platform are presented in **Chapter 5**.

4. The study of the interaction between NCD films grown on highly doped silicon substrates and CO_2 laser is presented in **Chapter 6**, both numerically and experimentally; which provides an affordable and fast patterning technique for NCD films.

5. After the study of NCD single substrate platform, the attention is shifted towards hybrid multi-substrate PICs. In **Chapter 7**, the design of the multi-substrate PIC is presented. Each component is designed for both multi-substrate silicon PIC and multi-substrate NCD PIC. And **Chapter 8** is dedicated to the fabrication process of the multi-substrate silicon PIC. According to time constraints, the fabrication phase was not completed and is an ongoing work at the moment.

Finally a conclusion is delivered in **Chapter 9** to sum up the work done in this project, along with some suggested future work. **Chapters 3** to **8** are self-contained, including the required literature review, methodology and results. If the reader is familiar with the material presented in **Chapter 2**, **chapters 3** to **8** can be read independently.

Chapter 2

Theoretical Foundation

In this chapter, we present the general background required for the study conducted in this work.

2.1 Maxwell's equations

The design of photonic components and circuits requires the understanding of electromagnetism. The laws of electromagnetism are described by Maxwell's equations [18]. Maxwell's equations are the integration of several laws for electric and magnetic fields, which led to the discovery that light is an electromagnetic disturbance in space. Table 2.1 [19] shows both the integral and differential forms of Maxwell's equations. For light beams, solving Maxwell's equations with no sources for electric and magnetic fields leads to the wave equation.

When light is propagating through material, different material properties affect its propagation. The magnetic permeability and electric permittivity determine both magnetic and electric fields, respectively. As light consists of different wavelengths, each wavelength propagates with different velocity, which is referred to as material dispersion. Also, depending on the waveguide cross-section perpendicular to the propagation direction, different wavelengths propagate at different speeds, which is the structural dispersion. The change in the waveguide's cross-section and orientation along the propagation direction affects the magnetic and electric fields inside the waveguide.

The following sections review briefly the optical materials used in this work, along with waveguiding losses. This information is crucial to designing building blocks for photonic circuits.

Table 2.1 Maxwell's equations and the wave equation

Law	Differential Form	Integral Form
Gauss's law of electricity	$\vec{\nabla} \bullet \vec{E} = \frac{\rho}{\varepsilon_0}$	$\oint_s \vec{E} \bullet \hat{n}\, da = \frac{q_{enc}}{\varepsilon_0}$
Gauss's law of magnetism	$\vec{\nabla} \bullet \vec{B} = 0$	$\oint_s \vec{B} \bullet \hat{n}\, da = 0$
Faraday's law	$\vec{\nabla} \times \vec{E} = -\frac{\partial \vec{B}}{\partial t}$	$\oint_c \vec{E} \bullet d\vec{l} = -\frac{d}{dt} \int_s \vec{B} \bullet \hat{n}\, da$
Ampere-Maxwell law	$\vec{\nabla} \times \vec{B} = \mu_0(\vec{J} + \varepsilon_0 \frac{\partial \vec{E}}{\partial t})$	$\oint_c \vec{B} \bullet d\vec{l} = \mu_0(I_{enc} + \varepsilon_0 \frac{d}{dt} \int_s \vec{E} \bullet \hat{n}\, da)$
Wave equation	Electric field	Magnetic field
	$\nabla^2 \vec{E} = \mu_0 \varepsilon_0 \frac{\partial^2 \vec{E}}{\partial^2 t}$	$\nabla^2 \vec{B} = \mu_0 \varepsilon_0 \frac{\partial^2 \vec{B}}{\partial^2 t}$

2.2 Dielectric optical waveguide

In principle, electromagnetic waves can propagate in any material. One distinguishing feature between them is how far the wave propagates. The general case is a lossy dielectric material, where electromagnetic waves decay as they propagate. The two special cases are: the lossless (perfect) dielectric or free space where waves do not decay; and the perfect conductor where propagation is inhibited (i.e. a perfect reflector) [20].

For optical wavelengths, metals are considered conductors and hence have not usually been used in photonic circuits, though the advent of plasmonics is changing this [21]. Free space is the only perfect dielectric, and as it is not very practical to use vacuum as a waveguide, lossy dielectrics are used instead. Since the photonic chips are in the scale of microns and millimetres, and the attenuation factor (wave decay factor) is very small, many semiconductors are considered approximations of lossless dielectrics like silica glass, silicon and recently nanocrystalline diamond (NCD).

2.2.1 Optical materials

In this section, we present a brief background about the optical materials that are used in this work. Through this thesis, we only work with dielectric optical materials, the use of metallic optical materials (plasmonic) is beyond the scope of this thesis, any reference to optical resonator or waveguide is for a dielectric one.

2.2.1.1 Silicon and silicon oxide

Using silicon and silicon oxide as guiding materials have been studied intensively, e.g. [22]. Silicon is opaque in the visible range, but it is transparent in the near infrared (telecommunication band). Silicon has a high refractive index which leads to smaller waveguides than

using silica. Hence, it is promising for miniaturizing photonic circuit components due to the higher confinement of light waves.

Silicon, as a semiconductor, has a very low electrical conductivity and very low optical absorbance in the $1.3-1.6\mu m$ range. Several materials, like Boron, Phosphorus and Arsenic, have been used to improve silicon's electrical conductivity at the price of higher optical absorbance. Fortunately, a good compromise between electrical conductivity and optical transmissivity is achievable [23–28].

Silicon's abundance in nature, the maturity of silicon wafer fabrication, and the high demand for silicon wafers have made silicon wafers with high purity commercially available at reasonable prices.

Silicon dioxide or silica glass is widely used for optical communications (optical fibres). Doping silica can change its refractive index to be used as the core and cladding of the waveguide. It is widely used because of its flexibility, ease of manufacturing and transparency at visible and near infrared wavelengths [29], due to very low propagation losses. And it can be easily grown on top of silicon using thermal oxidation [30] or deposition processes.

Silicon-on-insulator (SOI) wafers, as shown in Fig. 2.1, are being used in photonic chips. SOI wafers are widely available with customized device layer properties; from layer thickness to doping type and concentration.

The refractive index difference between silicon (~ 3.5) and its oxide (~ 1.5) provides high light confinement in silicon waveguides with oxide cladding, which promotes nano-

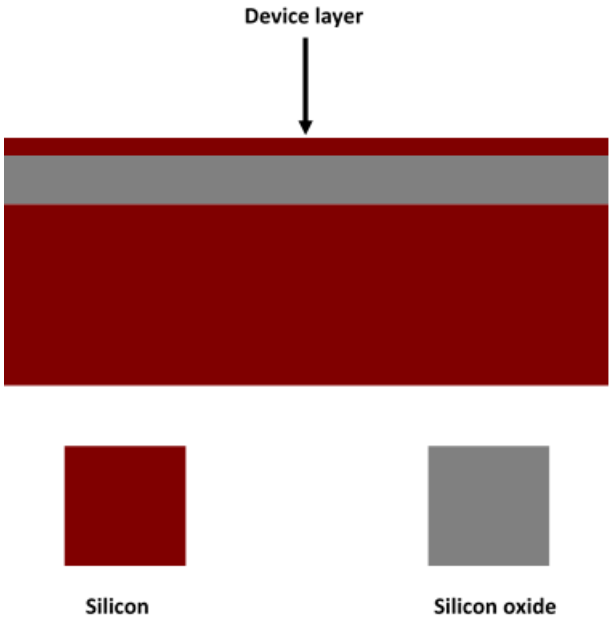

Fig. 2.1 Diagram of SOI chip.

photonics with sub-micron features. What makes SOI wafers more appealing for PICs is the etching selectivity between silicon and silicon oxide, which offers easy fabrication.

Integrated circuits' (IC) fabrication techniques are well developed, which uses silicon and SOI substrates. The enhanced electrical properties of doped silicon allow for its use as an electrical and optical material. SOI chips are used for building optoelectronic circuits, which allows for integrating electrical and optical circuits on the same chip using the same fabrication techniques. This has led to numerous number of research papers studying SOI photonic integrated circuits and showed a lot of advancements.

2.2.1.2 Synthetic diamond

Synthetic diamond comes in many forms based on crystallinity; single-crystal-diamond, microcrystalline-diamond, and nanocrystalline–diamond (NCD). They all possess similar characteristics, but differ in the grain size and surface smoothness.

NCD, which is used in this work, has grain sizes in the range of 5-100 nm with films grown with grain sizes below 10 nm being referred to as Ultra-NCD. These small grain sizes are the reason behind the smooth surfaces exhibited by NCD. Reference [31] offers a good NCD review.

NCD is an interesting material due to its superior mechanical and thermal properties [32]. As it is optically transparent over a wide range of wavelengths [33, 34], using it as an optical waveguide material has attracted much attention [35].

Semiconducting diamond has been produced to overcome the electrical resistivity problem. p-doped diamond has been produced [36] and its electrical and optical properties have been studied [37–39]. Recently, n-doped diamond has, also, been produced and studied [40–42]. Unlike silicon, diamond doping introduces high optical losses.

2.2.2 Optical losses

As waves propagate through waveguides they lose energy. These losses can be either material loss or structure loss.

2.2.2.1 Scattering loss

Scattering loss in a waveguide occurs due to the presence of a rough waveguide surface. Scattering loss can be minimized by creating smooth surfaces. In many cases surface roughness cannot be fully eliminated; but usually, scattering loss is ignored during the design phase as it can differ from one sample to another.

2.2.2.2 Material loss

Material loss occurs when light gets absorbed or disturbed by atoms or molecules in the material's crystal lattice. When operating above the conduction band, this loss is due to impurities in the material, which are usually intentionally introduced in the material's crystal lattice to alter its properties; e.g. change flexibility, melting point, strength; or, for optoelectronics, increase electrical conductivity.

2.2.2.3 Bend loss

As a curvature is introduced into the waveguide, the guided mode shifts away from the centre of curvature. This shift implies that the effective refractive index inside the waveguide increases radially from the centre of curvature. Depending on the waveguide's refractive index, cladding's refractive index, radius of curvature, wavelength and waveguide's cross-section, a portion of the power will start leaking outside the waveguide. Unless this leakage is intentional, it is considered a loss and should be minimized. Research has established mathematical relations between all bend loss parameters; and this problem has been studied both theoretically [43] and experimentally [44]. Also, techniques to minimize bend loss were proposed [45].

2.3 Optical micro-resonators

Optical resonators are simply optical cavities that resonate at certain "resonant" wavelengths. They could be in the form of linear resonators, e.g. Fabry-Perot resonator, or circular resonators. Circular resonators attract attention in photonics due to the applicability of miniaturization and compatibility to integrate with planar optical structures. Circular resonators can be in the form of a disk, sphere, race-track or a ring. In this study, we work with micro-ring-resonators, also referred to as toroid micro-resonators.

Ring resonators are whispering-gallery mode (WGM) resonators. They confine light by total internal reflection at the interface between two dielectric media (around the outer circumference of the ring). WGM resonators are characterized by resonant frequencies (wavelengths), free spectral range FSR, finesse F, and quality-factor Q. Chapter 4 in [46] gives a detailed analysis of ring resonators, and [8] provides a concise overview with the mathematics behind them.

To determine resonant frequencies, first we need to define the optical path *OP*. *OP* is the distance the light travels along the ring circumference to complete one round, therefore:

$$OP = 2\pi r n_{eff}, \tag{2.1}$$

where r is the ring radius and n_{eff} is the resonant mode effective index. To consider the effect of different wavelengths, n_{eff} is usually replaced by the group refractive index n_g, therefore

$$OP = 2\pi r n_g, \tag{2.2}$$

where

$$n_g = n_{eff} - \lambda \frac{\partial n_{eff}}{\partial \lambda}. \tag{2.3}$$

Also, the *OP* should be a multiple of the resonant wavelengths

$$OP = m \times \lambda_m, \tag{2.4}$$

where λ_m are the resonant wavelengths and m is a positive integer. So, we get the resonant frequencies as

$$\lambda_m = \frac{2\pi r n_g}{m}. \tag{2.5}$$

Equation 2.5 works very well for rings with large r. But for small radii, [47] presents the following formula, which produces more accurate results

$$\lambda_m = \frac{2\pi r n_g}{m - 2\pi r \frac{\partial n_{eff}}{\partial \lambda}}, \tag{2.6}$$

where λ_m is the centre wavelength of the resonant band.

Resonators can support several resonant wavelengths that are separated by the *FSR*. The *FSR* is defined by

$$FSR = \frac{\lambda^2}{n_g L} \approx \frac{\lambda^2}{n_g 2\pi r}. \tag{2.7}$$

As seen in equation 2.7, *FSR* is inversely proportional to resonator's radius. Therefore, resonators with small radii are preferable for higher wavelength selectivity. But on the other

hand, large resonators are beneficial for optical frequency combs [48]. Such combs find many applications like high precision clocks rivaling to atomic clocks and precise length measurements.

As seen from equations 2.3, 2.5, and 2.6, due to material dispersion, a band of wavelengths centered around the resonant wavelength are coupled to the resonator. The ratio between FSR to the Full Width at Half Maximum $FWHM$ of resonant bands is the resonator Finesse $'F'$

$$F = \frac{FSR}{FWHM}. \tag{2.8}$$

Resonator selectivity is then defined by both FSR and F. Depending on the optical signal band of wavelengths, either FSR or F can be of more importance. For broadband signals FSR is more important as it can filter a higher ratio of the unwanted wavelengths, while for quasi-monochromatic signals, F is more important.

The most important parameter of micro-ring-resonators is the quality factor Q, as it is an indicator of the temporal behaviour of the resonator. Q is defined by

$$Q = \frac{E_{stored}}{E_{dissipated}} = \omega\,\tau, \tag{2.9}$$

where E_{stored} is the field energy stored in the resonator, $E_{dissipated}$ is the energy dissipated by the resonator, ω is the wave angular frequency, and τ is the photon decay time. And by following the derivation in [46], we can find that the field intensity inside the resonator is directly proportional to the square root of Q. This makes resonators with high Q-factors favourable in applications as nonlinear optics and wave mixing.

The Q factor is affected by resonator's losses; material loss, bend loss, scattering loss, two-photon absorption loss, and WGM loss. Two-photon absorption loss is a third-order nonlinear effect in the electric field that takes place at high field intensities. Reference [49] measures the two-photon absorption in silicon. As ring resonators are WGM resonators with curved surfaces, they experience incomplete total internal reflection leading to WGM losses (bend loss); and subsection **2.6.2** in [50] presents a good description of WGM loss.

Here we should distinguish between the loaded-Q and the unloaded-Q. Loaded-Q is measured when the resonator is coupled to waveguide(s), while unloaded-Q is when the resonator is not coupled. The Loaded-Q is always lower than the unloaded-Q due to an additional coupling loss, which requires the description of the coupling relations of optical signal between a ring-resonator and a waveguide.

The description of coupling relations between ring resonators and waveguides is concisely described by Yariv in [51], and a more detailed one in section **4.8** of his book [46]. It was

customary to derive the coupling parameters assuming a lossless coupler. But it was shown that this assumption is unnecessary and we refer the reader to [52], where the new derivation is reviewed and the coupling and loss coefficients of ring resonator were extracted. Here we only present the coupler parameters presented in [52] without their exact derivation, and refer the interested reader to the mentioned references.

From Fig. 2.2 we can conclude that

$$b_1 = t_c a_1 + K_c' a_2 \tag{2.10}$$

$$b_2 = t_c' a_2 + K_c a_1, \tag{2.11}$$

where a_1 is the input signal into the waveguide, a_2 is the input from the resonator, b_1 is the output signal from the waveguide, b_2 is the output into the resonator, t_c is the through-coupling in the waveguide, t_c' is the through-coupling in the resonator, K_c is the cross-coupling from the waveguide to the resonator, and K_c' is the cross-coupling from the resonator to the waveguide. Since the output b_2 circulates the ring and is coupled back to a_2 we get

$$a_2 = t_r' b_2. \tag{2.12}$$

Using the analysis in [52], due to energy conservation, we get

$$|b_1|^2 + |b_2|^2 = \alpha_c^2 |a_1|^2 + \alpha_c'^2 |a_2|^2, \tag{2.13}$$

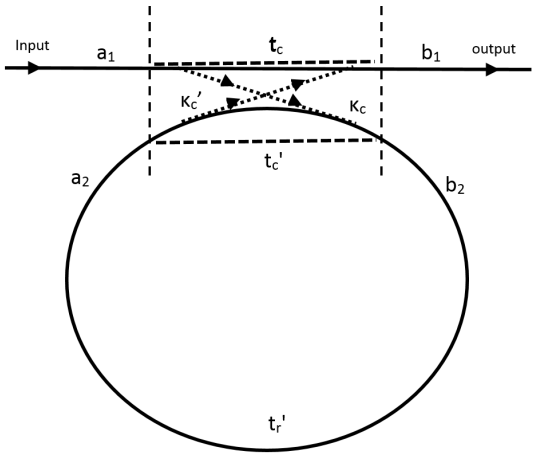

Fig. 2.2 Schematic of resonator waveguide coupler.

where α_c and α_c' are separate loss functions. Substituting 2.10, 2.11 and 2.12 in 2.13, then deriving the ratio between b_1 and a_1 we get

$$\frac{b_1}{a_1} = \left(\frac{t - \alpha\, e^{-i\Phi}}{1 - \alpha\, t\, e^{i\Phi}}\right) \frac{t_c}{t_c'^*}\, \alpha_c'\, e^{-i\Phi_c'}, \tag{2.14}$$

with

$$t \equiv \frac{|t_c'|}{\alpha_c'} \tag{2.15}$$

$$\alpha \equiv |t_r'|\, \alpha_c' \tag{2.16}$$

$$\Phi \equiv \Phi_c' + \Phi_r', \tag{2.17}$$

where Φ_c' is the coupling phase and Φ_r' is the transmission around the ring phase, and are defined by

$$t_r' = |t_r'|\, e^{i\Phi_r'} \tag{2.18}$$

$$t_c' = |t_c'|\, e^{i\Phi_c'}, \tag{2.19}$$

where t_r' is the 'transmission around the ring' loss factor. Now we have derived all the input and output equations, and left with the coupling coefficients. We have 5 coupling coefficients to derive, where t_r' is a complicated function of ring loss, but it can be defined as

$$t_r' = 1 - ring\, loss. \tag{2.20}$$

And the ring losses were defined previously and can be practically measured not analytically calculated, due to the complexity of loss mechanisms in ring resonators. The other four coefficients can be analysed using the coupled mode theory.

The coupled mode theory was originally developed for microwave coupling, and has been extended to include optical couplers later. The theory has been presented in numerous papers e.g. [53], and a review of it has been presented in [54]. The crucial factor we are interested in is the separation gap between the coupled waveguides. The coupled power is a function of the separation distance between the waveguides as seen in Fig. 2.3.

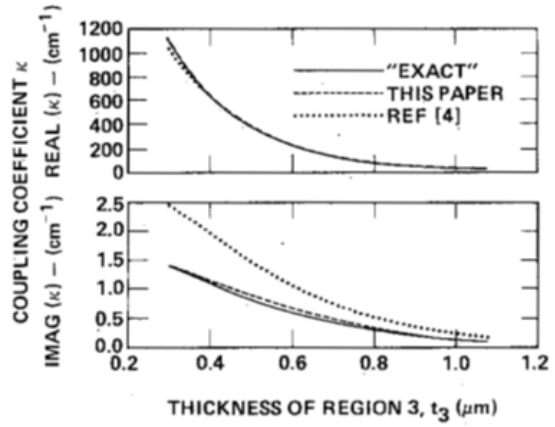

Fig. 2.3 Coupling coefficient vs separation gap. Adopted from[55].

Extending the coupled mode theory from parallel waveguides to curved surfaces, as the case of ring resonators, introduces more complexity, which require numerical methods to be used. But analytic solutions are available, e.g. [56], which show that the separation gap is a critical parameter in coupler design.

The dependency of the coupled power on the separation distance requires accurate design of the coupler. Inaccuracies in micro- and nano-fabrication techniques cause couplers' performance to deviate from the required optimum condition. A MEMS actuated coupler overcomes this problem, and adds extra advantages of total control over coupler's performance.

Numerical methods are essential for analysing and designing optical components. In **section 2.4** we briefly describe some of the numerical techniques used in photonics.

2.3.1 Nonlinear effects in optical micro-resonators

Ultra-high-Q micro-cavities are excellent platforms for studying nonlinear optical processes [57]. The high-Q factor translates to a longer photon decay time, which in turn allows for interactions between higher number of photons decreasing the nonlinear effects threshold power. Two of the micro-toroid cavities' nonlinear effects are the 'stimulated Raman scattering' and the 'optical parametric oscillations (OPOs)'.

To the best of my knowledge, only 'Anti-Stokes' stimulated Raman scattering has been reported to take place in optical micro-cavities. 'Anti-Stokes' means the photon frequency increases due to an inelastic scattering accompanied by the emission of an optical phonon. This increase in frequency (decrease in wavelength) is used for several applications including spectroscopy.

OPOs are easier described using the four-wave-mixing principle. The four-wave-mixing is described by the following equation:

$$\omega_{I1} + \omega_{I2} = \omega_{O1} + \omega_{O2}, \tag{2.21}$$

where ω_{I1} and ω_{I2} are two input photons, and ω_{O1} and ω_{O2} are two output photons. For OPOs, $\omega_{I1} = \omega_{I2}$ and are labeled 'pump wavelength', which is the input laser wavelength. And ω_{O1} and ω_{O2} are called the 'Idler' and 'Signal' wavelengths and are evenly spaced around the pump wavelength, with twice the FSR distance between them. Fig. 2.4 shows measured OPO spectrum.

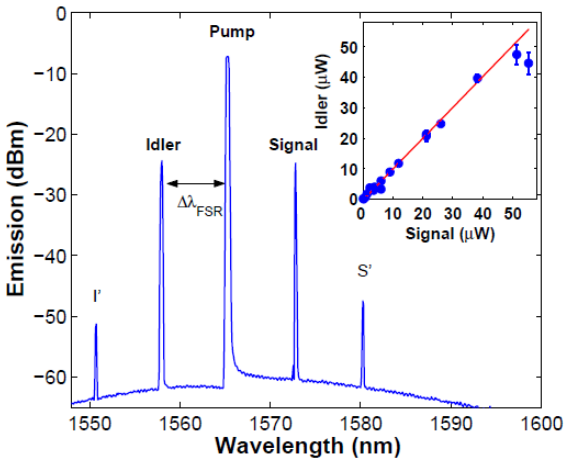

Fig. 2.4 Parametric oscillation spectrum showing pump, idler, and signal wavelengths. Inset: idler emission power vs signal emission power. Adopted from [57].

2.3.2 Silica micro-toroid resonators

Silica micro-toroid resonators are ultra-high-Q optical cavities that can be easily fabricated on chips and wafers. They are fabricated in three basic steps; 1) defining silica disc of radius slightly larger than the required toroid radius using lithography and pattern transfer techniques, 2) undercutting the silica disc by etching the underlying material, and 3) forming the toroid by melting the outer edges of the silica disc using CO_2 laser; as illustrated in Fig. 2.5. The detailed fabrication steps are presented in **Chapter 6**. For a comprehensive review about micro-toroidal resonators we direct the reader towards reference [57].

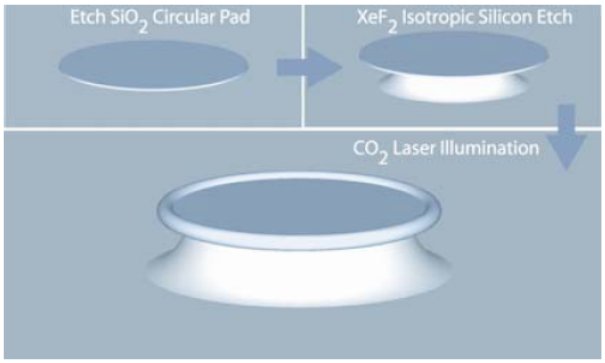

Fig. 2.5 Schematic of silica micro-toroid resonator fabrication. Image obtained from [57].

2.4 Numerical methods

Analytical methods provide exact solutions, but, unfortunately, for dielectric optical waveguides they do not usually yield accurate results. For a metallic waveguide filled with a dielectric, the electromagnetic wave vanishes at the interfaces. Such zero amplitude sets an exact predetermined condition for solving Maxwell's equations. For a dielectric waveguide, such rigid predetermined condition does not exist, which leaves the problem with more variables than can be solved for.

The classical way of solving problems with more variables than equations is the "trial and error" method. But this method becomes very time consuming when the number of variables is much higher than the number of equations to solve for. Several techniques try to reduce the number of steps required. And thanks to such techniques and computers, numerical methods nowadays provide easy and fast approaches of solving these problems.

In this section, we review some of these numerical methods that have been used to analyze optical components. Chapter **15** in [20] deals with numerical methods in depth.

2.4.1 Finite Difference Method (FDM)

This method is used to solve differential equations in a spatial domain that has boundary and/or initial conditions. This method can be broken down to 3 main steps:

1. Dividing the spatial domain into a grid of nodes,
2. setting approximate linear algebraic equations for the differential equations and boundary conditions, and
3. solving the algebraic equations.

The iteration method can be used to solve the algebraic equation after setting initial guesses. Alternatively matrix forms of the equations can be constructed and solved using Matrix operations.

An extension to this method is the Finite-Difference-Time-Domain method (FDTD), which was proposed by Yee [58]. It introduces temporal incrementing along with spatial incrementing of the domain. Reference [59] presents a good study of FDTD methods.

2.4.2 The Method Of Moments (MOM)

Also called "The moment method", is a simple method that is usually used to solve integral equations with known function limits. To better explain this method, we will resort to a simple 1D example, where the domain can be described by its length L. Let's assume we want to calculate a value called V which is defined by the equation

$$V = \int_0^L \frac{\rho_v}{constants} dl \tag{2.22}$$

This problem is then solved in the following steps:

1. Dividing the domain into small equal increments of size Δ, and use the center point of each element as the calculation node,
2. use one node as a fixed point and measure the length between it and every other node Δ_{mn}, then repeat this process for every node to form a matrix $[A]$ whose elements are defined as

$$A_{mn} = \frac{\Delta}{\Delta_{mn}}, \tag{2.23}$$

3. define column vector $[B]$ which includes the constants and the column vector V_m, then
4. define a column vector $[\rho]$ of the unknown elements, so we get

$$[B] = [A][\rho]. \tag{2.24}$$

Then we try to match the left-hand side to the right-hand side of the equation. And by using matrix inversion

$$[\rho] = [A]^{-1}[B] \tag{2.25}$$

the unknown quantities could be found.

2.4.3 Finite Element Method (FEM)

This method is useful for solving differential equations, and overcomes the limitation of the FD method in dealing with irregular shapes. It comprises of four steps:

1. Dividing the problem domain into small similar or different shaped elements,
2. assume the fields to be constant within each element; and define the governing equations for them,
3. gather the equations of all elements and form a global matrix, and
4. solve the equations simultaneously using the iterative method, or the global matrix using matrix methods.

The problem with optical simulations is that it requires very large volume to compensate for the space surrounding the waveguide. Most mechanical and thermal problems do not require huge volumes due to less effects of back-reflections. But with electromagnetics, reflections play a role. One way to deal with this is to set the outer boundaries to be scattering surfaces, or to use a Perfectly Matched Layer (PML), which acts as an infinite domain where waves decay very fast.

The FEM method is very powerful and produces accurate results. In this work, most of the optical, electromechanical and mechanical components have been simulated using the FEM through COMSOL® Multiphysics.

2.4.4 Eigenmode Expansion Method

Unlike the previously mentioned methods, this method relies on dividing the domain into a number of layers where the refractive index is constant [60, 61]. Then the fields at each layer are described by the sum of the eigenmodes of that specific layer. Dividing the domain into few number of layers ($\sim< 200$), massively decreases the calculation times compared to spatial discretisation methods, FDM, MOM and FEM ($\sim 1000s$ and $10,000s$ of elements). PML boundary conditions can be used in this method as well. The limitation of this method is that it can not calculate complex structures where the 6 components of the electric and magnetic fields are necessary. As the domain is divided into layers, the structure is reduced to 2D by assuming one dimension is infinite. This method is fast and accurate for simulating grating couplers for example.

Chapter 3

Grating Coupler Design

The grating coupler is an efficient robust mechanism for coupling light in/out of photonic chips. Its main drawbacks are that it has lower coupling efficiency than inverse taper edge couplers with lensed fibres, and has larger footprint. But it overcomes the problems with non-flat, unsmooth edges. Also, it provides higher coupling efficiency from/to regular optical fibres. As will be shown in **Chapter 5**, photonic platforms with suspended edges suffer from angular misalignment between the optical fibres and the on-chip edge coupling mechanisms. Grating couplers, being built away from chip edges, overcome this problem, as well as allowing for integrating the propagation waveguides and the coupling mechanisms into one e-beam write-field. In this chapter, SOI grating couplers' design is presented. These designs will be tested in future work to confirm the validity of the used design tool. The information presented here along with the application in **Appendix A** provide the used tool for designing straight and curved symmetric grating couplers. While using the application for designing apodised grating couplers is an ongoing work, it is expected to be ready in the near future.

3.1 Introduction

Grating couplers are being used for easy coupling of light in and out of photonic chips. They provide an out-of-plane mechanism for coupling light into nano-photonic wires; while overcoming edge coupling problems. They occupy a large area of integrated chips, which is one of their main drawbacks. On the other hand, grating couplers are not prone to a decrease in efficiency due to slight misalignments.

Symmetric grating couplers (periodic structure with elements having equal pitch, fill factor(W/period) and etch depth as depicted in Fig. 3.1) are studied and presented as periodic perturbations of refractive index in photonics textbooks (e.g. [46]). And [62] is a good reference for the basic principles behind grating couplers. Symmetric grating couplers suffer

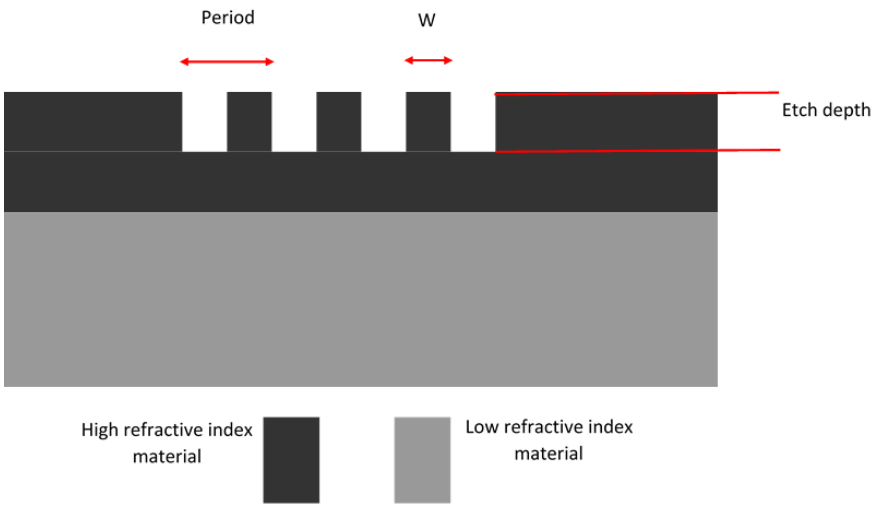

Fig. 3.1 Schematic of symmetric grating coupler.

from low efficiency due to losses. Due to the symmetry of the structure, half of the coupled power propagates in the opposite direction. Tilting the input beam by a small angle with the normal to the coupler top surface breaks the symmetry of the structure and improves the directionality of the coupled power. Adding grating back reflectors, as the work presented in [63], helps in redirecting the backward propagating power into the forward direction. Also, some of the power is lost to the substrate, and by adding bottom-reflectors, the power lost to the substrate can be minimized. These reflectors can either be layers of dielectrics [63], or metals.

The field distribution of symmetric grating couplers along the propagation direction does not match the gaussian profile of the optical fibre field, as shown in Fig. 3.2. This mode mismatch is the biggest contributor to the limited coupling efficiency. Asymmetry can be introduced in the grating coupler to reshape the couplers' field distribution to a closer fit with a gaussian profile. Asymmetry is achieved by varying the etch depth for each period, or more practically by varying the period width and fill factor for each grating element [64] (apodised grating coupler). Different methods have been conducted for improving grating couplers' efficiencies, like adding an overlay [65], or double etch depth apodized grating couplers [66]. The work by Dirk Taillaert et al. in [67] and his doctorate thesis [68] provide a comprehensive study about straight grating couplers. To avoid processing the guiding layer, refractive index perturbation has been achieved with metal gratings [69], which showed high coupling efficiencies.

Straight grating couplers, have large width in the perpendicular direction to the propagation direction. And for efficient decrease in the mode size from few microns down to few

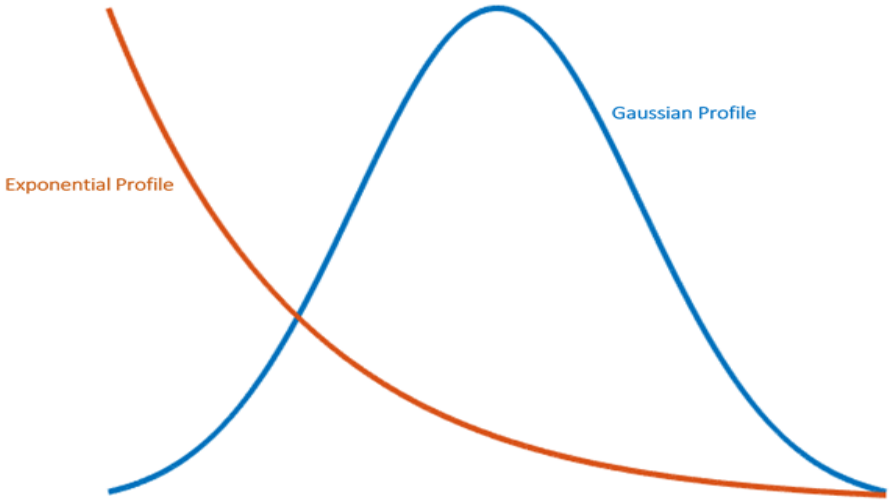

Fig. 3.2 Optical fibre's field gaussian profile vs grating coupler's field exponential profile.

hundreds nanometers (width of photonic wires), adiabatic tapers with lengths of hundreds of microns are required [70]. To eliminate the need for long transition tapers, focused grating couplers have been developed (e.g. [71]). A curved grating structure is used to focus the coupled light from an optical fibre down to the photonic wire width. Using focusing grating coupler shortens the taper length more than an order of magnitude, which enables more compact denser photonic chips.

3.2 Design

3.2.1 First principles (symmetric straight grating coupler)

Here, the design of the input coupler is presented. And according to the reciprocity principle, an identical output coupler will behave in the exact same manner. The 2D cross-section of the symmetric grating coupler (Fig. 3.1) is considered for the study where its width (normal to the page plane) is assumed infinite during simulations. As the width is at least an order of magnitude larger than the coupler's thickness and the element's period, it is safe to consider it infinite to simplify the coupler's structure from 3D to 2D [72]. The starting point of design is derived from the Bragg law for infinite periodic structures [64]

$$\frac{2\times n_{cl}}{\lambda}\times cos(\theta_{out}) = \frac{2\times n_{eff}}{\lambda}\times cos(\theta_{in}) + \frac{2\times q}{\Lambda} \tag{3.1}$$

where n_{cl} is the superstrate refractive index, λ is the wavelength, θ_{out} is the off-vertical tilt angle of the incident beam, n_{eff} is the coupler's effective index, θ_{in} is the input angle into the waveguide with respect to the propagation direction, q is the diffraction order and Λ is the grating period. For subwavelength waveguide thicknesses, θ_{in} is effectively zero. The first diffracted order beam is the coupled light, therefore q equals -1. So, equation 3.1 becomes

$$\frac{n_{cl}}{\lambda} \times cos(\theta_{out}) = \frac{n_{eff}}{\lambda} - \frac{1}{\Lambda}. \tag{3.2}$$

By choosing the operation wavelength according to the required application ($1.55\mu m$), two variables have to be determined, θ_{out} and Λ. When light falls from a low refractive index medium on its boundary with a higher refractive index medium, light diffraction and reflection occur. To increase the grating couplers' efficiency, the back reflections should be minimized. The etch depth of the grating coupler determines its effective index and hence, the back reflection. The effective index and back reflections were calculated numerically by assuming that the grating coupler is an infinite periodic structure with infinite width. As a matter of fact, the back reflection (transmittance) from the boundary between the grating coupler's top surface and superstrate increases (decreases) with increasing θ_{out}. The back-reflections were calculated using COMSOL® Multiphysiscs.

An example of back reflection (transmission) is presented in Fig. 3.3 for the SOI structure with air superstrate. Since we assume an infinite periodic grating coupler, only one cell of the grating coupler has been simulated with boundary conditions as shown in Fig. 3.4. Different grating structures (variable etch depths, periods and fill factors) have been studied, and it was observed that all the structures behave in a similar fashion as shown in Fig. 3.3. Tilt angles below 12^o show almost the similar maximum (minimum) transmission (reflection) percentage. In general, it is customary to use $8-12^o$ tilt angles.

The back reflection from the boundary between the coupler and the substrate is a secondary reflection. It can be calculated after calculating the transmitted power from the coupler's top surface. If the substrate thickness is a controllable parameter, it should provide an integer multiple of half the operation wavelength in the substrate medium [63]. The multiple of half the wavelength condition is to ensure constructive interference between the incident and reflected waves. For constructive interference, the wave travel distance needs to be a multiple of the wavelength, therefore the wave requires one half of the wavelength in the forward direction and one half in the reflected direction. However, the multiple of half the wavelength has been confirmed, it does not provide the exact thicknesses for maximising the efficiency. The maxima in the efficiency plots, as shown in Fig. 3.5, confirm the half wavelength periodicity, but they do not coincide with thicknesses equal to multiples of half

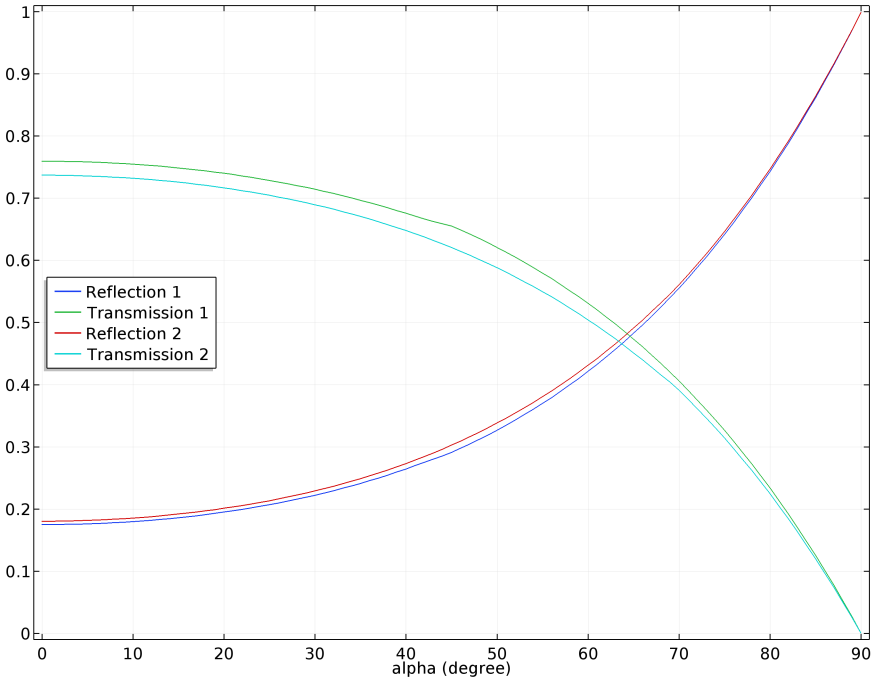

Fig. 3.3 Sample reflection (R) and transmission (T) plot for grating couplers, highlighting the identical nature of R and T among the different grating couplers' structures.

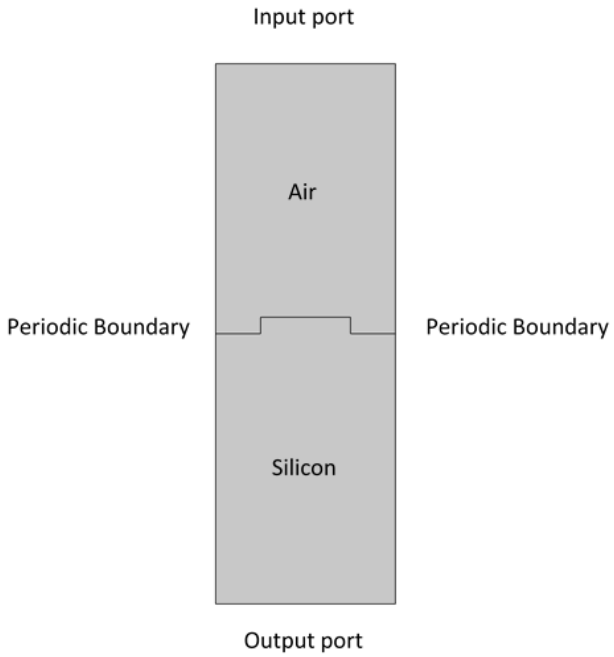

Fig. 3.4 Domain materials and boundary conditions for reflection and transmission simulations.

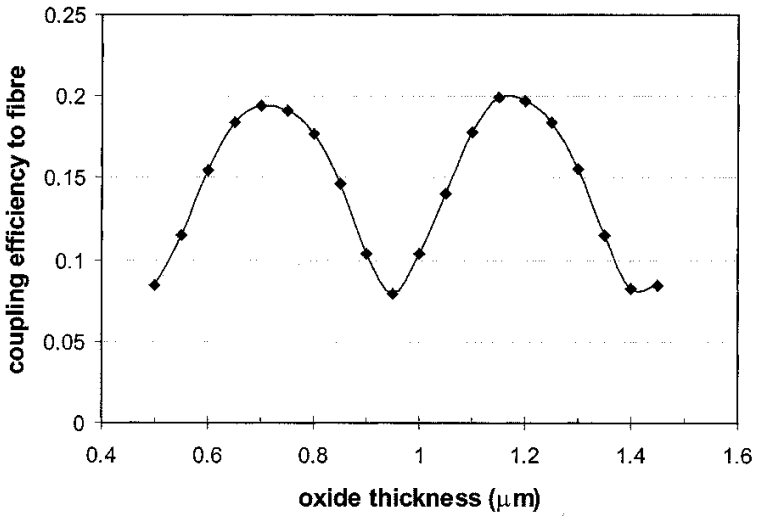

Fig. 3.5 Effect of substrate thickness on grating coupler's efficiency. Adopted from [63].

the wavelength in the material. This behaviour occurs because the first half-wavelength propagation distance occurs in the grating layer and the cladding layer. After that, the wave propagates solely in the cladding medium. Due to this fact, we produced the following formula for calculating the substrate thickness

$$t_{sub} = (\frac{\lambda}{2 \times RI} - \frac{t_{eff} \times n_{eff}}{RI}) + \frac{m \times \lambda}{2 \times RI},\ m = 0, 1, 2, ... \tag{3.3}$$

where t_{sub} is the substrate thickness, RI is the refractive index of the substrate, n_{eff} is the grating effective index, and t_{eff} is the grating effective thickness. Here we used an effective thickness for the grating coupler as the field does not couple exactly at the top surface of the structure. Producing exact mathematical formulas of equation 3.3 and t_{eff} is beyond the scope of this work, here we merely attempt at producing an approximate formula when exact simulations of the substrate thickness on efficiency is not possible, where t_{eff} is assumed to be

$$t_{eff} = groove\,thickness + \frac{tooth\,thickness - groove\,thickness}{2}. \tag{3.4}$$

Equation 3.3 was tested with several reported results and proved to be a good approximation.

Even after optimising the substrate thickness, portion of the energy gets lost in the underlaying layer. To minimise this loss, a metal reflector can be introduced at the bottom of the substrate to maximise the upward reflected energy. Or by adding multiple dielectric layers to form a Bragg back-reflector as the case with optical fibres [73]. These dielectric

layers should be spaced according to the Bragg equation for back-reflection

$$\Lambda_B = \frac{\lambda}{2 \times n_B} \tag{3.5}$$

where Λ_B is the Bragg reflector period and n_B is the Bragg reflector effective index.

After optimising all the previous parameters to minimise losses, we are left with one loss mechanism that needs to be tackled that is the backward propagating energy. Backward propagating energy is all the field energies that propagate in the opposite direction than the direction of the propagation waveguide. One can add a second waveguide in the opposite direction to collect this lost energy and reintroduce it to the main propagation waveguide. The main drawback to this method is that it increases the Grating coupler's footprint. A better approach is to redirect the backward propagating energy into the forward direction using back reflectors. Back reflectors can be thought of as a second grating coupler where the angle between the input and output fields is 180^o. To redirect the field back into the grating coupler, the back-reflector periods should match the Bragg condition in equation 3.5.

After deciding on the incident angle, substrate thickness, back and bottom reflectors, the grating period can be calculated from equation 3.2. The effective index in equation 3.2 can be calculated from the equation

$$n_{eff} = \sqrt{ff \times (n_{eff-high})^2 + (1-ff) \times (n_{eff-low})^2} \tag{3.6}$$

where ff is the fill factor, $n_{eff-high}$ and $n_{eff-low}$ are the effective indices of the tooth and the groove, respectively. As the first principle values are calculated based on the assumption of an infinite periodic structure, the practical values will deviate slightly from these results. Therefore, several periods around the calculated value and different fill factors should be examined to reach the optimal value. CAMFR[1] [74] was used to calculate the coupling efficiency for the different parameters (the application in **Appendix A**). CAMFR is a fast, free and widely used tool for studying grating couplers.

In this work the device layer and oxide thicknesses were fixed, hence, the design variables were limited to the period, fill factor, and etch depth. The scattered fields from the SOI symmetric grating coupler were simulated using CAMFR, then the mode matching with a Gaussian optical fibre field of $5.2\mu m$ radius was calculated. A sample field plot of one of the grating designs is shown in Fig. 3.6. The efficiency calculations of different SOI grating couplers' designs with 20 periods, $260nm$ device layer and $2\mu m$ oxide substrate at 8^o incident angle are presented in Fig. 3.7. The way CAMFR works introduces some errors

[1] CAMFR is a full-vectorial eigenmode expansion Maxwell solver.

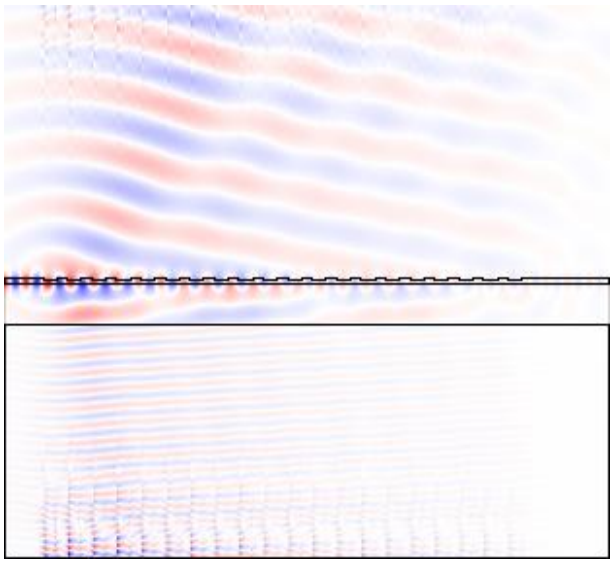

Fig. 3.6 Simulated grating coupler scattered field using CAMFR.

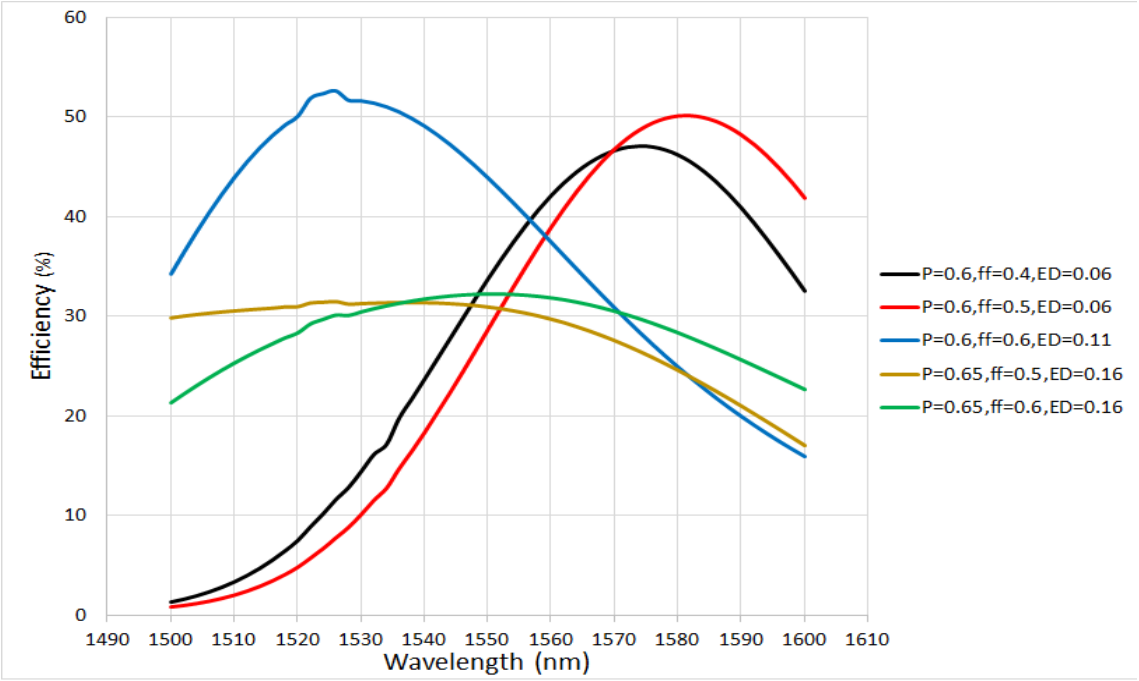

Fig. 3.7 Efficiency plots for silicon grating couplers with 260nm device layer on top of 2μm oxide layer at 8^o incident angle. P = period, ff = fill factor, and ED = etch depth.

at certain wavelengths during a parametric wavelength sweep (the dips and bumps in the efficiency curves in Fig 3.7). These errors have occurred in other works (e.g. [75]). The code for the presented application has been modified to reduce these errors, and has been eliminated from most simulations. These errors have been left here for pointing out this fact

for other users of this application. In the rare occasion of encountering few errors, simple interpolation operations can easily remedy them.

3.2.2 Apodised straight grating coupler

Although the design of an apodised grating coupler is an ongoing work, this section is included here for completeness.

The symmetric grating coupler suffers from low efficiency, due to the mismatch in the structure's field shape and the fibre's field shape, as shown in Fig. 3.2. A symmetric structure has a decaying exponential field shape along the propagation direction. This behaviour is due to the similarity in the amount of the diffracted field from each period. To improve the coupling efficiency, asymmetry between the grating elements has to be introduced (apodised grating coupler). As well as, apodised grating couplers allow for vertical input/output coupling with high efficiency [64].

To better explain the purpose of apodised grating couplers, assume a grating coupler consisting of N number of elements. The energy diffracted from the structure should match the stepwise approximation of the Gaussian distribution shown in Fig. 3.8. The analogy presented here is qualitative not quantitative.

Deciding on the input tilt angle for apodised grating couplers is not as straightforward as in the case of symmetric grating couplers. The grating structure is not periodic, therefore simulating the back reflection is challenging. But small tilt angles ($< 12^o$) are usually used. Another difference between symmetric and apodised grating couplers is the fact that apodised grating couplers show high coupling efficiencies with vertical coupling (0^o tilt angle). The

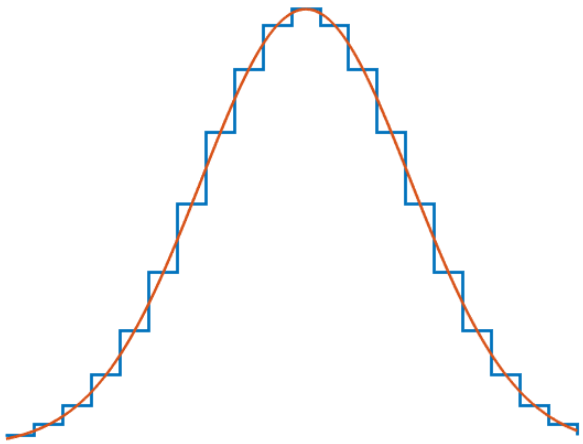

Fig. 3.8 Stepwise approximation of grating coupler field to better match the Gaussian distribution of the optical fibre.

common practice is to decide the tilt angle based on physical constraints, go with the $8-12^o$ tradition, or implement it with the efficiency calculations. For back and bottom reflectors, they follow the same rules as for the symmetric grating coupler design.

Apodised grating couplers can have an infinite number of different structures (periods, fill factors and etch depths). It is impossible to design them based on the first principles, but a symmetric structure will provide a good starting point for the design. Then, large number of iterations of the design parameters has to be run to settle on the best (or one of the best) design. Randomly varying the design structures is not an efficient technique, as it might drift from the optimum conditions easily. A better approach is to use a genetic algorithm to search for the optimum design. A good introduction about genetic algorithm can be found on the website [http://www.obitko.com/tutorials/genetic-algorithms/index.php], and a good explanation for the genetic algorithm approach for designing grating couplers is presented in chapter **4** of [76].

3.2.3 Curved grating coupler

A curved grating coupler is simply a straight coupler that is curved in an elliptical shape to focus the coupled light into the waveguide. Therefore, all design parameters are similar to the straight coupler. Then the coupler lines are curved according to the equation [77]

$$m \times \lambda = n_{eff}\sqrt{Y^2+Z^2} - Z \times n_{cl} \times sin(\theta_{out}) \tag{3.7}$$

where m is an integer corresponding to each grating line, and Y and Z are the coordinates for each point on the curved line as shown in Fig. 3.9, where Z is the propagation direction and the waveguide input is the origin. All ellipses have the same focal point, which coincides with the coupler's optical focal point.

The optical focal radius, which determines the number of the closest line, is determined by calculating the distance a spherical wave diffracting from the waveguide needs to match the optical fibre mode size. This can be obtained from the Gaussian beam's far-field equation [78]

$$\omega(Z) = \omega_0 \sqrt{1+(\frac{Z}{Z_R})^2} \tag{3.8}$$

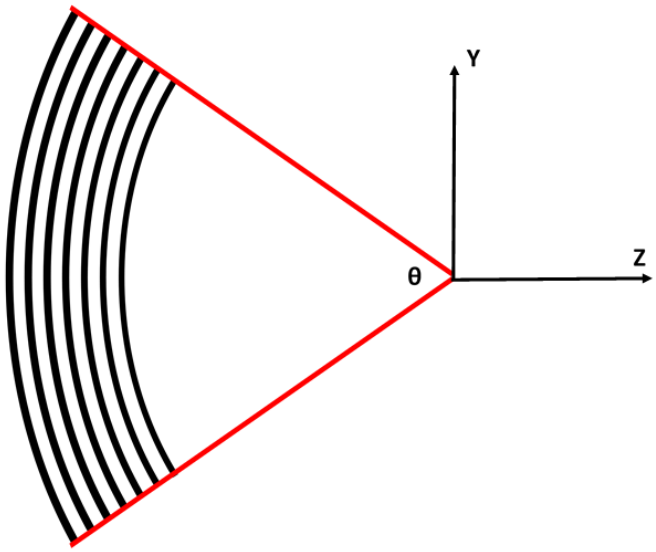

Fig. 3.9 Schematic of curved grating coupler.

where $\omega(Z)$ is the fibre beam radius, ω_0 is half the waveguide's effective mode width, Z is the optical focal distance, and Z_R is the Rayleigh range that is defined as

$$Z_R = \frac{\pi \times \omega_0^2 \times n_{eff}}{\lambda} \tag{3.9}$$

where n_{eff} is the effective index of a slab waveguide with thickness equal to the nanowire thickness. Or simply, as the focal radius is much larger than the Rayleigh range, it can be calculated from

$$Z = \frac{\pi \times \omega_0 \times n_{eff} \times \omega(Z)}{\lambda} \tag{3.10}$$

ω_0 differs from the waveguide's width and was expected to be larger, as the mode is not fully confined in the nano-waveguide. ω_0 can be calculated from the mode effective area which is defined by [79]

$$A_{eff} = \frac{(\iint_{-\infty}^{\infty}((E \times H).\hat{z}).dx.dy)^2}{(\iint_{-\infty}^{\infty}((E \times H).\hat{z})^2.dx.dy)} \tag{3.11}$$

where $(E \times H).\hat{z}$ is the Poynting vector's time-averaged z-component, and $\hat{z}$ is the unit vector along the propagation direction. Equation 3.11 can be calculated numerically (e.g. using COMSOL®) and ω_0 get extracted from the results. A simpler, numerical, method for calculating ω_0 is to measure the width at which the electric field of the waveguide

drops to $1/e^2$ of its maximum value (assuming Gaussian field distribution, which is an acceptable approximation for isotropic waveguides). Then the ellipse section angle can be easily determined from

$$\theta = 2 \times tan^{-1}(\frac{\omega(Z)}{Z}) \tag{3.12}$$

When the focus is at ∞ we get a straight waveguide.

For the SOI grating coupler with the aforementioned parameters in the 'symmetric grating coupler' section, equation 3.10 was used to calculate the curved grating coupler's focal radius. The grating coupler couples to a $500 \times 260nm$ photonic wire, which according to COMSOL® simulation has half effective mode width of $422nm$. Using this value along with the $260nm$ slab mode effective index of 2.94, $5.2\mu m$ fibre radius, and $1.55\mu m$ wavelength, the curved coupler focal radius was calculated to be $\sim 13.1\mu m$. $13.1\mu m$ is the Z distance of the first grating line along the waveguide axis. Each consecutive line has a Z distance of $13.1\mu m + n \times period$, where n = number of grating line -1.

3.3 Summary

The design steps, along with brief explanation, have been presented for SOI symmetric grating coupler. The results presented here is very beneficial for the future design of a grating coupler for the suspended NCD platform presented in **Chapter 5**. Also, the design steps of an apodised grating coupler have been presented and a genetic algorithm code for calculating its performance is being developed.

Chapter 4

Scattering Loss from Asymmetric Rough Rectangular Waveguides

4.1 Loss from symmetric slab waveguide

Scattering loss is a serious concern in photonic chips. Scattering loss arises from waveguide's surface imperfections, mainly roughness. Estimating scattering loss beforehand provides confirmation about the practicality of the waveguide design and the fabrication method. Here we attempt to use the effective index method [80] in calculating the scattering loss from rectangular dielectric waveguides with rough surfaces. An approximate, with high accuracy, theory for predicting scattering loss due to roughness in symmetric slab waveguides was first introduced by Maracus [81]. We use a simpler model that was introduced by [82] for the same case, where the scattering loss (α) is given by

$$\alpha = \frac{\sigma^2}{\sqrt{2}.k_0.d^4.n_1}.g(V).f(x,\gamma) \tag{4.1}$$

for calculating the scattering loss from asymmetric slab waveguide, as in Fig. 4.1a. And use the result in calculating the scattering loss from a second asymmetric slab waveguide, Fig. 4.1b. Then add both results to produce the scattering loss from the resultant rectangular waveguide, Fig. 4.1c.

In Equation 4.1, σ is the RMS surface roughness, k_0 is the wavevector in free space, d is the slab half thickness, n_1 is the core refractive index, and $g(V)$ and $f(x,\gamma)$ are dimensionless functions depending on waveguide structure and roughness spectral density function,

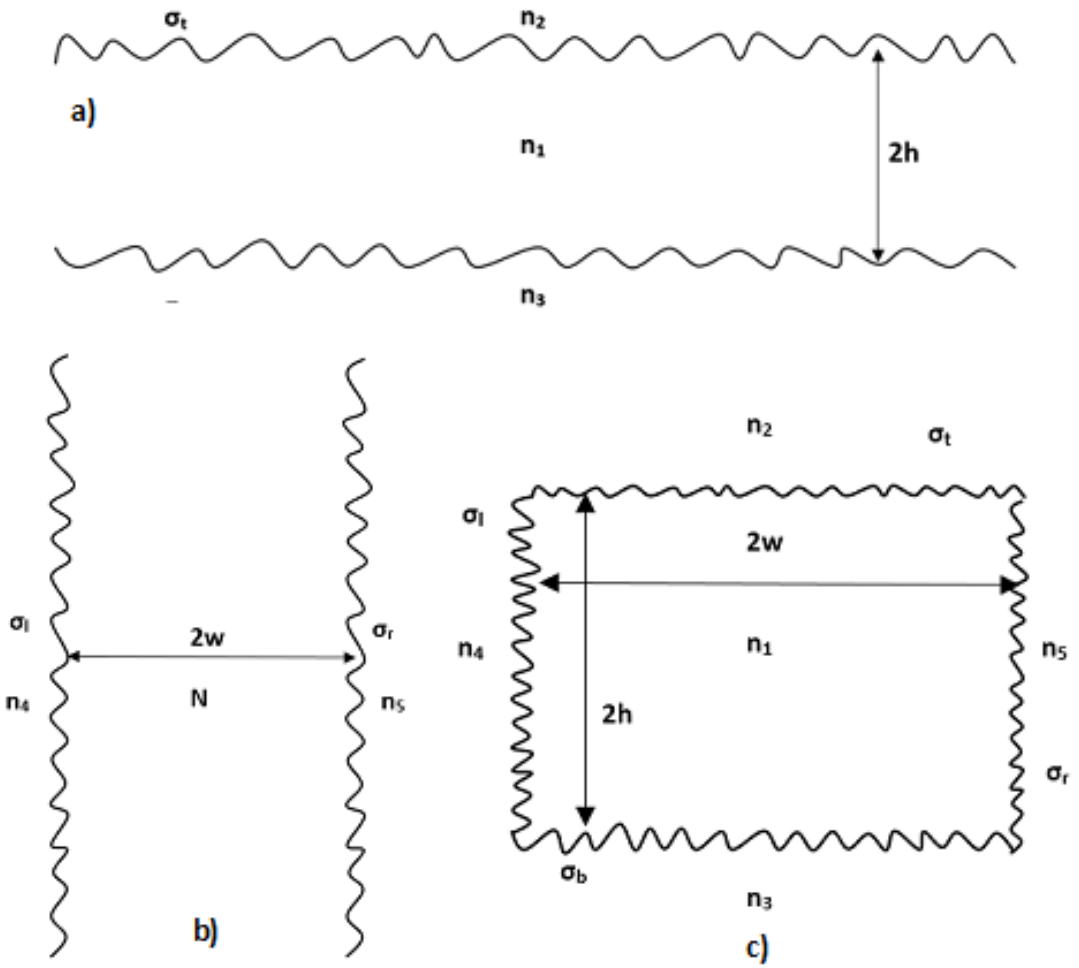

Fig. 4.1 Asymmetric rough horizontal slab (a), vertical slab (b) and rectangular (c) waveguides.

respectively. $g(V)$ is defined as

$$g(V) = \frac{U^2.V^2}{1+W} \tag{4.2}$$

where

$$U = k_0.d\sqrt{{n_1}^2 - {n_{eff1}}^2} \tag{4.3}$$

$$V = k_0.d\sqrt{{n_1}^2 - {n_{cladding}}^2} \tag{4.4}$$

$$W = k_0.d\sqrt{{n_{eff1}}^2 - {n_{cladding}}^2} \tag{4.5}$$

And $f(x,\gamma)$, for surface roughness defined by exponential correlation function, is given by

$$f(x,\gamma) = \frac{x[(1+x^2)^2 + 2x^2\gamma^2]^{0.5} + 1 - x^2]^{0.5}}{[(1+x^2)^2 + 2x^2\gamma^2]^{0.5}} \tag{4.6}$$

where

$$x = W\frac{L_c}{d} \tag{4.7}$$

$$\Delta = \frac{{n_1}^2 - {n_{cladding}}^2}{2{n_1}^2} \tag{4.8}$$

$$\gamma = \frac{n_{cladding}.V}{n_1.W\sqrt{\Delta}} \tag{4.9}$$

where L_c is the roughness correlation length.

4.2 Loss from asymmetric rectangular waveguide

Equation 4.1 was produced based on the assumption that scattering loss occurs independently from both surfaces of symmetric slab waveguide, where each surface contributes to one half of the scattering loss. Due to this independency, we examine the equation for the variables that has to be altered for the formula to be applicable for asymmetric slab waveguide. Here we revert to the original scattering loss formula for symmetric slab waveguide presented in [82], where scattering loss is defined as

$$\alpha = \Phi^2(d).({n_1}^2 - n^2_{cladding})^2.\frac{{k_0}^3}{3\pi n_1}\int_0^\pi R(k_0.n_{eff1} - k_0.n_{cladding}.cos(\theta))d\theta. \tag{4.10}$$

$\frac{{k_0}^3}{3\pi n_1}$ is a constant for a waveguide and is not affected by the cladding material, therefore, it can be excluded. $({n_1}^2 - n^2_{cladding})^2$ is the refractive indices difference and can be different at each surface. $R(k_0.n_{eff1} - k_0.n_{cladding}.cos(\theta))$ describes surface roughness and can be different for each surface; in the above equation roughness was assumed to be similar on both surfaces. The only parameter that will be affected by the asymmetry of the waveguide

is $\Phi(d)$, as it describes the modal shape at the surface. $\Phi(d)$ is introduced in [83] as

$$\Phi^2(d) = \frac{2.V.(1-b)}{d(V+\frac{1}{\sqrt{b}})} \tag{4.11}$$

where

$$b = \frac{{n_{eff1}}^2 - {n_{cladding}}^2}{{n_1}^2 - {n_{cladding}}^2} \tag{4.12}$$

By referring to Fig. 4.2 and using similar analysis for asymmetric slab waveguide as in [84] we can conclude that

$$\Phi^2(d) = \frac{2.V.(1-b_t)}{d(V+\frac{1}{\sqrt{b_t}})} \tag{4.13}$$

$$\Phi^2(-d) = \frac{2.V.(1-b_b)}{d(V+\frac{1}{\sqrt{b_b}})} \tag{4.14}$$

where the subscript "t" refers to the top surface and the subscript "b" refers to the bottom surface. It is obvious from equations 4.13 and 4.14 that $\Phi(y)$ can be calculated independently at each surface. Therefore, the scattering loss for asymmetric slab waveguide can be calculated at each surface independently by using symmetric slab with identical parameters on

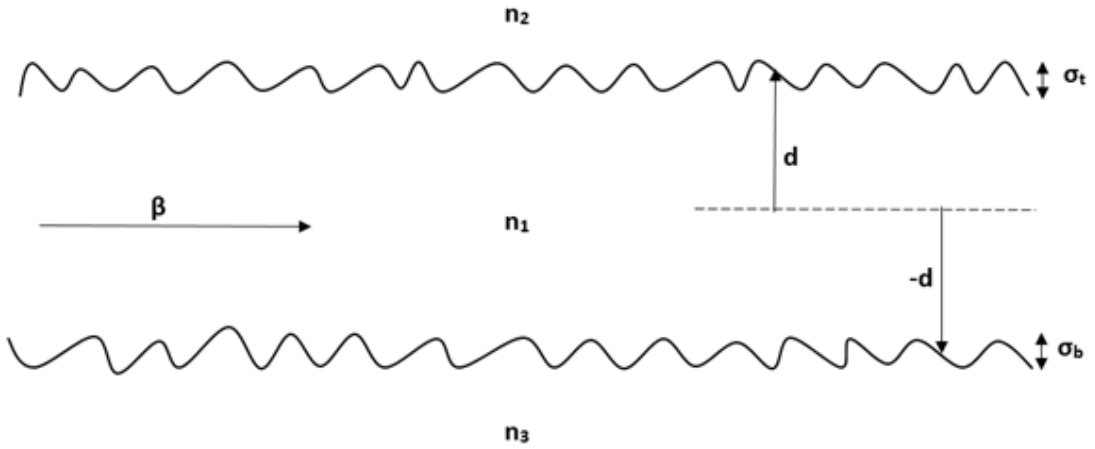

Fig. 4.2 Asymmetric slab waveguide

both surfaces that match one of the asymmetric slab surfaces. Then substitute these values in equation 4.1 and dividing the result by two. This process is then repeated for the second surface of the asymmetric slab waveguide. Finally, both results are combined to produce the total loss from the asymmetric slab waveguide.

For asymmetric slab waveguide, the scattering loss from the top and bottom surfaces are given by

$$\alpha_t = \frac{{\sigma_t}^2}{\sqrt{2}.k_0.h^4.n_1}.g_t(V).f_t(x,\gamma) \times 0.5 \tag{4.15}$$

$$\alpha_b = \frac{{\sigma_b}^2}{\sqrt{2}.k_0.h^4.n_1}.g_b(V).f_b(x,\gamma) \times 0.5 \tag{4.16}$$

respectively; where we substitute the surface roughness and cladding refractive index of each surface in the corresponding equation. Then we calculate the total scattering loss from the asymmetric slab waveguide by

$$\alpha_{total} = \alpha_t + \alpha_b. \tag{4.17}$$

Then, we convert the total scattering loss to extinction coefficient using the equation

$$k = \frac{\alpha.\lambda}{4.\pi} \tag{4.18}$$

where λ is the propagation wavelength. In the effective index method, the effective index of the first slab waveguide is used as the core refractive index of the second slab waveguide. Instead of using n_{eff1} (the slab waveguide effective index) as the core refractive index, the complex refractive index N is used, which is defined as

$$N = n_{eff1} + i.k \tag{4.19}$$

Then n_1 in equation 4.1 is replaced by N for calculating the scattering loss from the right and left surfaces of the second slab waveguide in Fig. 4.1b, as

$$\alpha_r = \frac{{\sigma_r}^2}{\sqrt{2}.k_0.w^4.N}.g_r(V).f_r(x,\gamma) \times 0.5 \tag{4.20}$$

$$\alpha_l = \frac{{\sigma_l}^2}{\sqrt{2}.k_0.w^4.N}.g_l(V).f_l(x,\gamma) \times 0.5 \tag{4.21}$$

And the total scattering loss from the rectangular waveguide in Fig. 4.1c, will be

$$\alpha_{total} = \alpha_t + \alpha_b + \alpha_r + \alpha_l \tag{4.22}$$

Equation 4.22 can be easily calculated using a computer program, and a sample code is presented in **Appendix B**. But here we attempt to derive a simple, approximate, solution for highlighting the effect of using the complex refractive index for the second slab calculations rather than ignoring the extinction coefficient effect on scattering loss.

For simplicity, the derivation of $f(x,\gamma)$ will not be conducted and will be assumed as factor of the equation. Hence, we get the scattering loss equation to be

$$\alpha = \frac{\sigma^2}{\sqrt{2}.k_0.w^4.(n_{eff1}+ik)}.\frac{U^2.V^2}{1+W}.f(x,\gamma) \tag{4.23}$$

For a specific waveguide and operation conditions, σ, k_0, and w are constants, which can be impeded with $f(x,\gamma)$ in one coefficient A. So, we get

$$\alpha = A.\frac{U^2.V^2}{1+W} \tag{4.24}$$

W is not affected by the complex refractive index, therefore, A and $(1+W)$ will be omitted from the derivation for brevity. After substituting the equations for U and V, with n_{eff} is the rectangular waveguide effective index real part

$$\alpha = \frac{{k_0}^4.w^4[(n_{eff1}+ik)^2 - {n_{eff}}^2][(n_{eff1}+ik)^2 - {n_{cladding}}^2]}{(n_{eff1}+ik)} \tag{4.25}$$

By performing the complex number division and some lengthy algebra, we arrive at

$$\alpha_{real} = \frac{{k_0}^4.w^4}{{n_{eff1}}^2+k^2}\left(n_{eff1}.\left[({n_{eff1}}^2 - k^2 - {n_{eff}}^2)({n_{eff1}}^2 - k^2 - {n_{cladding}}^2) - 4.k^2.{n_{eff1}}^2\right]\right.$$
$$\left. +2.k^2.n_{eff1}\left[({n_{eff1}}^2 - k^2 - {n_{eff}}^2) + ({n_{eff1}}^2 - k^2 - {n_{cladding}}^2)\right]\right) \tag{4.26}$$

$$\alpha_{imaginary} = \frac{i.{k_0}^4.w^4}{{n_{eff1}}^2 + k^2}\left(k.\left[({n_{eff1}}^2 - k^2 - {n_{eff}}^2)({n_{eff1}}^2 - k^2 - {n_{cladding}}^2) - 4.k^2.{n_{eff1}}^2\right] + 2.k.{n_{eff1}}^2\left[({n_{eff1}}^2 - k^2 - {n_{eff}}^2) + ({n_{eff1}}^2 - k^2 - {n_{cladding}}^2)\right]\right) \tag{4.27}$$

From the complex representation in Fig. 4.3, and as

$$k \perp n_{eff} \tag{4.28}$$

and as α is proportional to k we can conclude that the real part of alpha will contribute towards the scattering loss, while the imaginary part will contribute towards the real part of the propagation constant (n_{eff}). This can be physically represented by the amount of the scattered light, from two parallel faces of the rectangular waveguide, that gets reflected back into the waveguide due to the presence of the other two orthogonal surfaces.

For most practical applications, $k \leqslant 10^{-5}$, therefore it can be shown that the back scattering will not contribute much towards the real part of the effective index. But for waveguides with large scattering loss, k will be large enough to have a positive/negative effect on the real part of the effective index.

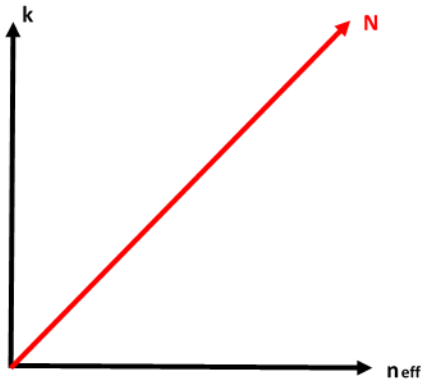

Fig. 4.3 Complex representation of refractive index.

4.3 Results

The scattering loss from the diamond rib-waveguide structure presented in **Chapter 5** was calculated for the wavelength range $0.2\mu m$ to $3\mu m$. The waveguide was estimated by a rectangular waveguide with the same width and height as the ridge-section of the

waveguide. The ridge width and height are $0.6\mu m$ and $0.456\mu m$, respectively. The RMS surface roughness of the top ridge surface was assumed $2nm$ (maximum possible value), and the bottom surface roughness was set to zero as the diamond was grown on atomically flat silicon wafer. The rib top surface RMS roughness was measured using an AFM (Veeco Metrology Group) in tapping mode and found to be $3.1nm$, and the average correlation length was estimated to be $81nm$. The sidewall roughness parameters were assumed to be similar to the rib roughness parameters. Varying the wavelength over the specified range resulted in the loss curve presented in Fig. 4.4.

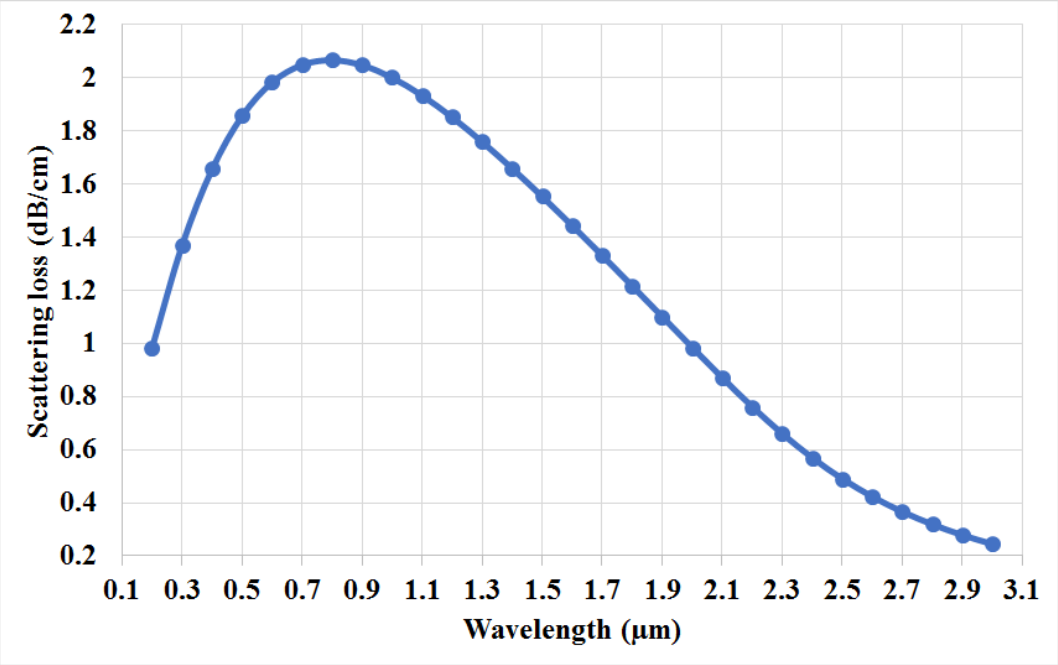

Fig. 4.4 Scattering loss from rough waveguide surfaces vs operation wavelengths.

4.4 Summary

In summary, we believe the results presented in this study is essential for predicting the practicality of using specific waveguide design, operation wavelength, and/or fabrication technique. Estimating the scattering loss for rough surfaces beforehand is very beneficial for low-loss material waveguides, as the scattering loss from surface is the dominant loss mechanism. For example, it is concluded that the proposed diamond waveguide structure presented in **Chapter 5** will show low propagation loss when operating at wavelengths higher than $2\mu m$, as depicted in Fig. 4.4.

Chapter 5

Nanocrystalline Diamond Waveguide[1]

5.1 Introduction

Integrated photonic chip technology has developed into a mature technology, with silicon and III-V semiconductor platforms and the telecommunication spectral window being the main focus of research in this area. Expanding this research into other parts of the optical spectrum requires new materials and architectures, mainly due to the absorption bands of the aforesaid materials. In particular, the use of the silicon-on-insulator platform at middle and long infrared wavelengths is limited by the spectral transmission windows of both the buried oxide and silicon device layers.

Diamond is a wide bandgap material with a much larger optical transmission window [7] and is therefore an excellent candidate for photonic chips operating in the UV, visible and infrared spectral regions. Due to its high refractive index (2.39), it allows for the fabrication of sub-micron optical waveguides in integrated photonic chips. Many instances of photonic integrated circuits have been demonstrated using bonded and thinned single crystal diamond layers [10, 85, 86]. While the optical quality of these diamond thin films is very good, the bond and transfer process adds an additional layer of complexity to the fabrication process. In addition, large area single crystals of diamond are expensive and difficult to obtain.

As an alternative, polycrystalline diamond thin films can be readily grown on a variety of large area substrates (such as silicon and silicon dioxide wafers [87, 88]) by seeding the substrate surface with diamond nanoparticles. Polycrystalline diamond films with nanoscale grain sizes (nanocrystalline diamond (NCD)) inherit a great deal of the optical, mechanical and thermal properties of single crystal diamond and can be used in place of single crystal

[1]The work presented in this chapter is being considered for publication under the suggested title "Aly R. Abdou, Parashara Panduranga, Jens Richter, Oliver Williams, Jeremy Witzens, and Maziar P. Nezhad. Suspended nanocrystalline diamond photonics platform."

diamond thin films in numerous applications. Such films can be grown using a variety of techniques, as reviewed in [31].

Several instances of integrated photonic components realised in NCD have been demonstrated (e.g. [12, 35]), where NCD grown on silica substrates or layers to create vertical confinement. While this is perfectly acceptable for operation in the visible and near IR, it prohibits operation at longer wavelengths due to absorption in the silica cladding.

To address this issue here we report, for the first time, air-clad diamond waveguides fabricated using NCD thin films grown on silicon substrates. This architecture not only creates the necessary vertical and lateral confinement needed to create a confined mode, it also offers a path for complete utilization of the optical transmission window of diamond.

In the next section we present the architecture, associated waveguide simulations and design steps. Then we present details of the fabrication process and finally present optical measurements on these suspended waveguides, followed by a discussion on future potential applications of this waveguide platform.

5.2 Design

Synthetic crystalline diamond possesses interesting optical properties, with wide transmission window being among the most attractive attributes. NCD has a bandgap of $5.47eV$ between the conduction band at the ultraviolet region ($\sim 230nm$) and the valence band at the mid-infrared region ($\sim 20\mu m$) [89]. It is also a viable candidate for integrated photonics thanks to its high refractive index, varying between 2.38 at $20\mu m$ and 2.7 at $230nm$ [32].

Two of the NCD competitors are silicon and silicon oxide. Silicon offers higher refractive index than NCD (~ 3.5), which leads to smaller waveguide structures. However, silicon suffers from a narrow bandgap of only $1.1eV$ [90]. On the other hand, silicon oxide has a wide bandgap [91]. However, silica's optical absorption coefficient is very low below $1\mu m$ wavelength, but it increases almost linearly from $1\mu m$ up to $8\mu m$ where it becomes highly absorptive [29]. Another drawback to silicon oxide is the low refractive index being around 1.5 for the majority of its transmission window. Therefore, NCD outperforms silicon and silicon oxide as a wide bandgap high refractive index semiconductor.

While the refractive index of diamond is high, it is still less than that of silicon. As a result, a thin film of diamond grown on silicon will not create vertical confinement. While this can be remedied by using a lower index interlayer (such as an oxide layer a few microns thick), we have chosen an alternative route, namely creating a suspended rib waveguide with air cladding above and below it, Fig. 5.1. This architecture has the advantage of being limited only by the diamond transmission window. In addition, since an appreciable portion of the

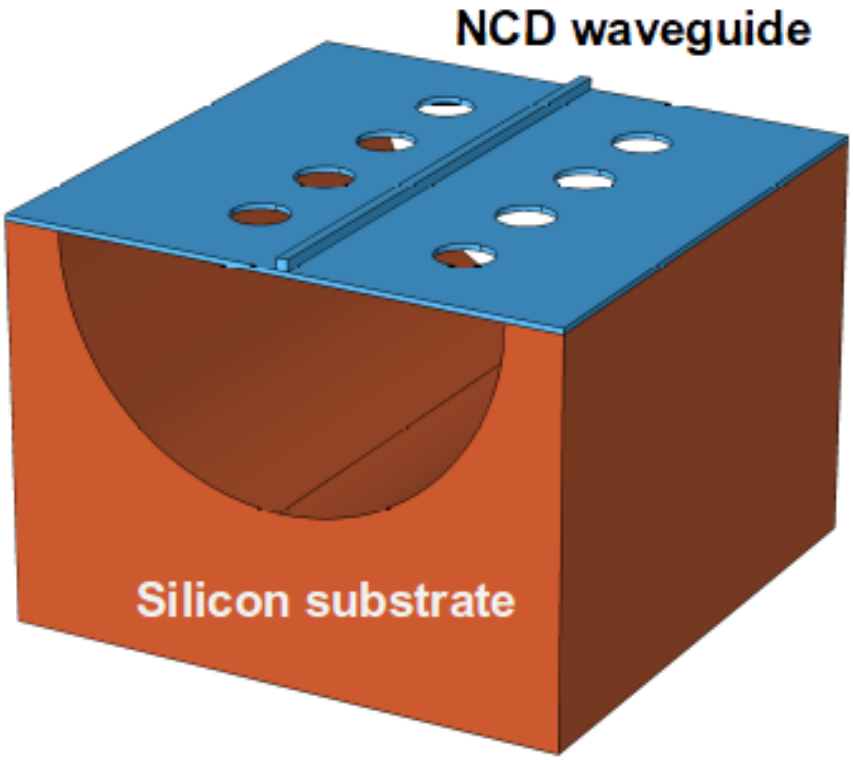

Fig. 5.1 Schematic of the proposed suspended NCD structure.

optical mode lies in the air cladding above and below the waveguide, it offers a convenient platform for sensing applications, in particular gas sensing. Similar suspended platforms have been proposed and demonstrated in silicon [15].

Three main components were designed for the suspended platform, straight waveguide, curved waveguide, and input/output coupling mechanism. A rib-waveguide was chosen to provide mechanical support at the outer rims of the structure. For mechanical rigidity, 150*nm* rib thickness was chosen to resist external forces (e.g. vibrational forces from nearby equipment), as explained in **Chapter 7**. To ensure high confinement of the propagating mode in the middle section, a total waveguide thickness of at least 450*nm* (3$\times$ rib-thickness) was required. We have opted for 500*nm* waveguide thickness. For dominant quasi-TE mode, middle section width of 600*nm* was considered.

The waveguide's cross-sectional dimensions and effective index were simulated using the finite element method through the use of COMSOL® Multiphysics, and are shown in Fig. 5.2. As can be seen, the field is concentrated inside the core and in the near vicinity, with relatively high effective index. Such dimensions provide a good compromise between the confined and the evanescent fields, which can be very beneficial for several applications, e.g.

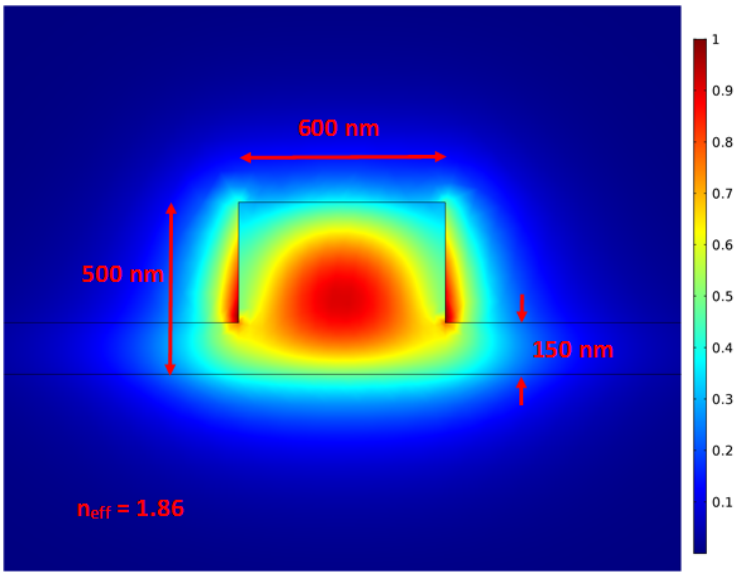

Fig. 5.2 Designed waveguide electric field distribution (V/m) with dimensions and effective index.

sensing. The high percentage of the evanescent field of the mode increases the sensitivity to the surrounding environment changes.

The bent-to-straight refractive index transformation model presented in [92] was used to simulate the loss from 90^o bends. The derivation of the transformation model is presented in **Chapter 7**. The bend-loss can be identified by the leakage of the mode from the mid-section into the slab region. Bend loss versus bend radius curves are presented in Fig. 5.3 for various rib-etch depths. As can be seen, the bend loss is inversely proportional to bend radius and etch depth. The importance of having ridge-height $\sim 3\times$ the rib-height is clearly noticeable from the different etch-depths' losses. The high mode confinement in the ridge with $350nm$ etch depth ($150nm$ rib thickness) limited the bend loss in the curved waveguide below $10^{-4}dB/90^obend$ for curvature radii as small as $20\mu m$ and drops to $2.5\times10^{-15}dB/90^obend$ for $50\mu m$ radius. For propagation loss measurements, radius of curvature must be large enough to minimize bend loss, so that the loss from the curved waveguide can be attributed to the scattering loss only. $200\mu m$ radius has been chosen to reduce bend loss to a point that it can be neglected during loss measurements. According to simulation results, bend loss of $350nm$ etch-depth and $200\mu m$ radius is below $10^{-19}dB/90^obend$. The mode shape, inset of Fig. 5.3, of the curved waveguide was proven to be identical to the straight waveguide presented in Fig. 5.2 with negligible power leakage observed in simulations.

Inverse-nano-taper edge couplers were chosen for coupling light in and out of the waveguides. The inverse taper edge coupler was chosen because of its small footprint compared to other coupling structures (e.g. grating coupler). Using this coupling mechanism reduces the

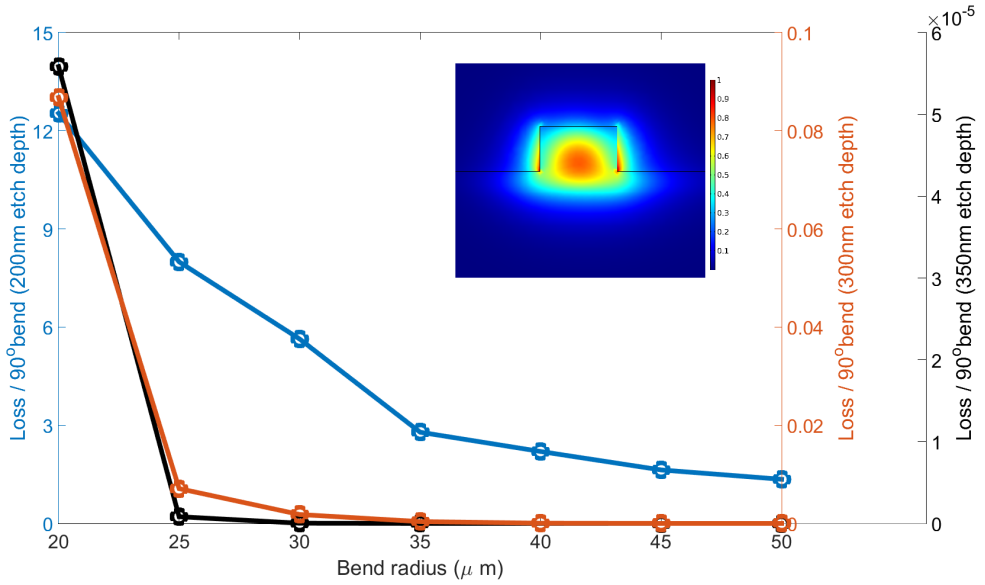

Fig. 5.3 Bend loss in $dB/90^o$bend vs bend radius and etch depth for suspended diamond rib waveguide. Inset showing mode shape of curved waveguide with 350nm rib-etch depth and 200μm curvature radius.

area of the diamond layer that has to be undercut during fabrication, and hence, produces a mechanically rigid structure. Fabrication simplicity was more important than the coupling efficiency at this stage, therefore only two etch steps were to be implemented during fabrication. Fixing the height and the etch depth along the waveguide limited the number of variables in designing the inverse taper coupler to the ridge width only. After examining different widths numerically, a 300nm wide inverse taper coupler was chosen for the highest overlap between the waveguide's and the input/output fibre's modes, with coupling efficiency of $\sim 83.13\%$ between the waveguide and a lensed fiber. A theoretical treatment of inverse-nano-taper couplers is presented in **Chapter 7**.

5.3 Fabrication

It is evident from the simulated mode field that the interaction of the field is greatest with the vertical side walls at the core-cladding interface; this contributes most to the scattering. Therefore, designing an etching recipe that produces smooth side walls is imperative. It is also clear that the bottom surface of the diamond film and the horizontal surface below the ridge show significant interaction with the mode field, requiring the growth of the diamond film to be made on an atomically smooth surface. This also means that the horizontal

smoothness of the surface after etching is important. Since the top of the ridge interacts least with the mode field, the growth of a very smooth diamond film is not essential.

The NCD was grown on a $380\mu m$ thick, highly doped silicon wafer, as reported in [93]. The standard SC-1 cleaning process of 30% H_2O_2: NH_4OH:DI H_2O (1:1:5) at 75^oC for 10 minutes was used to clean the silicon wafer prior to NCD growth. The wafer was then rinsed in DI H_2O in an ultrasonic bath for 10 minutes and spun dry. For growth, a mono-dispersed nanodiamond solution was used for seeding the silicon wafer in an ultra-sonic bath for 10 minutes. The $600nm$ thick layer of diamond was grown on top of the silicon surface through chemical vapour deposition (CVD). This growth was achieved by a combination of CH_4 at $5sccm$ and H_2 at $475sccm$ at pressure = $40Torr$, power = $3500W$ and took 298 minutes at 842^oC. The film was then thinned down to $520nm$ using Chemical Mechanical Polishing (CMP) to achieve an RMS surface roughness value below $2nm$. This helps in reducing the top surface roughness after partially etching the ridge waveguide.

An array of L-shaped suspended diamond ridge waveguides of lengths ranging from 1.524 to $4.524mm$ was chosen for the study. The waveguides were constructed via consecutive lithography and dry etching steps. First, the ridge was patterned in HSQ using E-beam lithography. The diamond film was then etched anisotropically down to $170nm$ in order to form the ridge waveguide. This was through Reactive Ion Etching (RIE) with O_2 at $30sccm$, pressure = $65mTorr$ and RF power = $100W$. This recipe provided the desired smooth vertical side walls and had an etch rate of roughly $60nm/minute$. A $40nm$ thick chromium layer was then deposited on top of the partially etched diamond film. Optical lithography was used to pattern the etch holes, and the chromium layer was subsequently etched using the commercially available etchant CR-7. This pattern was transferred to the diamond film through a second anisotropic etching step using the same parameters after which the entire chromium film was then removed using CR-7. It is critical all the wet processing is performed before undercutting the diamond film, so that the chances of damaging the very thin hanging membrane is greatly reduced. Finally, the silicon substrate was isotropically dry etched in an Induction Coupled Plasma (ICP)-RIE system to create the suspended structure, with the patterned diamond film acting as an etch mask. The silicon isotropic parameters were $50sccm$ SF_6 plasma at $30mTorr$, $1500W$ ICP power. An SEM image of the fabricated structure is shown in Fig. 5.4.

The dimensions of the completed structure deviated from the designed structure, and the fabricated structure was simulated in order to determine the deviation from the designed waveguide. The final dimensions and the mode profile are shown in Fig. 5.5. It is noticeable from the figure that the mode shape is very similar to the designed device. However, because of the change in dimensions the effective index changed from 1.86 to 1.8.

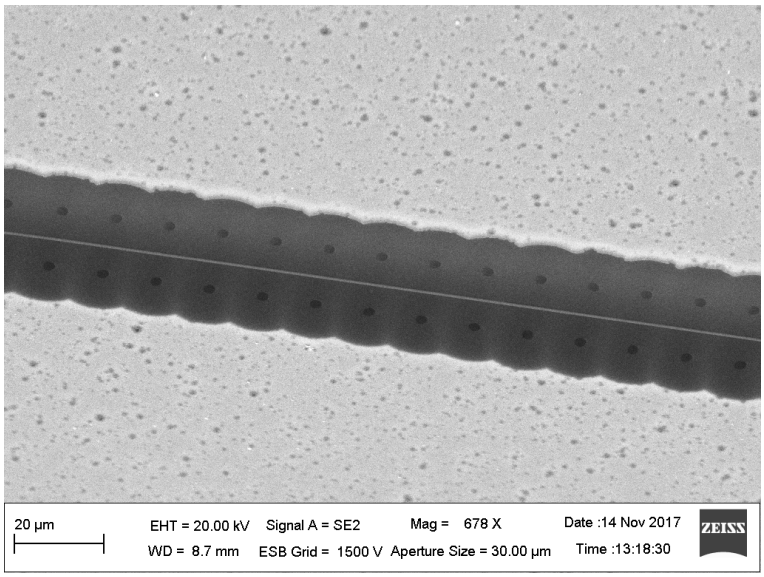

Fig. 5.4 SEM image of the fabricated suspended NCD platform.

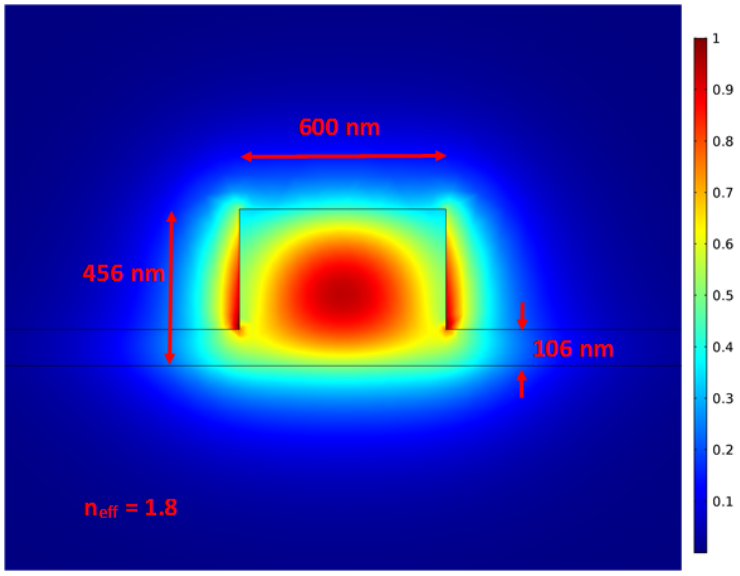

Fig. 5.5 Fabricated waveguide final dimensions with mode electric field distribution (V/m) and effective index.

The circular holes for the silicon etch step were $1\mu m$ in radius. Such small radius increased the silicon etch time considerably (58 minutes for $30\mu m$ etch depth). NCD etch rate in SF_6 is very slow, but the long etch step affected the NCD thickness. The final thickness was measured through SEM images to be $106nm$ for the rib-thickness and $456nm$ for the ridge height, which gives the NCD etch rate in SF_6 to be $\sim 1.1nm/minute$. The final RMS roughness of the rib top surface was measured using an AFM (Veeco Metrology Group) in

tapping mode and found to be $3.1nm$, and the average correlation length was estimated to be $81nm$.

Silicon etch rate at the edges of the chip was shown to be higher than the etch rate through the etch-holes. The prolonged etching time created a cantilever structure with considerable overhang length ($\sim 160\mu m$). The cantilever deflected due to its own weight (as shown in Fig. 5.6), which added a misalignment to the edge coupler; and in turn reduced the coupling efficiency.

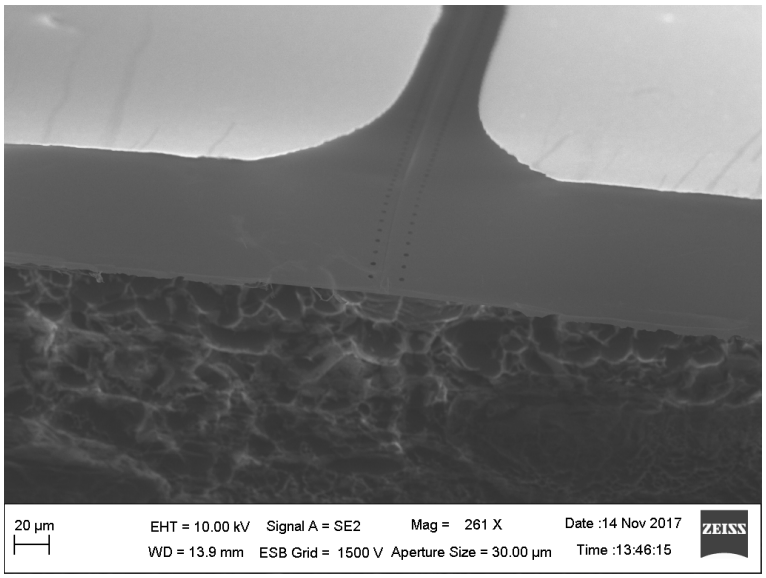

Fig. 5.6 SEM image showing the deflection of the suspended edge.

5.4 Loss measurements

Light from a tunable telecommunications laser was edge coupled into the waveguides using a lensed fibre. Near infrared images (Fig. 5.7) of the light propagating in the waveguides were captured using an InGaAs digital camera (Xenics Xeva 640). The measurement setup is shown in Fig. 5.8. The obtained images were processed using MATLAB®. Several images of the different lengths waveguides were processed to estimate the propagation loss.

Two approaches were used to calculate propagation loss. The first approach was the cut-back method. A rectangular box around the output was used to sum the pixels of the scattered light, and the loss coefficient was calculated using the formula:

$$\alpha(\frac{dB}{mm}) = \frac{10 \times log(\frac{P1}{P2})}{L(mm)} \tag{5.1}$$

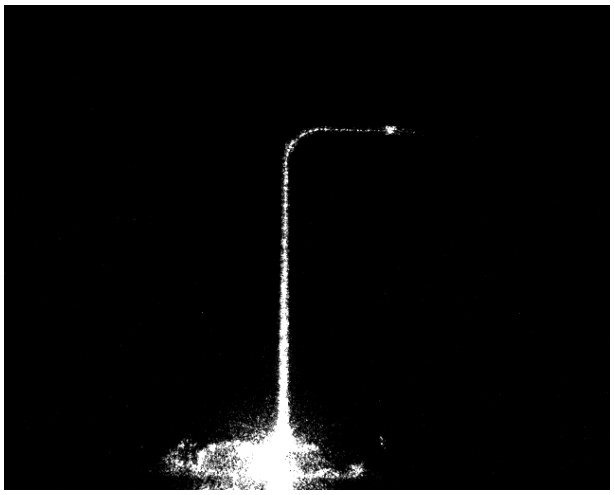

Fig. 5.7 Near Infra-red image at 1550*nm* for the fabricated waveguides.

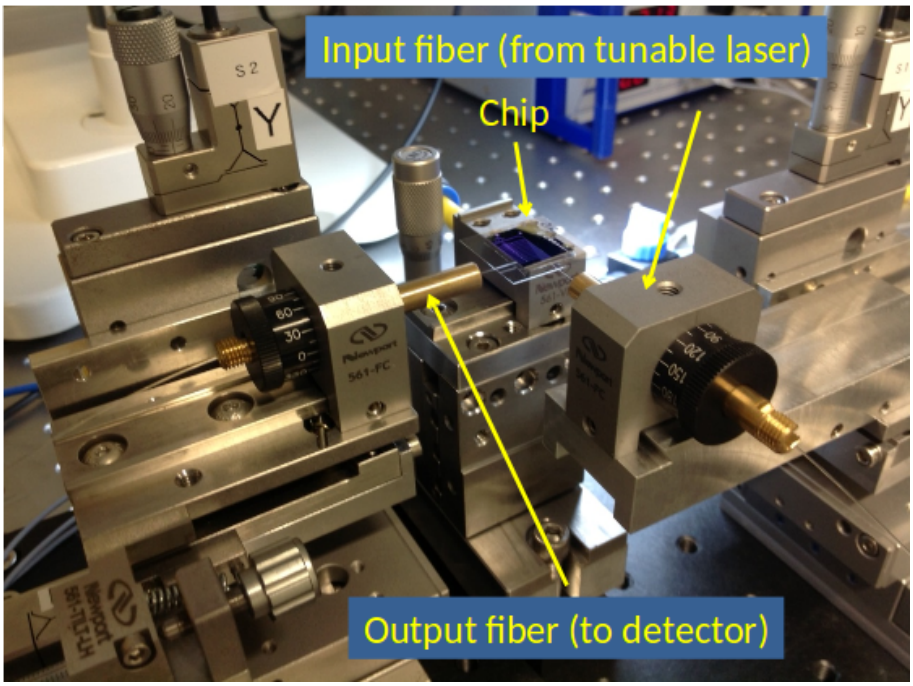

Fig. 5.8 Image of measurement setup.

where $P1$ is the output power from the shorter waveguide, $P2$ is the output power from the longer waveguide, and L is the longer length.

The second approach depends on calculating the power drop along a segment L of the waveguide. Then fitting the results to the exponentially decaying function:

$$\frac{P(L)}{P(0)} = e^{-\alpha \times L} \tag{5.2}$$

where $P(L)$ is the power at the end of the segment and $P(0)$ is the power at the beginning of the segment. First, the pixels in each row across the width of the waveguide were added to determine the total power at each point along the propagation direction. To eliminate any discrepancies, the total number of points along the propagation direction is divided into equal size arrays, then the pixel count is averaged over each array. The exponential formula (equation 5.2) is then fitted to the data points to extract the propagation loss coefficient.

Calculating the propagation loss coefficient using the cut-back method yielded a $1.2 dB/mm$ loss coefficient. This value is lower than what was expected. We believe that the input coupling efficiency is different among the different waveguides, hence, we relied on the power decay measurements along the waveguides (second approach).

Fig. 5.9 shows an example of the scattering loss measurements, with the abscissa being the distance in μm and the ordinate is the normalised scattered light intensity. Light intensity decrease translates directly into power drop. An exponential fit to the measured points has been conducted to extract the propagation loss coefficient. An average loss coefficient of $5.06 \pm 0.46 dB/mm$ has been extracted from the measurements with good fit (R^2 value above 0.9). The high loss coefficient is attributed to the scattering from the grains of the films. And the large variation in the loss coefficient is attributed to the random crystalline formation of NCD, which scatters light differently. NCD crystal structure is formed of randomly distributed grains of random shape and size [31]. And depending on the distribution in

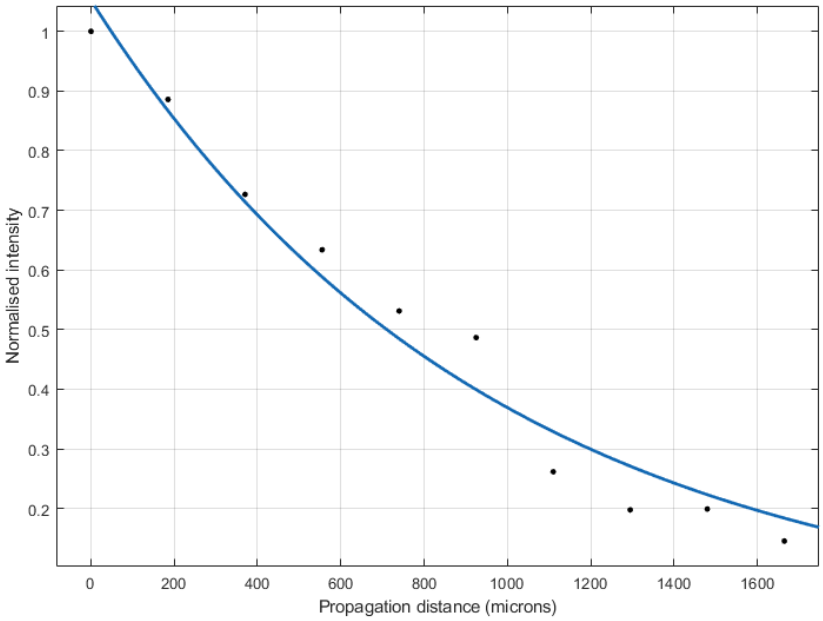

Fig. 5.9 Example of power decay measurements fitting ($R^2 = 0.97$).

each waveguide, the scattering varies accordingly. Despite the random variation in the crystalline formation, there exists an upper and lower limit to the maximum and minimum sizes depending on the growth mechanism. Such limit dictates the maximum and minimum loss coefficients.

One measurement showed high loss of 8.2 dB/mm. We attributed the high loss observed in this measurement to the contaminations on the waveguide, which contribute to the scattering loss. The average loss coefficient obtained in this work is in very good agreement with the results reported in [12].

In attempt to find a mathematical formula relating NCD grain size to scattering loss, we resorted to the treatment of grain boundaries as irregular particles of different refractive index ($n2$) to the homogeneous surrounding ($n1$) in the Rayleigh-Gans-Debye (RGD) approximation [94]. The irregular particles with average size (G) are approximated by spheres with diameter $D = G$. The RGD approximation is applicable when $|\frac{n2}{n1} - 1| << 1$ and the phase shift is negligible ($\delta|\frac{n2}{n1} - 1| << 1$, where $\delta = (\pi * D)/\lambda$). From Fig. 5.7 it is obvious that the scattering angle in the forward direction is very small as indicated by the non-diverging propagating beam, which translates to $|\frac{n2}{n1} - 1| << 1$. Also, with average grain size $D = 0.225\mu m$ and the operating wavelength $= 1.55\mu m$ so $\delta < 1$, both conditions for the RGD approximation are satisfied. The formula relating grain-size to scattering loss (α_{gb}) is given by [95]

$$\alpha_{gb} = 3\,\frac{\pi^2 \times r}{\lambda^2}(\Delta n)^2 \tag{5.3}$$

where r is the particle radius, and Δn is the induced birefringence by the grain boundaries.

The total propagation loss from our ultra-pure no-pores film is defined by

$$\alpha = Absorption + \alpha_{rs} + \alpha_{gb} \tag{5.4}$$

where α_{rs} is the scattering due to rough waveguide surfaces. NCD absorption at $1.55\mu m$ is estimated to be about $0.0434 db/mm$ [96]. α_{rs} was estimated using the formula produced in **Chapter 4** to be about $0.1565 db/mm$. So, α_{gb} is estimated using equation 5.4 to be $\sim 4.86 db/mm$. Using this value in equation 5.3 results in $\Delta n = 0.0284$.

To further confirm this value, we used it to estimate the loss due to grain boundaries in the waveguide in [12]. The waveguide in that study is a rib-waveguide with ridge height and width of 0.6 and $1\mu m$, respectively, and the RMS surface roughness is $15nm$. We have estimated α_{rs} from their rough waveguide assuming similar statistical distribution of the remaining roughness parameters as our waveguide to be $2.617 dB/mm$. The NCD film in their study has smaller grains and the average grain size was $100nm$. By substituting $\Delta n = 0.0284$

and $r = 0.05\mu m$ (average grain radius in their film), α_{gb} in their film is estimated to be $2.15dB/mm$. After adding absorption, α_{rs}, and α_{gb} the total propagation loss in their study adds up to $4.81dB/mm$, which is within their calculated tolerance.

5.5 Summary

A suspended NCD photonic platform has been designed and demonstrated. A sub-micron rib NCD waveguide with ridge dimensions of $600 \times 456nm$ and rib thickness of $106nm$ has been fabricated and proven to be mechanically rigid with no deflection observable due to gravity. The demonstrated platform proved to be efficient for mid-infrared applications at $1.55\mu m$, with acceptable propagation loss coefficient of $\sim 5dB/mm$.

The demonstrated platform is very beneficial for several applications, including sensing and wide transmission widow photonic chips. The wide transmission window of diamond allows for its use in photonic chips operating at the UV, visible, near-, mid-, and far-infrared regions, and make it a viable candidate for both biological and chemical sensing. The inert and high resistance to corrosive and reactive chemicals nature of diamond makes it ideal for use in corrosive and hazardous environments. As diamond has low thermal expansion coefficient, it can be used safely in high-temperature environments. High-intensity optical signals can be guided with the presented platform with minimal effects on the structure.

The demonstrated platform suffered from two main problems: 1) the thinning of the NCD layer during the silicon etching steps, which can be easily avoided by using a compatible masking layer; and 2) the low coupling efficiency of the inverse-nano-taper edge coupler due to the deflection of the suspended edges. Two proposed methods can be used to remedy the second issue: 1) increase silicon etch-holes to shorten etching times, and hence shortens the edge overhang; which in turns reduces the magnitude of the deflection, 2) shift from an edge-coupling mechanism to grating coupler.

The first concern about using grating couplers is the mechanical stability problem of the larger footprint of the mechanism; as the higher refractive index silicon substrate is required to be etched. But with proper design of the mechanical supports and the etch-holes of the platform, a stable suspended grating coupler can be fabricated. Another benefit to using grating couplers is the ability to fit all the chip components in one e-beam writer write-field, which eliminates the misalignment issues during writing patterns. A suspended NCD platform with grating coupler is being designed for future testing. The design of grating coupler is more complicated than the inverse-nano-taper coupler, hence **Chapter 3** is dedicated to the design of grating couplers.

Chapter 6

CO_2 Laser Micromachining of Diamond Films[1]

We present the interaction between the nanocrystalline diamond and a CO_2 laser beam observed during the fabrication of the photonic integrated chip in **Chapter 8**. At $10.6\mu m$ (CO_2 laser wavelength), both low doped silicon and nanocrystalline diamond (NCD) show very low optical absorption. Highly doped silicon is highly absorptive at $10.6\mu m$, where optical energy is converted into thermal energy causing the silicon substrate to heat up. Diamond's very high thermal conductivity allows the thermal ablation of the diamond top surface. Here we present finite element analysis of the optical and thermal effects in the structure, along with experimental demonstration of micro-patterning of the thin diamond film. This patterning technique is both rapid and cost effective.

6.1 Introduction

With excellent mechanical, thermal and optical properties, NCD is an attractive wide bandgap semiconductor. Although being relatively new material, it has been well integrated with mature semiconductor materials like silicon and silicon-on-insulator. Such integration is thanks to the development in the material growth and bonding techniques; which led to many applications such as MEMS, electronics and photonics [97–100]. Growth and bonding alone cannot provide the required structures for these applications, therefore, NCD patterning was required. Fortunately, advances in NCD patterning has been developed, including oxygen

[1]The work presented in this chapter has appeared in "Richter, J.*, Abdou, A.*, Williams, O.A., Witzens, J. and Nezhad, M.P., 2016. CO 2 laser micromachining of nanocrystalline diamond films grown on doped silicon substrates. Optical Materials Express, 6(12), pp.3916-3926." *Equal contribution

based reactive ion etching [101], pre-patterning of the growth seed layer [102], and laser micromachining [103].

Patterning of NCD using laser beams can be achieved by one of two main processes, vaporization ablation, or laser induced chemical etching [103]. Vaporization ablation takes place either in vacuum or in an inert atmosphere. High power laser beams heat the NCD above its sublimation temperature ($\sim 4000^oK$) [104, 105]. On the other hand, chemical etching takes place in a reactive environment such as oxygen, and occurs at much lower temperature ($\sim 1000^oK$) [103]. Chemical etching of NCD is the combustion of diamond (carbon). A high-power laser beam heats diamond's surface, where graphitisation is possible in the presence of air. The graphitised diamond has higher optical absorption than un-graphitised diamond, as well as, lower thermal conductivity. The combination of those two characteristics leads to the fast increase in the graphitised layer temperature leading to its combustion, and hence, the underlying layers.

High-power laser beams with photon-energies below diamond bandgap were not expected to cause chemical etching of diamond, due to diamond's transparency at those wavelengths. Polycrystalline diamond films grown on silicon have been etched using 1064 nm 50 nanosecond pulsed Nd:YAG laser beam at a $1.5J/cm^2$ fluence [106]; while it required about $7J/cm^2$ to damage free-standing diamond. This unexpected phenomenon was attributed to substrate surface modification and thermally induced mechanical stress in the diamond film. This experiment was reported again in [107]. Laser ablation of chemical-vapour deposited free-standing diamond has been reported with laser wavelengths of $1078nm$, $539nm$, and $270nm$ [105], where the ablation rate was insensitive to the wavelength. M. Rothschild, et al. [108] attributed surface graphitisation leading to higher absorption of the laser beam to the patterning of the diamond films in [105] and [107].

The previously mentioned studies make the assumption that high intensity laser beams can initiate diamond graphitisation very reasonable. Either the graphitisation process is initiated directly through multiphoton, multiphonon or surface state absorption processes, or indirectly through impurity absorption and localised heating in the bulk of diamond, high intensity laser beams are required. Hence, low intensity (low power) laser beams would be expected to be incapable of initiating diamond graphitisation, which is contradictory to what has been reported in [109]. Ral'chenko et al. [109] demonstrated patterning of polycrystalline diamond films grown on silicon and molybdenum using continuous wave (CW) $488nm$ argon laser beam at relatively low peak powers. They have attributed the patterning process to surface graphitisation, although unclear how it would be initiated at such, relatively, low optical power.

We believe, in most reports on laser induced chemical etching of diamond thin films on silicon substrates, that the substrate role has been neglected. So, in this work we performed thermooptic simulations and laser micromachining experiments on thin NCD films grown on silicon substrates to assess a novel explanation to the chemical etching of diamond using CW low power laser beams far from the band edges (CO_2 laser operating at $10.6\mu m$). The proposed explanation is based on the optical absorption of the dopants in silicon, which leads to the heating of the silicon substrate. In turn, the thin diamond film heats up to temperatures above its graphitisation temperature leading to chemical ablation. Instead of graphitisation originating by optical absorption and heating at the top surface of diamond, we attribute graphitisation to the heat generation in the silicon substrate underneath the diamond; then diamond thermal conductivity heats the top surface in contact with air to the graphitisation temperature.

6.2 Infrared optical properties of diamond and silicon at elevated temperatures

CW CO_2 laser operating at $10.6\mu m$ has been used in patterning NCD films grown on silicon wafers. The CO_2 laser is a widely used equipment in the micromachining industry due to its relatively low cost of ownership and high optical power. The photon energy of the CO_2 laser is much lower than the bandgap of both silicon and diamond, hence, patterning the diamond films grown on silicon substrates would be deemed impossible. However, the free carriers present in doped silicon substrates will facilitate such process, as will be shown later.

At first, an overview of the optical properties of both diamond and silicon at $10.6\mu m$ wavelength is required. NCD has a bandgap of $5.47eV$, refractive index of 2.38, and is highly transparent from the UV regime up to $20\mu m$ [110], with some peaked absorption between $2.6\mu m$ and $6.2\mu m$ due to the lattice absorption. Such high transparency over a wide wavelength window has led to the use of diamond in several infrared optical applications, including high power infrared transmission windows. Nanophotonic diamond based waveguides has been used in integrated photonic circuits using wafer-bonding hybrid diamond on oxide substrates [85] and CVD nanocrystalline diamond grown on oxide [12].

Diamond has an absorption coefficient below $1cm^{-1}$ from room temperature until the graphitisation temperature at 1000^oK [110]. CVD deposited diamond films possess very similar optical properties to single crystal diamond, although, in some cases, they show slightly higher optical losses due to the scattering from rough surfaces and grain boundaries [12]. As this work is based on the use of thin diamond films (few microns at most) and

as highly doped silicon has orders of magnitude higher optical absorption, the absorption in the thin diamond film can safely be neglected. On the other hand, graphite has high infrared absorption coefficient, but it is not considered here as this work aims at studying the graphitisation initiation mechanism only.

The dominant heat generation mechanism in our structure is the absorption due to lattice absorption and free carrier absorption in silicon at $10.6\mu m$. Lattice absorption is the main absorption mechanism at $10.6\mu m$ at low silicon doping and low temperature levels [111]. At elevated temperatures, intrinsic carrier absorption dominates. For highly doped silicon at low temperatures, induced free carrier absorption dominates the absorption mechanism. But at elevated temperatures, it is comparable to intrinsic carrier absorption.

The model presented in [112] has been used to model the free carrier absorption increase due to thermal effects. This simplified model is in reasonable agreement with the experimental results in [111]. The approximate form of the absorption coefficient as a function of doping and temperature is:

$$\alpha(N,T) = \sigma(T)[N + n_i(T)] + \alpha_0 \tag{6.1}$$

where $\sigma(T)$ is the absorption cross-section as a function of temperature in cm^2, N is the extrinsic doping concentration in cm^{-3}, $n_i(T)$ is the intrinsic carrier absorption as a function of temperature in cm^{-3}, and α_0 is the lattice vibration absorption in cm^{-1}. After substituting the values and equations from [112] for n-doped silicon, we arrive at:

$$\alpha(N,T) = (1.9 \times 10^{20}.T^{1.5})[N + 3.87 \times 10^{16}.T^{1.5}.e^{\frac{-7020}{T}}] + 2. \tag{6.2}$$

Fig. 6.1 shows the calculated absorption coefficient for various doping levels [112]. All curves converge to a common asymptote at elevated temperatures as a result of the domination of the thermally generated intrinsic carriers. The behaviour of p-doped silicon is qualitatively similar to n-doped silicon; however, we were not able to find quantitatively reliable optical models that were backed up by experimental data at the wavelength and temperatures of interest.

6.3 Modelling and simulations

COMSOL® Multiphysics was used to model the interaction between the incoming laser beam and a doped silicon substrate with a diamond layer grown on top. The substrate was assumed to have a diameter of 2 inches and a thickness of $380\mu m$. The mechanical support was modelled by a metal heatsink on its lower rim ($5mm$ overlap between the substrate

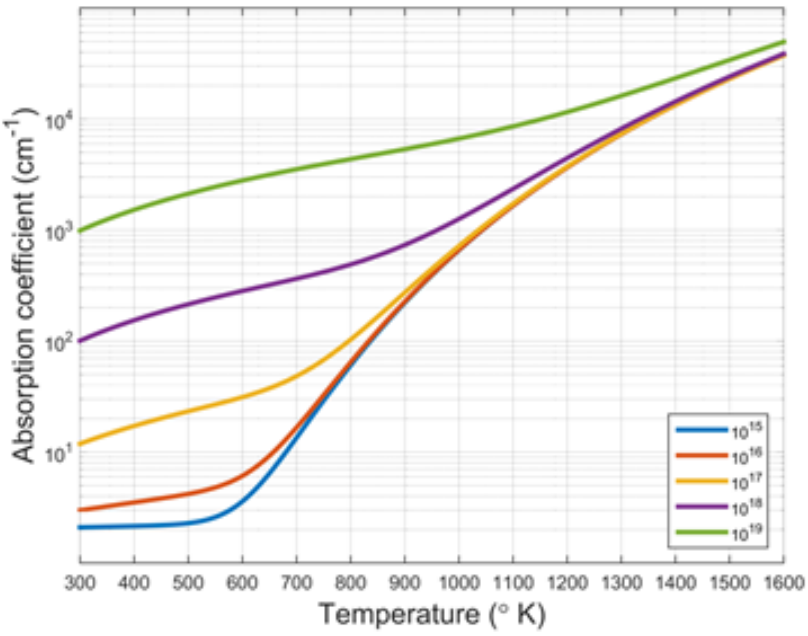

Fig. 6.1 Calculated optical absorption coefficient of silicon at $10.6\mu m$ for different doping levels and temperatures (calculated using the absorption model described in [112]).

and the heatsink). Steady state simulations were conducted to study the effect of varying the doping concentration, incident laser beam power, and diamond layer thickness on the temperature profile within the structure. Radiative, conductive and convective heat loss mechanisms were all considered, with the relevant parameters listed in Tables 6.1 and 6.2. The laser beam was assumed to have a Gaussian profile with a radius of $50\mu m$. Due to the beam radius being large compared to the wavelength, and the relatively short propagation distance in silicon compared to the Rayleigh range, the beam was assumed to have a constant cylindrical shape throughout the substrate. We used an axisymmetric Beer-Lambert model to simulate the propagation of the laser beam through the wafer. Reflections at the thin film interfaces were modelled using a transfer matrix analysis [46] of the silicon-diamond-air multilayer structure under normal plane wave illumination.

The objective of these simulations is to predict, under various conditions, the attainable temperature of the diamond surface. We assume that once the graphitization temperature (1000^oK) is achieved, the laser assisted chemical etching process will be initiated, resulting in sustained local removal of the diamond film. As mentioned above, we do not attempt to simulate the process past the point of graphitization.

The doping of the substrate has a drastic effect on the laser penetration depth and substrate heating. At low doping levels the optical absorption is low and the beam passes through

Table 6.1 Silicon physical parameters used in the COMSOL® modelling steps.

Parameter	Value	Units	Comments
Density	$\rho(T) = 2330 - 2.19 \times 10^{-2} \times (T - 293.15)$	kg/m^3	From [113].
Heat capacity	$C_p(T) = 641 + 74.2 \times (T/300)$	$J/kg.^oK$	From [114].
Thermal conductivity	$K(T) = 156 \times (T/300)^{-4/3}$	$W/m.^oK$	After modifying the equation in [114], also the effect of doping on thermal conductivity has been ignored.
Emissivity	0.5		Using average value from [115].

Table 6.2 Diamond physical parameters used in the COMSOL® modelling steps.

Parameter	Value	Units	Comments
Density	3515	kg/m^3	From [110].
Heat capacity	$C_p(T) = 3T - 400$	$J/kg.^oK$	Extrapolated and extended from [110].
Thermal conductivity	$K(T) = \frac{2.833 \times 10^6}{T^{1.245}}$	$W/m.^oK$	From [116].
Emissivity	0.03		Average value from [116].

the wafer, resulting in very little heating. At sufficiently high levels of doping, however, the optical absorption is substantially increased and the beam only penetrates a thin layer near the top surface of the silicon wafer. This creates a hot spot which, in turn, locally increases the number of thermally generated carriers, resulting in even higher absorption and runaway thermal heating.

Fig. 6.2 shows two sets of simulations pertaining to these two cases, for a beam power of $15W$. In Fig. 6.2a and Fig. 6.2b the steady state optical intensity distributions and corresponding temperature profiles are shown for an n-type silicon wafer doped at $10^{18}cm^{-3}$ and covered with a $500nm$ diamond layer. As can be seen, the maximum temperature of 670^oK is occurring at a point about 10 microns below the silicon surface. The maximum temperature on the diamond surface is about 1 degree lower (669^oK), which is far below the graphitization temperature.

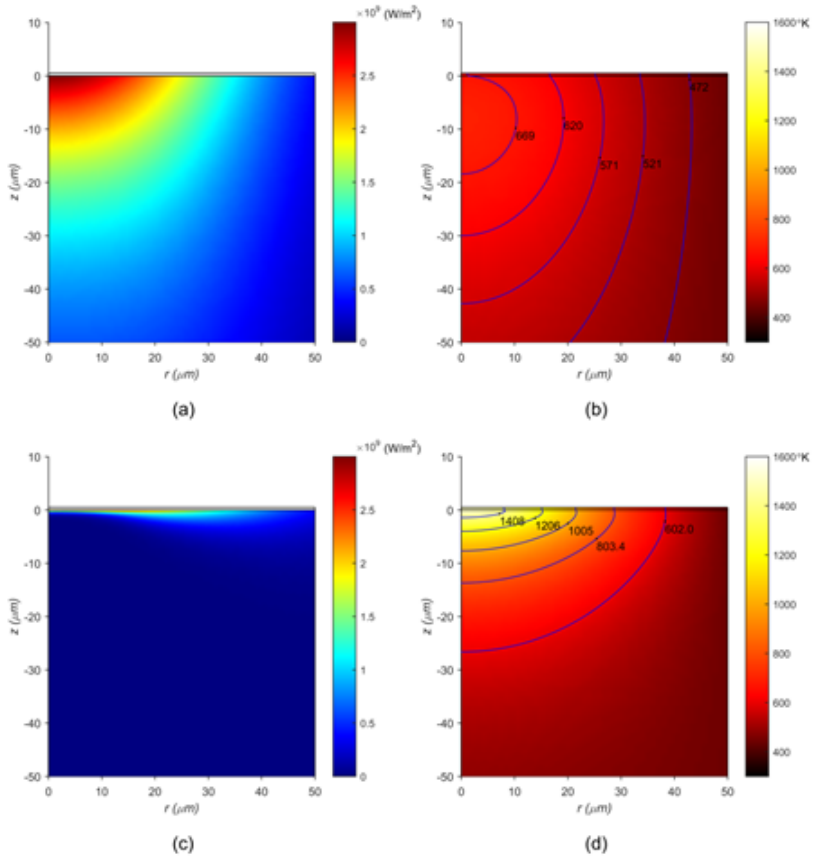

Fig. 6.2 Simulated laser beam penetration (left) and resulting temperature profiles (right) for n-type silicon substrate doping levels of $10^{18}cm^{-3}$ (a and b) and $10^{19}cm^{-3}$ (c and d).

Fig. 6.2c shows the optical intensity distribution for a substrate doped at $10^{19}cm^{-3}$. In this case the room temperature optical absorption coefficient is already quite high (about $1000cm^{-1}$, see Fig. 6.1). The runaway thermal process results in localized heating at the centre of beam to about $1500^{o}K$, resulting in an increased local absorption coefficient of $2 \times 10^{4}cm^{-1}$. The effect of this increase can be seen in Fig. 6.2d, where the penetration depth at the centre of the beam is smaller than at its edges. In this case the locally generated heat will be more than sufficient to initiate graphitization.

To further explore this effect we carried out a set of simulations over varying beam power and substrate doping. We consider a silicon substrate covered with a $500nm$ layer of diamond with n-type doping levels ranging from 10^{16} to $10^{20}cm^{-3}$. The colour map in Fig. 6.3 shows the steady state surface temperature of the diamond surface for incoming laser beam powers varying between 1 and $20W$. As can been seen, at low powers and low doping levels the laser beam is not able to sufficiently heat up the diamond surface to the graphitization temperature.

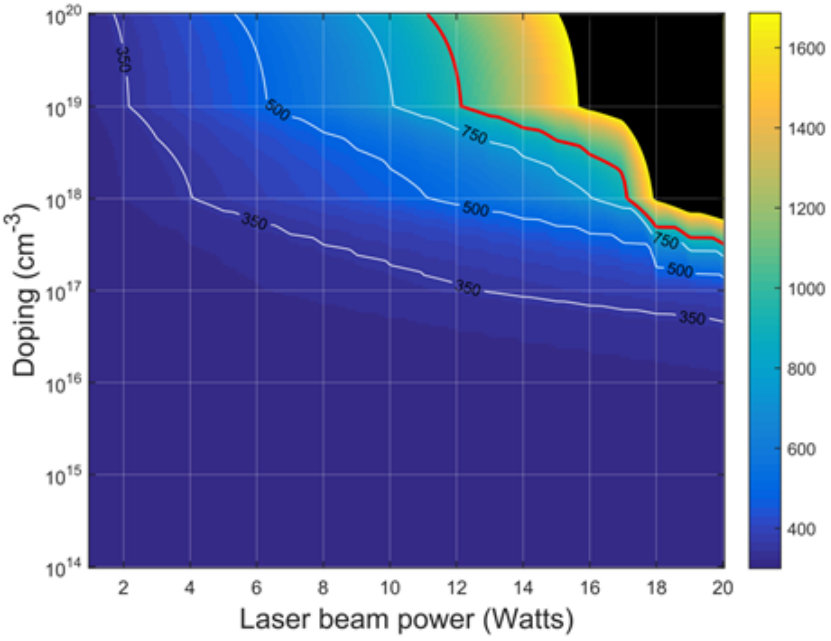

Fig. 6.3 Maximum diamond surface temperature for different substrate doping and beam power combinations, assuming a $500nm$ thick diamond layer and a $50\mu m$ beam radius. The red line marks the graphitization temperature of 1000^oK. The black area corresponds to temperatures higher than the melting point of silicon.

As the doping and laser power are increased, the heat generated by the initial beam absorption is able to create sufficient carriers such that it leads to a runaway build-up of further carriers. The red line in Fig. 6.3 denotes the boundary beyond which graphitization is initiated. The black area corresponds to points where the temperature exceeds the melting point of the silicon substrate (where our modelling assumptions would be rendered invalid).

As the thickness of the diamond layer is increased, more optical power is required to reach the graphitization temperature on the surface. This is mainly due to increased lateral and longitudinal heat loss in the diamond film as heat is transferred from the hot spot on the silicon surface to the surface of the diamond layer. To investigate this effect we simulated a silicon/diamond structure in the aforesaid mounting and illumination conditions, assuming fixed $10^{19}cm^{-3}$ doping, the power varying in the range of $12W$ to $20W$ and the diamond thickness varying between $250nm$ and $3\mu m$. Fig. 6.4 shows the colour map corresponding to the steady state temperature of the diamond surface for each of these conditions. As before, the points past (below) the red line correspond to attainment of the surface graphitization temperature and the black area corresponds to temperatures above the melting point of silicon.

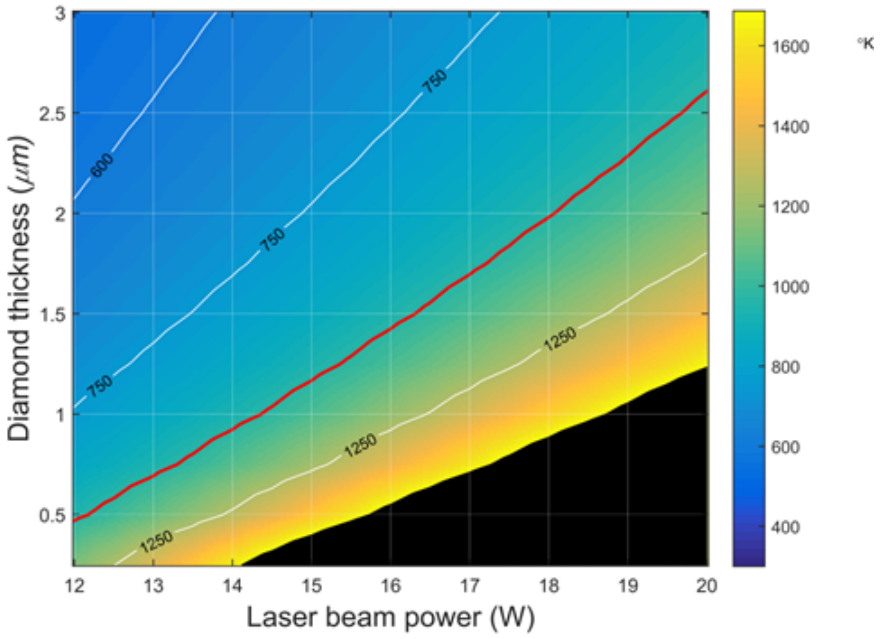

Fig. 6.4 Maximum diamond surface temperature for different diamond thickness and beam power combinations, assuming a substrate doped at $10^{19} cm^{-3}$ and a $50\mu m$ beam radius. The red line marks the graphitization temperature of 1000ºK. The black area corresponds to temperatures higher than the melting point of silicon.

This set of simulations show that diamond layers as thick as $2.5\mu m$ can be patterned with CO_2 laser beams under $20W$ of power, assuming a beam radius of $50\mu m$. The limit on layer thickness and patterning resolution can be improved by using a more focused beam to create a smaller, more intense, laser beam spot.

6.4 Experimental results

A custom-built CO_2 laser micromachining setup has been used to demonstrate the patterning of NCD films grown on doped silicon substrates. The setup comprised a CO_2 laser (Coherent Diamond C-20A) and a computer controlled 3D positioning stage, as depicted in Fig. 6.5. The mode quality (M^2) of the emitted beam was specified to be better than 1.2 and the nominal maximum specified optical output power was $20W$, controllable to a precision of approximately $50mW$. Optical output power of $22W$ was achievable in practice. The laser beam was focused down to a spot with a beam radius of approximately $130\mu m$ by the use of a biconvex zinc selenide lens with a focal length of $100mm$. An image acquisition system performed live capture and control of the illumination process of samples.

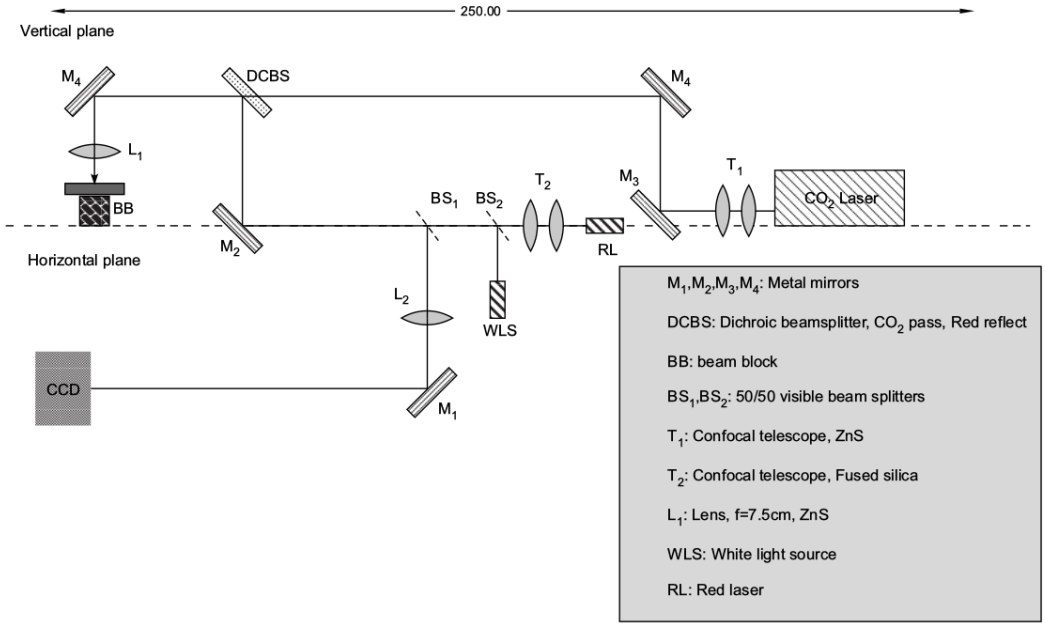

Fig. 6.5 Schematic of CO_2 laser setup.

A $520nm$ NCD film grown on $380\mu m$ highly boron-doped silicon substrate was used in this experiment. Silicon surface conductivity was measured, using a four-point probe measurement system (Jandel, $1mm$ probe spacing), to be $79.4m\Omega/\Box$, which translates to $0.003\Omega.cm$ conductivity and $3.7 \times 10^{19} cm^{-3}$ doping level. The diamond film was grown from monodispersed hydrogenated diamond nanoparticles using chemical vapor deposition in a microwave plasma reactor with methane and hydrogen gases [93]. The growth conditions were set to (CH_4 : $5sccm$, H_2 : $475sccm$, Power: $3500W$, Pressure: $40Torr$) at a temperature of 842^oC, for a growth duration of 298 minutes, resulting in a $600nm$ thick unpolished film. The grain sizes were estimated to be in the range of $150-300nm$ as inferred from the growth conditions and similarly grown samples [93]. The effect of growth parameters on the film morphology is detailed in [31]. Final thickness of $520nm$ and surface smoothness with roughness less than $2nm$ (RMS) were achieved using chemical mechanical polishing.

The chip was supported on a horizontal metal platform with a beam exit hole, without the use of any additional heatsinking compounds. The diamond film on the chip edge was undercut and released using a XeF_2 silicon dry etch (Fig. 6.6a). The absence of ripples in the undercut membrane indicates very little residual stress in the diamond film. Exposure of this section of the chip to a focused CO_2 laser beam did not result in any perceptible changes in

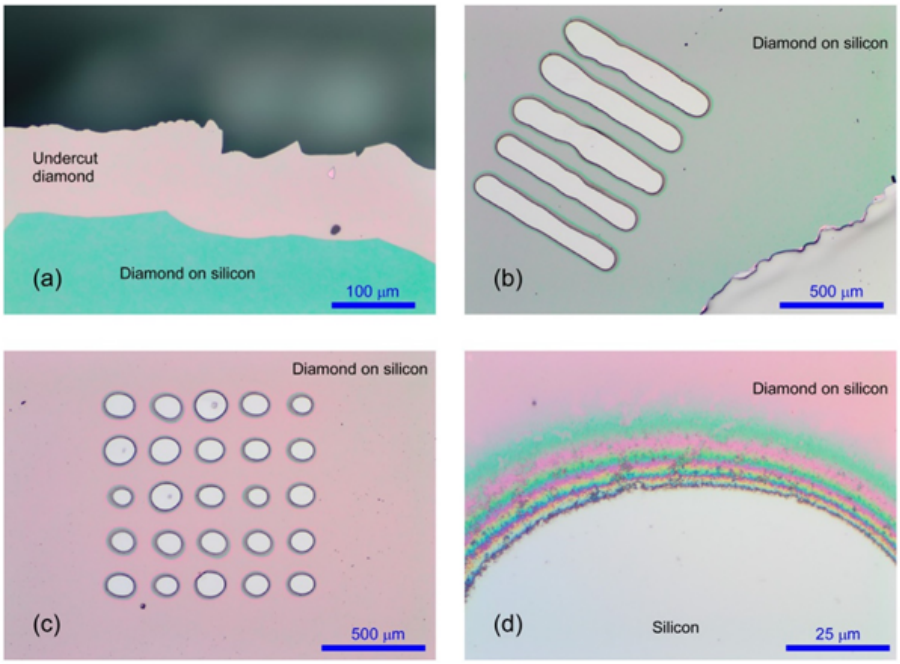

Fig. 6.6 (a) Undercut nanocrystalline diamond film on silicon substrate. Lines (b) and dots (c) patterned in diamond. (d) Zoomed-in image of a dot showing interference fringes and debris.

the film appearance, even at high powers up to $20W$. This confirms the very low absorption coefficient of the diamond film at $10.6\mu m$. However, when the beam was directed to sections with an underlying silicon layer, the diamond film was rapidly removed at beam powers above $9W$ (with a beam radius of $\approx 130\mu m$), resulting in a clean and unblemished exposed silicon surface. The beam intensity levels required for patterning the diamond film in our experiment are lower than the levels predicted by the simulations. We attribute this to the smaller size of the actual chip compared to the full 2 inch wafer used in the simulations and also the use of an ideal heat heatsink boundary condition in the simulations. In practice we also observed that points closer to the chip edge were machined faster and at lower power levels compared to the centre of the chip, which is due to the difference in the heat loss parameters at these points.

It may be argued that initiation of the diamond etch process could also be due (in part, or fully) to surface absorption processes in the diamond film. These would consist of absorption at the nanocrystal diamond surfaces on the air/diamond interface and a silicon carbide layer ($< 1nm$ thick) existing on the silicon/diamond interface. However, both of these surface effects would also be present in the suspended diamond film, since silicon carbide is not etched in XeF_2 gas. Since the experiments show that the suspended diamond film is not affected by the incoming laser beam, we can conclude that the heating effect of any

surface absorption in the diamond film is negligible compared to the heat generated through absorption in the silicon substrate.

Using the automated stage controls, arrays of dots and lines were written into the diamond film (Figs. 6.6b, 6.6c). Closer inspection of the patterned areas shows interference fringes, indicating a gradual increase in the film thickness away from the etched diamond edge. Also, some dark micron-scale and sub-micron-scale particles can be seen in the periphery of the etched edge which are possibly residual graphite or diamond nanoparticles generated during the heating process.

It should be mentioned that the focused CO_2 laser beam was not optimized for achieving the smallest focused spot size and we expect that a patterning resolution substantially higher than shown in Fig. 6.6 should be achievable in practice. In the ideal case of a diffraction limited spot, assuming a numerical aperture of unity, a focused CO_2 laser beam would have a spot diameter of $2w_0 = 2\lambda_0/\pi = 6.8\mu m$, which is about 40 times smaller than the spot size used in the experiments. Additional improvement in resolution can also be achieved by using a high-power laser source with a shorter wavelength, such as a fibre laser operating in the near IR. It should however be noted that free carrier absorption in silicon is approximately proportional to the square of the wavelength [111], therefore operating at shorter wavelengths will require higher laser powers and substrate doping levels in order to reach the graphitization temperature.

6.5 Summary

Patterning of NCD films using CO_2 laser beam at modest optical power levels is achievable with the right doping conditions of the underlying silicon substrate. It has been demonstrated theoretically, through simulations, and experimentally. The doping level of the silicon substrate plays a key role in this process, as shown by the simulations. Such role seems to have been ignored in previous work done in this area. The proposed chemical etching of diamond films in this work prove that diamond patterning is achievable without direct graphitisation of diamond films with high intensity laser beams; which opens the possibility of patterning diamond films using the industrial CW CO_2 laser. The micromachining mechanism proposed here is not exclusive for diamond films, it can be used for any other transparent material if they are patternable using thermal methods. Also, different CW and pulsed laser equipment can be used for patterning transparent films, if they provide the required optical energy to heat up the doped silicon substrate.

Chapter 7

Photonic Integrated Chip Design

The design of the MEMS actuated micro-resonator chip in this work is divided into three main parts, optical, electromechanical and mechanical. In each section, we present the required literature review, methodology and, finally, report the final results.

7.1 Device model

As explained in **chapter 2**, an electromechanically actuated waveguide platform was required to provide tunability to a "waveguide micro-resonator" coupler. Fig. 7.1 shows an exploded view of the device. The micro-resonator and the optical waveguide (device layer) are demonstrated on two separate chips. The first chip contains 3 main layers, 1) the micro-resonator defined in the silica layer on top of silicon handle layer, 2) deposited molybdenum lower electrode for electromechanical actuation, and 3) a channeled polymer layer to provide separation distance between the lower and top chips. While the second chip consists of two main layers, 1) polymer layer that serves as a lower cladding and bonding material, and 2) silicon/NCD device layer where the optical waveguide is defined. The next sections explain the device design, and **Chapter 8** explains its fabrication.

7.2 Optical design

The optical design was the biggest design challenge. Several designs and approaches have been tried, but in the next subsections we only present the final designs we have achieved.

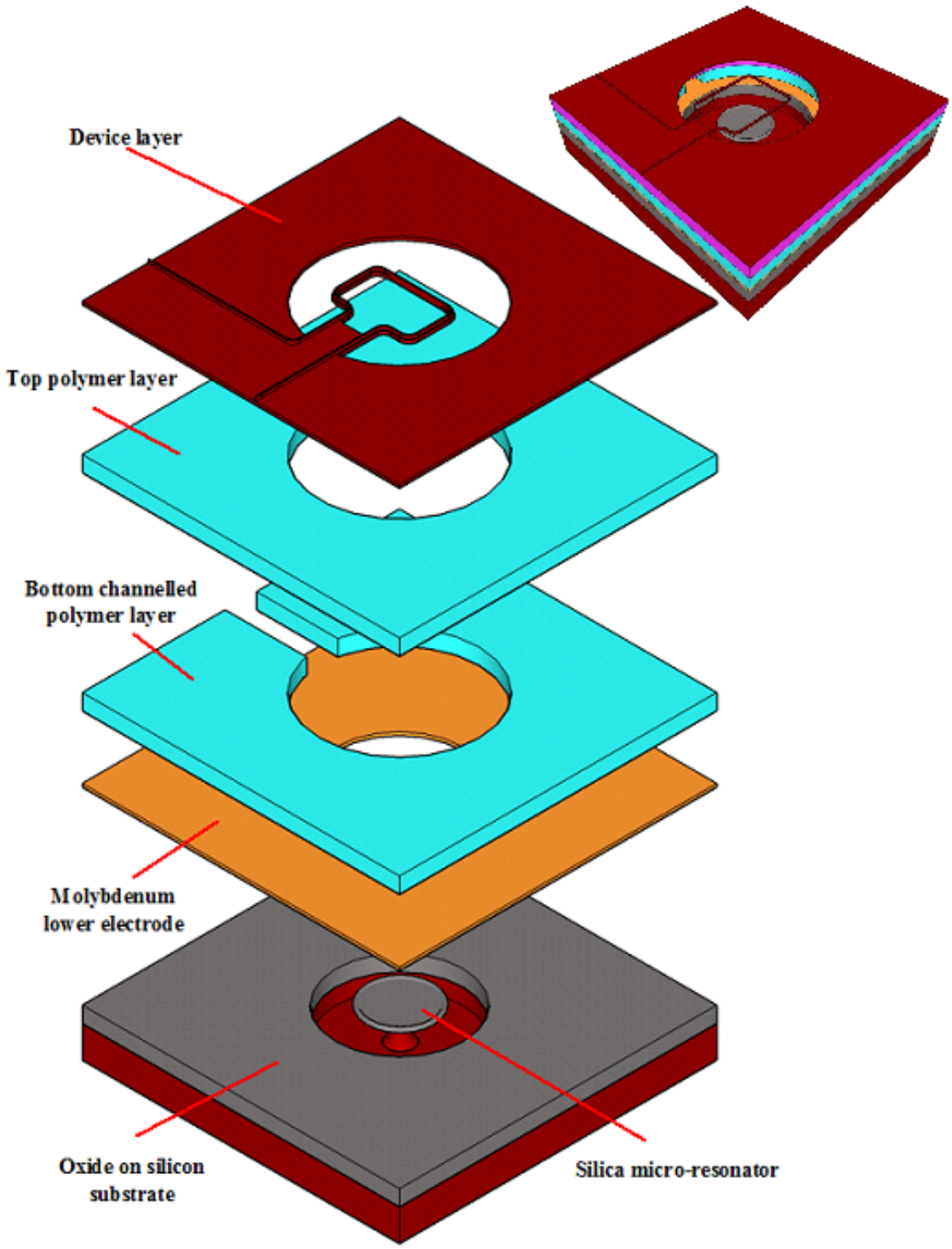

Fig. 7.1 Device exploded view with an unexploded view in the inset.

7.2.1 Micro-toroid resonator mode analysis

The primary aim of this chapter was to report on the design of a microresonator-waveguide coupler that is fully tuneable. Besides the structural and mechanical designs, the optical design is the most critical. Most of the optical components can be easily modified to produce an optimum design. But, the resonator had to possess a high Q-factor (little power leakage).

Resonators experience power leakage, which is a serious issue. And for toroid-resonators three main factors affect power leakage, toroid radius, surface smoothness, and mode confinement. Toroid radius defines bend loss in the resonator, and has minor effects for resonators with large radii. Rough surfaces cannot be always controlled and depend on the fabrication technique, and surface-tension-induced micro-resonators possess very smooth surfaces. Mode confinement is directly proportional to mode's effective index (or propagation constant) and is a function of the resonator and the cladding refractive indices, and resonator's cross-sectional area.

Surface-tension-induced melted silica micro-resonator with $100\mu m$ principal radius was chosen as a baseline for this project, to minimize power leakage from bend loss and scattering loss. Three minor radii (r) have been tested, $2.5\mu m$, $3.5\mu m$, and $4.5\mu m$; and their mode shape and effective index were simulated using COMSOL® Multiphysics. Fig. 7.2 shows the cross-section of a micro-toroidal resonator and its parameters, while modes shapes and effective indices are shown in Fig. 7.3.

As seen from Fig. 7.3, all three resonator sizes will provide a well confined mode with effective index very close to the maximum possible (silicon dioxide refractive index is 1.444 [117]). Therefore, a micro-resonator with an effective index around 1.43 provides the starting point for the optical design of the photonic integrated chip (PIC).

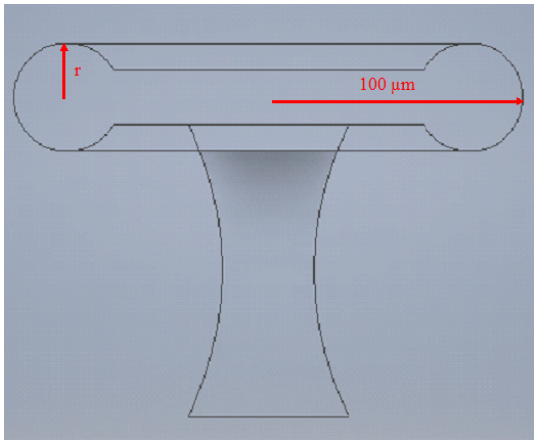

Fig. 7.2 toroid micro-resonator parameters.

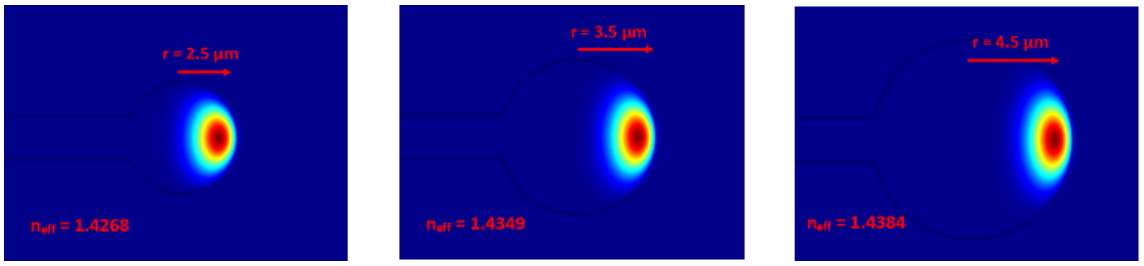

Fig. 7.3 toroid micro-resonator mode and effective index vs minor radius.

7.2.2 Waveguide design

Waveguides can take any arbitrary uniform shape as long as it can support the guided modes. For optical communication, circular waveguides (optical fibres) are the used shape due to the similarity along the two axes in the plane perpendicular to the propagation direction. And most importantly, circular optical fibres are easily and cheaply fabricated.

On the other hand, circular waveguides are difficult to build on PICs. Rectangular waveguides are easier to fabricate. The waveguide cross-section can be a rectangle with comparable height and width, slab waveguide, or ridge/rib waveguide. Each one of these structures is explained in a following subsection.

Slab waveguide

Fig. 7.4 shows the structure of a slab waveguide. The core and cladding layers' width is much larger than the thickness of the waveguide. The upper and lower claddings can either be the same or different materials. The slab waveguide is very simple to fabricate, but does not suit many different applications as the mode expands across the whole structure's width; and it consumes large area of the used chip.

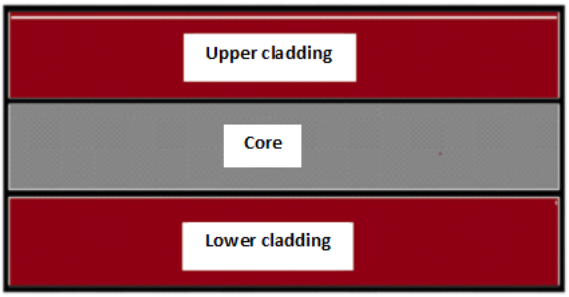

Fig. 7.4 Slab waveguide.

As the width is infinite, so it can, theoretically, support infinite number of modes in the horizontal direction. And the thickness determines how many modes can be supported vertically. Due to its transverse multi-mode nature, a slab waveguide was not used in this work.

Ridge (rib) waveguide

The ridge waveguide structure is shown in Fig. 7.5. The cladding materials can either be the same or different. The etched parts on both sides helps to confine the mode in the central part. Ridge waveguide combines the advantages of the slab waveguide, which offers rigid structure, and the rectangular waveguide, which is the mode confinement in small cross-sectional area. Ridge waveguide structures were intensively studied, and many papers provide parameters and criteria for their design [118–122]. They are used for different applications, e.g. couplers [123].

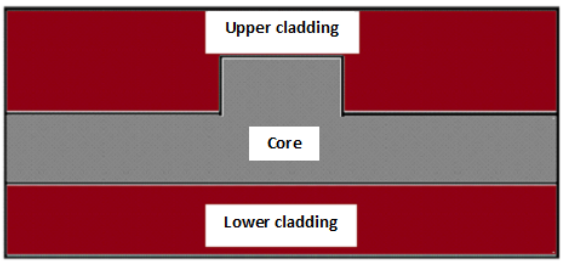

Fig. 7.5 Ridge (rib) waveguide.

Rectangular waveguide

Rectangular waveguides are widely used due to their simple structure, and their wide range of applications. Fig. 7.6 shows a schematic of a rectangular waveguide. They are a special case of ridge waveguides with fully etched sides. Many components and photonic circuits are designed with rectangular waveguides including filters and modulators [124], Polarization splitter [125], and large scale photonic circuits [12, 16].

Waveguide modes

Modes are the field energy distributions of an optical signal. The number of field maxima determines the order of the mode, and field spatial components (electric and magnetic) determines the type of the mode. Practically, dielectric optical waveguides can support two types of modes [84], which are denoted E^x_{mn}, where the field is predominantly polarized in

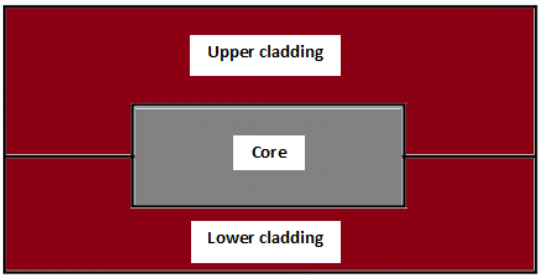

Fig. 7.6 Rectangular waveguide.

the x-direction and E^y_{mn}, where the field is predominantly polarized in the y-direction; where z is the propagation direction in the Cartesian coordinate system. Conventionally the E^x_{mn} mode is called the **quasi-TE** mode (Transverse Electric), or **TE** mode for brevity, and the E^y_{mn} mode is called the **quasi-TM** mode (Transvers Magnetic), or **TM** mode for brevity. The m and n subscripts denotes the number of field maxima in the x- and y-directions.

For a slab-waveguide, as the width reaches infinity in x-direction, E^x_{mn} modes dominate with infinite number of modes in the x-direction (m $\rightarrow$ infinity). Therefore, analyzing slab waveguide ignores the x-direction and concentrate on the y-direction; hence, modes are denoted E_n. With width being infinite, the electric field occupies a transverse plane perpendicular to the propagation direction. And by further analysis of the fields, it can be found that the 6 field components in the 3 Cartesian directions reduce to E^x, H^y, and H^z.

On the other hand, a rectangular waveguide confines light in both transverse directions, which complicates the analysis as all 6 field components exist.

A rib-waveguide combines both slab- and rectangular-waveguide modes. The central region provides mode confinement in x- and y-directions, as shown in Fig. 7.7, while the slab sides can support an infinite number of modes that are polarized in the x-direction.

7.2.2.1 Coupler waveguide

The starting point for the waveguide design was the coupler. The aim is to achieve the highest possible coupling efficiency. By reverting to the coupled mode theory [46], we find that the coupled power from the input waveguide into the resonator after a distance z is given by

$$P(z) = P_0 \frac{K_c^2}{K_c^2 + \delta^2} \sin^2 \sqrt{K_c^2 + \delta^2}\, z \tag{7.1}$$

where P_0 is the power in the input waveguide at the start of the coupler region, K_c is the coupling coefficient from the waveguide into the resonator, and δ is the phase mismatch

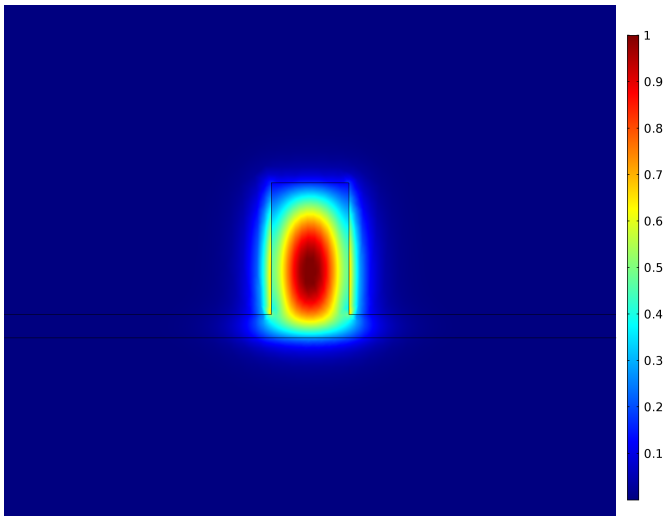

Fig. 7.7 Rib-waveguide confined mode.

between the waveguide mode and the resonator mode, and is defined as

$$2\delta = (\beta_R + K_R) - (\beta_W + K_W) \tag{7.2}$$

where β_W is the propagation constant of the waveguide mode, β_R is the propagation constant of the resonator mode, K_W is the dielectric perturbation to the waveguide due to the presence of the resonator in its proximity, and K_R is the dielectric perturbation to the resonator because of the waveguide. From equation 7.1, we find that the maximum coupling occurs with phase matching between the waveguide and the resonator modes.

Based on experience, the coupler waveguide was expected to be $\sim 0.25\mu m^2$ or less, so the perturbation it causes to the resonator ($\sim 20\mu m^2$ minimum) can be neglected and K_R can be omitted from equation 7.2. On the other hand, K_W cannot be ignored for accurate calculations, but since it is hard to be determined for a variable-separation-gap coupler, a slightly lower propagation constant for the waveguide β_W (or n_{eff_W}) would be chosen to compensate for the omission of K_W.

A sweep across a range of sizes to find the dimensions of the coupler waveguide was conducted using COMSOL® Multiphysics. The telecommunication $1.55\mu m$ wavelength was chosen for this device, so the effective index of crystalline silicon was chosen as 3.4757 [117]. And for the diamond waveguide, the refractive index was calculated to be 2.3855 from the Sellmeier equation in [32]

$$n = \sqrt{\frac{0.3306\lambda^2}{\lambda^2 - 175^2} + \frac{4.3356\lambda^2}{\lambda^2 - 106^2} + 1} \tag{7.3}$$

where λ is the wavelength in nm. Fig. 7.8a shows the areas for single- and multi-mode operation for silicon waveguide with air cladding, and Fig. 7.8b for diamond waveguide with air cladding.

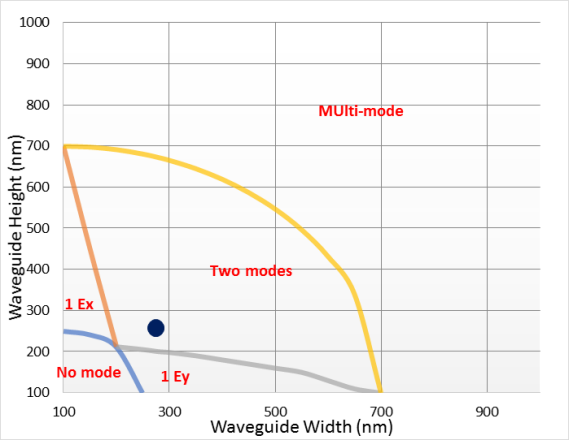

(a) Silicon waveguide

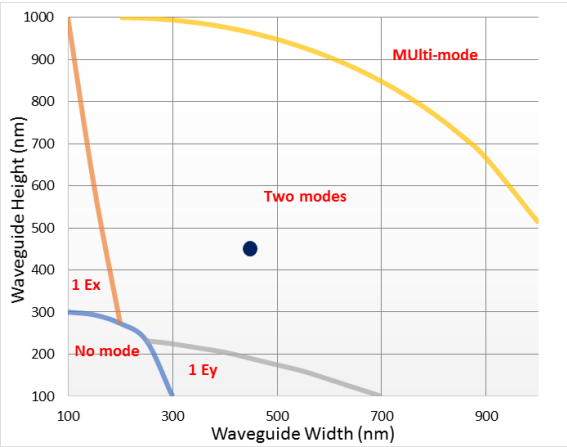

(b) Diamond waveguide

Fig. 7.8 Single and multi-mode cut-off dimensions for silicon and diamond waveguides with air cladding. The blue dot is the chosen size for the coupler waveguide.

As seen in Fig. 7.3, the effective index of the resonator mode varies from 1.4268 to 1.4384; therefore waveguides with dominant modes of ~ 1.4 effective index were required. The used SOI wafers restricted the waveguide thickness to $260nm$, therefore a $280nm \times 260nm$ waveguide was chosen, which supports 1 mode in the x-direction and 1 mode in the y-direction. Fig. 7.9a shows the mode shape and its effective index. The dominant field component is E_x for the silicon coupler waveguide. On the other hand, E_y mode was chosen

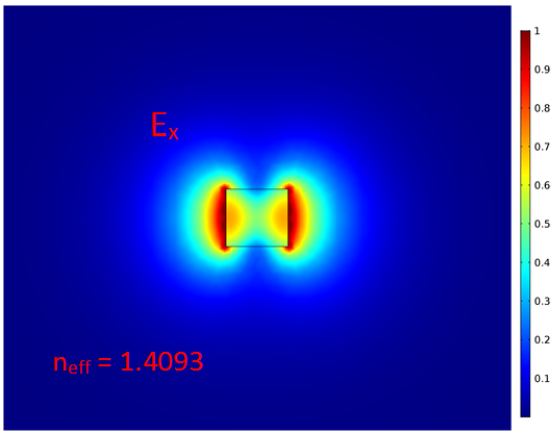

(a) Silicon waveguide

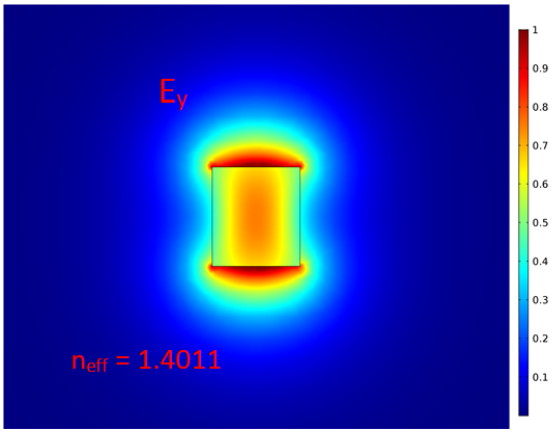

(b) Diamond waveguide

Fig. 7.9 Mode shape and effective index of silicon and diamond coupler waveguides.

for the diamond coupler waveguide, which supports 2 modes as well. Since the waveguide thickness was restricted to 450nm, which dictated the use of 400$nm \times 450nm$ waveguide as shown in Fig. 7.9b.

7.2.2.2 Waveguide dispersion

Since the waveguide dimensions, based on fabrication constraints, will not meet the exact design values, therefore perfect mode matching at the design wavelength is very unlikely. Hence, wavelength dispersion study is required to determine the wavelength with highest coupling efficiency. COMSOL® Multiphysics has been used to calculate the effective indices with sweeping the wavelength from 1.45μm to 1.65μm. Fig. 7.10 shows the wavelength of perfect phase matching (not taking into account the effect of K_W) between the silicon coupler waveguide and the 3.5μm silica toroid. It, also, shows the dispersion curve between the coupler diamond waveguide and the same silica toroid. Both effective indices of the silicon and diamond waveguides will be shifted upwards after adding the effect of K_W, which in turns will shift the coupling wavelength to higher value close to 1.55μm.

7.2.2.3 Straight waveguide

For fabrication simplicity, a rib-waveguide structure with middle section of similar dimensions as the rectangular coupler waveguide was chosen for both silicon and diamond waveguides. The rib structure provides rigid structure and capability of being used as an electrical contact for electromechanical actuation. Rib-thicknesses were chosen to be 150nm in both the silicon and diamond waveguides for electromechanical reasons, which are explained in section **7.3**. The mode shapes along with their refractive indices are shown in Fig. 7.11.

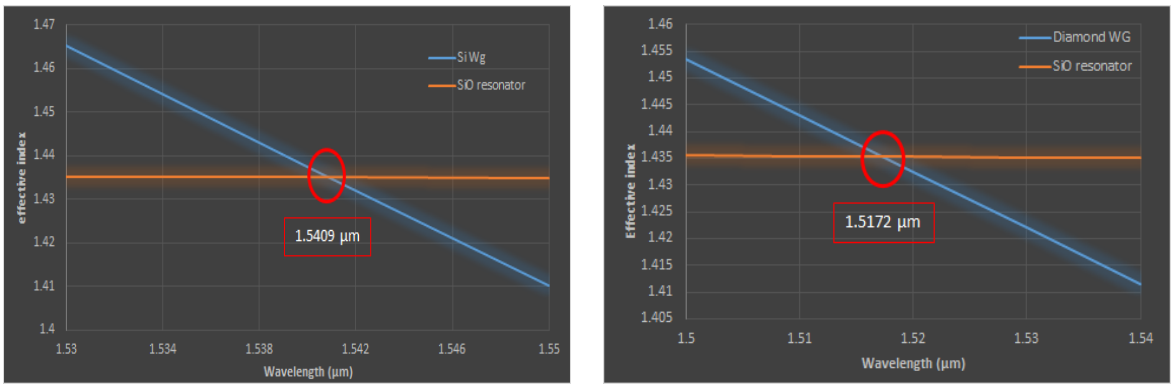

(a) Silicon waveguide (b) Diamond waveguide

Fig. 7.10 Coupler waveguides and resonator wavelength dispersion.

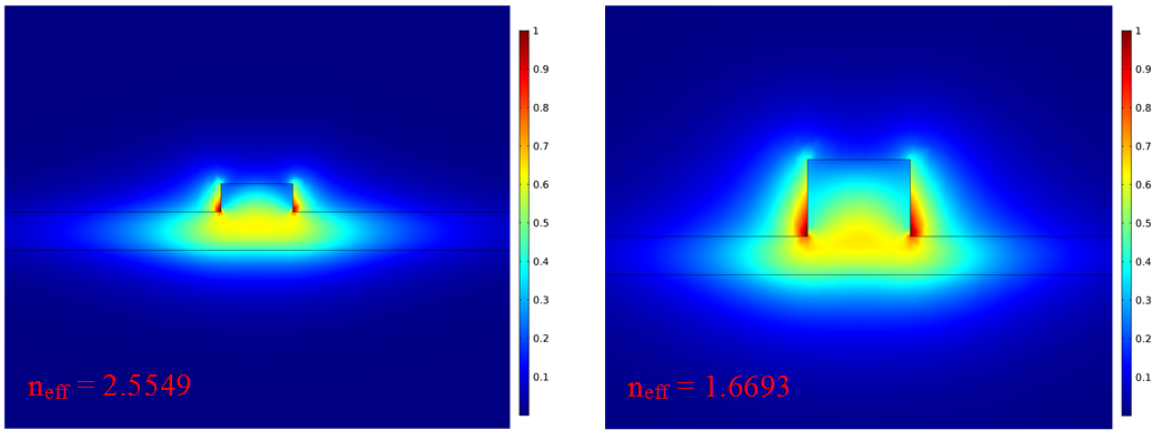

(a) Silicon waveguide (b) Diamond waveguide

Fig. 7.11 Mode shape and effective index of the rib-waveguide.

7.2.2.4 Bends

Solving the wave equation for bent waveguides is more challenging than straight waveguides. Although some analytical methods are available [126], they are approximate and in most cases inaccurate. Numerical methods attracted attention for solving bend losses, but setting simulation parameters and boundaries is challenging. Approximating the bent waveguide to a straight one under certain conditions and assumptions helped to give an insight about bend losses, but is not accurate [127]. A recent paper [92] has proposed an exact solution to convert bent waveguides into straight waveguides for simulation. The proposed method defines the relative permeability and permittivity as diagonal matrices, in the 3-main axes, with a function for the change of refractive index with bent radius.

The proposed method is capable of producing exact transformation matrix of bent and twisted waveguides into straight ones, where the bend radius is R and the twist pitch is $2\pi P$ as shown in Fig. 7.12. For better definition of the waveguide structure, the Cartesian coordinates (x,y,z) are transformed into helical coordinates (u,v,w) as follows:

$$x = u \tag{7.4}$$

$$y = v.cos(u/P) + w.sin(u/P) \tag{7.5}$$

$$z = -v.sin(u/P) + w.cos(u/P) \tag{7.6}$$

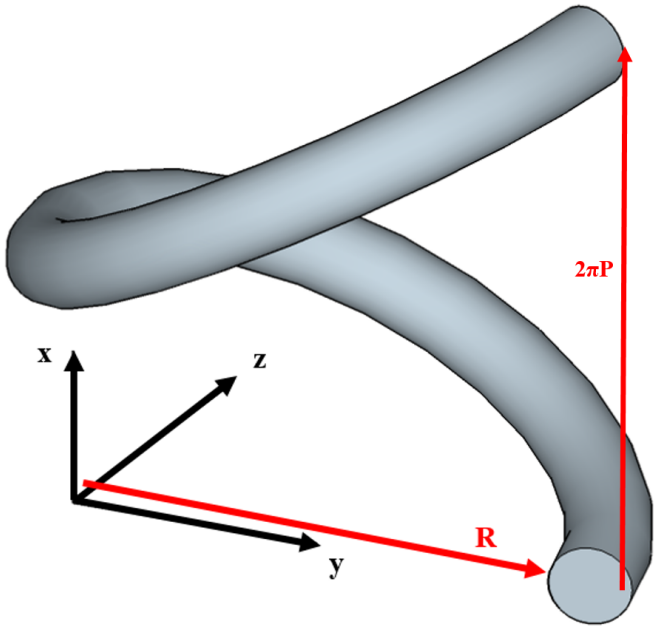

Fig. 7.12 Twisted and bent waveguide structure with bend radius R and twist pitch $2\pi P$.

The numerical transformations of permittivity and permeability from Cartesian to helical coordinates are

$$\varepsilon^{ij} = \sqrt{g}\, g^{ij}\, \varepsilon_c \qquad \mu^{ij} = \sqrt{g}\, g^{ij} \mu_c \tag{7.7}$$

where ε^{ij} and μ^{ij} are, respectively, permittivity and permeability tensors in the helical coordinate system with i and j are variables of the coordinates. $g = v^2/R^2$, ε_c and μ_c are the material permittivity and permeability in Cartesian coordinates, and g^{ij} is the transformation tensor and is defined by

$$g^{ij} = \begin{bmatrix} g^{uu} & g^{uv} & g^{uw} \\ g^{vu} & g^{vv} & g^{vw} \\ g^{wu} & g^{wv} & g^{ww} \end{bmatrix} = \begin{bmatrix} \frac{1+(P/v)^2}{1+(P/R)^2} & 0 & \frac{1-(R/v)^2}{R/P+P/R} \\ 0 & 1 & 0 \\ \frac{1-(R/v)^2}{R/P+P/R} & 0 & \frac{(R/v)^2+(P/R)^2}{1+(P/R)^2} \end{bmatrix} \tag{7.8}$$

For an isotropic planar waveguide with no twist, $P = 0$, the transformation tensor becomes

$$g^{ij} = \begin{bmatrix} 1 & 0 & 0 \\ 0 & 1 & 0 \\ 0 & 0 & (R/v)^2 \end{bmatrix} \tag{7.9}$$

And the non-zero permittivity components, from equation 7.7, become

$$\varepsilon^{uu} = \varepsilon^{vv} = \varepsilon_c \,.v/R \qquad \varepsilon^{ww} = \varepsilon_c \,.R/v \tag{7.10}$$

and similarly for the permeability. Then we need to transform the permittivity and permeability back to the Cartesian coordinates for numerical calculations. By shifting the origin to the waveguide edge at $v = R$, we get

$$x = u \quad y = v - R \quad z = w \tag{7.11}$$

hence

$$\varepsilon^{xx} = \varepsilon^{yy} = \varepsilon_c \,.\, (1 + y/R) \quad \varepsilon^{zz} = \varepsilon_c \,.\, (1 + y/R)^{-1}. \tag{7.12}$$

With equations 7.12 and similar ones for the permeability, a diagonal material property tensor for the refractive index is construct as

$$n^2 = \begin{bmatrix} \varepsilon_c(1+y/R).\mu_c(1+y/R) & 0 & 0 \\ 0 & \varepsilon_c(1+y/R).\mu_c(1+y/R) & 0 \\ 0 & 0 & \varepsilon_c(1+y/R)^{-1}.\mu_c(1+y/R)^{-1} \end{bmatrix} \tag{7.13}$$

Studies of bend loses and mode delocalization have been conducted for slab, rib and rectangular waveguides using COMSOL® Multiphysics. All the bent waveguides in the device are rib waveguides, so we report their results in Fig. 7.13. The mode shifts outwards from the bend radius, and it only starts being confined in the middle section at bend radius of $40\mu m$ for silicon waveguides and as small as $10\mu m$ for diamond waveguides. With $50\mu m$ bends, the mode is confined in the middle section of the silicon waveguide, therefore it was the chosen bend radius in the silicon device. And bends of $20\mu m$ were chosen for the diamond device.

The main reason for mode localization in the diamond waveguide is because of the significant difference between the ridge height and the rib height. For the silicon waveguide, the difference is not big enough to ensure high confinements at small bend radii.

7.2.2.5 Input- and output-couplers

After designing the waveguide, a mechanism to couple the optical signal in and out of the chip was needed. Prism-, nano-taper-, grating-, and inverse-nano-taper-coupling are the known mechanisms. Prism-coupling requires depositing and processing an extra layer on

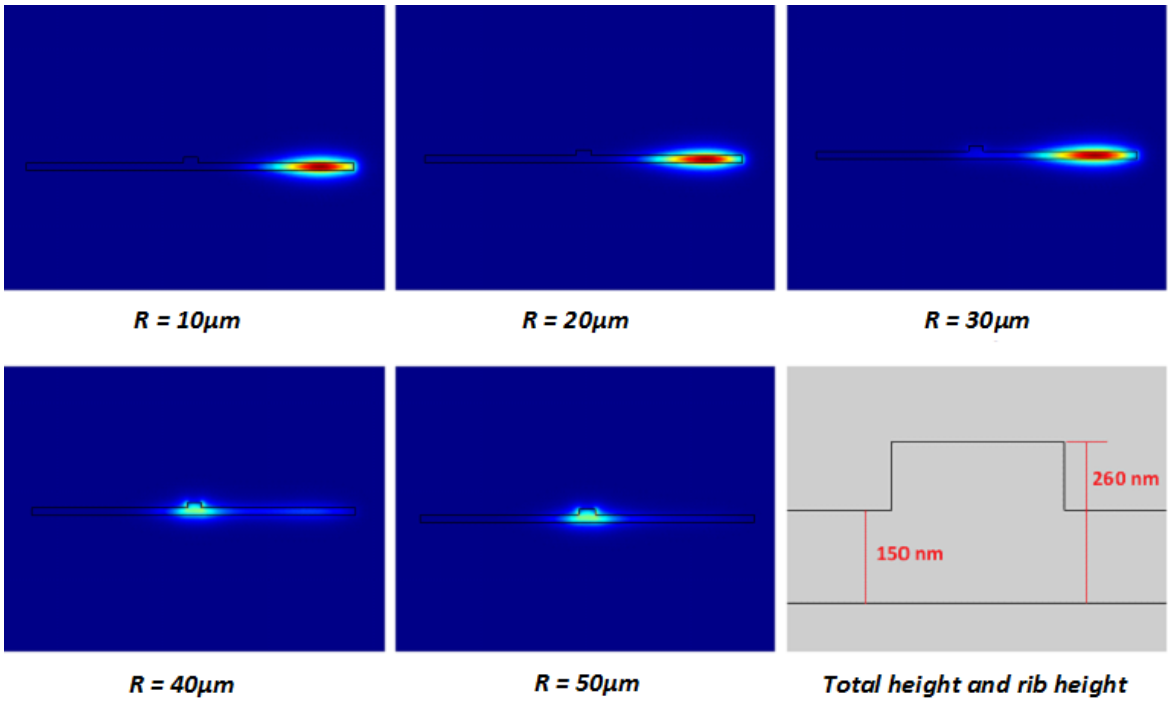

(a) Silicon waveguide.

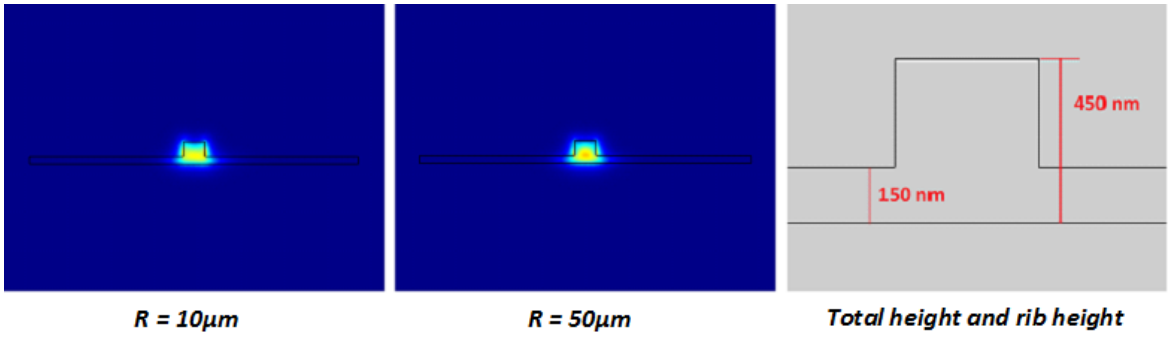

(b) Diamond waveguide.

Fig. 7.13 Mode shape and location for bent waveguides of different bend radii.

top of the chip, and is not very efficient. Fig. 7.14a shows a schematic of the prism-coupler with light coupling mechanism. Nano-taper-coupler is a very effective mechanism that is easily fabricated. But as shown in Fig. 7.14c it has large dimensions. Grating couplers have an acceptable efficiency and overcomes the chip-side-facet coupling reflection and alignment problems in the taper-coupler, but its design and fabrication are challenging. Periodic perturbations in the waveguide refractive index are introduced, and Fig. 7.14b shows an example of grating-coupler. A detailed study of grating couplers is presented in **Chapter 3**. Inverse-nano-taper-coupling, Fig. 7.14d, is efficient [128] and is very easy to design and fabricate. It does not have large footprint, but it is very sensitive to misalignments. Practically,

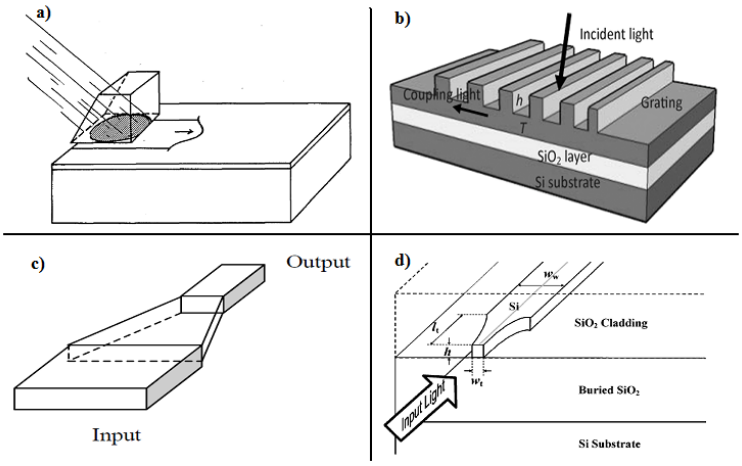

Fig. 7.14 Input and output coupling mechanisms. a) prism coupler (image from [129]), b) grating coupler (image from [130]), c) taper coupler (image from [131]), and d) inverse-taper coupler (image from [132]).

inverse-nano-taper-coupling offers a good compromise between design, fabrication and operation parameters, therefor it is the chosen mechanism for our device. The design of grating couplers has also been conducted, refer to **Chapter 3** of this work.

Inverse-nano-taper-coupling depends on mode shape matching, which means coupling efficiency depends on how similar the mode shapes are between the waveguide and coupling fibre. Mathematically it is described by overlapping integral as

$$A_s = \frac{1}{\mu_0.\omega}\frac{\beta_f.\beta_w}{\beta_f+\beta_w}\int_{-\infty}^{\infty}\int_{-\infty}^{\infty}\varepsilon_f(x,y).\varepsilon_w(x,y)\,dx\,dy \tag{7.14}$$

where A_s is the coupled field amplitude, μ_0 is magnetic permeability of free space, ω is the angular frequency, β_f and β_w are the fiber and waveguide propagation constants, respectively, and $\varepsilon_f(x,y)$ and $\varepsilon_w(x,y)$ are the fibre and waveguide field functions, respectively. Equation 7.14 is extended from the 1D equation in [133].
Having a single mode optical fibre, with radius r, we can assume the field inside it to take the form

$$\varepsilon_f(x,y) = 2\frac{\omega.\mu_0}{\beta_f\sqrt{r^2\sin\Phi.\cos\Phi}}.\cos(\frac{\pi x}{r.\cos\Phi}).\cos(\frac{\pi y}{r.\sin\Phi}) \tag{7.15}$$

And for the waveguide with width W and height H to be

$$\varepsilon_w(x,y) = 2\frac{\omega.\mu_0}{\beta_w\sqrt{W\times H}}.\cos(\frac{\pi x s_x}{W}).\cos(\frac{\pi y s_y}{H}) \quad ,s_x = 1,3,\cdots \quad ,s_y = 1,3,\cdots \tag{7.16}$$

$$\varepsilon_w(x,y) = 2\frac{\omega.\mu_0}{\beta_w\sqrt{W\times H}}.\sin(\frac{\pi x s_x}{W}).\cos(\frac{\pi y s_y}{H}) \ \ , s_x = 2,4,\cdots \ \ , s_y = 1,3,\cdots \tag{7.17}$$

$$\varepsilon_w(x,y) = 2\frac{\omega.\mu_0}{\beta_w\sqrt{W\times H}}.\cos(\frac{\pi x s_x}{W}).\sin(\frac{\pi y s_y}{H}) \ \ , s_x = 1,3,\cdots \ \ , s_y = 2,4,\cdots \tag{7.18}$$

$$\varepsilon_w(x,y) = 2\frac{\omega.\mu_0}{\beta_w\sqrt{W\times H}}.\sin(\frac{\pi x s_x}{W}).\sin(\frac{\pi y s_y}{H}) \ \ , s_x = 2,4,\cdots \ \ , s_y = 2,4,\cdots \tag{7.19}$$

Since coupling occurs with mode overlapping and the input fiber is a single mode fiber with $s_x, s_y = 1$, therefore the antisymmetric modes ($s_x, s_y = 2,4,\cdots$) will not couple; and only equation 7.16 is used for the overlap integral. Performing the integration in equation 7.14, we find that

$$A_s \propto 1/s \tag{7.20}$$

As the second lowest mode that can be coupled has $s_x \, or \, s_y = 3$, and the coupled power P_c is

$$P_c = |A_s|^2 \tag{7.21}$$

we find that the power coupled from the fibre into the second lowest mode of the waveguide is 10% of the total power, hence it can be ignored in the numerical calculations.

To calculate the coupled power in and out of the waveguide, we used the Gaussian distribution for the fiber fields as

$$E_f = e^{-(x^2+y^2)/r^2} \tag{7.22}$$

$$H_f = e^{-(x^2+y^2)/r^2}/\eta_0 \tag{7.23}$$

where x and y are the cross-sectional Cartesian coordinates, and η_0 is free space resistance and is equal to μ_0/ε_0, where ε_0 is the free space permittivity. And input/output coupler fields' distribution has been solved numerically using COMSOL® Multiphysics by choosing a domain size sufficient to contain all fields, then the overlap integral has been carried out using MATLAB® software.

Two SMFs (single mode fibres) were used in this experiment, a $2\mu m$ and a $10\mu m$ fibres coupling into a rib-waveguide. Waveguide and rib heights have been fixed for fabrication consideration, while the waveguide central width varied from 50 to 250nm in steps of 50nm

for silicon waveguide and from 50 to 450*nm* in steps of 50*nm* for diamond waveguide. The results are tabulated in Table 7.1 and Table 7.2 for silicon and diamond, respectively, with the design values being highlighted.

Table 7.1 Silicon coupler efficiency vs coupler width

Wavelength	$2\mu m$ fibre		$10\mu m$ fibre	
	Width	% coupled	Width	% coupled
$1.5\mu m$	$50\mu m$	43.5981	$50\mu m$	30.334
	$100\mu m$	58.9667	$100\mu m$	27.386
	$150\mu m$	65.6761	$150\mu m$	22.017
	$200\mu m$	65.6807	$200\mu m$	18.2123
	$250\mu m$	63.2904	$250\mu m$	15.8145
$1.55\mu m$	$50\mu m$	43.7997	$50\mu m$	30.8883
	$100\mu m$	59.0447	$100\mu m$	28.2695
	$150\mu m$	66.422	$150\mu m$	22.9657
	$200\mu m$	66.9979	$200\mu m$	19.0511
	$250\mu m$	64.9092	$250\mu m$	16.5335
$1.6\mu m$	$50\mu m$	44.0118	$50\mu m$	31.4423
	$100\mu m$	59.0743	$100\mu m$	29.1396
	$150\mu m$	67.0817	$150\mu m$	23.9292
	$200\mu m$	68.2355	$200\mu m$	19.9151
	$250\mu m$	66.4786	$250\mu m$	17.2794

7.2.2.6 Waveguide transitions

As explained in previous sections, the waveguide has different structures and widths. And a smooth transition between such different sections was required, to minimize transition losses [134]. The transition between different waveguide structures can cause mode conversion or splitting due to asymmetry in the waveguide. Mode conversion is undesirable as it changes the characteristics of the signal and can jeopardise the device operation. Also mode splitting transfers a percentage of the signal power to higher order modes, which are considered as losses.

The change in waveguide structure changes the effective indices of the different modes supported by the waveguide. If two or more modes have similar effective indices, they will merge forming hybrid modes (Fig. 7.15). Fig. 7.16a shows the effective indices of different modes supported by a silicon rib-waveguide vs waveguide width. Below 200*nm*, the refractive indices of several modes are similar to each other, which might cause power transfer

Table 7.2 Diamond coupler efficiency vs coupler width

Wavelength	$2\mu m$ fibre		$10\mu m$ fibre	
	Width	% coupled	Width	% coupled
$1.5\mu m$	$50\mu m$	49.5811	$50\mu m$	40.4861
	$100\mu m$	61.1612	$100\mu m$	40.1222
	$150\mu m$	72.5151	$150\mu m$	36.8226
	$200\mu m$	79.1842	$200\mu m$	32.1982
	$250\mu m$	81.7334	$250\mu m$	28.0418
	$300\mu m$	81.5429	$250\mu m$	24.7203
	$350\mu m$	79.7588	$250\mu m$	22.157
	$400\mu m$	77.2593	$250\mu m$	20.2123
	$450\mu m$	74.7155	$250\mu m$	18.7811
$1.55\mu m$	$50\mu m$	49.918	$50\mu m$	41.5792
	$100\mu m$	60.8879	$100\mu m$	41.3954
	$150\mu m$	72.2876	$150\mu m$	38.4851
	$200\mu m$	79.5423	$200\mu m$	33.9816
	$250\mu m$	82.7497	$250\mu m$	29.7329
	$300\mu m$	83.1278	$300\mu m$	26.2467
	$350\mu m$	81.7508	$350\mu m$	23.5061
	$400\mu m$	79.4755	$400\mu m$	21.3929
	$450\mu m$	76.9894	$450\mu m$	19.8118
$1.6\mu m$	$50\mu m$	50.2302	$50\mu m$	42.6867
	$100\mu m$	60.5867	$100\mu m$	42.654
	$150\mu m$	71.922	$150\mu m$	40.1307
	$200\mu m$	79.697	$200\mu m$	35.7957
	$250\mu m$	83.5432	$250\mu m$	31.4837
	$300\mu m$	84.5043	$300\mu m$	27.8447
	$350\mu m$	83.5746	$350\mu m$	24.929
	$400\mu m$	81.5773	$400\mu m$	22.6449
	$450\mu m$	79.2024	$450\mu m$	20.9089

from one mode to another. The Inverse-coupler width falls within this region, therefore, the transition from coupler to straight waveguide and vice versa was required to be adiabatic (smooth transition to ensure higher order modes do not get excited); and similarly for widths below $200nm$ for the diamond waveguide (Fig. 7.16b).

Another transition is supported-to-hanging transition, where the waveguide lower cladding changes from PMMA to air or the opposite. Here it was essential that the transition will not trigger higher order modes.

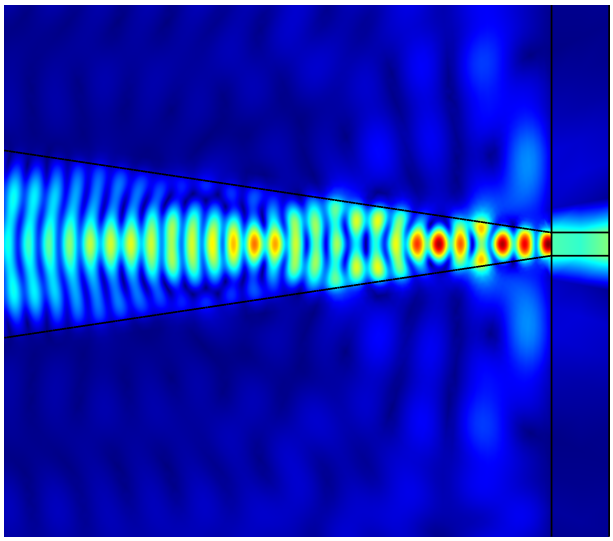

Fig. 7.15 Example of TE_0 mode input merging with higher order modes in a non-adiabatic transition.

The parameters for designing transitions are 1) the widths at the start and end of the transition, 2) transition structure (slab, rib, or rectangle waveguide), 3) core and cladding materials, and 4) transition length. For taper-transition, all the parameters were fixed except for the taper length. Simply, taper length should be long enough to overcome mode conversion, splitting or free space scattering. For supported-to-hanging transition, a rib-waveguide structure with no taper was chosen to limit the transition change to only a lower-cladding material change. A rib-waveguide was chosen, to provide higher mode confinement, which

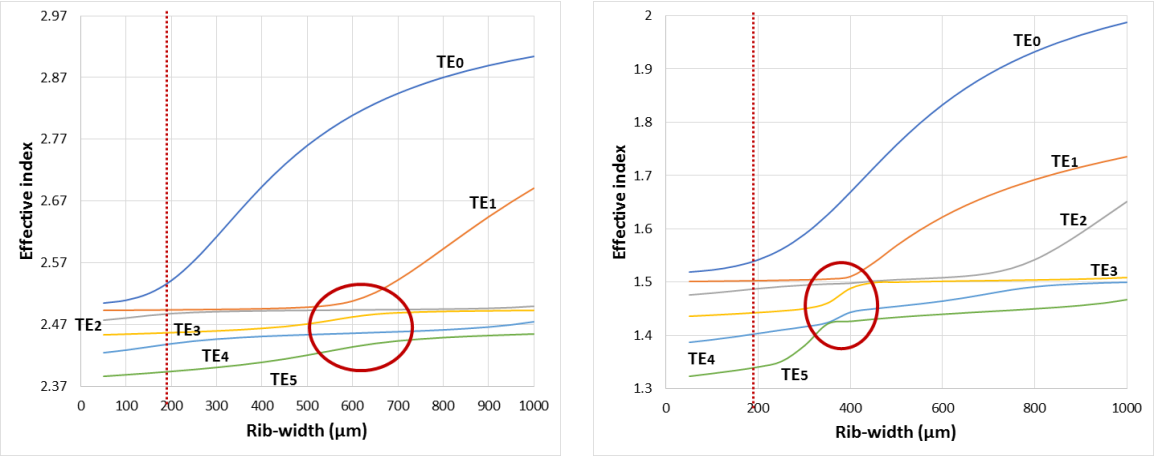

(a) Silicon waveguide (b) Diamond waveguide

Fig. 7.16 Refractive indices of first 6 modes of rib waveguides.

lowers mode interaction with waveguide surfaces and hence, lowers the probability of higher mode excitation.

Also, a transition from rib to rectangular coupler waveguide was required (Fig. 7.17). But according to the high mode confinement in the central region of both silicon (Fig. 7.11a) and diamond (Fig. 7.11b) waveguides, the rib-to-rectangular transition was shown to be adiabatic for short transition lengths (Fig. 7.18), therefore a $20\mu m$ taper was chosen to reduce the transition footprint.

Rectangular taper transition has been simulated using COMSOL® Multiphysics for a $50nm$ to $280nm$ transition in silicon and $50nm$ to $400nm$ transition in diamond. A $20\mu m$ transition length was chosen in both cases as 1) it is long enough to provide adiabatic

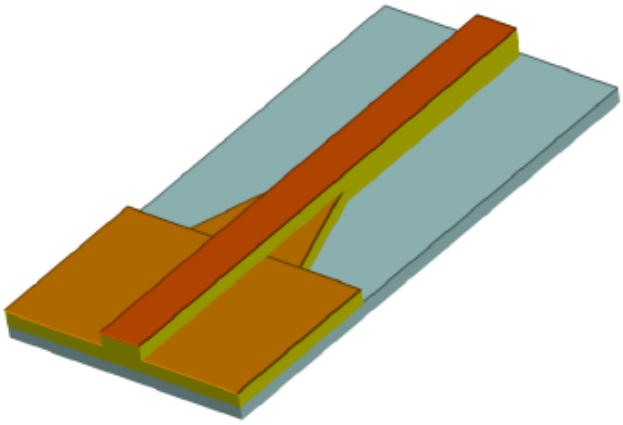

Fig. 7.17 Rib-to-rectangular waveguide transition. Adapted from [134].

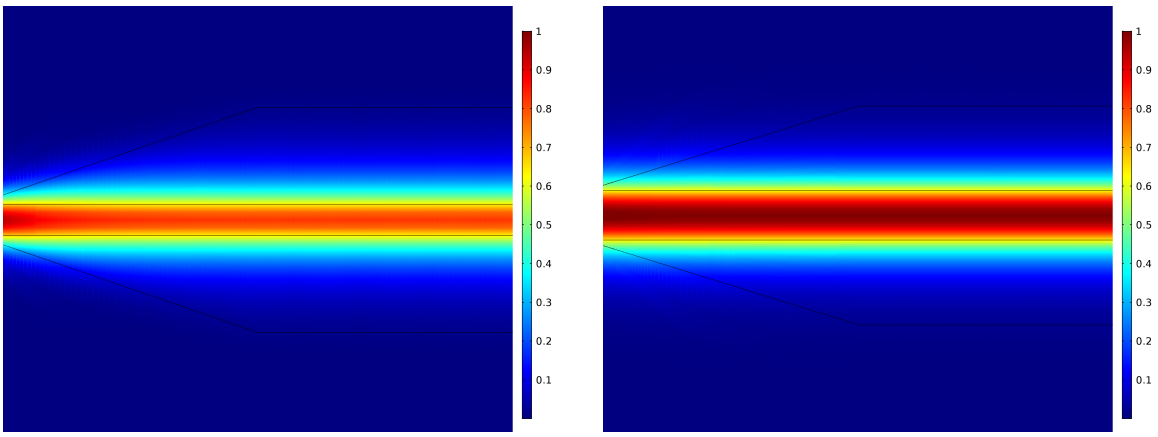

(a) Silicon waveguide (b) Diamond waveguide

Fig. 7.18 Adiabatic transition from rib to rectangular waveguides.

transition and 2) does not have a large footprint. Fig. 7.19 shows the adiabatic taper transition for silicon and diamond waveguides.

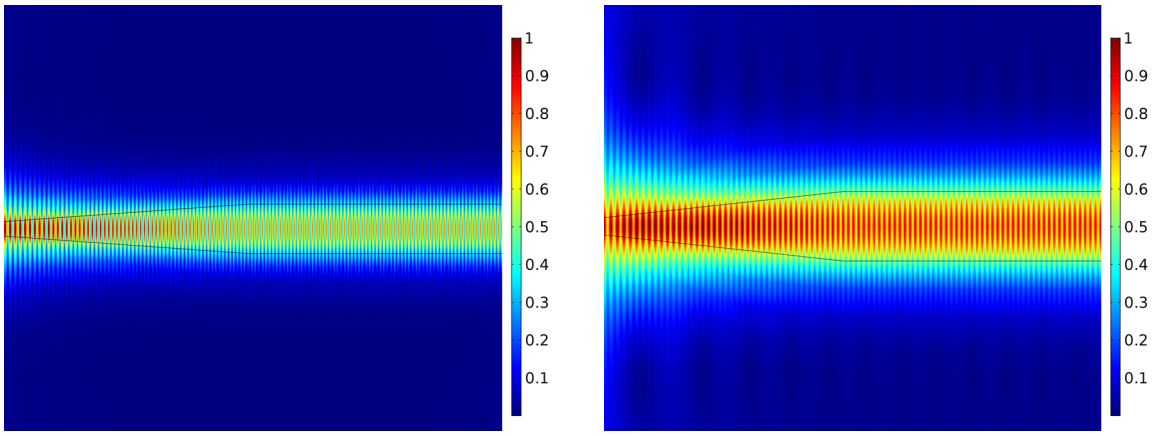

(a) Silicon waveguide (b) Diamond waveguide

Fig. 7.19 Adiabatic rectangular taper transition.

A supported-to-hanging transition was chosen to be $50\mu m$ long before any alteration to the waveguide structure takes place for two reasons: 1) compensate for fabrication imperfections and roughness that might contribute to mode conversion/splitting, and 2) to provide large surface area for electromechanical actuation. The results are presented in Fig. 7.20a for silicon waveguide and Fig. 7.20b for diamond waveguide, where a smooth transition is evident. By taking a closer look at the transition point in the diamond waveguide, it is clear that the mode intensity distribution differs for supported (left) and suspended (right) structures, due to the change in the effective index of the propagating mode. Such transition is not obvious in the silicon waveguide as the effective indices at both sides of the transition are very similar.

7.3 Electromechanical design

This section focuses on the actuator design to provide at least one micron deflection with reasonable applied voltages. The main aim is to allow for the coupler waveguide to deflect from its static position of large separation gap from the resonator, with zero power coupling, to a zero-separation gap. This large deflection range has a twofold benefit: 1) provides total control over the amount of coupled power, and 2) offers large tolerance in the fabrication process.

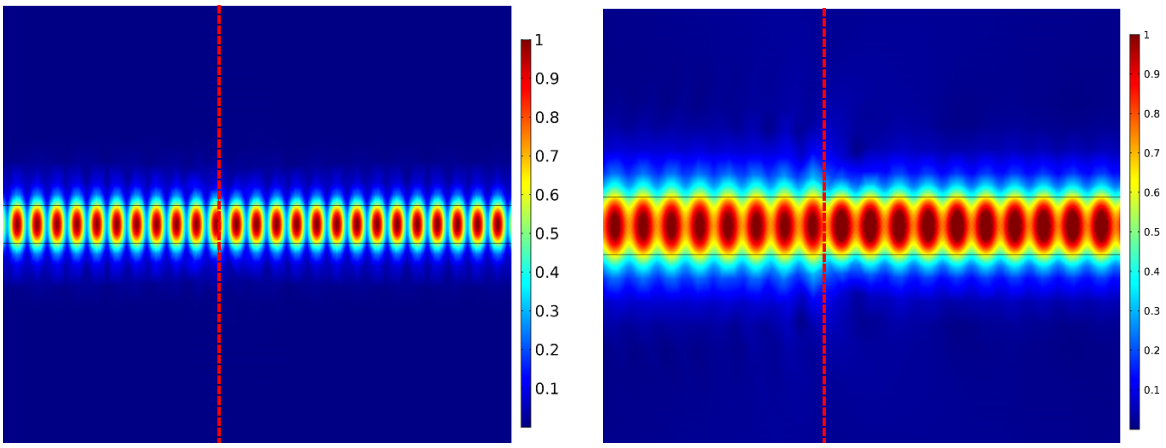

(a) Silicon waveguide (b) Diamond waveguide

Fig. 7.20 Smooth supported-to-hanging transitions.

The electromechanical actuator design has several parameters, 1) separation gap between the actuator electrodes, 2) electrodes materials, 3) actuation voltage, and 4) electrodes shape, thickness and size.

Separation gap Conventionally, the separation gap for MEMS (Micro-Electro-Mechanical-Systems) actuators has been around $5\mu m$ or less for faster actuations with lower voltages [135, 136]. By referring to Fig. 7.1, the gap should be large enough to ensure that the coupler waveguide is far enough for no coupling. The oxidized silicon chips used in this project to fabricate the resonator had a $1.3\mu m$ thick oxide layer. With resonator minor radius varying from 2.5 to $4.5\mu m$, and having a gap between the resonator and the coupler waveguide of at least $1\mu m$, a gap between 3 and $5\mu m$ was required. For structure stability, the $4.5\mu m$ ring radius was excluded. Therefore, gaps of 3 to $4\mu m$ were selected.

Electrodes materials One of the benefits of using silicon as a platform for photonics is that it can act as an optical and electrical material at the same time. As mentioned in **Chapter 2**, dopants can be used to increase the electrical conductivity without compromising the optical absorption coefficient beyond acceptable limits. Therefore, doped silicon for the upper electrode (device layer in Fig. 7.1) was used. For the lower electrode, molybdenum layer was used.

For the diamond chip, molybdenum lower upper electrodes were chosen, as doping NCD introduces very high optical losses. Silicon and diamond doping is discussed in more details in **subsection 7.3.1**.

Actuation voltage Actuation voltages as high as $200V$ can be used [135, 136], but lower actuation voltages are preferable. The separation gaps were fixed to $3\mu m$ for chips with $2.5\mu m$ resonator radius and $4\mu m$ for the ones with $3.5\mu m$ resonators, and the material between both electrodes is air, therefore the only two parameters left that affects actuation voltage were the overlapping area between both electrodes and the actuator thickness. Therefore, different actuator designs and sizes have been studied to reach a final design that can provide $1.5\mu m$ of deflection at voltages below $25V$.

Electrodes shape, thickness and size COMSOL® Multiphysics has been used to simultaneously calculate the deflection of the actuator waveguide due to its weight and the applied voltage. After trying several attempts, the design in Fig. 7.21 was chosen as it provides the largest overlap area while being mechanically resilient.

According to [135] the actuator deflection Δg is described by

$$\Delta g = \frac{F}{k} \tag{7.24}$$

where F is the applied force (electrostatic force), and k is the actuator spring constant (defines resistance to deflection). The electrostatic force is given by

$$F = \frac{1}{2} V^2 \frac{dC}{dg} \tag{7.25}$$

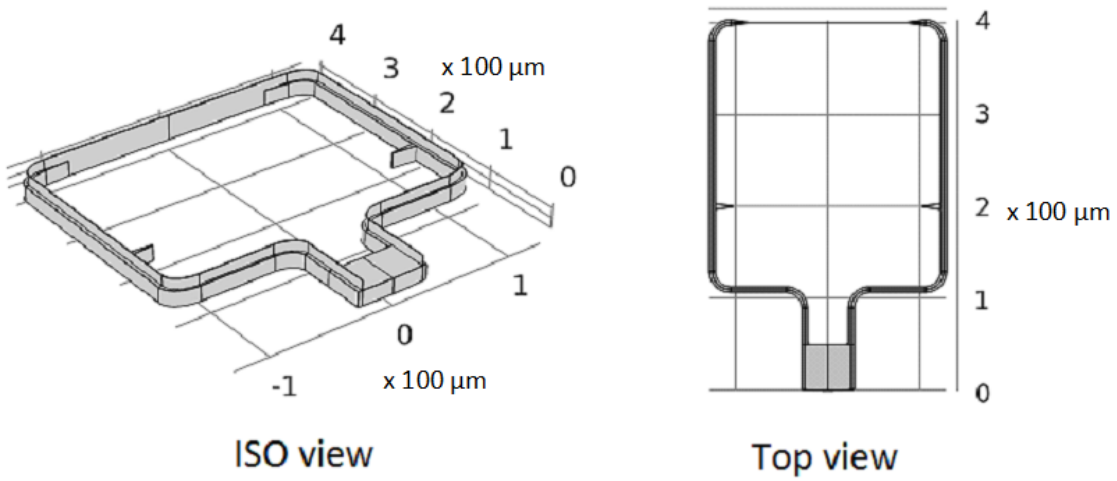

Fig. 7.21 Coupler structure - ISO view scale $x : y : z = 100 : 100 : 1$.

where V is the applied voltage, C is the capacitance and g is the gap between the electrodes. As C changes with the change in the separation gap (dC/dg) according to the equation

$$C = \frac{\varepsilon_0 \times A}{g} = \frac{\varepsilon_0 (w \times l)}{g} \tag{7.26}$$

where ε_0 is the permitivity of air, and A is the overlapping area between the electrodes, and w and l are the actuator's width and length, respectively; a dynamic numerical simulation was more accurate in calculating the electrostatic force than the static analytical solution.

On the other hand, k is a constant for each structure and is defined by

$$k = k' + k" \tag{7.27}$$

where k' is due to the stiffness of the structure and is defined by the structure dimensions and Young's modulus of elasticity, and k'' is due to the residual stress from the fabrication processes. For a cantilever structure supported from one end, the residual stress gets relieved after fabrication and k'' vanishes. For a simple cantilever beam, k' is defined by

$$k' = \frac{3}{2} \times E \times w \times (\frac{t}{l})^3 \tag{7.28}$$

where E is Young's modulus of elasticity, and t is the thickness of the cantilever. From this analysis it is found that we need to increase F and reduce k, so we conclude that:

1. As w increases, both F and k increase. Therefore, an optimum width for the supported edge that provides large enough width for actuation without compromising the deflection resistance was essential. Such optimum width can be calculated by differentiation techniques. But according to the complexity of the structure, this was very time consuming to solve analytically and would introduce large errors if approximated with simple structures. Trial and error methods have been used to approach an efficient width of $56.6\mu m$.

2. Longer length l was preferable to decrease k and increase F, but it will compromise the structure's mechanical strength according to the equation

$$F_{mech} = \frac{\sigma \times w \times t^2}{3 \times l} \tag{7.29}$$

where F_{mech} is the maximum allowable force, σ is the maximum allowable stress that is constant for each material. Therefore, the length of the actuator was chosen to be $50\mu m$ as it was the shortest supported-to-hanging transition length determined.

3. For the thickness t equations 7.28 and 7.29 contradict, but it was not time and computer power consuming, therefore numerical simulations were conducted to determine the optimum t. The actuator thickness (rib-height for the waveguide) varied from 50 to 200nm for the silicon device, and from 50 to 400nm for the diamond device. And a 150nm rib-thickness for both silicon and diamond actuators provided the best results.

7.3.1 Material doping

Silicon and diamond doping has been studied in this work to assess the possibility of using the device's structures as, both, optical waveguides and electrical contacts, which can reduce device fabrication steps and offer more compact designs.

The requirements needed from doping are:

1. Low extinction coefficient ($k < 10^{-5}$). The extinction coefficient, which defines the wave decay through propagation, is the imaginary refractive index of the material as in

$$N = n + ik \tag{7.30}$$

where N is the total refractive index, n is the real refractive index, i is the imaginary number, and k is the extinction coefficient. For transparent materials, k is very small that it can be ignored and $N = n$, where n is referred to as the refractive index. But doping optical materials increases the extinction coefficient above a threshold limit that it no longer can be ignored. k is related to optical absorbance (α) by the equation

$$k = \frac{\lambda\, \alpha}{4\pi} \tag{7.31}$$

where λ is the operation wavelength in m, and the α is in units of m^{-1}. And as a function of dopant concentration α is defined as [23]

$$\alpha = \frac{q^3\, \lambda^2\, N_A}{4\pi^2\, \varepsilon_0\, c^3\, n\, m^{*2}\, \mu_A} \tag{7.32}$$

where q is the electron charge, N_A is the dopant concentration, m^* is the effective mass, and μ_A is the mobility. q and ε_0 are constants, λ is the operation wavelength and is fixed at 1.55μm, and n can be assumed constant for silicon and diamond (more on this later), so we are left with three variables, m^*, N_A, and μ_A, where m^* is depending on the dopant type.

2. High electrical conductivity σ, or low electrical resistivity ρ ($\rho < 1\ \Omega.cm$). Where ρ is defined by [137]

$$\rho = \frac{1}{q\ (\mu_n \times n + \mu_p \times p)} \tag{7.33}$$

where μ_n and μ_p are the electron and hole mobility in the lattice, and n and p are the electron and hole concentration respectively. Or approximately

$$\rho = \frac{1}{q \times \mu_A \times N_A}. \tag{7.34}$$

By examining equations 7.32 and 7.34, determining dopant type (μ_A and m^*) and concentration (N_A) were required for the silicon and diamond waveguides to achieve $k < 10^{-5}$ and $\rho < 1\ \Omega.cm$.

7.3.1.1 Silicon doping

Optical properties of silicon are not as well established as the electrical properties, due to the maturity of the field of silicon electronics compared to the relatively recent field of silicon photonics. Some literature is available for crystalline silicon optical properties, but a formula for absorption versus dopant concentration is not available for all parameters. The lack of a unified formula is due to the high complexity of equation 7.32. For instance, μ_A is a function of dopant type and concentration [137]

$$\mu_A = \frac{\mu_{max} - \mu_{min}}{1 + (\frac{N_A}{N_{ref}})^{\gamma}} + \mu_{min} \tag{7.35}$$

where μ_{max}, μ_{min}, γ and N_{ref} are experimental fit parameters. And m^* is a fraction of the electron rest mass depending on the velocity of the carrier, where the velocity is a function of the carrier mobility, which in turn is a function of dopant concentration. So, an exact formula for m^* is not available and, the formulas available are approximations for specific applications with certain approximations. Therefore, an approximate formula is derived for each dopant type for a certain range of concentrations at a certain wavelength band. An exact equation should be in the form

$$\alpha = \frac{q^3\ \lambda^2\ N_A}{4\pi^2\ \varepsilon_0\ c^3\ n\ m^{*2}\ (\frac{\mu_{max} - \mu_{min}}{1 + (\frac{N_A}{N_{ref}})^{\gamma}} + \mu_{min})}. \tag{7.36}$$

Solving equation 7.36, all the parameters are constants, where n is assumed to be constant according to the results in Fig. 7.22. It can be seen that the change in refractive index is in the order of 10^{-4} to 10^{-3} for moderate doping concentrations and less than 10^{-4} for lightly doped silicon.

To get at an initial guess for doping concentration, the linear formulas from [23] were used, which at $1.55\mu m$ wavelength gives

$$\alpha_n \approx 2.4025 \times 10^{-18}\, n, \tag{7.37}$$

$$\alpha_p \approx 6.48675 \times 10^{-18}\, p. \tag{7.38}$$

These formulas are for the $4 \rightarrow 10\mu m$ wavelengths, but according to Fig. 7.23, we would expect a lower loss than achieved by formulas 7.37 and 7.38. $\alpha < 0.81 cm^{-1}$ is required to satisfy the condition of $k < 10^{-5}$. Hence, we get

$$n \leqslant 3.37 \times 10^{15}, \tag{7.39}$$

$$p \leqslant 1.25 \times 10^{17}. \tag{7.40}$$

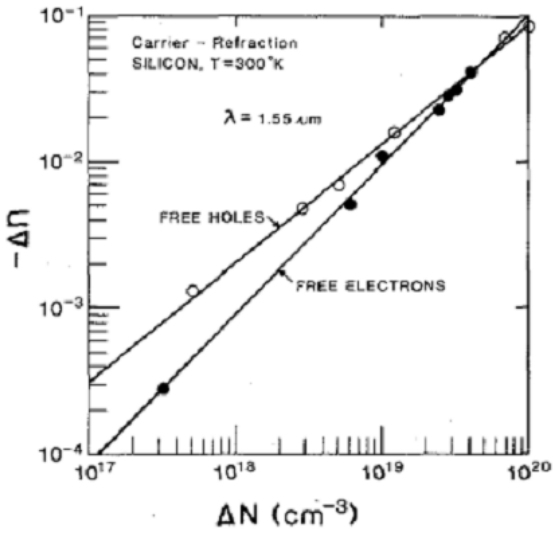

Fig. 7.22 Carrier refraction in crystalline-Si at $\lambda = 1.55\mu m$ as a function of free carrier concentration. Adapted from [26].

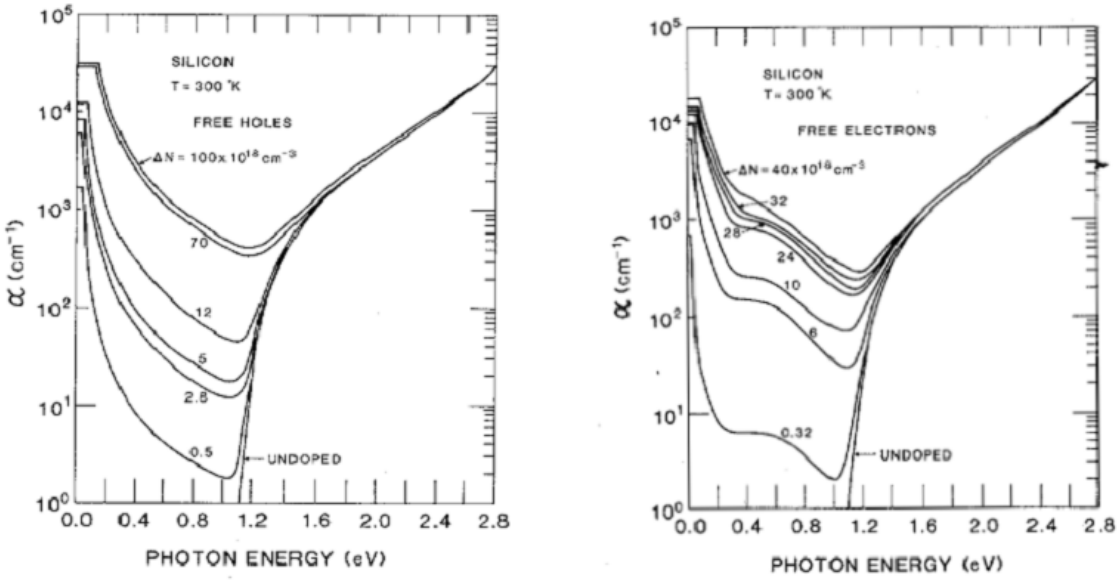

Fig. 7.23 Optical absorption spectra of crystalline-Si showing the influence of various concentration of free carriers. Adapted from [26].

By comparing these results with the experimental results in Fig. 7.24, it can be found that the obtained value for n-doping is an order of magnitude lower than the experimental value, and the value for p-doping is close enough to the experimental value, therefore the final doping values to achieve low optical losses are 3.37×10^{16} for n-doping and 1.25×10^{17} for p-doping.

For resistivity, solving equations 7.34 and 7.35 simultaneously gives the results for $\rho \leqslant 1\ \Omega.cm$ as

$$n \geqslant 5 \times 10^{15}, \tag{7.41}$$

$$p \geqslant 1.5 \times 10^{16}. \tag{7.42}$$

The range of doping is summarized in Table 7.3. And it shows that both types of doping will meet the requirement for electrical conductivity without compromising the optical transparency beyond the required values, while offering large range of doping.

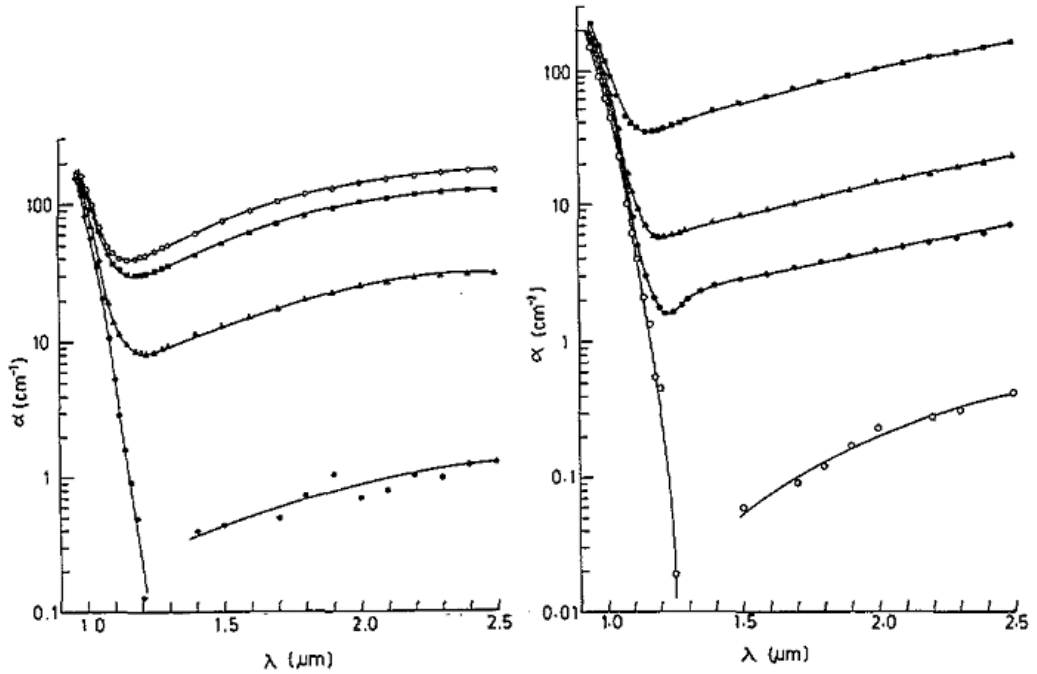

Figure 1. The absorption curves for n-Si samples at 294 K. (●) 6.5×10^{16} cm^{-3}; (▲) 1.6×10^{17} cm^{-3}; (■) 6.4×10^{18} cm^{-3}; (○) 9.2×10^{18} cm^{-3}.

Figure 2. The absorption curves for p-Si samples at 294 K. (○) 1.5×10^{16} cm^{-3}; (●) 3.3×10^{17} cm^{-3}; (▲) 1.2×10^{18} cm^{-3}; (■) 7.3×10^{18} cm^{-3}.

Fig. 7.24 Absorption curves for n- and p-Si samples at 294^o K. Adapted from [27].

Table 7.3 Silicon doping requirements

Dopant type	Minimum value	Maximum value
n-doping	5×10^{15}	3.37×10^{16}
p-doping	1.5×10^{16}	1.25×10^{17}

7.3.1.2 Diamond doping

Preparing semiconducting diamond attracted attention due to the application potential ahead of it as a result of its superior mechanical, thermal and optical properties. Therefore, enhancing its electrical properties will open the way for several applications.

To our knowledge, boron-doping has been the main and only doping mechanism used to prepare semiconducting diamond since the 1980s, but lately, n-doped diamond has been prepared.

By examining the result in [36] presented in Fig. 7.25, it is evident that to reach a $\rho < 1\ \Omega.cm$ ($\sigma > 1\ (\Omega.cm)^{-1}$) $p > 10^{20}$ is required. By inspection of the experimental

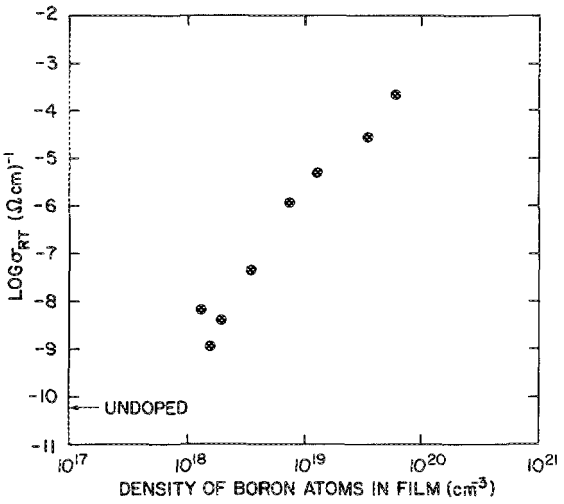

Fig. 7.25 Effect of boron doping on the logarithm of the room-temperature electrical conductivity of diamond. Adapted from [36].

results in [38], the boron doping should be in the range

$$2.3 \times 10^{20} < p < 2.9 \times 10^{20}. \tag{7.43}$$

By their absorption measurements, as shown in Fig. 7.26 (where sample S4 doping is 2.7×10^{19} and S12 doping is 3.3×10^{21}), we conclude that the absorption for the doping

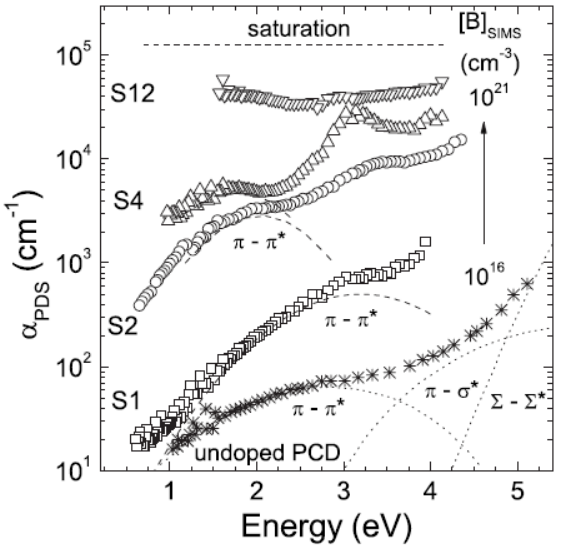

Fig. 7.26 Absorption coefficient α calculated for NCD samples. Adapted from [38].

range in 7.43 would be in the order of $10^4 cm^{-1}$ at 0.8 eV (1.55μm wavelength). Such high loss is beyond acceptable limits; hence, p-doped diamond has been discarded.

n-doped diamond is not mainstream and has very few experimental results compared to p-doped diamond. Optical absorption results were not available, but electrical resistivity was reported. For oxygen-doped diamond to achieve 1 $\Omega.cm$ the doping should be, roughly [41],

$$8.01 \times 10^{17} < n < 2.28 \times 10^{18}; \tag{7.44}$$

which if introduces similar absorption as p-doped, they will not be accepted. For phosphorous-doped diamond, the lowest reported resistivity was $10.92\Omega.cm$ with $n = 3.99 \times 10^{15}$. But resistivity is a function of both doping and annealing temperature, where annealing temperature reduces the dopant concentration, so extrapolating the results for lower resistivity was not possible.

To better understand the cause for the high absorption, we referred back to "as-grown unintentionally-doped" diamond. It was found that at about 0.8 eV a transition from π to π^* state is introduced to the band gap, which causes the increase in absorption [34]. And by referring to Fig. 7.27, we find that the lowest absorption at 0.8 eV for unintentionally-doped diamond is in the order of $10^2 cm^{-1}$. Therefore, ultra-pure undoped diamond films were used to reduce the optical absorption, and using a deposited metal on diamond surface as an electrode instead. The deposited metal had to be, at least, 3μm apart from the rib-waveguide central region to avoid optical losses.

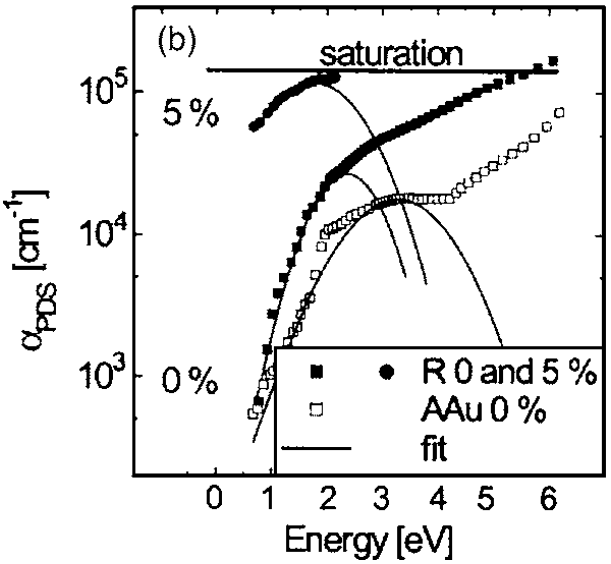

Fig. 7.27 Absorption coefficient for undoped diamond samples. Adapted from [34].

7.3.2 Deflection vs actuation voltage

After deciding all actuator parameters, deflection versus applied voltage has been studied numerically using COMSOL® Multiphysics. A visual representation of the bending waveguide is shown in Fig. 7.28.

Silicon actuator deflections against actuation voltages are presented in Fig. 7.29a and Fig. 7.29b for 3 and $4\mu m$ gaps, respectively. The required $1.5\mu m$ deflection can be achieved with about $3.3V$ actuation voltage for the $3\mu m$ gap, and about $4.3V$ for the $4\mu m$ gap. Such low voltages are ideal for battery operated devices and do not require special operational safety precautions.

Fig. 7.29c and Fig. 7.29d show deflections versus actuation voltages for 3 and $4\mu m$ separation gaps for the diamond waveguide. Again, less than $25V$ actuation voltage was achievable. Less than $10V$ to achieve $1.5\mu m$ deflection for the $3\mu m$ gap, and $13.5V$ to achieve $1.5\mu m$ deflection with the $4\mu m$ gap are presented.

The deflection with zero voltage represents structure's deflection due to gravity and it is $307nm$ for the silicon structure and $54.4nm$ for the diamond one. Diamond ($3515\,kg/m^3$) is denser than silicon ($2330\,kg/m^3$), but diamond's resistance to bending is much higher than silicon as a result of the higher Young's modulus of elasticity ($1050\,GPa$ for diamond and $125\,GPa$ for silicon); hence, the lower deflection due to its weight.

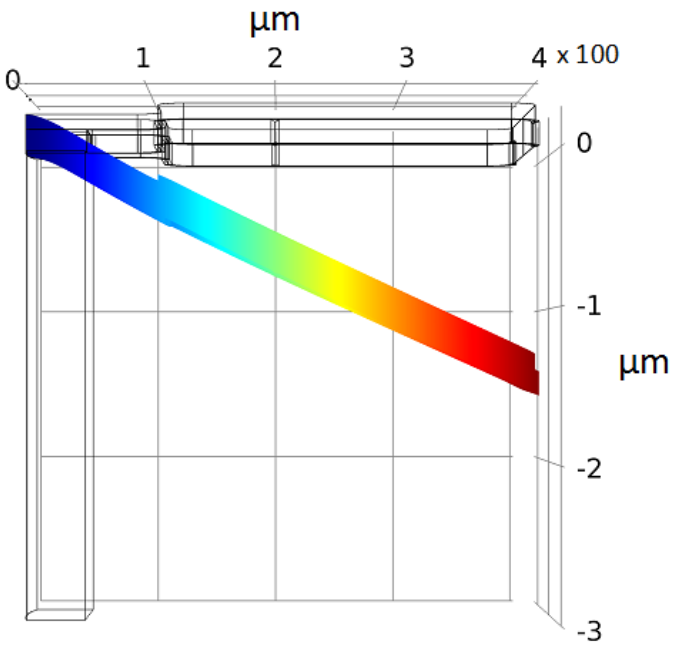

Fig. 7.28 Exaggerated visual representation of coupler deflection.

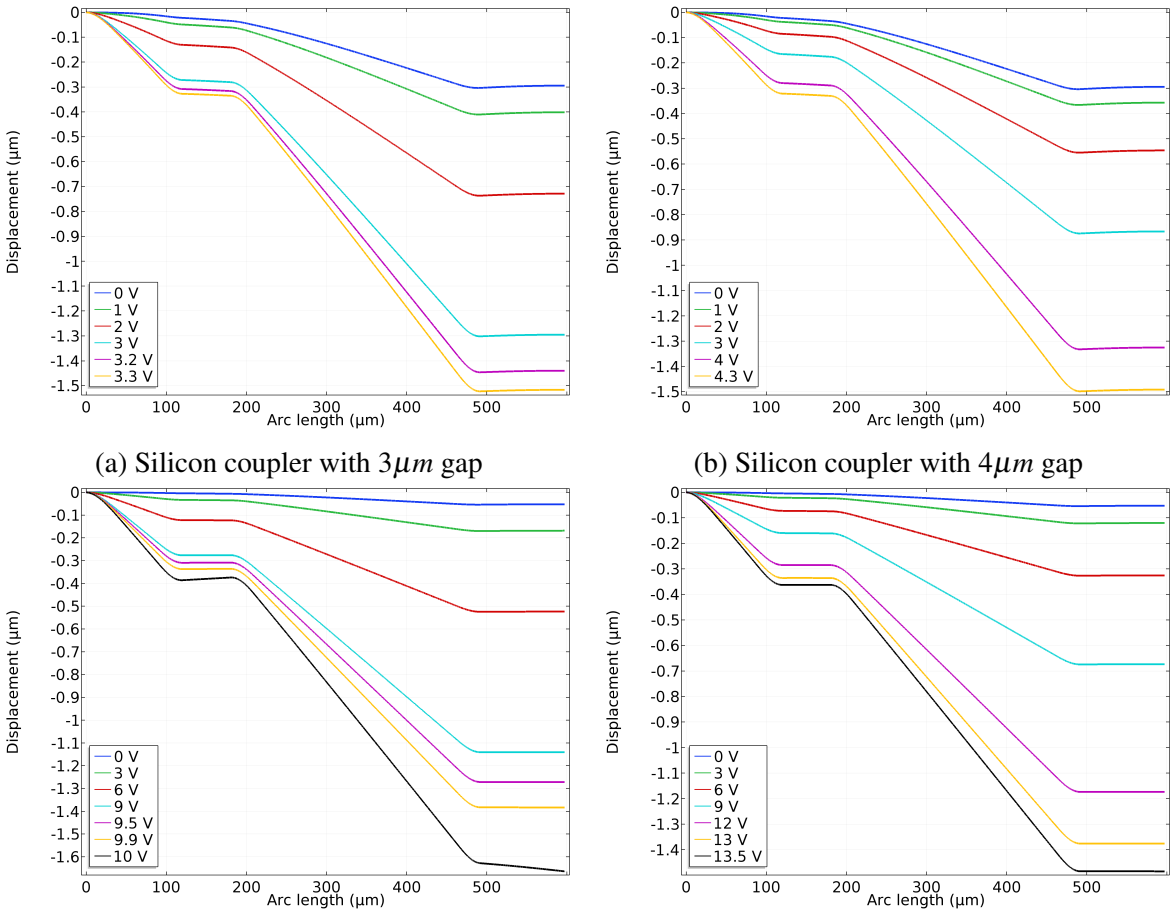

(a) Silicon coupler with $3\mu m$ gap

(b) Silicon coupler with $4\mu m$ gap

(c) Diamond coupler with $3\mu m$ gap

(d) Diamond coupler with $4\mu m$ gap

Fig. 7.29 Deflection vs voltage for silicon and diamond couplers.

7.4 Mechanical design

Two issues needed to be considered to ensure safe fabrication and operation of the chip: 1) the external vibration effects on the hanging cantilever structure, and 2) any vacuum voids trapped within the device at some fabrication steps.

7.4.1 Vibration analysis

For the vibrational effects, it was necessary to make sure that any external force or periodic excitation will not harm the hanging cantilever. Therefore, the natural frequencies of the devices needed to be calculated.

The natural frequency is a characteristic property of the body and is defined by [138]

$$f = \frac{1}{2\pi}\sqrt{\frac{k}{m}} \tag{7.45}$$

where k is the spring constant and is a function of the body material and dimensions, and m is the body mass. The importance of the natural frequency is determining the resonant frequency. If the external harmonic excitation frequency coincides with the natural frequency, the body will resonate. If oscillation is not shifted away from resonance, vibration amplitude will build up until the structure breaks-down. Therefore, the body natural frequency should be determined in advance to make sure the device does not sit in close proximity to sources vibrating at resonant frequency.

Due to the complexity of the device, the resonant frequency has been calculated numerically. But to get an initial guess for the simulation, an analytical study on a simplified cantilever structure has been carried out. The natural frequency was carried out by calculating m and k in equation 7.45 as [139]

$$m = density \times volume \tag{7.46}$$

$$k = \frac{3}{2} \times E \times width \times (\frac{thickness}{length})^3. \tag{7.47}$$

The approximate m, k, and resonant frequencies (f) are tabulated in Table 7.4 for silicon and diamond hanging structures. Then we used these initial guesses and fed them to COMSOL® Multiphysics, and the resulting natural frequencies are tabulated in Table 7.4. And a visual representation of the first six natural frequencies of the silicon and diamond structures are presented in Fig. 7.30a and Fig. 7.30b, respectively.

Table 7.4 Calculated and simulated natural frequencies

Structure	Approximate m	Approximate k	Approximate f	Exact f
Silicon	$1.9572 \times 10^{-13}\, k.g$	$1.83105 \times 10^{-5}\, N.m$	$1539.4\, Hz$	$973.5\, Hz$
Diamond	$2.9536 \times 10^{-13}\, k.g$	$1.538 \times 10^{-4}\, N.m$	$3632.5\, Hz$	$2342.7\, Hz$

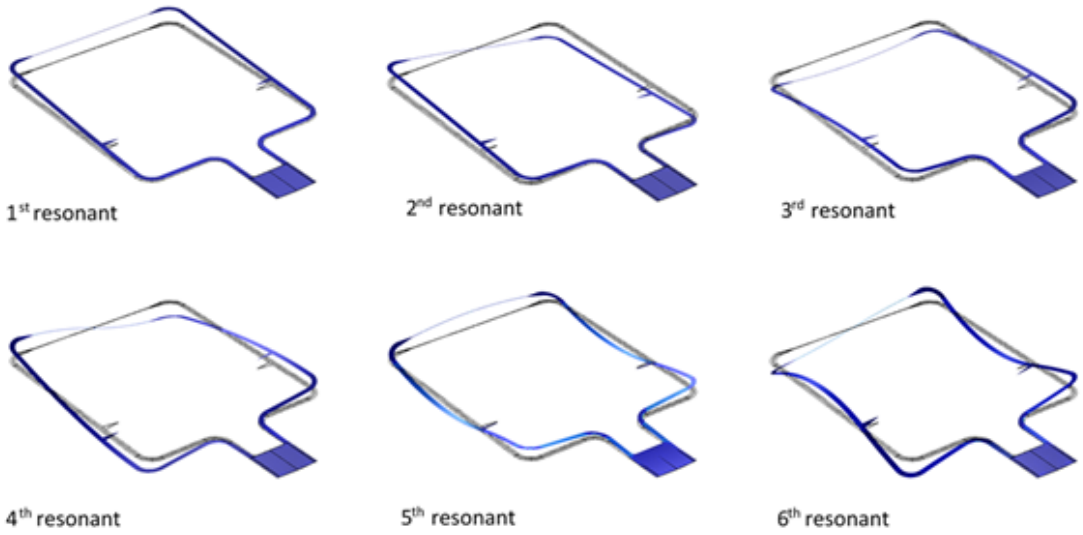

(a) Silicon structure.

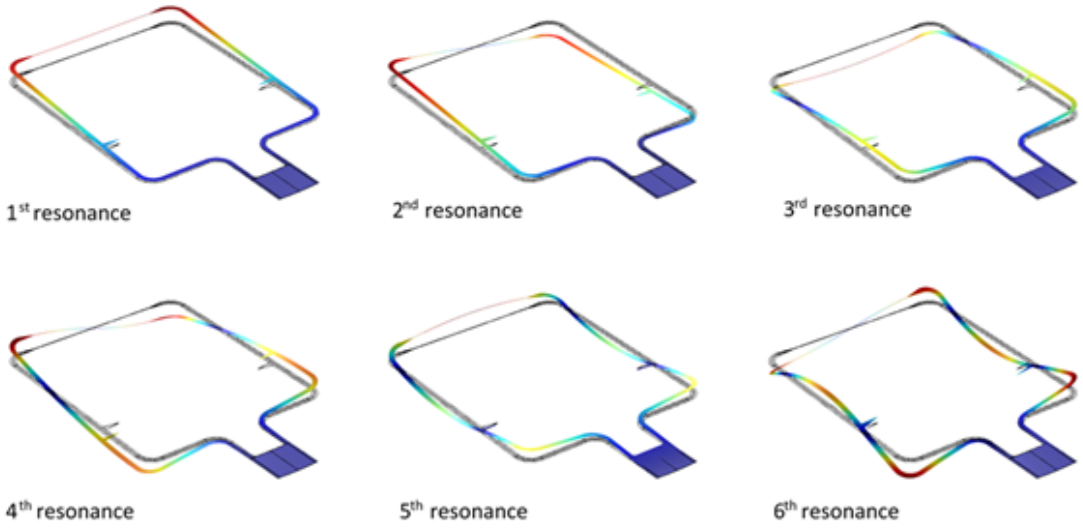

(b) Diamond structure.

Fig. 7.30 The first 6 natural frequencies of silicon and diamond couplers.

7.4.2 Vacuum breaking channels

For the vacuum issue, it was essential to create a ventilation duct in the structure to balance the pressure difference that might be created. For example, the device was fabricated on two separate chips then bonded together, and a proposed bonding method was using vacuum bonding. Vacuum bonding works by bringing two smooth adhesive surfaces together while applying some force under vacuum conditions. Since the device fabricated in this work had a

void where the micro-resonator resides, the vacuum created in this void will not be released, unless a venting void has been fabricated in one of the bonding layers (the lower polymer layers in Fig. 7.1).

To avoid any undesired effects, a laminar flow of air into the void when venting was required. Laminar flow can be determined by Reynold's number as [140, 141]

$$Re = \frac{\rho.V.D_H}{\mu} < 2300 \tag{7.48}$$

where ρ is the density of air, V is the flow velocity, D_H is the hydraulic diameter and is defined as $4 \times Area/Perimeter$, and μ is the dynamic viscosity of air.

A venting duct of cross sectional dimensions of $2 \times 100\mu m$ was studied. According to the mask design presented in **Chapter 8**, the shortest duct length was $0.4mm$ and the longest was $5.35mm$. As the duct length decreases, the flow velocity increase. Therefore, a flow study for the shortest duct was required, and as a margin of safety, a duct length of $0.1mm$ was studied instead. And for comparison, the flow in a $10mm$ duct has been studied as well.

After simulating the flow velocity in the ducts using COMSOL® Multiphysics, the resulting Reynold number was compared to the inequality 7.48. Flow velocity and Reynold's numbers for 0.1 and $10mm$ ducts are presented in Table 7.5. As can be seen from the results, the flow is laminar at the extreme end of the laminar flow regime. These results ensure that venting the vacuum voids is safe with the proposed ducts' dimensions.

Table 7.5 Flow velocity and Reynold's number in venting ducts

Duct length	Flow velocity	Reynold's number
$0.1\,mm$	$41.3\,m/s$	11.06
$10\,mm$	$1\,m/s$	0.26

Chapter 8

Photonic Integrated Chip Fabrication

The micro-resonator device fabrication process flow diagram is shown in Fig. 8.1 and outlined in Table 8.1. This chapter starts with a literature review about the various fabrication techniques used in this project. Then, the fabrication process and results are presented in chronological order.

The aim is to fabricate an optical resonator and an optical waveguide on two bonded substrates to form a multi-substrate photonic integrated chip (PIC) with adequate separation layer. Silicon and nanocrystalline diamond waveguides were considered. However, only the process for silicon waveguides has been fully developed; but the limited time restrained the completion of the fabrication phase. The fabrication steps shown in Fig. 8.1 have been tested individually; but during consequential fabrication, problems showed up. Some of the challenges along the way have been resolved, while others are still in the process of being resolved. At the time of writing this thesis, successful completion up to step **14** in Fig. 8.1 has been achieved. However, tests for the later steps (**15**-**22**) have been performed as individual steps, where fabrication recipes have been obtained.

Process	Details	Images
1) Oxidised silicon chip	• Start with a silicon wafer with $1.3\mu m$ thermal oxide layer on top	
2) Spin-coat photoresist	• Spin coat $0.6\mu m$ AZ1505® positive photoresist layer. o 1000 rpm for 10 seconds o 4000 rpm for 50 seconds o Acceleration 1000 rpm/s • Soft-bake on hot-plate for 1 minute at 100^o C	

3) Pattern photoresist	• Expose with 112 mJ/cm^2 broadband Hg UV lamp • Develop for 1 minute in diluted AZ726® MIF developer (AZ726:DI water = 2:1) • Hard-bake on hot-plate for 5 minutes at 120^o C (reflow to decrease edge roughness)	Fig. 8.14
4) Etch silica	• Wet silica etching in buffered oxide etchant (Buffered hydro fluoric acid 7:1) at a rate of 100nm/min	Fig. 8.14
5) Deposit Molybdenum	• Sputter 90nm of Molybdenum at a rate of $\sim$ 3 Å/sec	
6) Spin-coat photoresist	• As in step 2)	
7) Etch Molybdenum	• Wet etch Molybdenum in Aluminium etchant type A at a rate >100nm/min	Fig. 8.16
8) Remove resist	• Flood expose positive-resist with > 200mJ/cm^2 broadband Hg UV lamp • Develop for 2 minutes in AZ726® MIF developer	Fig. 8.16
9) Spin-coat SU-8	• Spin-coat 1.73 μm of diluted SU8-5 in PGMEA o 500 rpm for 5 seconds o 3500 rpm for 30 seconds o Acceleration 200 rpm/s • Pre-bake on hot-plate at 65^o C for 1 minute • Soft-bake on hot-plate at 95^o C for 3 minutes	
10) Pattern SU-8	• Expose SU-8 with $\sim 85mJ/cm^2$ broadband Hg UV • PEB 1 at 65^o C for 1 minute • PEB 2 at 95^o C for 1 minute • Develop for 90 seconds in PGMEA • Hard-bake at 200^o C for 5 minutes	Fig. 8.20
11) Isotropically etch silicon	• Isotropic dry etching of Silicon in ICP-RIE with 50$sccm$ SF_6 plasma at 30mTorr , 1500W ICP power and 0W RIE power at a rate of 5μm/min	Fig. 8.21
12) Melt silica	• Irradiate the silica disc with CO_2 laser (power $\sim$ 100 MW/m^2, beam radius slightly larger than the disc's)	Fig. 8.25

13) Coat PMMA on SOI chip	• Spin-coat 1.75 μm of 950PMMA A10 o 500 rpm for 10 seconds o 3500 rpm for 50 seconds o Acceleration 1000 rpm/s • Soft-bake on hot-plate at $185 - 190^o$ C for 5 minutes	
14) Bonding	• Spin-coat 1.75 μm of 950PMMA A10 as in step 13) on the PMMA coated SOI chip • Bring the PMMA coated SOI chip in contact with the SU-8 coated chip (ensure accurate alignment) • Apply some pressure using tweezers to ensure full contact all over the chips surfaces • Cool down the chips for the PMMA bond to cure	
15) Deep etching of top layers	• Etch silicon as in step 11) • Dry etch silica using fluorocarbon gases	
16) Spin-coat ebeam resist	• Spin-coat HSQ at 3000rpm	
17) Pattern ebeam resist	• Expose HSQ with $5000\mu C/cm^2$ at 100kV	
18) Anisotropic partial etch of silicon	• Anisotropically dry etch silicon in ICP-RIE C_4H_8:SF_6 = 50:25 sccm plasma at 20 mTorr, 20W RF and 1200W ICP power, at a rate of 0.2 μm/min	Fig. 8.28
19) Spin-coat photoresist	• As in step 2)	
20) Pattern photoresist	• As in step 3)	
21) Fully etch silicon	• As in step 18)	
22) Etch PMMA and resist	• Isotropically dry etch polymers in RIE 30 sccm O_2 plasma at 65 mTorr and 20W RF power, at a rate of 1 μm/min for PMMA and 0.6 μm for photoresist	

Table 8.1 Outline of fabrication steps.

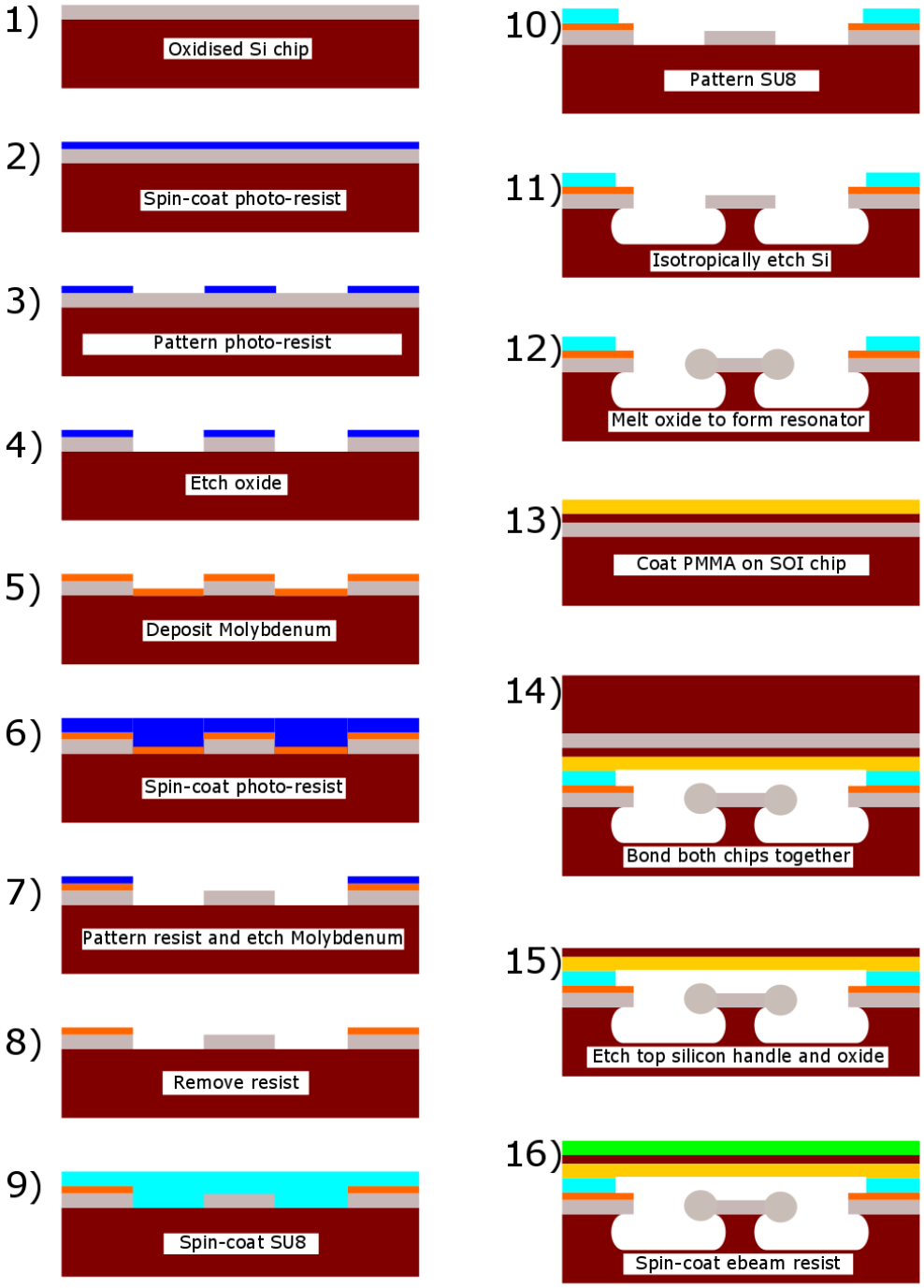

Fig. 8.1 Flow diagram of fabrication steps.

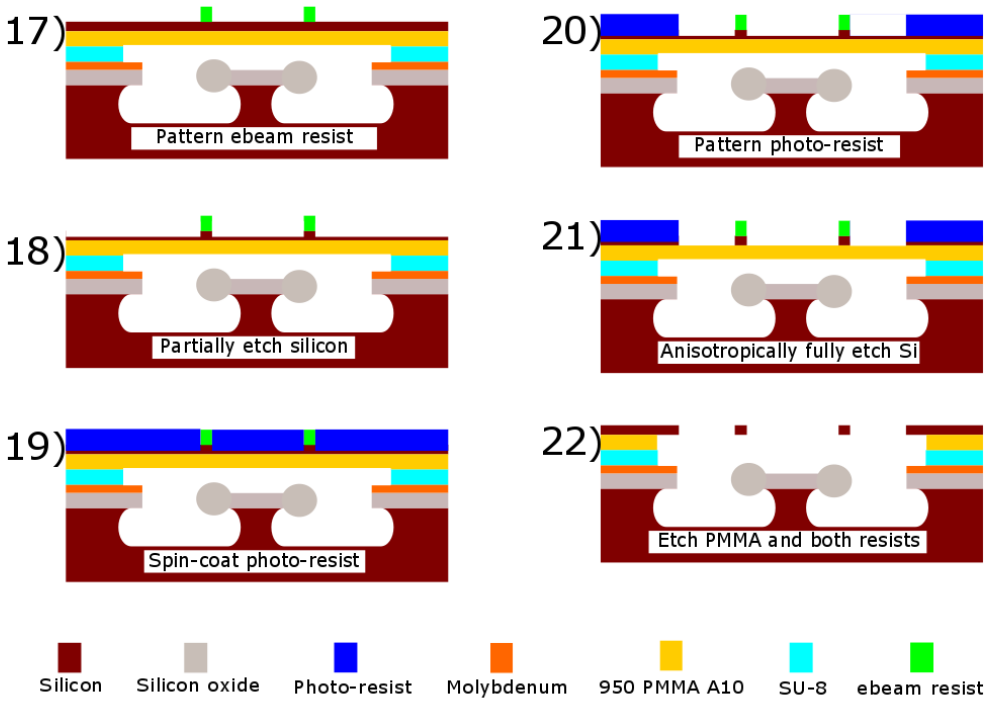

Fig. 8.1 Flow diagram of fabrication steps (cont.).

8.1 Theory

8.1.1 Sputtering

Sputtering is bombarding the surface of a material with a beam of particles with enough energy to break the bonds between the material's atoms/molecules [142]. The bombarding particles could be ions, atoms or electrons, among others. The released atoms/molecules scatter away from the material in all directions, where some of it fall on the surface of the substrate (Fig. 8.2). A diagram of a standard sputtering system is shown in Fig. 8.3. By increasing the energy of the bombarding particles, the scattered atoms/molecules on the surface scatter with higher angles as shown in Fig. 8.4.

The RF-diode plasma system works by creating a plasma of ionised gas, which forms the bombarding particles. Diode plasma system is simply an anode and a cathode inside a vacuum chamber. When introducing an inert gas under the right conditions, it will form a uniform plasma discharge with very high electric field near the cathode. The high electric field accelerates the ions towards the cathode causing collisions between the ions and the source material. Such collisions result in sputtering atoms/molecules off the source, and the

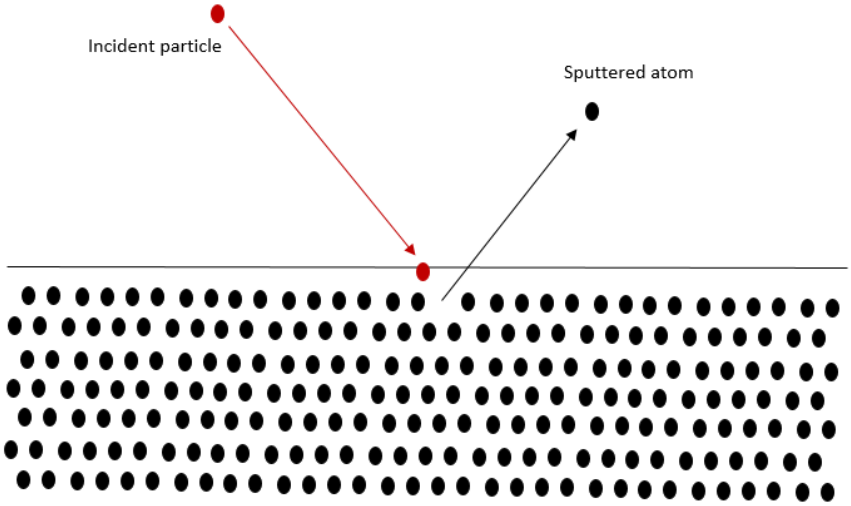

Fig. 8.2 Representation of physical sputtering.

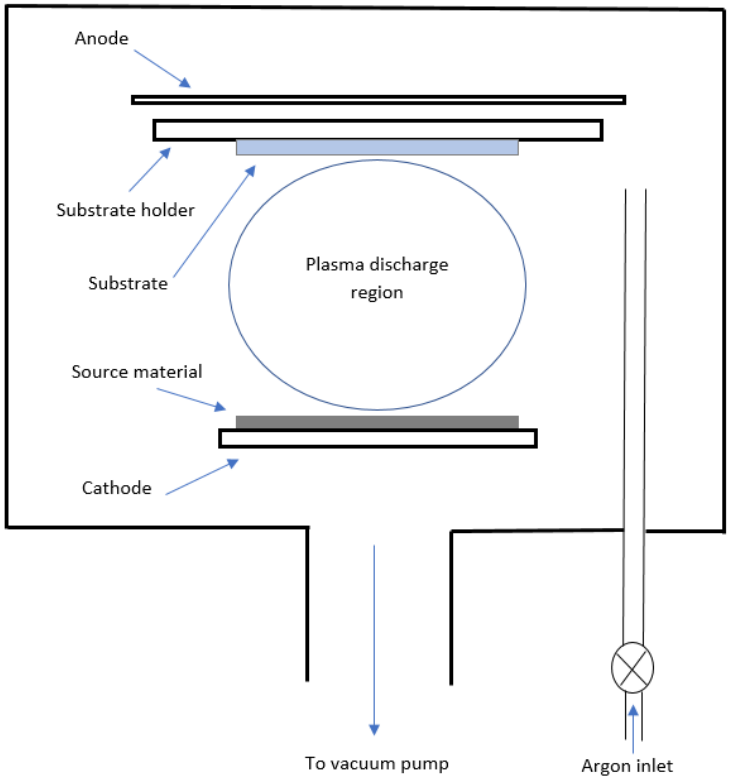

Fig. 8.3 Schematic of a standard sputtering system.

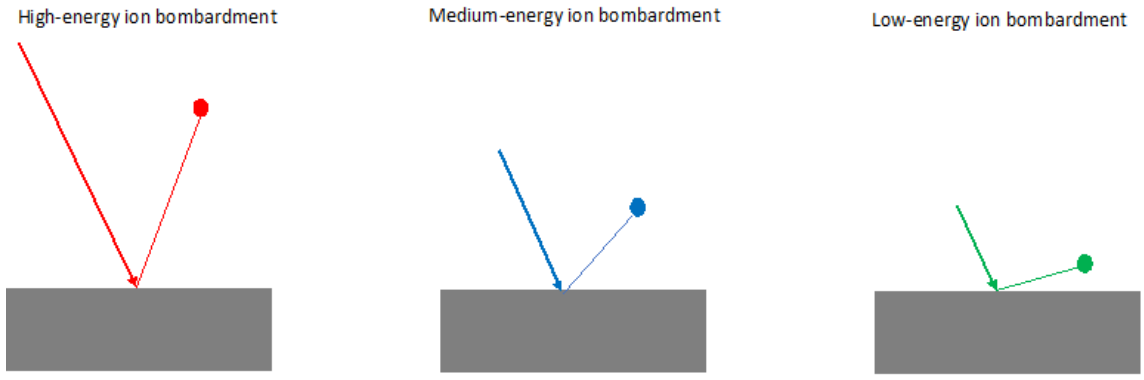

Fig. 8.4 Sputtered atom scattering angle vs bombardment particle energy.

emission of secondary electrons. These secondary electrons collide with the inert gas and form new ions, which help sustain the plasma discharge.

DC-diode plasma does not work efficiently when sputtering insulating materials. Therefore, an alternating current is used instead. The frequency for the alternating current in the sputtering systems is 13.56 MHz (industry frequency), which falls in the radio frequency regime, hence, the name “RF-diode plasma” sputtering. The alternating current increases the electron movement inside the chamber, causing more gas ionisation and an increase in the sputtering rate.

It is obvious that increasing the RF source power will increase the sputtering rate. Also, decreasing the gas flow rate will increase the sputtering rate. By decreasing the gas density, the mean free path increases according to the proportionality [143]

$$mean\,free\,path \propto 1/gas\,density \tag{8.1}$$

As the mean free path increases, the ions accelerate over a longer distance so that the final velocity before bombardment increases. The increase in velocity will cause a square increase in the kinetic energy (momentum), and hence more atoms/molecules scatter off the source’s surface.

8.1.2 Thermal evaporation

Thermal evaporation takes place in a resistive evaporator as shown in Fig. 8.5, or e-beam evaporator as in Fig. 8.6. The material to be evaporated (source material) is placed in the "Boat" or "crucible" and heated until it boils. Then the vaporised atoms travel all the way up until being deposited onto the substrate. Several heating methods can be used:

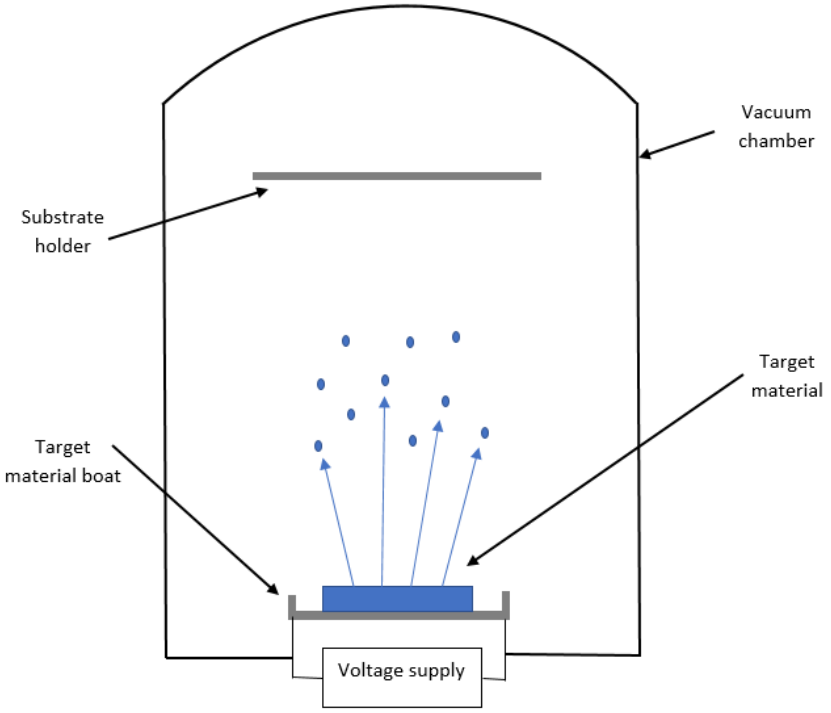

Fig. 8.5 Schematic diagram of resistive thermal evaporator system.

1. Direct or indirect resistive heating, where an electrical current run across the material or the "Boat".
2. Inductive heating, where a conductive material is heated by frequency induction.
3. e-beam heating, where a high energy electron beam is used to melt and evaporate the material.
4. Laser evaporation/ablation, where a focused laser beam is used to heat up the source material.

The range of materials that can be evaporated depends on the boiling point and the equipment capabilities, but theoretically, almost all metals can be evaporated. As the gas travels from the source to the substrate, it will collide with air molecules, hence, the need for the process to be conducted under vacuum to ensure a free path from the source to the substrate. The mean free path (λ) is defined by [143]

$$\lambda = \frac{1}{n\,\sigma} \tag{8.2}$$

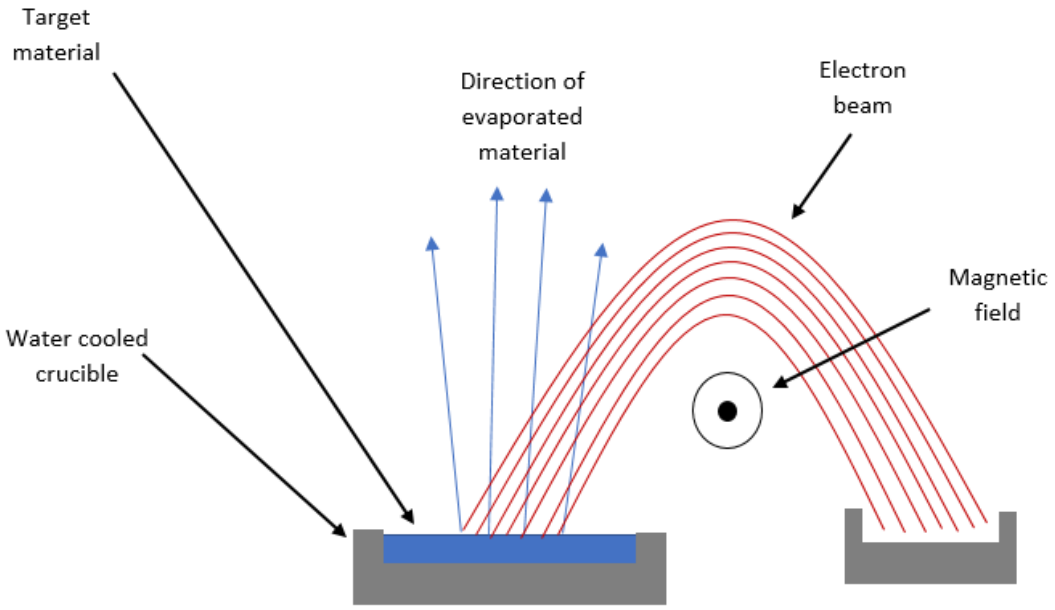

Fig. 8.6 Schematic of ebeam thermal evaporator.

where n is the particle density, and σ is the interaction cross-section (the probability that two particles will collide). According to [144] at ambient conditions, air's mean free path is $\sim 65nm$. For a $15cm$ distance between the evaporation boat and the substrate, we will require a decrease in air particle density by a factor of $\sim 4.33 \times 10^{-7}$ as

$$\frac{\lambda_{ambient}}{\lambda_{15cm}} = \frac{n_{15cm}}{n_{ambient}}. \tag{8.3}$$

Using the ideal gas law

$$PV = nRT \tag{8.4}$$

where P is gas pressure, V is volume, n particle density, R is the gas constant, and T is the temperature, we can conclude that the pressure is directly proportional to particle density under the assumption of constant temperature (before starting evaporation). Therefore, we find that the pressure should decrease by, at least, $\sim 4.33 \times 10^{-7}$ for efficient evaporation, which corresponds to $\sim 4.4 \times 10^{-4}$ mbar.

For resistive evaporation, usually the "Boat" and its holders are made from materials with high melting temperatures and have large surface area to avoid melting and contaminating

the evaporated material. For e-beam evaporation, very high energies are used that water cooling is essential. The only materials that cannot be evaporated are materials with very high melting temperatures like tungsten.

8.1.3 Silicon etching

Silicon atoms are formed in a diamond cubic crystal structure with crystal lattices having different orientations as shown in Fig. 8.7. Conventionally, isotropic etching means there is no preferred etch direction, unlike anisotropic etching, as shown in Fig. 8.8. In this work we have a slightly different, but widely accepted, definition of isotropic etching, which is

"the etch rates of the different crystal lattice orientations are comparable."

And when the etch rate for one crystal lattice orientation is considerably higher than the other orientations, the process is referred to as anisotropic etching.

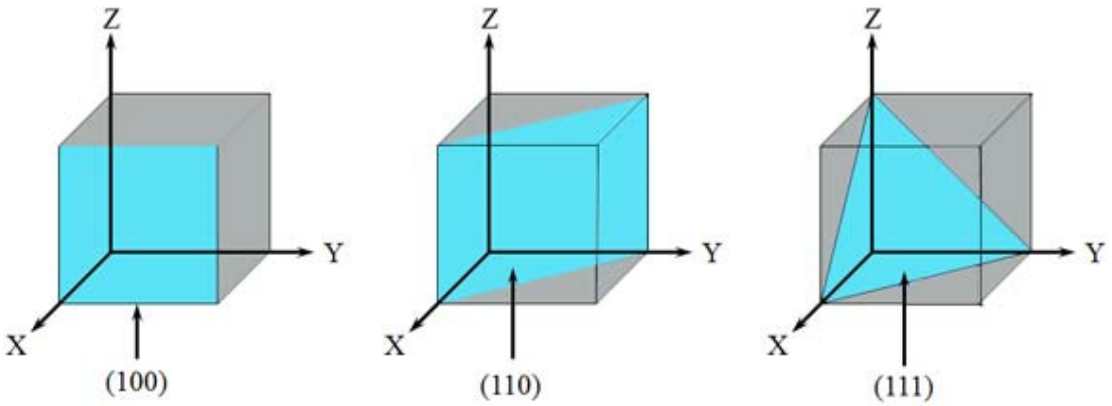

Fig. 8.7 Main crystal orientations in silicon lattice. Image obtained from [145].

Fig. 8.8 Isotropic (left) vs anisotropic (right) etching.

Wet isotropic etching

Isotropic silicon etching can be conducted using the common wet etchant HNA (hydro-fluoric, nitric, and acetic acids). The nitric acid oxidises the silicon, and the hydro-fluoric acid etches the formed oxide. The acetic acid acts as a buffering agent and a stabiliser to prevent the

dissociation of the nitric acid into nitrite (NO_{2-}) and nitrate (NO_{3-}) ions [146]. As the main etching process is etching silicon oxide, and since the device is fabricated on oxidised and SOI chips, the HNA etchant cannot be used for isotropic etching of silicon.

KOH (potassium hydroxide) is a reliable silicon isotropic etchant. It etches silicon oxide but at a very slow rate. KOH etching of silicon is discussed briefly in **Appendix C**.

Dry isotropic etching

Fluorine containing chemicals are expected to remove silicon by forming silicon fluoride gases [146]. Depending on reactivity, some chemicals are expected to perform better than others, while some fluorine based chemicals will not react at all.

Dry etching can be performed either as a "vapour phase etching" or "plasma phase etching." Each has its own advantages and disadvantages. The vapour phase etching is cheaper than the plasma phase one. Vapour phase etching depends on the reactivity of the used gas with silicon atoms to produce volatile silicon fluoride (SiF_4). Xenon difluoride (XeF_2) is the most commonly used chemical.

To improve the etching process, a physical etching mechanism can be added to the chemical etching mechanism in the vapour phase etching technique. This is achieved by using a plasma discharge similar to the sputtering processes. Radicals (ionised atoms) of reactive chemicals are produced by an alternating voltage at RF frequency of 13.56 MHz. Such ions bombards silicon surface and enhance the etching process. This process is referred to as RIE (reactive ion enhanced) etching, and it uses the plasma phase of reactive chemicals as a catalyst to improve chemical reaction (e.g. reduce reaction temperature and/or time).

To further improve the amount and quality of ions at silicon surface, ICP-RIE mechanism is used. ICP stands for "inductive coupled plasma." And as the name suggests, and inductive field is added by surrounding the plasma chamber with an inductive coil. The presence of a magnetic field from the inductive coil creates an electric field inside the plasma chamber. Accurate control of the inductive field can provide total control over the plasma phase inside the chamber.

Deep silicon etching

As shown in step **15** in Fig. 8.1, the removal of the handle silicon of the SOI chip was essential. The handle silicon was $\sim 680\mu m$ thick, so it required high-etch-rate processing. Although high-etch-rate wet etching of silicon is available, deep silicon etching refers to high-etch-rate dry etching of silicon. KOH (Potassium hydroxide) at 100^oC can provide etch rate approaching $6\mu m$ per minute for the <110> crystal plane. On the other hand, deep silicon

etching can reach etch rates exceeding $25\mu m$ per minute (Oxford Instruments® PlasmaPro 100 Estrelas). Wet and dry removal of the handle silicon of the SOI chip were conducted. The removal of the handle silicon of the SOI chip in KOH is reported in **Appendix C**, while here we only review silicon deep etching as it is more practical and more accurate for our process.

Two technologies are used for deep etching, the Cryogenic process and the Bosch process. The Cryogenic process operates at very low temperatures, while the Bosch process operates at room temperature. Deep silicon etching has been studied in other works (e.g. [147]), where the interested reader can find detailed explanation of the different processes. In this work, we only had access to a Bosch etcher, so we only briefly describe the process here.

The high etch rate of the Bosch process is achieved by high operation powers and high-density plasma (HDP). Hence, the Bosch process is an ICP-RIE etch process. Two chemicals are used, SF_6 (sulphur hexafluoride) and C_4F_8 (octofluorocyclobutane). SF_6 is ionised to provide fluorine ions and radicals, which are responsible for the chemical etching. C_4F_8 is ionised to form a chain polymer of CF_2, which acts as a passivation (protective) layer on vertical and horizontal surfaces of silicon. The high energy fluorine ions and radicals remove the passivation layer off the horizontal surfaces and leave it on the vertical walls. Such process allows for high-etch-rate anisotropic etching of silicon. It is required for the milling rate to be higher than the polymer deposition rate, hence, there is a minimum threshold power below which no etching can occur. As a rule of thumb for most cases, the slower the etch rate, the smoother the side walls are. The rough side walls are referred to as scalloping and is depicted in Fig. 8.9. For an isotropic etch, SF_6 plasma is used without any fluorocarbon

Fig. 8.9 Scalloping effect in anisotropic dry etching showing rough side walls (left) and smoother side walls (right).

gases. But since the handle silicon needed to be removed without affecting any of the other silicon layers in the device, SF_6 and C_4F_8 plasma might be essential to eliminate any lateral etch from the chip edges.

8.1.4 Silica dry etching

Rapid etching of silicon, silicon oxide and silicon nitride are very mature fabrication techniques. For a quick comparison of etch rates for these materials in different gases, we refer the reader to the 1993 paper by S. K. Ray et al. [148]. The brief review introduced here for silica dry etching forms the basis for future work on the silica removal after the silicon deep etching step.

Silica (SiO_2) can be etched using fluorine chemicals as SF_6. But when high selectivity over silicon is required, a fluorocarbon gas is required. The main idea is to have higher deposition rate of the passivation layer than the milling of it using the fluorine ions and radicals. As the polymer is composed of carbon and fluorine atoms, under high energy it will react with the silicon and oxygen atoms in the silica and form the volatile SiF_4, CO, and CO_2 gases. While the layers protecting the silicon will not decompose due to the absence of atoms to react with the carbon atoms in the polymer chain.

According to this reaction, fluorocarbons have been the preferred chemicals for silicon dioxide dry etching. C_4F_8, CF_4 (Tetrafluoromethane) or CHF_3 (Fluoroform) can be used on their own. Each molecule of silicon dioxide requires one carbon atom and four fluorine atoms to react. Therefore, carbon atoms will precipitate when gases with F/C ratio below 4 are used. Two approaches can be used to remove the carbon: 1) introduce oxygen in the gas mixture where the oxygen reacts with the carbon to form carbon oxides, 2) introduce fluorine rich chemical in the mixture. When oxygen is used for silica etching, it reacts with the passivation layer, which jeopardise the selectivity of oxide etching over silicon. Hence, introducing fluorine rich gases in the mixture is preferable. The plasma power has to be below the threshold value to avoid the milling of the passivation layer that is covering the silicon.

8.1.5 Electron-beam lithography

For dimensions below the diffraction limit of light, ebeam lithography, among other techniques, provides a pathway for patterning. The working principle is derived from the scanning electron microscope, which consists of scanning a beam of electrons over a thin film that is sensitive to the electrons in the beam [149]. ebeam lithography main characteristics are:

1. High resolution

2. Works with a variety of materials
3. Almost infinite number of patterns
4. Slow technique, orders of magnitude slower than optical-lithography
5. More expensive and technologically complicated compared to optical-lithography.

A block diagram of the main components of ebeam lithography equipment is shown in Fig. 8.10. The electron gun is a high voltage source that emits electrons. The column contains the components of forming and correcting the electron beam with the desired characteristics.

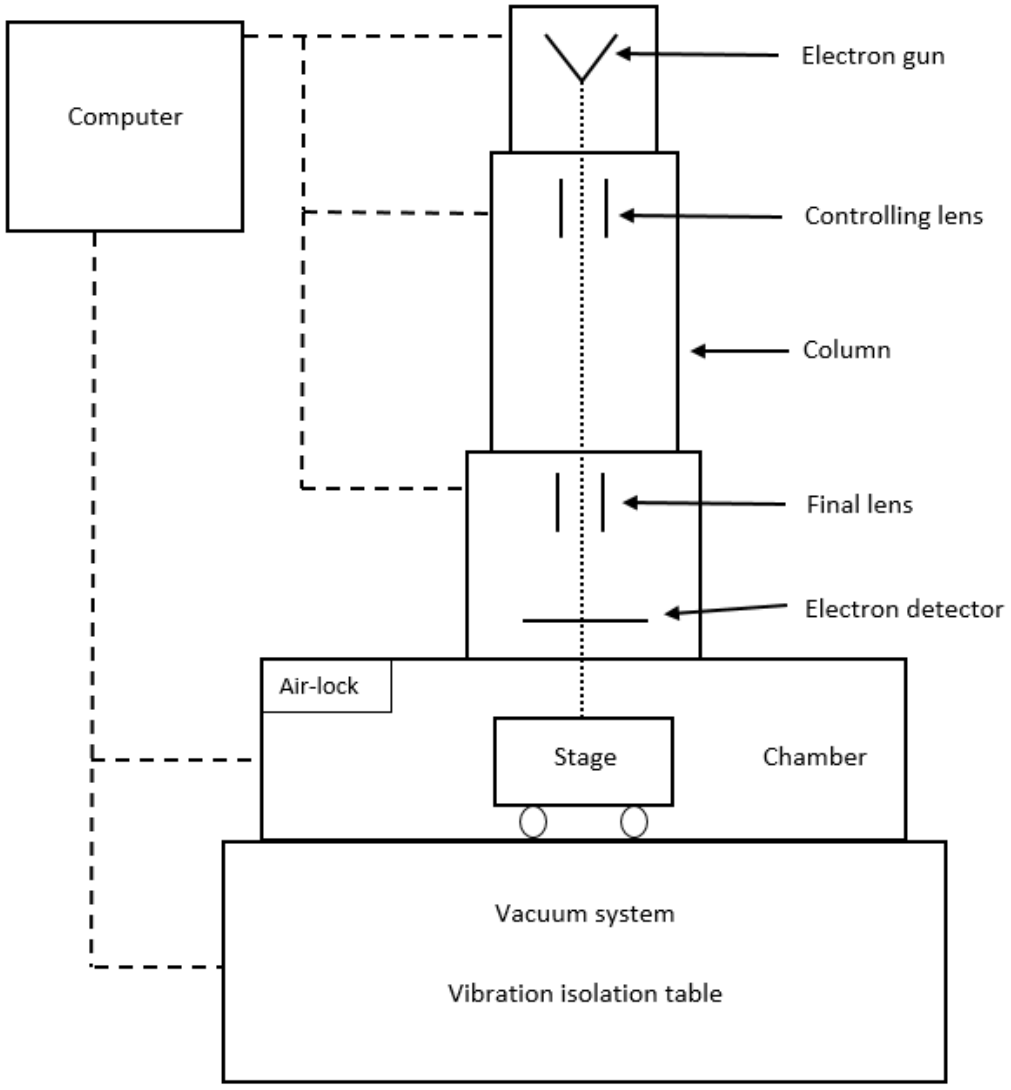

Fig. 8.10 Block diagram of the major components of ebeam lithography system [149].

Typically, the column consists of the electron source, at least two electron beam lenses, beam deflector, mechanism for turning the beam on and off, stigmator for correcting any astigmatism in the beam, alignment mechanism, and beam detector to assist with locating the beam. The chamber underneath the column contains a controllable positioning stage that in usually integrated with laser interferometer for precise positioning. A vacuum system is an essential component of any ebeam lithography equipment to maintain the required vacuum throughout the equipment [149]. The whole ebeam equipment is controlled by a computer, from loading and unloading of samples, through aligning and focusing of the beam, to generating patterns on the required samples.

Similar to photolithography, ebeam resists can have either a negative tone or a positive tone. PMMA is an example of positive resists, and HSQ (Hydrogen silsesquioxane $[HSiO_{3/2}]_n$) is an example of negative resists. Substrate charging is a significant issue when exposing ebeam resist on insulating substrates. Charging is not as serious for semiconductors, but it might contribute to significant errors in patterning [149]. Therefore, dose tests should be conducted for every combination of resist material, resist thickness, and substrate material.

8.2 Bottom chip processing

The bottom chip included the micro-toroid resonator, bottom electrode for electromechanical actuation, and a separation layer. Fig. 8.11 shows the outline of the chip. The $6.5mm \times 6.5mm$ square in the middle is where all the features are fabricated. The outer edges are for handling

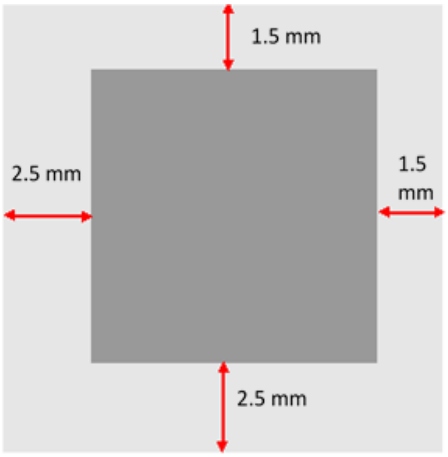

Fig. 8.11 $1cm \times 1cm$ chip layout with pattern position from edges indicated.

and spin-coating edge bead tolerance. The chip contains eight duplicates of the same structure spread diagonally across the chip.

Fabricating the micro-toroid resonator is explained systematically in [150] with video demonstration online. Here we briefly report the steps:

1. Pattern rings with $200\mu m$ inner diameter and $500\mu m$ outer diameter in a $1.3\mu m$ oxide layer on top of a silicon substrate.

2. Isotropically etch silicon to produce a $15-20\mu m$ silicon oxide undercut.

3. Blast the oxide discs using focused CO_2 laser beam to $130\mu m$ radius spot until a smooth toroid is produced. Alignment is crucial for symmetric smooth toroid. The produced toroid would have a minor radius of about $2.5-2.9\mu m$ and major radius of about $80-85\mu m$.

Before conducting the second step, the lower electrode and the separation layer were deposited. The third step can either be done before bonding the bottom and top chips, or as the last step in the whole fabrication procedure to avoid contaminating the ring-resonator. Fig. 8.12 shows the final bottom chip before bonding to the top chip.

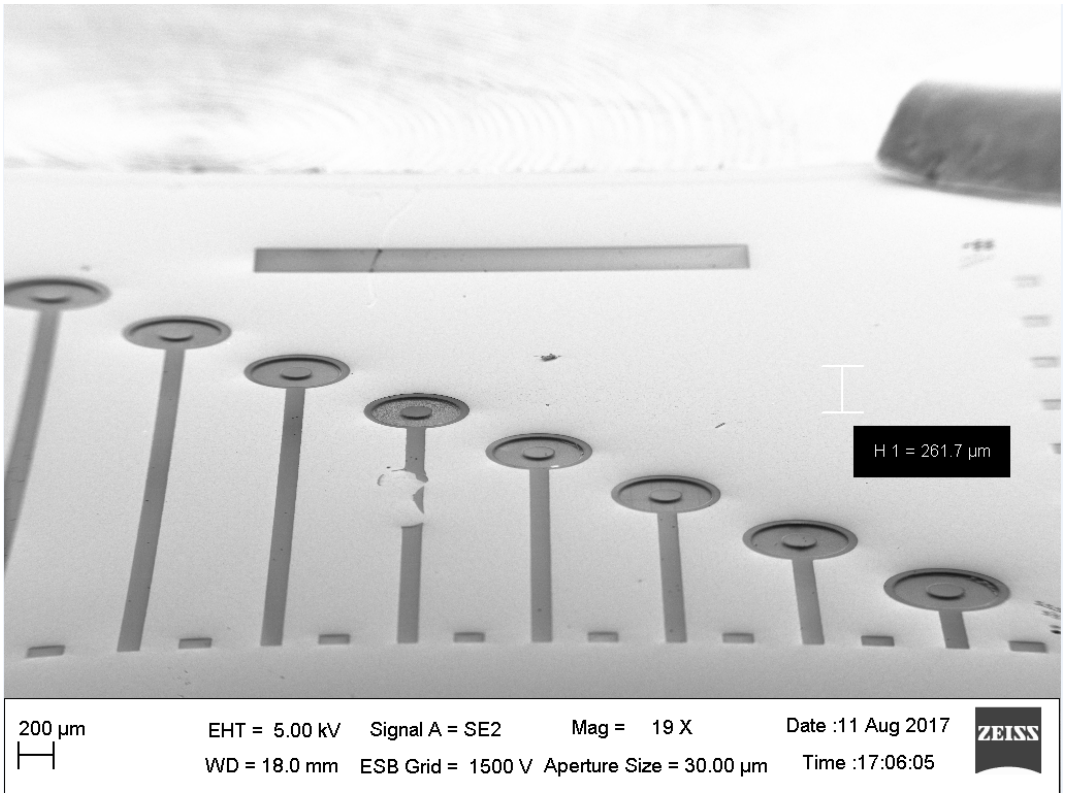

Fig. 8.12 SEM image of the fabricated bottom chip.

8.2.1 Wet silicon dioxide (silica) etching (steps 2-4 in Fig. 8.1)

Eight rings with $200\mu m$ inner diameter and $500\mu m$ outer diameter were required to be etched, as shown in Fig. 8.13. Silica can be wet or dry etched. Each has its own benefits and drawbacks. Since silica etching is the first step in the fabrication process, there was no constraint about using either method. Silica wet etching is more economical than dry etching, but it has serious health hazards if safety precautions are not followed. Since safety measures can be easily employed, we have opted for wet silicon oxide etching.

Wet silica etching can be done using hydrofluoric acid (HF). HF is a very aggressive etchant that etches silica at very high rates ($> 2\mu m/min$) and attacks most materials [151]. Buffering agent can be added to HF to form buffered HF (BHF), which reduces the etch rate and aggressiveness. Also, BHF decreases the lateral etch rate under the mask layer remarkably [152]. The used BHF is the 7:1 BHF with buffering agent:acid (40 wt% NH_4F:HF) ratio of 7:1, which etches silica at a rate of $100nm/min$ at room temperature [151, 152].

Three materials were available as BHF etch mask in this project, crystalline silicon, chromium, and positive photoresist [151]. <100> crystalline silicon is resilient to BHF with zero etch rate. For having silicon as an etch mask, two approaches were available: 1) start with silicon on insulator (SOI) chips, and 2) sputter-coat silicon on oxidised silicon chips. Both approaches introduce extra costs, and complicate and prolong the process, hence using silicon as an etch mask was discarded.

Chromium has been used as BHF etch mask with other metals [153], where it proved to be a resilient mask against BHF. Using chromium has been tested and proved to be a good etch mask. But, chromium still needs to be patterned using photoresist, therefore we opted

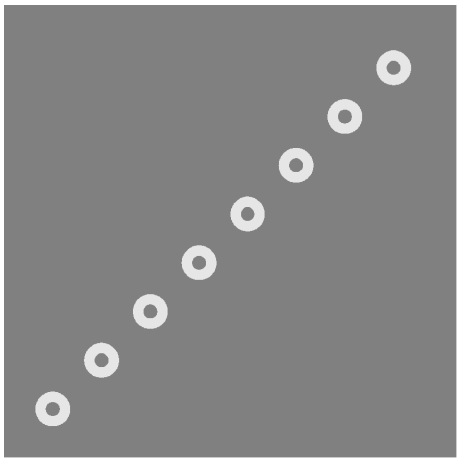

Fig. 8.13 Oxide etch mask.

towards only using positive photoresist. This approach eliminated the need for depositing chromium and etching it.

AZ1505® positive photoresist from MicroChem® was tested and proved to be an excellent etch mask for BHF with no decrease in thickness after etching times of up to 40 minutes. The $1.3\mu m$ oxide layer requires 13 minutes of BHF etch. A safety factor of 1.5 was employed to ensure the complete removal of the oxide layer, so the etching time was chosen to be 20 minutes with agitation. The lateral etching under the mask layer was not a serious concern due to the very slow lateral etch rate of silica in BHF. Fig. 8.14 shows the resultant structure.

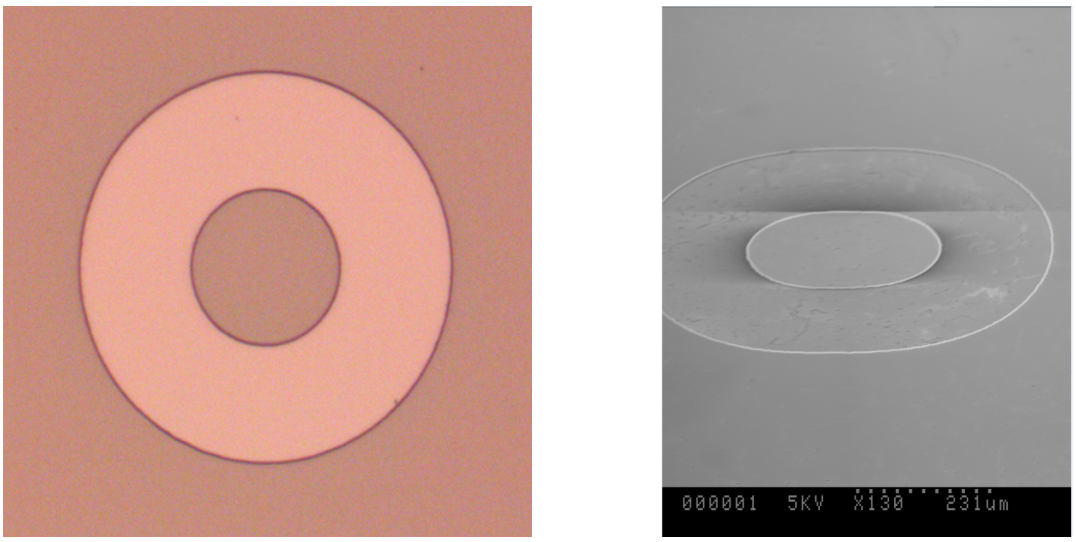

Fig. 8.14 Optical image of ring patterned in Photoresist (left), and SEM image of etched silica ring (right).

8.2.2 Lower electrode deposition (step2 5-8 in Fig. 8.1)

An electrical conductive layer was required to be deposited on top of the silica layer to form a lower electrode for electromechanical actuation. Molybdenum (Mo) has been chosen for its high electrical conductivity and compatibility with the next fabrication steps. Mo has been sputtered on top of the oxide layer using an RF-diode plasma system (Leybold® Univex350). Mo was sputtered at 2×10^{-5} mbar pressure with 250 W RF power and 150 sccm flowrate of argon. These conditions provided ~ 3 Å/s deposition rate, and the final Mo lower electrode thickness was ~ 90 nm. The electrode etch mask to expose the micro-resonators and the surrounding voids is shown in Fig. 8.15, and the images after Mo etching are shown in Fig. 8.16.

Fig. 8.15 Lower electrode etch mask.

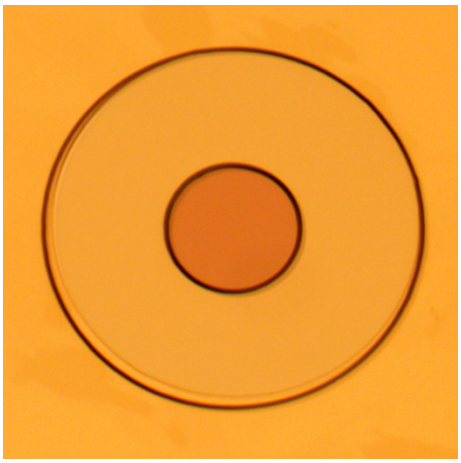

(a) Optical image after patterning the lower molybdenum electrode. Silicon and Molybdenum have very similar appearance, while silica on silicon is clearly differentiable.

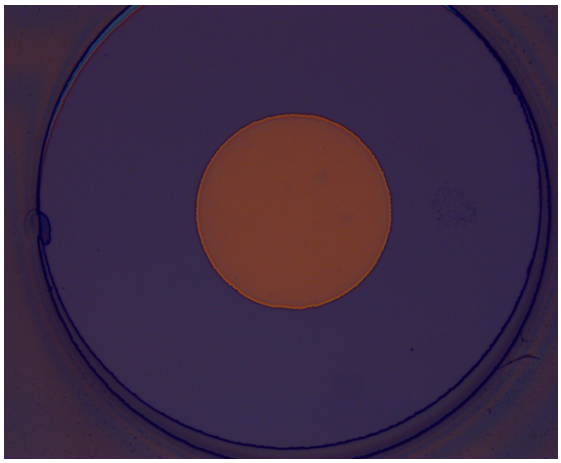

(b) Optical image of the etched Mo. The colours are adjusted to clearly show silica on silicon (middle disk), silicon (the ring), and the photoresist (outmost edges).

Fig. 8.16 Patterning Molybdenum.

8.2.3 Separation layer (steps 9 and 10 in Fig. 8.1)

A separation layer with $1.5-2\mu m$ thickness was required to provide adequate separation gap before bonding. This separation layer will ensure no pressure is exerted on the micro-resonator during bonding, as well as, providing the required gap for micromechanical actuation. Also, it will contain the vacuum venting channels to release any vacuum trapped inside the voids in the lower chip during bonding, if bonding under vacuum is conducted. The mask used for patterning the separation layer is shown in Fig. 8.17.

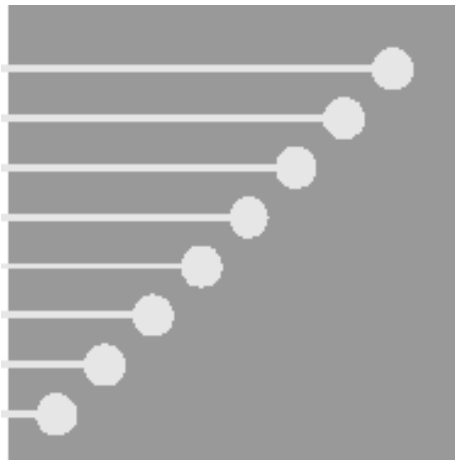

Fig. 8.17 Voids and vacuum breaking channels mask.

Poly-methyl methacrylate (PMMA) has been considered for the separation layer due to its optical, mechanical and electrical compatibility. PMMA is transparent at the $1.55\mu m$ (operation) wavelength and is structurally resilient. It is also a good electric insulator to prevent short circuiting the top and lower electrodes.

$\sim 1.75\mu m$ of 950PMMA A (MicroChem®) layer was spun coated on the lower chip and soft-baked with the recommended parameters in the datasheet (180^oC for 60-90 seconds). Then a $30nm$ chromium etch mask was thermally evaporated on the PMMA layer. Evaporating chromium on cured PMMA produced cracks in the PMMA layer as shown in Fig. 8.18.

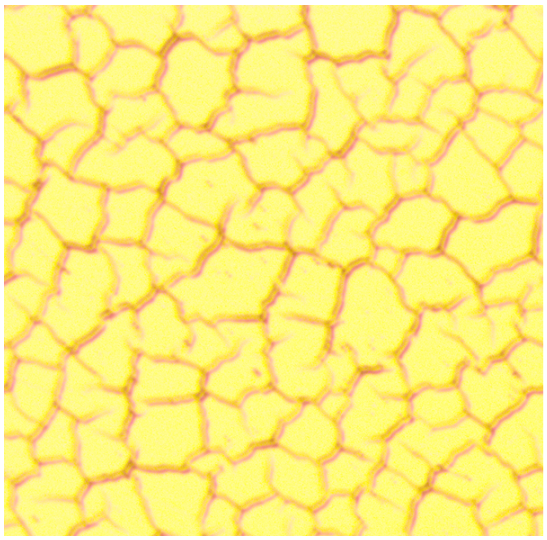

Fig. 8.18 Optical image showing the cracks in the PMMA layer after chromium deposition.

Resistive thermal evaporation, using a Leybold® Univex250 equipment, has been used to deposit chromium as a PMMA etch mask. Film thickness was not critical for this process, but it had to be more than 30 nm to ensure a protective film with no pinholes or discontinuities. The evaporation parameters are shown in Table 8.2. We attributed the crack formation in the PMMA layer to the thermal stress from the exposure to the hot source. To increase PMMA resistance against heat, the soft-bake temperature was increased to $185 - 190^{o}C$ for 5 minutes. The new soft-bake parameters produced hard PMMA layer that can withstand the high evaporation temperatures.

Unfortunately, hard PMMA cracked under the pressure from the photolithography mask aligner. We used 1 bar for soft contact during exposure, and that was high enough to crack the hard PMMA layer. We have attributed this cracking to the edge beads, and the non-uniformity in the layer due to the presence of voids, as shown in Fig. 8.19.

Therefore, we changed our attention towards using SU-8 as the separation layer. It is optically and electrically compatible, and provides high mechanical rigidity. SU-8 processing is simpler than PMMA. Patterning PMMA requires the deposition of a masking layer, patterning the mask, then dry-etching PMMA. While processing SU-8 requires a single development step in PGMEA. A $1.73\mu m$ SU-8 separation layer was spun-coated and patterned over the patterned silica layer. Fig. 8.20 shows an optical and an SEM images of the structure before the silicon undercut step.

Table 8.2 Chromium resistive thermal evaporation parameters.

Parameter	Value
Pressure	5×10^{-6} mbar
Deposition rate	1.5 Å/s
Final Thickness	$30nm$

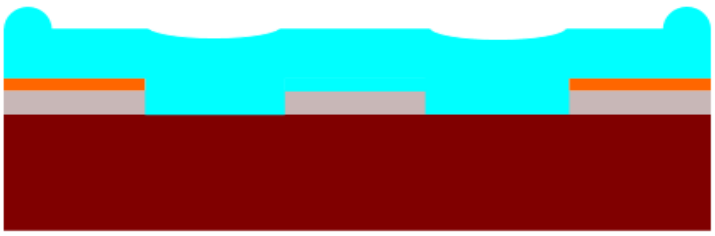

Fig. 8.19 Edge beads and wavy surface due to void presence in spin-coated films.

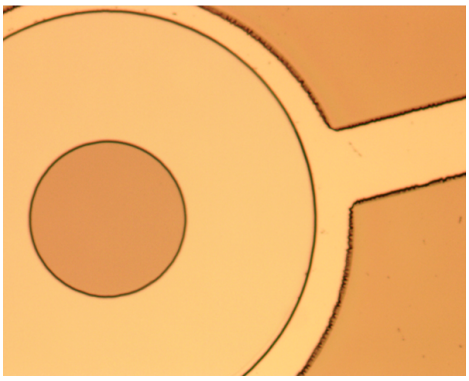

(a) Optical image of the SU8 separation layer showing the venting channels.

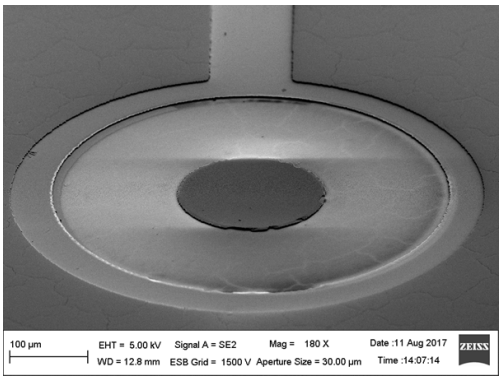

(b) SEM image of the separation layer showing the venting channels.

Fig. 8.20 Patterning SU-8.

8.2.4 Silicon isotropic etching (step 11 in Fig. 8.1)

Both RIE and ICP-RIE SF_6 (Sulfur hexafluoride) dry etching of silicon has been tried for the silicon under-cut in the process of forming the micro-toroid ring-resonator. ICP-RIE provided smoother etched surfaces than RIE, as depicted in Fig. 8.21. RIE process was conducted using JLS Plasma Pod system, and the process parameters were 30 mTorr operation pressure, 100 W RF power, and 26 sccm SF_6 flow rate, which provided $0.6\mu m/min$ etch rate. The ICP-RIE etch was conducted with an Oxford P100 equipment at a pressure of 30mTorr, 0W RIE power and 1500W ICP power with 50sccm SF_6 plasma and had an etch rate of $5\mu m$/min. Fig. 8.22 shows a zoomed-out view of the silicon undercut. The isotropic dry etching of silicon does not affect the SU-8 layer as depicted in Fig. 8.23 of a test sample. The SU-8 surface does not seem to be affected by etching nor does the thickness.

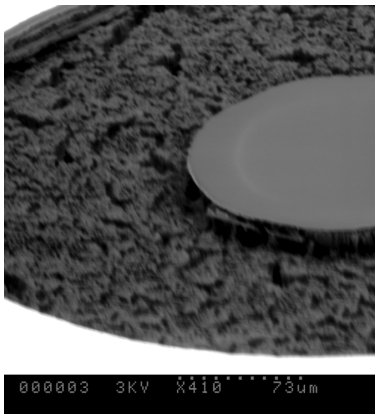

(a) Rough silicon surface after RIE etching.

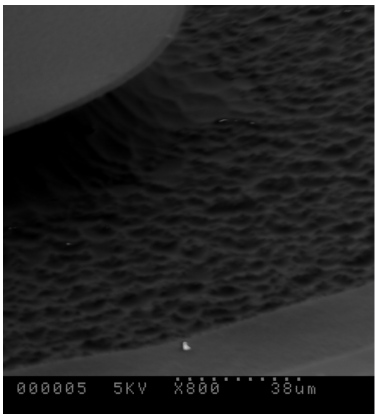

(b) Smooth silicon surface after ICP-RIE etching.

Fig. 8.21 SEM images of silicon isotropic etching.

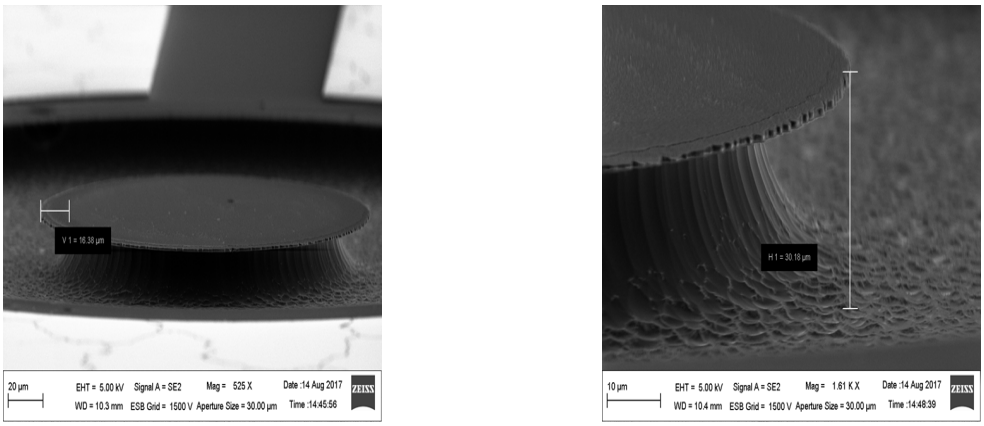

Fig. 8.22 SEM images showing the vertical and lateral silicon undercut.

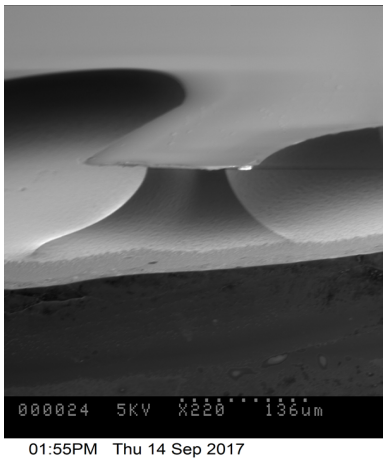

Fig. 8.23 SEM image of silicon isotropic etch using SU-8 mask.

8.2.5 Silica melting (step 12 in Fig. 8.1)

Forming micro-toroid resonators in silica was reported in [154]. As explained earlier, the silicon was etched to undercut a prepatterned silica disc. Then a CO_2 laser beam was focused on the structure to melt and reflow the silica disc. The flow diagram illustrating the micro-toroid resonator fabrication is shown in Fig. 8.24.

As reported in [154], silicon has higher transmissivity at the CO_2 laser wavelength of $10.4\mu m$ than silica. Silicon can be considered transparent, while silica can be considered opaque. By focusing, the approximately gaussian laser beam to spot diameters slightly larger than the silica disc diameter, and adjusting the power around $100MW/m^2$ [154], the silica disc will melt and reflow. As silicon has much higher thermal conductivity than silica, the silicon pillar underneath the middle part of the silica disc will act as a heat sink during the reflow process. The fast heat dissipation from the silicon pillar will prevent the silica on top

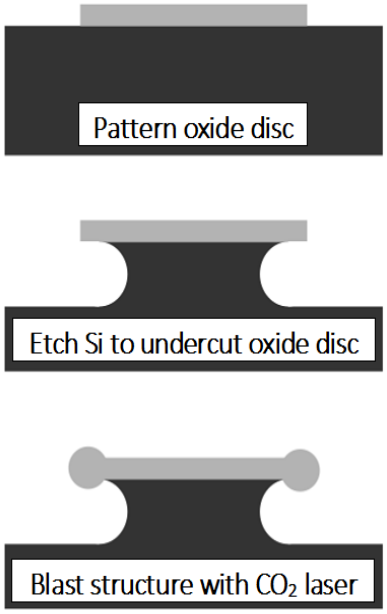

Fig. 8.24 Schematic showing toroid microresonator fabrication steps.

from reaching its melting temperature. As the outer periphery of the disc is suspended in air, where heat dissipation is very slow, the silica at the periphery will melt. The surface tension of the fluidic phase of silica will form a toroid shape with very high smoothness. Such toroid is defined by two radii, the major radius (the radius of the disc) and the minor radius (the radius of the bulb). The size of both radii is controllable by the patterning and undercutting steps.

As un-doped and moderately doped silicon and diamond are highly transparent at $10.4\mu m$ wavelength, reflowing the silica resonator as the last step after fabricating the hanging waveguide was considered. Examining this procedure was conducted by shinning the CO_2 laser beam through hanging silicon and diamond, where both structures proved to be transparent.

Focusing the CO_2 laser beam on diamond films grown on highly doped silicon substrates resulted in the ablation of micro-dots in the diamond films. The study of this effect is the subject of **Chapter 6**.

For $200\mu m$ silica discs, $130\mu m$ beam radius was used at a power of 15 W. The resulting toroid is shown in Fig. 8.25. The rough silicon around the resonator has been eliminated with the ICP-RIE silicon etch recipe.

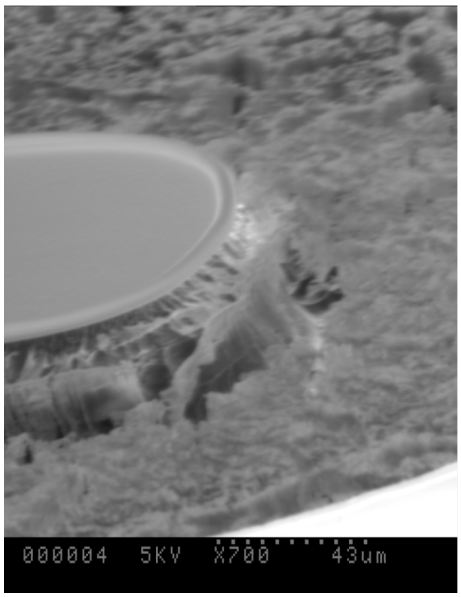

Fig. 8.25 SEM image of melted silica ring resonator.

8.3 Bonding (steps 13 and 14 in Fig. 8.1)

One of the biggest obstacles that faced the fabrication process was the bonding step. The requirement was for a strong bond that can withstand the subsequent fabrication steps, as well as, having reasonable sheer stress resistance.

EPO-TEK® 301 bonding epoxy was considered as it provides high resistance against sheer and tension stresses, as well as, being optically compatible. EPO-TEK® 301 is a 2-part epoxy that needs to be mixed properly for strong adhesion. Such mixing step introduces air inside the mixture, which requires degassing step. It was found that the air-bubbles trapped in the mixture cannot be fully eliminated.

Also, the separation layer was required to be $2-3\mu m$ thick, but the epoxy was $18\mu m$ thick as shown in Fig. 8.26. Spin-coating the epoxy was not effective due to the high viscosity, 100-200 CPS compared to 6 CPS for AZ1505® photoresist. Therefore, epoxy bonding was discarded.

Finally, we resorted to PMMA wet bonding due to its simplicity and optical compatibility. First, a $1.75\mu m$ PMMA layer was spun on the device layer of the top SOI chip and cured to form a smooth cladding. A second $1.75\mu m$ PMMA layer was coated on the device layer. The SOI with the uncured PMMA layer was then brought in contact with the bottom chip and pressure with a pair of tweezers was applied on them to ensure full adhesion. PMMA curing resulted in a strong bond that was compatible with the later fabrication processes.

Bonding the bottom chip to a top SOI chip was the last step conducted in the device fabrication process. However, all the top-chip fabrication steps have been tested individually and are reported in the next section.

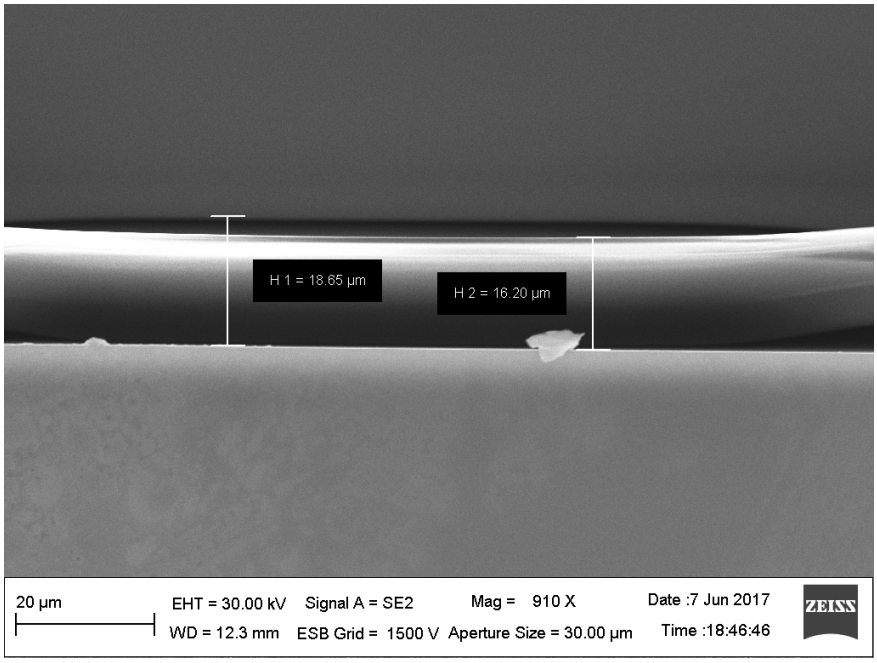

Fig. 8.26 SEM image showing epoxy thickness.

8.4 Top chip processing

All optical components, except for the micro-toroid resonator, in the fabricated PIC were composed on the top chip. All fabrication steps of the top chip were tested individually, but the final fabrication of the top chip is still an ongoing work. Some challenges appeared at certain sequential fabrication steps that prevented the completion of the device, but they are currently being resolved. Here we report the tests being conducted to finalise fabricating the top chip.

8.4.1 Deep silicon etching (step 15 in Fig. 8.1)

In this work we need to completely remove the handle silicon layer off the top substrate. As there is no need for vertical side walls, there was no need to use the anisotropic Bosch etching process. An ordinary ICP-RIE process using an Oxford Cobra machine with SF_6 is being tested. The current work is aimed towards extracting the practical etch rates for the available

machine, as well as, examining the effect of this etch step on the other layers of the chip. The back side of the handle silicon on the SOI wafer had a slightly thick oxide layer, which is not specified in the data-sheet but was confirmed after discussions with the manufacturer. Due to the high-selectivity of SF_6 etching for silicon over silica, etch tests have failed until lapping the back side of silicon to remove the oxide layer. Dry silicon etching is still an ongoing work.

8.4.2 Silica dry etching (step 15 in Fig. 8.1)

Dry etching of the silica layer has been tested using fluorine rich fluorocarbons in an Oxford Cobra machine. But due to the delays in dry etching the handle silicon, it was not conducted in the fabrication process.

8.4.3 Electron-beam lithography (steps 16 and 17 in Fig. 8.1)

Defining the partially etched waveguide sections required Electron-beam (ebeam) lithography. The partially etched waveguide ebeam pattern is presented in Fig. 8.27. ebeam lithography has been tested with HSQ ebeam resist for the structure included. As the ebeam pattern has to be written on a thin silicon layer with different under-layer cladding structures, ebeam dose tests had to be conducted to achieve the optimum dosing level for each section. The dose tests for the silicon on supported PMMA cladding was straight forward, but the tests for the silicon on suspended PMMA needed to be optimised. However, the ebeam pattern at the transition from supported to suspended still needs further optimisation.

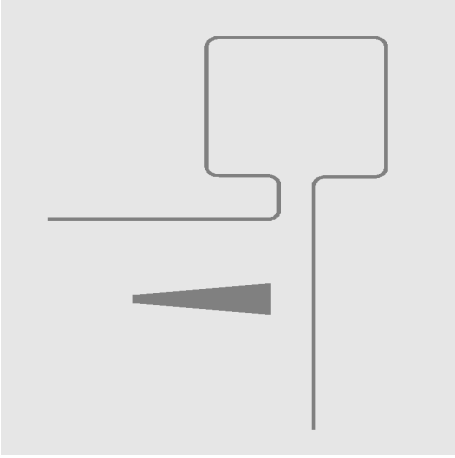

Fig. 8.27 ebeam pattern with inverse-taper coupler magnified in the inset.

8.4.4 Silicon anisotropic etching (steps 18-21 in Fig. 8.1)

As described in **section 8.1.3**, anisotropic dry etching of silicon is achieved with fluorine rich fluorocarbon plasma. As this step defines the waveguides, a smooth etch was required. Several etch recipes have been tried for both RIE and ICP-RIE etchers. For smooth side walls we used ICP-RIE etcher with slow etch rate of $0.2\mu m$ per minute. 50sccm C_4F_8 and 25sccm SF_6 flow rates at 20mTorr with 30W RF power and 1200W ICP power were chosen for the best compromise between etch rate and side wall verticality and smoothness. Fig. 8.28 shows an SEM image of partially etched silicon waveguide. The fabricated partially etched silicon waveguide is a stand alone structure and has not been integrated in the final chip yet.

Also, anisotropically fully etched silicon is required to define the hanging waveguide sections. Unlike the partially etched sections, the fully etched parts were defined using photo-lithography. The photo-lithography exposure mask is shown in Fig. 8.29. The array of circular holes at the wide actuator section are etch-holes for proper removal of the underlying PMMA layer during polymer etching to release the suspended structure.

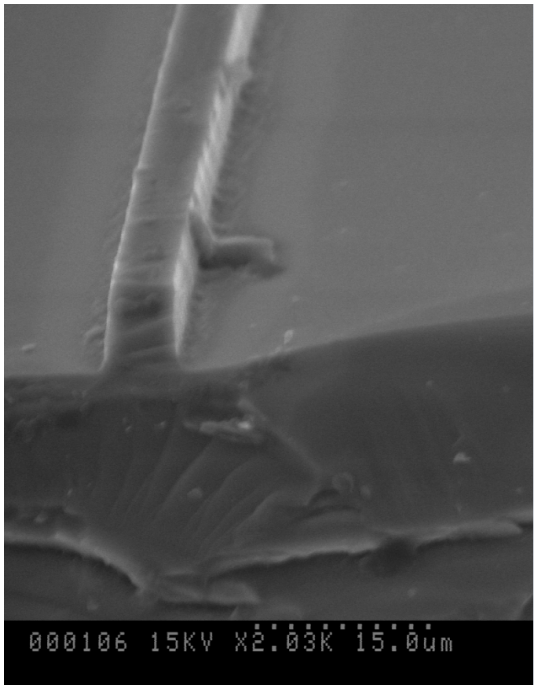

Fig. 8.28 SEM image of partially etched waveguide.

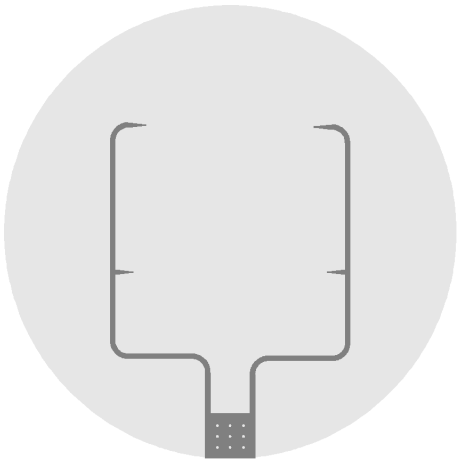

Fig. 8.29 Mask for fully etched waveguide.

8.4.5 Polymer dry etching (step 22 in Fig. 8.1)

Polymer dry etching is simple, flexible and very controllable [152]. Dry etching of polymers is usually conducted under low pressure to reduce the scattering of the reactive species and enhance the anisotropic profiles and the smoothness of the etched surfaces [152].

In general, polymer etch rate is proportional to both RIE and ICP powers. The process pressure's effect on etch rate is dependable on the plasma chamber volume and shape, hence, it needs to be optimised for each equipment and polymer similar to the work presented in [155].

In this work the two polymers that required etching were PMMA and EPO-TEK® 301 bonding epoxy. PMMA is soluble in acetone, which acts as an isotropic etchant. But according to our experience, PMMA removal using acetone is uncontrollable and not accurately repeatable. EPO-TEK® 301 bonding epoxy is very resilient against most wet chemicals and, to our knowledge, there are no available reports describing wet chemical removal. As most polymers, PMMA and EPO-TEK® 301 bonding epoxy can be patterned with dry etching using O_2 plasma.

PMMA anisotropic dry etching of the cladding and bonding layers was conducted using RIE plasma etcher. Low power plasma produces isotropic etching process, while high power increases the anisotropic behaviour of etching. Improving the aspect ratio of the etched structures in PMMA has attracted a lot of research. One study [156] has reported introducing CHF_3 to O_2 RIE etching of PMMA to increase the aspect ratio of the etched structures.

In this work, the processes parameters were adjusted to provide the best compromise between sidewall smoothness and etch rate. For RIE plasma etching, the optimal process pressure was 65 mTorr, RF power was 200W, and oxygen flow rate was 30 sccm, which

provided etch rate of $1\mu m/min$. Fig. 8.30 shows an SEM image of the RIE etched PMMA layers.

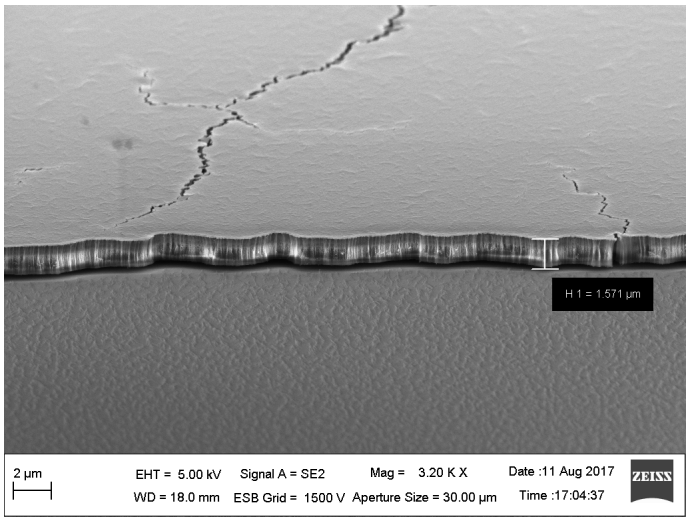

Fig. 8.30 SEM image of dry-etched PMMA.

The EPO-TEK® 301 bonding epoxy was used as a protective coating for KOH etching, which is discussed in **Appendix C**. Etching EPO-TEK® 301 bonding epoxy using RIE etcher has been tried. The optimal process pressure was 65 mTorr, RF power was 200 W, and oxygen flow rate was 30 sccm, which provided etch rate of $\sim 0.75\mu m$/min. Since the protective epoxy layer was very thick (10s of microns), the provided etch rate was very slow. Therefore, introducing argon (Ar) in the plasma chamber will provide sputtering of the epoxy layer. As Ar ions will sputter silicon when the epoxy is fully etched, therefore, when the epoxy thickness reaches $2-5\mu m$, only oxygen plasma should be used.

8.5 Summary

The fabrication process for hybrid-multi-layer MEMS actuated PIC, which allows a tunable coupling between ultra-high-Q micro-toroid-resonator and silicon optical waveguide was developed. The fabrication process comprises processing an oxidised silicon chip to act as a bottom chip, bonding the processed bottom chip to an SOI top chip, then processing the top chip. The fabrication process consists of 22 primary steps including photo-lithography, ebeam-lithography, dry and wet etching, and physical vapour deposition (PVD) techniques.

All fabrication steps have been tested individually where a processing recipe is produced for each step. During consecutive processing, challenges appeared that required slight adjustments of some fabrication recipes. One of the main contributors to the delays in the

fabrication phase is the various fabrication locations. The fabrication process is planned to take place at different cleanrooms in different cities due to the availability of required equipment. Successful completion of the bottom chip fabrication and the bonding step has been achieved. Fabrication tests for processing the top chip have started where the completion of top chip processing is expected soon, provided that no more issues arise.

The fabrication process of the hybrid-multi-layer PIC relies on traditional widely used fabrication techniques, which makes its realisation into a commercial device easy and affordable. Also, the presented design and fabrication protocol compensate for relatively large fabrication errors with negligible performance price, which increases the practicality of the proposed design and fabrication protocol.

The completed hybrid-multi-layer PIC will be a novel structure allowing the use of different dielectric materials for each optical component. Such structure will eliminate the need for compromises in PIC design and fabrication due to the limited material choices in the commercially available substrates used for single-substrate PICs. According to our designs, the new MEMS actuated optical coupler will provide a large deflection range with actuation voltages below $5V$, which is ideal for battery operated devices and eliminates the electrical hazards of using high actuation voltages.

Chapter 9

Conclusion

In this work, several studies have been conducted. A concise systematic grating coupler design chapter with a freely distributed grating coupler simulator are presented. Also, an analytical treatment of scattering loss from rough surfaces of asymmetric rectangular dielectric waveguides is presented with a MATLAB® code. Then, a new suspended nanocrystalline diamond (NCD) platform has been presented. A patterning technique for thin NCD films grown on doped silicon substrates has been studied as well, and a deep insight about the mechanism behind it has been delivered. Finally, the design of a hybrid multilayer photonic integrated chip (PIC) has been reported; and its fabrication process has been designed and initiated.

The analytical treatment for the scattering loss off rough waveguide surfaces is based on previous analytical treatments of scattering loss from symmetric slab waveguides. These studies were extended to include asymmetric slab waveguide structures with different cladding materials and surface roughness parameters. Then the effective index method was used to obtain the scattering loss formula for rectangular asymmetric waveguides with different material and roughness parameters at each waveguide-core boundary. The produced formula is very beneficial for determining the practicality of waveguide design, used material, operation wavelength, and fabrication techniques. The obtained results would require experimental verifications in the future.

A suspended NCD photonic platform has been designed and simulated using the finite element method. The suspended structure allows the use of the NCD wide transmission window without any limitations from an underlying cladding layer. The platform contains submicron rib-waveguides that are compatible with dense Photonic Integrated Circuits (PICs). The final rib-waveguide structure measures $600nm$ in width and $456nm$ in width with $106nm$ rib-height. The small waveguide dimensions are believed to be among the smallest (if not the smallest) demonstrated NCD waveguides to-date. Also, the suspended platform is a novelty

for NCD waveguides, where previously NCD waveguides have been demonstrated on lower refractive index substrates (e.g. silica on silicon substrates).

The realization of the suspended NCD platform has been shown to be simple with standard fabrication techniques. The fabrication protocol consists of consecutive lithography and etching steps. The anisotropic diamond etching recipe developed in this study produces smooth side-walls, which dramatically lowers the scattering loss. However, propagation loss remains relatively high due to the polycrystalline nature of NCD, which might affect its practical usage compared to single-crystalline diamond waveguides. Loss measurements has been conducted at the $1.55\mu m$ wavelength, and an average loss coefficient of $5.03 \pm 0.46 dB/mm$ has been extracted. Propagation loss can be dramatically reduced when using NCD films with smaller grain sizes. The average grain size of the film used in this study is $225nm$, where films with $100nm$ average grain sizes are estimated to have propagation loss that is less than half what is measured in this study. Regardless of the propagation loss, the demonstrated photonic platform structure can be very beneficial for several applications including sensing and metrology, and for the use in harsh environments.

Patterning NCD films grown on silicon substrates using CO_2 laser has been studied. Previous studies on patterning thin diamond films using laser beams with photon-energy below the band-gap did not provide a satisfactory enough explanation. The ablation mechanism described in these studies ignored the role of the substrate on which the diamond is grown. And for transparent substrates at the used wavelength, doping role was not considered. Diamond grown on highly doped silicon wafers was used in this study. We hypothesised a theory for the ablation mechanism where silicon doping plays the major role in ablation at ambient temperature. The effect of the silicon substrate doping has been studied through numerical simulations, and the results shed the light on its major effect on the ablation process. The numerical results proved our hypothesis, and experimental demonstration was the next logical step. Tests using CO_2 laser were performed, which confirmed the theoretical results. The reported results can lead to fast, affordable, and easy micro-machining technique. The reported results are not specific for patterning NCD films, but for other transparent materials using laser beams with photon-energies below the band gap, if they are pattern-able using similar thermal mechanisms.

A major part of this study is dedicated to the design of a hybrid multi-layer PIC. The presented PIC consists mainly of an ultra-high-Q silica micro-resonator, which possesses the highest Q-factor to date, and an optical waveguide made of a different material. The ultra-high-Q micro-resonator was chosen for the potential of use in multiple applications. In the research lab, ultra-high-Q micro-resonators are very beneficial for studying non-linear optical effects using modest laser powers. Using modest laser powers does not only have

the advantage of reducing operational hazards, but it is also economical in terms of startup and running costs. For practical applications, ultra-high-Q micro-resonators offer a mean of accurate time measurements rivaling the atomic clock, and precise metrology. The hybrid multi-layer nature of the presented PIC combines the advantages of using silica micro-resonator, with the highest Q-factor to-date, and an optical waveguide of different material that offers the best performance according to the required application. Two materials are considered for the optical waveguide, silicon and NCD. Silicon is a viable candidate for dense PICs thanks to its high refractive index; while NCD will overcome the limitation in silicon transmission window with its superior transmissivity.

Besides the hybrid multi-layer structure of the presented PIC, a MEMS actuated coupler mechanism is implemented that offers total controllability over the coupled optical energy. The presented MEMS coupler mechanism overcomes the usual problem of using bulky coupling setups. Also, it allows for integrating both the ultra-high-Q micro-resonator and the coupler waveguide into one PIC, which brings using ultra-high-Q micro-resonators one step closer to practical implementation. The presented MEMS coupler mechanism allows for $1.5\mu m$ silicon coupler deflection with actuation voltages below $5V$, which is compatible with battery-operated devices.

The different optical components were simulated using the finite element method (FEM) through the use of COMSOL® Multiphysics. Phase matching conditions between the silica micro-resonator and the silicon or NCD waveguide were estimated for efficient power coupling from the waveguide into the micro-resonator. Modes' shapes, effective indices, waveguide transitions, and coupling mechanisms to and from optical fibres were designed to optimise the PIC operation. Also electromechanical simulations were conducted for several MEMS coupler structures to determine an optimum design to meet the tight requirement of large deflection distance with very low actuation voltages. The study also included practicality checks to ensure safe fabrication and operation of the presented chip. The proposed design consists of two bonded chips containing the different components of the PIC.

The fabrication process of the hybrid multi-layer PIC with silicon waveguides has been developed and tested for each fabrication step individually. But during the consecutive fabrication steps, obstacles emerged. Such obstacles were mainly due to the use of the fabrication at different fabrication sites and using different equipment. Throughout the course of this work, transition from one cleanroom to another was unavoidable because of equipment ownership issues. A considerable portion of the fabrication process has been tested in one facility, but fabricated in another. Currently, most of the obstacles have been overcome. Also, fabricating the final chip has started, but it is still an ongoing work. The main purpose of this work was proving the feasibility of fabricating the hybrid multi-layer PIC through theoretical

and numerical studies, which has been achieved. The full fabrication protocol has been presented in this work, but due to the external factors mentioned before, it has been delayed.

Finally, a chapter about grating coupler design is presented as the starting point for prospective experiments. For instance, the suspended NCD platform suffered from low input/output coupling efficiency because of the used inverse-taper edge coupler. The planned work is to replace the edge coupler with a grating coupler. A grating coupler will not just eliminate the problems with edge coupling misalignment, but it also allows for fabricating the whole photonic circuit on a smaller area. The chapter has been laid-out to offer a systematic approach for designing grating couplers. Also, a grating coupler simulation application based on CAMFR is freely available to simplify designing grating couplers. The results presented are for a symmetric grating coupler only. Designing asymmetric grating coupler required the development of genetic algorithms, which are being developed at the time of writing this thesis.

The prospective work after the achieved results is divided into five different tasks:

1. Re-examine the suspended diamond platform using grating couplers instead of edge couplers. The deflected edges of the suspended NCD platform introduced large misalignments to the input and output mechanism, which compromised the coupling efficiency to a high extent. Moving from an edge coupling mechanism to grating coupler, which can easily be fabricated away from the edges, will improve the performance of light coupling in and out of the PIC.

2. Finalise fabricating the hybrid multi-layer PIC. Overcoming the fabrication obstacles and demonstrating the final chip structure will bring using ultra-high-Q micro-resonators one step closer to commercialisation. If the presented design proved efficient, it will pave part of the way in front of using the ultra-high-Q micro-resonators in integrated practical devices.

3. Study the non-linear effects in the ultra-high-Q micro-resonator using the fabricated platform. Using the presented electro-mechanically actuated platform for studying non-linear optical effects has the advantage of high-repeatability by eliminating the inaccuracies in the conventional mechanical actuation setups. The high precision in controlling electrical signals, in electro-mechanistically actuated setups, is superior to the accuracy in actuation using purely mechanical means. The high precision in actuation translates to more precise repeatable results.

4. Develop Genetic algorithm for asymmetric grating couplers and incorporate it with the presented application. For scientists and engineers without professional expertise

in programming, developing genetic algorithms is very challenging. Developing a universal code for simulating asymmetric grating couplers and incorporating it with an easy-to-use free application will help and accelerate the research and design of asymmetric grating couplers.

5. Verify the scattering loss formula with experimental data. In the majority of experimental work on dielectric waveguides, estimating the scattering loss from rough surfaces is rarely estimated. Although the current fabrication techniques are capable of producing extremely smooth waveguides, reaching zero roughness (beyond atomic roughness) is still not achievable with most techniques. Therefore estimating scattering loss beforehand will help determine the practicality of a certain design and fabrication technique. And for materials with extremely low absorption loss, scattering loss from rough surfaces dominates. Practical experimentation to verify the proposed formula will help in modifying it to match the actual loss values, and hence, gives better insight to improve PIC efficiencies.

References

[1] E. A. Marcatili, "Dielectric rectangular waveguide and directional coupler for integrated optics," *Bell Labs Technical Journal*, vol. 48, no. 7, pp. 2071–2102, 1969.

[2] S. E. Miller, "Integrated optics: An introduction," *Bell Labs Technical Journal*, vol. 48, no. 7, pp. 2059–2069, 1969.

[3] H. Wang, Y. He, Y.-H. Li, Z.-E. Su, B. Li, H.-L. Huang, X. Ding, M.-C. Chen, C. Liu, J. Qin, *et al.*, "High-efficiency multiphoton boson sampling," *Nature Photonics*, 2017.

[4] IBM website: http://www-03.ibm.com/press/uk/en/pressrelease/51765.wss.

[5] M. Mohseni, P. Read, H. Neven, S. Boixo, V. Denchev, R. Babbush, A. Fowler, V. Smelyanskiy, and J. Martinis, "Commercialize quantum technologies in five years," *Nature*, vol. 543, pp. 171–174, 2017.

[6] R. Wentorf Jr and H. P. Bovenkerk, "Preparation of semiconducting diamonds," *The Journal of Chemical Physics*, vol. 36, no. 8, pp. 1987–1990, 1962.

[7] Z. Hu, P. Prunici, P. Hess, and K. Chen, "Optical properties of nanocrystalline diamond films from mid-infrared to ultraviolet using reflectometry and ellipsometry," *Journal of Materials Science: Materials in Electronics*, vol. 18, no. 1, pp. 37–41, 2007.

[8] W. Bogaerts, P. De Heyn, T. Van Vaerenbergh, K. De Vos, S. Kumar Selvaraja, T. Claes, P. Dumon, P. Bienstman, D. Van Thourhout, and R. Baets, "Silicon microring resonators," *Laser & Photonics Reviews*, vol. 6, no. 1, pp. 47–73, 2012.

[9] N. Vermeulen, J. Sipe, L. G. Helt, and H. Thienpont, "Opportunities for wavelength conversion with on-chip diamond ring resonators," *Laser & Photonics Reviews*, vol. 6, no. 6, pp. 793–801, 2012.

[10] B. Hausmann, I. Bulu, V. Venkataraman, P. Deotare, and M. Lončar, "An on-chip optical parametric oscillator in diamond," in *Nonlinear Optics*, pp. PTh3A–6, Optical Society of America, 2013.

[11] S. M. Spillane, T. J. Kippenberg, D. K. Armani, and K. J. Vahala, "Ultra-high-q toroid microcavities on a chip," in *Conference on Lasers and Electro-Optics*, p. CMM1, Optical Society of America, 2003.

[12] P. Rath, N. Gruhler, S. Khasminskaya, C. Nebel, C. Wild, and W. Pernice, "Waferscale nanophotonic circuits made from diamond-on-insulator substrates," *Optics express*, vol. 21, no. 9, pp. 11031–11036, 2013.

[13] M. Tanaka, "An industrial and applied review of new mems devices features," *Microelectronic engineering*, vol. 84, no. 5, pp. 1341–1344, 2007.

[14] A. C. Fischer, F. Forsberg, M. Lapisa, S. J. Bleiker, G. Stemme, N. Roxhed, and F. Niklaus, "Integrating mems and ics," *Microsystems & Nanoengineering*, vol. 1, p. 15005, 2015.

[15] C. Errando-Herranz, F. Niklaus, G. Stemme, and K. B. Gylfason, "Low-power microelectromechanically tunable silicon photonic ring resonator add–drop filter," *Optics letters*, vol. 40, no. 15, pp. 3556–3559, 2015.

[16] S. Han, T. J. Seok, N. Quack, B.-W. Yoo, and M. C. Wu, "Large-scale silicon photonic switches with movable directional couplers," *Optica*, vol. 2, no. 4, pp. 370–375, 2015.

[17] J. Yao, *Tunable optical microresonators with micro-electro-mechanical-system (MEMS) integration*. University of California, Berkeley, 2007.

[18] J. C. Maxwell, "A dynamical theory of the electromagnetic field," *Philosophical transactions of the Royal Society of London*, vol. 155, pp. 459–512, 1865.

[19] D. Fleisch, *A student's guide to Maxwell's equations*. Cambridge University Press, 2008.

[20] M. N. Sadiku, *Elements of electromagnetics*. Oxford university press, 2014.

[21] C. Hössbacher, A. Josten, B. Bäuerle, Y. Fedoryshyn, H. Hettrich, Y. Salamin, W. Heni, C. Haffner, C. Kaiser, R. Schmid, *et al.*, "Plasmonic modulator with> 170 ghz bandwidth demonstrated at 100 gbd nrz," *Optics Express*, vol. 25, no. 3, pp. 1762–1768, 2017.

[22] L. Tong, J. Lou, and E. Mazur, "Single-mode guiding properties of subwavelength-diameter silica and silicon wire waveguides," *Optics Express*, vol. 12, no. 6, pp. 1025–1035, 2004.

[23] D. Schroder, R. N. Thomas, and J. C. Swartz, "Free carrier absorption in silicon," *IEEE Journal of solid-state circuits*, vol. 13, no. 1, pp. 180–187, 1978.

[24] H. Engstrom, "Infrared reflectivity and transmissivity of boron-implanted, laser-annealed silicon," *Journal of Applied Physics*, vol. 51, no. 10, pp. 5245–5249, 1980.

[25] L. Vina and M. Cardona, "Effect of heavy doping on the optical properties and the band structure of silicon," *Physical Review B*, vol. 29, no. 12, p. 6739, 1984.

[26] R. Soref and B. Bennett, "Electrooptical effects in silicon," *IEEE journal of quantum electronics*, vol. 23, no. 1, pp. 123–129, 1987.

[27] S. Aw, H. Tan, and C. Ong, "Optical absorption measurements of band-gap shrinkage in moderately and heavily doped silicon," *Journal of Physics: Condensed Matter*, vol. 3, no. 42, p. 8213, 1991.

[28] M. Van Exter and D. Grischkowsky, "Optical and electronic properties of doped silicon from 0.1 to 2 thz," *Applied Physics Letters*, vol. 56, no. 17, pp. 1694–1696, 1990.

[29] R. Kitamura, L. Pilon, and M. Jonasz, "Optical constants of silica glass from extreme ultraviolet to far infrared at near room temperature," *Applied optics*, vol. 46, no. 33, pp. 8118–8133, 2007.

[30] T. Yeh, "Thermal oxidation of silicon," *Journal of Applied Physics*, vol. 33, no. 9, pp. 2849–2850, 1962.

[31] O. Williams, "Nanocrystalline diamond," *Diamond and Related Materials*, vol. 20, no. 5, pp. 621–640, 2011.

[32] "The cvd diamond booklet, diamond materials, advanced diamond technology."

[33] Z. Yin, Z. Akkerman, B. Yang, and F. Smith, "Optical properties and microstructure of cvd diamond films," *Diamond and Related Materials*, vol. 6, no. 1, pp. 153–158, 1997.

[34] P. Achatz, J. Garrido, M. Stutzmann, O. A. Williams, D. Gruen, A. Kromka, and D. Steinmüller, "Optical properties of nanocrystalline diamond thin films," *Applied Physics Letters*, vol. 88, no. 10, p. 101908, 2006.

[35] V. Prajzler, M. Varga, P. Nekvindova, Z. Remes, and A. Kromka, "Design and investigation of properties of nanocrystalline diamond optical planar waveguides," *Optics express*, vol. 21, no. 7, pp. 8417–8425, 2013.

[36] J. Mort, D. Kuhman, M. Machonkin, M. Morgan, F. Jansen, K. Okumura, Y. LeGrice, and R. Nemanich, "Boron doping of diamond thin films," *Applied Physics Letters*, vol. 55, no. 11, pp. 1121–1123, 1989.

[37] R. Locher, J. Wagner, F. Fuchs, C. Wild, P. Hiesinger, P. Gonon, and P. Koidl, "Boron doped diamond films: electrical and optical characterization and the effect of compensating nitrogen," *Materials Science and Engineering: B*, vol. 29, no. 1-3, pp. 211–215, 1995.

[38] W. Gajewski, P. Achatz, O. A. Williams, K. Haenen, E. Bustarret, M. Stutzmann, and J. A. Garrido, "Electronic and optical properties of boron-doped nanocrystalline diamond films," *Physical Review B*, vol. 79, no. 4, p. 045206, 2009.

[39] R. Bogdanowicz, "Characterization of optical and electrical properties of transparent conductive boron-doped diamond thin films grown on fused silica," *Metrology and Measurement Systems*, vol. 21, no. 4, pp. 685–698, 2014.

[40] O. A. Williams, S. Curat, J. E. Gerbi, D. M. Gruen, and R. B. Jackman, "n-type conductivity in ultrananocrystalline diamond films," *Applied Physics Letters*, vol. 85, no. 10, pp. 1680–1682, 2004.

[41] X. Hu, J. Ye, H. Liu, Y. Shen, X. Chen, and H. Hu, "n-type conductivity and phase transition in ultrananocrystalline diamond films by oxygen ion implantation and annealing," *Journal of Applied Physics*, vol. 109, no. 5, p. 053524, 2011.

[42] X. Hu, J. Ye, H. Hu, X. Chen, and Y. Shen, "Phosphorus ion implantation and annealing induced n-type conductivity and microstructure evolution in ultrananocrystalline diamond films," *Applied Physics Letters*, vol. 99, no. 13, p. 131902, 2011.

[43] L. Prkna, M. Hubálek, and J. Ctyroky, "Vectorial eigenmode solver for bent waveguides based on mode matching," *IEEE Photonics technology letters*, vol. 16, no. 9, pp. 2057–2059, 2004.

[44] E. Chow, S. Lin, J. Wendt, S. Johnson, and J. D. Joannopoulos, "Quantitative analysis of bending efficiency in photonic-crystal waveguide bends at $\lambda = 1.55\ \mu$m wavelengths," *Optics letters*, vol. 26, no. 5, pp. 286–288, 2001.

[45] Y. Qian, S. Kim, J. Song, G. P. Nordin, and J. Jiang, "Compact and low loss silicon-on-insulator rib waveguide 90 bend," *Optics express*, vol. 14, no. 13, pp. 6020–6028, 2006.

[46] A. Yariv and P. Yeh, *Photonics: optical electronics in modern communications*, vol. 6. oxford university press New York, 2007.

[47] A. Wageeh, S. El-Sabban, and D. Khalil, "Resonance wavelength of integrated optical ring resonator with small radius of curvature," *IEEE Photonics Technology Letters*, vol. 26, no. 7, pp. 641–644, 2014.

[48] T. J. Kippenberg, R. Holzwarth, and S. Diddams, "Microresonator-based optical frequency combs," *Science*, vol. 332, no. 6029, pp. 555–559, 2011.

[49] H. Tsang, C. Wong, T. Liang, I. Day, S. Roberts, A. Harpin, J. Drake, and M. Asghari, "Optical dispersion, two-photon absorption and self-phase modulation in silicon waveguides at 1.5 μ m wavelength," *Applied Physics Letters*, vol. 80, no. 3, pp. 416–418, 2002.

[50] T. J. A. Kippenberg, *Nonlinear optics in ultra-high-Q whispering-gallery optical microcavities*. PhD thesis, California Institute of Technology, 2004.

[51] A. Yariv, "Universal relations for coupling of optical power between microresonators and dielectric waveguides," *Electronics letters*, vol. 36, no. 4, pp. 321–322, 2000.

[52] W. McKinnon, D.-X. Xu, C. Storey, E. Post, A. Densmore, A. Delâge, P. Waldron, J. Schmid, and S. Janz, "Extracting coupling and loss coefficients from a ring resonator," *Optics express*, vol. 17, no. 21, pp. 18971–18982, 2009.

[53] A. Yariv, "Coupled-mode theory for guided-wave optics," *IEEE Journal of Quantum Electronics*, vol. 9, no. 9, pp. 919–933, 1973.

[54] H. A. Haus and W. Huang, "Coupled-mode theory," *Proceedings of the IEEE*, vol. 79, no. 10, pp. 1505–1518, 1991.

[55] A. Hardy and W. Streifer, "Coupled mode theory of parallel waveguides," *Journal of lightwave technology*, vol. 3, no. 5, pp. 1135–1146, 1985.

[56] B. E. Little, J.-P. Laine, and H. A. Haus, "Analytic theory of coupling from tapered fibers and half-blocks into microsphere resonators," *Journal of lightwave technology*, vol. 17, no. 4, p. 704, 1999.

[57] T. J. Kippenberg, S. M. Spillane, D. K. Armani, B. Min, L. Yang, and K. J. Vahala, "Fabrication, coupling and nonlinear optics of ultra-high-q micro-sphere and chip-based toroid microcavities,"

[58] K. Yee, "Numerical solution of initial boundary value problems involving maxwell's equations in isotropic media," *IEEE Transactions on antennas and propagation*, vol. 14, no. 3, pp. 302–307, 1966.

[59] U. Andersson, *Time-domain methods for the Maxwell equations*. PhD thesis, Numerisk analys och datalogi, 2001.

[60] P. Bienstman and R. Baets, "Optical modelling of photonic crystals and vcsels using eigenmode expansion and perfectly matched layers," *Optical and Quantum Electronics*, vol. 33, pp. 327–341, 2001.

[61] P. Bienstman, *Rigorous and efficient modelling of wavelenght scale photonic components*. PhD thesis, Ghent University, 2001.

[62] T. Tamir and S.-T. Peng, "Analysis and design of grating couplers," *Applied Physics A: Materials Science & Processing*, vol. 14, no. 3, pp. 235–254, 1977.

[63] D. Taillaert, W. Bogaerts, P. Bienstman, T. F. Krauss, P. Van Daele, I. Moerman, S. Verstuyft, K. De Mesel, and R. Baets, "An out-of-plane grating coupler for efficient butt-coupling between compact planar waveguides and single-mode fibers," *IEEE Journal of Quantum Electronics*, vol. 38, no. 7, pp. 949–955, 2002.

[64] J. Covey and R. T. Chen, "Efficient perfectly vertical fiber-to-chip grating coupler for silicon horizontal multiple slot waveguides," *Optics express*, vol. 21, no. 9, pp. 10886–10896, 2013.

[65] G. Roelkens, D. Van Thourhout, and R. Baets, "High efficiency silicon-on-insulator grating coupler based on a poly-silicon overlay," *Optics Express*, vol. 14, no. 24, pp. 11622–11630, 2006.

[66] C. Li, H. Zhang, M. Yu, and G. Lo, "Cmos-compatible high efficiency double-etched apodized waveguide grating coupler," *Optics express*, vol. 21, no. 7, pp. 7868–7874, 2013.

[67] D. Taillaert, F. Van Laere, M. Ayre, W. Bogaerts, D. Van Thourhout, P. Bienstman, and R. Baets, "Grating couplers for coupling between optical fibers and nanophotonic waveguides," *Japanese Journal of Applied Physics*, vol. 45, no. 8R, p. 6071, 2006.

[68] D. Taillaert, "Grating couplers as interface between optical fibres and nanophotonic waveguides.," 2005.

[69] S. Scheerlinck, J. Schrauwen, F. Van Laere, D. Taillaert, D. Van Thourhout, and R. Baets, "Efficient, broadband and compact metal grating couplers for silicon-on-insulator waveguides," *Optics express*, vol. 15, no. 15, pp. 9625–9630, 2007.

[70] R. Topley, *Erasable diffractive grating couplers in silicon on insulator*. PhD thesis, University of Southampton, 2014.

[71] Y. Wang, H. Yun, Z. Lu, R. Bojko, F. Zhang, M. Caverley, N. A. Jaeger, and L. Chrostowski, "Apodized focusing fully etched sub-wavelength grating couplers with ultra-low reflections," in *CLEO: Science and Innovations*, pp. SM1I–6, Optical Society of America, 2015.

[72] D. Taillaert, P. Bienstman, and R. Baets, "Compact efficient broadband grating coupler for silicon-on-insulator waveguides," *Optics letters*, vol. 29, no. 23, pp. 2749–2751, 2004.

[73] K. O. Hill and G. Meltz, "Fiber bragg grating technology fundamentals and overview," *Journal of lightwave technology*, vol. 15, no. 8, pp. 1263–1276, 1997.

[74] CAMFR website: http://camfr.sourceforge.net/.

[75] J. C. Wirth, *Silicon grating couplers for low loss coupling between optical fiber and silicon nanowires*. PhD thesis, Purdue University, 2011.

[76] J. L. Covey, *Ultrafast all-optical switching via grating-based fabry-perot resonators and surface normal fiber-to-waveguide couplers*. PhD thesis, 2014.

[77] F. Van Laere, T. Claes, J. Schrauwen, S. Scheerlinck, W. Bogaerts, D. Taillaert, L. O'Faolain, D. Van Thourhout, and R. Baets, "Compact focusing grating couplers for silicon-on-insulator integrated circuits," *IEEE Photonics Technology Letters*, vol. 19, no. 23, pp. 1919–1921, 2007.

[78] O. Svelto and D. C. Hanna, *Principles of lasers*, vol. 4. Springer, 1998.

[79] I. D. Rukhlenko, M. Premaratne, and G. P. Agrawal, "Effective mode area and its optimization in silicon-nanocrystal waveguides," *Optics letters*, vol. 37, no. 12, pp. 2295–2297, 2012.

[80] H. Jerrard, "An introduction to optical waveguides: Mj adams wiley, 1981, pp xv+ 401,£ 21.50," *Optics & Laser Technology*, vol. 14, no. 3, p. 161, 1982.

[81] D. Marcuse, "Mode conversion caused by surface imperfections of a dielectric slab waveguide," *Bell Labs Technical Journal*, vol. 48, no. 10, pp. 3187–3215, 1969.

[82] F. Payne and J. Lacey, "A theoretical analysis of scattering loss from planar optical waveguides," *Optical and Quantum Electronics*, vol. 26, no. 10, pp. 977–986, 1994.

[83] J. Lacey and F. Payne, "Radiation loss from planar waveguides with random wall imperfections," *IEE Proceedings J-Optoelectronics*, vol. 137, no. 4, pp. 282–288, 1990.

[84] D. Marcuse, *Theory of dielectric optical waveguides*. Elsevier, 2013.

[85] B. J. Hausmann, B. Shields, Q. Quan, P. Maletinsky, M. McCutcheon, J. T. Choy, T. M. Babinec, A. Kubanek, A. Yacoby, M. D. Lukin, *et al.*, "Integrated diamond networks for quantum nanophotonics," *Nano letters*, vol. 12, no. 3, pp. 1578–1582, 2012.

[86] B. J. Hausmann, I. Bulu, P. Deotare, M. McCutcheon, V. Venkataraman, M. Markham, D. Twitchen, and M. Loncar, "Integrated high-quality factor optical resonators in diamond," *Nano letters*, vol. 13, no. 5, pp. 1898–1902, 2013.

[87] Y. Hirose and Y. Terasawa, "Synthesis of diamond thin films by thermal cvd using organic compounds," *Japanese Journal of Applied Physics*, vol. 25, no. 6A, p. L519, 1986.

[88] Y. Liou, A. Inspektor, R. Weimer, and R. Messier, "Low-temperature diamond deposition by microwave plasma-enhanced chemical vapor deposition," *Applied Physics Letters*, vol. 55, no. 7, pp. 631–633, 1989.

[89] R. P. Mildren, "Intrinsic optical properties of diamond," *Optical Engineering of Diamond*, pp. 1–34, 2013.

[90] B. G. Streetman, S. Banerjee, *et al.*, *Solid state electronic devices*, vol. 2. Prentice-Hall Englewood Cliffs, NJ, 1995.

[91] E. Vella, F. Messina, M. Cannas, and R. Boscaino, "Unraveling exciton dynamics in amorphous silicon dioxide: Interpretation of the optical features from 8 to 11 ev," *Physical Review B*, vol. 83, no. 17, p. 174201, 2011.

[92] D. M. Shyroki, "Exact equivalent straight waveguide model for bent and twisted waveguides," *IEEE Transactions on Microwave Theory and Techniques*, vol. 56, no. 2, pp. 414–419, 2008.

[93] E. L. Thomas, G. W. Nelson, S. Mandal, J. S. Foord, and O. A. Williams, "Chemical mechanical polishing of thin film diamond," *Carbon*, vol. 68, pp. 473–479, 2014.

[94] S. Al-Chalabi and A. Jones, "Light scattering by irregular particles in the rayleigh-gans-debye approximation," *Journal of Physics D: Applied Physics*, vol. 28, no. 7, p. 1304, 1995.

[95] R. Apetz and M. P. Bruggen, "Transparent alumina: a light-scattering model," *Journal of the American Ceramic Society*, vol. 86, no. 3, pp. 480–486, 2003.

[96] "The element six cvd diamond handbook, elementsix, a de beers group company."

[97] I. Aharonovich, A. D. Greentree, and S. Prawer, "Diamond photonics," *Nature Photonics*, vol. 5, no. 7, pp. 397–405, 2011.

[98] P. Rath, S. Ummethala, C. Nebel, and W. H. Pernice, "Diamond as a material for monolithically integrated optical and optomechanical devices," *physica status solidi (a)*, vol. 212, no. 11, pp. 2385–2399, 2015.

[99] A. V. Sumant, O. Auciello, M. Liao, and O. A. Williams, "Mems/nems based on mono-, nano-, and ultrananocrystalline diamond films," *Mrs Bulletin*, vol. 39, no. 6, pp. 511–516, 2014.

[100] A. Aleksov, M. Kubovic, M. Kasu, P. Schmid, D. Grobe, S. Ertl, M. Schreck, B. Stritzker, and E. Kohn, "Diamond-based electronics for rf applications," *Diamond and related materials*, vol. 13, no. 2, pp. 233–240, 2004.

[101] M. P. Hiscocks, C. J. Kaalund, F. Ladouceur, S. T. Huntington, B. C. Gibson, S. Trpkovski, D. Simpson, E. Ampem-Lassen, S. Prawer, and J. E. Butler, "Reactive ion etching of waveguide structures in diamond," *Diamond and related materials*, vol. 17, no. 11, pp. 1831–1834, 2008.

[102] A. Masood, M. Aslam, M. Tamor, and T. Potter, "Techniques for patterning of cvd diamond films on non-diamond substrates," *Journal of The Electrochemical Society*, vol. 138, no. 11, pp. L67–L68, 1991.

[103] V. I. Konov, T. V. Kononenko, and V. V. Kononenko, "Laser micro-and nanoprocessing of diamond materials," *Optical Engineering of Diamond*, pp. 385–443, 2013.

[104] S. Preuss and M. Stuke, "Subpicosecond ultraviolet laser ablation of diamond: Nonlinear properties at 248 nm and time-resolved characterization of ablation dynamics," *Applied physics letters*, vol. 67, no. 3, pp. 338–340, 1995.

[105] T. Kononenko, V. Ralchenko, I. Vlasov, S. Garnov, and V. Konov, "Ablation of cvd diamond with nanosecond laser pulses of uv–ir range," *Diamond and related materials*, vol. 7, no. 11, pp. 1623–1627, 1998.

[106] S. Albin, A. D. Cropper, L. C. Watkins, C. E. Bvvik, and A. M. Buoncristiani, "Laser damage threshold of diamond films," *Optical Engineering*, vol. 28, no. 3, p. 283281, 1989.

[107] V. Migulin, V. G. Ralchenko, and Y.-J. Baik, "Oxygen-assisted laser cutting and drilling of cvd diamond," in *Lasers in Synthesis, Characterization, and Processing of Diamond*, pp. 175–179, International Society for Optics and Photonics, 1998.

[108] M. Rothschild, C. Arnone, and D. Ehrlich, "Excimer-laser etching of diamond and hard carbon films by direct writing and optical projection," *Journal of Vacuum Science & Technology B: Microelectronics Processing and Phenomena*, vol. 4, no. 1, pp. 310–314, 1986.

[109] V. Ral'Chenko, K. Korotushenko, A. Smolin, and E. Loubnin, "Fine patterning of diamond films by laser-assisted chemical etching in oxygen," *Diamond and related materials*, vol. 4, no. 7, pp. 893–896, 1995.

[110] R. Mildren and J. Rabeau, *Optical engineering of diamond*. John Wiley & Sons, 2013.

[111] I. Boyd, T. Binnie, J. Wilson, and M. Colles, "Absorption of infrared radiation in silicon," *Journal of Applied Physics*, vol. 55, no. 8, pp. 3061–3063, 1984.

[112] M. Blomberg, K. Naukkarinen, T. Tuomi, V.-M. Airaksinen, M. Luomajärvi, and E. Rauhala, "Substrate heating effects in co2 laser annealing of ion-implanted silicon," *Journal of Applied Physics*, vol. 54, no. 5, pp. 2327–2328, 1983.

[113] R. K. Endo, Y. Fujihara, and M. Susa, "Calculation of the density and heat capacity of silicon by molecular dynamics simulation," *High Temp High Press*, vol. 35, no. 36, pp. 505–511, 2003.

[114] J. Meyer, M. Kruer, and F. Bartoli, "Optical heating in semiconductors: Laser damage in ge, si, insb, and gaas," *Journal of Applied Physics*, vol. 51, no. 10, pp. 5513–5522, 1980.

[115] N. Ravindra, B. Sopori, O. Gokce, S. Cheng, A. Shenoy, L. Jin, S. Abedrabbo, W. Chen, and Y. Zhang, "Emissivity measurements and modeling of silicon-related materials: an overview," *International journal of thermophysics*, vol. 22, no. 5, pp. 1593–1611, 2001.

[116] D. C. Harris, "Development of chemical-vapor-deposited diamond for infrared optical applications. status report and summary of properties," tech. rep., Naval Air Warfare Center Weapons Div China Lake CA, 1994.

[117] Refractive index database: https://refractiveindex.info/.

[118] R. Halir, I. Molina-Fernández, A. Ortega-Monux, J. Wangüemert-Pérez, D.-X. Xu, P. Cheben, and S. Janz, "A design procedure for high-performance, rib-waveguide-based multimode interference couplers in silicon-on-insulator," *Journal of Lightwave Technology*, vol. 26, no. 16, pp. 2928–2936, 2008.

[119] M. M. Milošević, P. S. Matavulj, B. D. Timotijević, G. T. Reed, and G. Z. Mashanovich, "Design rules for single-mode and polarization-independent silicon-on-insulator rib waveguides using stress engineering," *Journal of Lightwave Technology*, vol. 26, no. 13, pp. 1840–1846, 2008.

[120] M. M. Milošević, P. S. Matavulj, P. Y. Yang, A. Bagolini, and G. Z. Mashanovich, "Rib waveguides for mid-infrared silicon photonics," *JOSA B*, vol. 26, no. 9, pp. 1760–1766, 2009.

[121] B. Bêche, N. Pelletier, E. Gaviot, and J. Zyss, "Single-mode te 00–tm 00 optical waveguides on su-8 polymer," *Optics Communications*, vol. 230, no. 1, pp. 91–94, 2004.

[122] J. Lousteau, D. Furniss, A. Seddon, T. Benson, A. Vukovic, and P. Sewell, "The single-mode condition for silicon-on-insulator optical rib waveguides with large cross section," *Journal of Lightwave technology*, vol. 22, no. 8, pp. 1923–1929, 2004.

[123] G. Collins and S. Haxha, "Analysis of coupling efficiency between the rib waveguide and single mode fibre (smf)," 2005.

[124] P. Rabiei, W. H. Steier, C. Zhang, and L. R. Dalton, "Polymer micro-ring filters and modulators," *Journal of lightwave technology*, vol. 20, no. 11, pp. 1968–1975, 2002.

[125] X. Cai, S. Yu, and D. Huang, "Numerical analysis of polarization splitter based on vertically coupled microring resonator," *PIERS Online*, vol. 4, no. 4, pp. 455–460, 2008.

[126] D. Marcuse, "Bending losses of the asymmetric slab waveguide," *Bell Labs Technical Journal*, vol. 50, no. 8, pp. 2551–2563, 1971.

[127] R. Deck, M. Mirkov, and B. Bagley, "Determination of bending losses in rectangular waveguides," *Journal of lightwave technology*, vol. 16, no. 9, p. 1703, 1998.

[128] J. Cardenas, C. B. Poitras, K. Luke, L.-W. Luo, P. A. Morton, and M. Lipson, "High coupling efficiency etched facet tapers in silicon waveguides," *IEEE Photon. Technol. Lett.*, vol. 26, no. 23, pp. 2380–2382, 2014.

[129] Wikipedia: https://en.wikipedia.org/wiki/Prism_coupler.

[130] J. Yang, Z. Jingjing, S. Xu, and S. Chang, "High-performance subwavelength grating coupler based on high-reflectivity grating reflector," *Optical Engineering*, vol. 53, no. 9, pp. 096107–096107, 2014.

[131] G. Jin, S. Shi, A. Sharkawy, and D. W. Prather, "Polarization effects in tapered dielectric waveguides," *Optics express*, vol. 11, no. 16, pp. 1931–1941, 2003.

[132] V. R. Almeida, R. R. Panepucci, and M. Lipson, "Nanotaper for compact mode conversion," *Optics letters*, vol. 28, no. 15, pp. 1302–1304, 2003.

[133] R. G. Hunsperger, A. Yariv, and A. Lee, "Parallel end-butt coupling for optical integrated circuits," *Applied optics*, vol. 16, no. 4, pp. 1026–1032, 1977.

[134] D. Dai, Y. Tang, and J. E. Bowers, "Mode conversion in tapered submicron silicon ridge optical waveguides," *Optics express*, vol. 20, no. 12, pp. 13425–13439, 2012.

[135] G. M. Rebeiz, *RF MEMS: theory, design, and technology*. John Wiley & Sons, 2004.

[136] V. K. Varadan, K. J. Vinoy, and K. A. Jose, *RF MEMS and their applications*. John Wiley & Sons, 2003.

[137] B. El-Kareh and L. N. Hutter, *Silicon Analog Components*. Springer, 2015.

[138] F. S. Tse, I. E. Morse, and R. T. Hinkle, *Mechanical vibrations*. Allyn and Bacon Boston, 1963.

[139] S. G. Kelly, *Mechanical vibrations: theory and applications*. Cengage learning, 2012.

[140] O. Reynolds, "Xxix. an experimental investigation of the circumstances which determine whether the motion of water shall he direct or sinuous, and of the law of resistance in parallel channels," *Philosophical Transactions of the Royal Society of London*, vol. 174, pp. 935–982, 1884.

[141] H. Schlichting, K. Gersten, E. Krause, and H. Oertel, *Boundary-layer theory*, vol. 7. Springer, 1955.

[142] K. Seshan, *Handbook of thin film deposition*. William Andrew, 2012.

[143] J. W. Rohlf, "Modern physics from aalpha to z0," *Modern Physics from aalpha to Z0, by James William Rohlf, pp. 664. ISBN 0-471-57270-5. Wiley-VCH, March 1994.*, p. 664, 1994.

[144] S. Jennings, "The mean free path in air," *Journal of Aerosol Science*, vol. 19, no. 2, pp. 159–166, 1988.

[145] Crystal-scientific website: http://www.crystal-scientific.com/xtal_orientation.html.

[146] G. T. Kovacs, N. I. Maluf, and K. E. Petersen, "Bulk micromachining of silicon," *Proceedings of the IEEE*, vol. 86, no. 8, pp. 1536–1551, 1998.

[147] M. D. Henry, *ICP etching of silicon for micro and nanoscale devices*. California Institute of Technology, 2010.

[148] S. Ray, C. Maiti, and N. Chakraborti, "Rapid plasma etching of silicon, silicon dioxide and silicon nitride using microwave discharges," *Semiconductor science and technology*, vol. 8, no. 4, p. 599, 1993.

[149] P. Rai-Choudhury, *Handbook of microlithography, micromachining, and microfabrication: microlithography*, vol. 1. Iet, 1997.

[150] A. J. Maker and A. M. Armani, "Fabrication of silica ultra high quality factor microresonators," *Journal of visualized experiments: JoVE*, no. 65, 2012.

[151] K. R. Williams, K. Gupta, and M. Wasilik, "Etch rates for micromachining processing-part ii," *Journal of microelectromechanical systems*, vol. 12, no. 6, pp. 761–778, 2003.

[152] P. Rai-Choudhury, "Handbook of microlithography, micromachining, and microfabrication(volume 2, micromachining and microfabrication),"

[153] V. Hagglund, "Characterization of masking layers for deep wet etching in borofloat glass," *Uppsala Universitet, Examensarbete*, vol. 30, pp. 1–36, 2013.

[154] D. Armani, T. Kippenberg, S. Spillane, and K. Vahala, "Ultra-high-q toroid microcavity on a chip," *Nature*, vol. 421, no. 6926, pp. 925–928, 2003.

[155] J. Park, S. Lee, K. Choi, H. Noh, J. Lee, and S. Pearton, "Comparison of dry etching of pmma and polycarbonate in diffusion pump-based o 2 capacitively coupled plasma and inductively coupled plasma," *Thin Solid Films*, vol. 518, no. 22, pp. 6465–6468, 2010.

[156] C. Zhang, C. Yang, and D. Ding, "Deep reactive ion etching of pmma," *Applied surface science*, vol. 227, no. 1, pp. 139–143, 2004.

[157] C. Kim, B. Jung, and C. Lee, "Analysis of dielectric rectangular waveguide by modified effective-index method," *Electronics Letters*, vol. 22, no. 6, pp. 296–298, 1986.

[158] O. Tabata, R. Asahi, H. Funabashi, K. Shimaoka, and S. Sugiyama, "Anisotropic etching of silicon in tmah solutions," *Sensors and Actuators A: Physical*, vol. 34, no. 1, pp. 51–57, 1992.

[159] E. Vazsonyi, K. De Clercq, R. Einhaus, E. Van Kerschaver, K. Said, J. Poortmans, J. Szlufcik, and J. Nijs, "Improved anisotropic etching process for industrial texturing of silicon solar cells," *Solar energy materials and solar cells*, vol. 57, no. 2, pp. 179–188, 1999.

[160] H. Seidel, L. Csepregi, A. Heuberger, and H. Baumgärtel, "Anisotropic etching of crystalline silicon in alkaline solutions i. orientation dependence and behavior of passivation layers," *Journal of the electrochemical society*, vol. 137, no. 11, pp. 3612–3626, 1990.

[161] H. Seidel, L. Csepregi, A. Heuberger, and H. Baumgärtel, "Anisotropic etching of crystalline silicon in alkaline solutions ii. influence of dopants," *Journal of the Electrochemical Society*, vol. 137, no. 11, pp. 3626–3632, 1990.

[162] P. Bressers, J. Kelly, J. G. Gardeniers, and M. Elwenspoek, "Surface morphology of p-type (100) silicon etched in aqueous alkaline solution," *Journal of the Electrochemical Society*, vol. 143, no. 5, pp. 1744–1750, 1996.

[163] G. Canavese, S. L. Marasso, M. Quaglio, M. Cocuzza, C. Ricciardi, and C. Pirri, "Polymeric mask protection for alternative koh silicon wet etching," *Journal of Micromechanics and Microengineering*, vol. 17, no. 7, p. 1387, 2007.

[164] M. Larsson, R. Syms, and A. Wojcik, "Improved adhesion in hybrid si-polymer mems via micromechanical interlocking," *Journal of micromechanics and microengineering*, vol. 15, no. 11, p. 2074, 2005.

Appendix A

Grating coupler simulator

An application has been built on CAMFR framework specifically for grating couplers' design. CAMFR is a scientific module for python programing language. The application adds a GUI to the code nature of CAMFR. Following are some screen-shots of the user interface of the application, along with some examples of the output files. The application is available from the following link

[https://www.dropbox.com/s/um4cpmsvvhl2owg/V6.0.zip?dl=0].

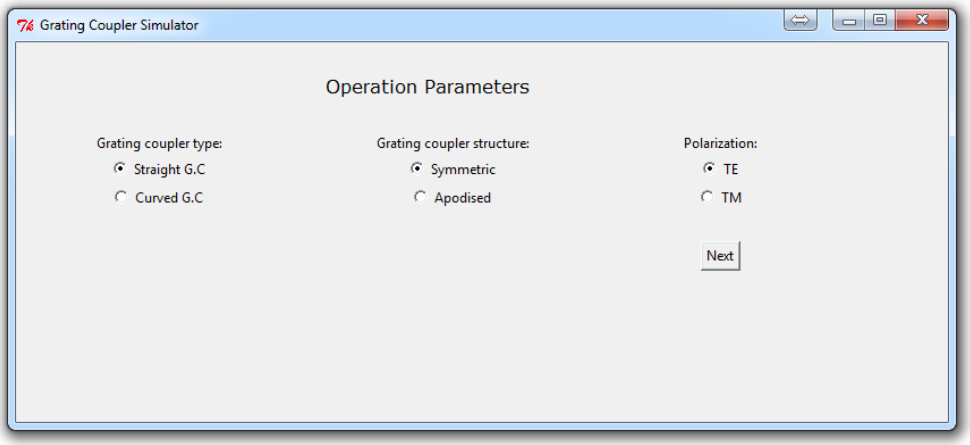

Fig. A.1 Operation parameters window.

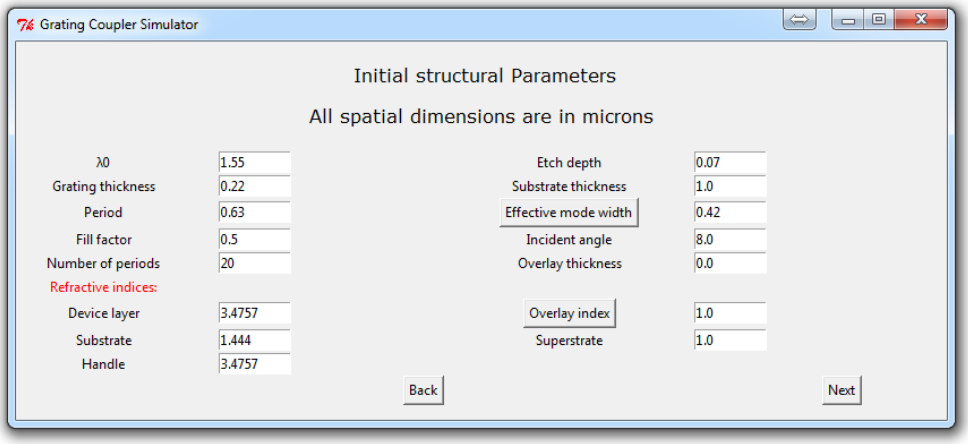

Fig. A.2 Operation variables window.

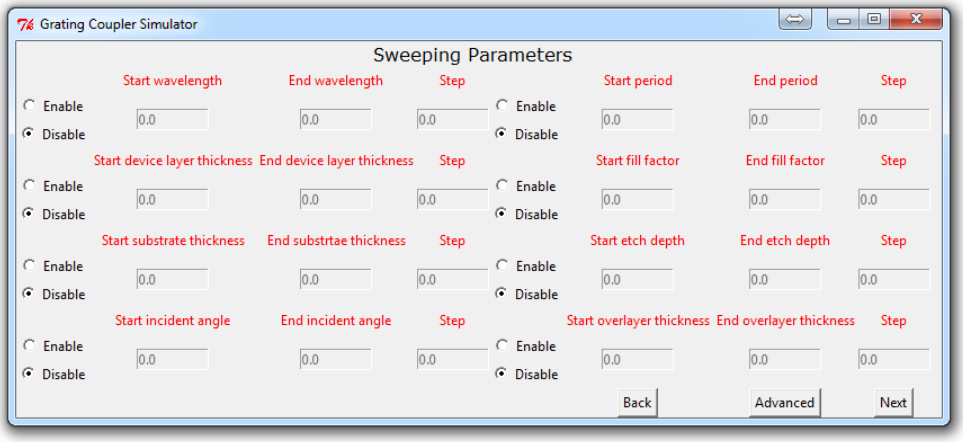

Fig. A.3 Parametric sweeps window.

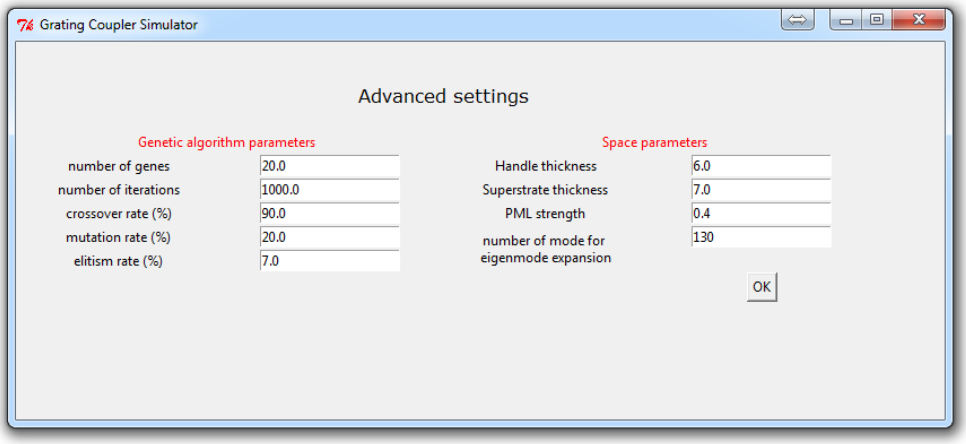

Fig. A.4 Advanced settings window.

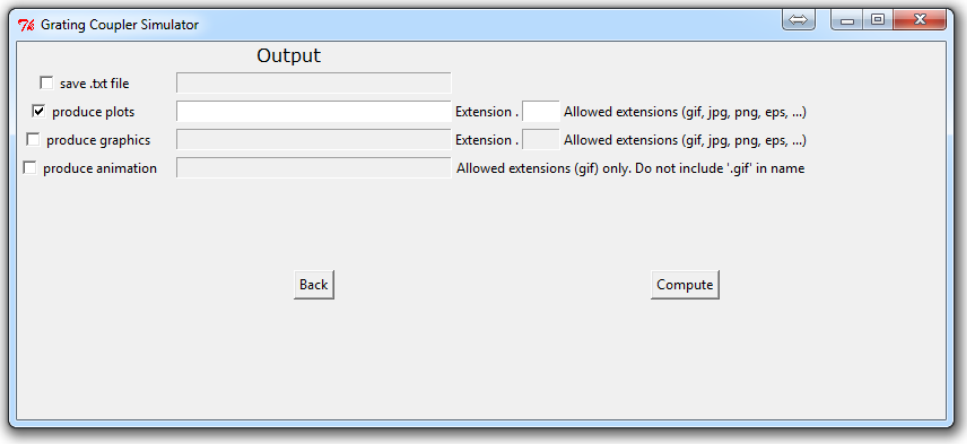

Fig. A.5 Output files window.

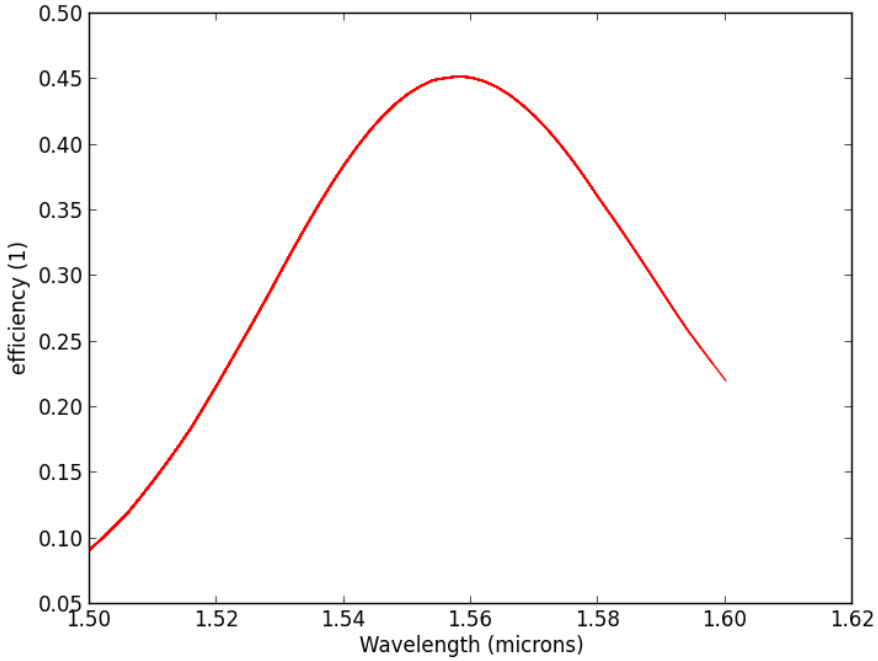

Fig. A.6 Sample plot output.

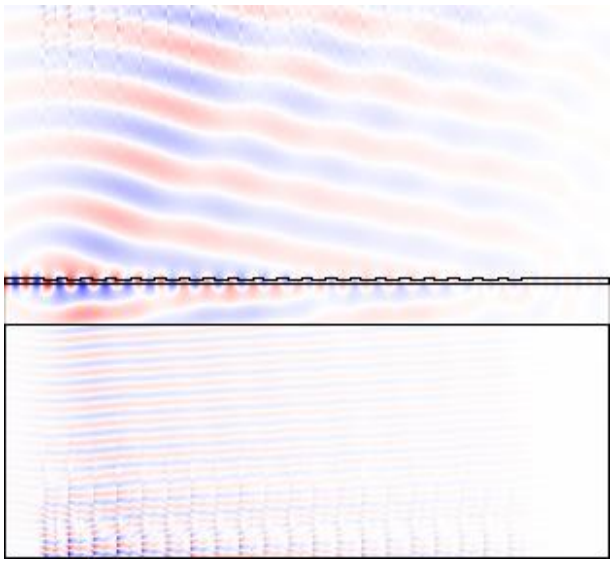

Fig. A.7 Sample field output.

A.1 CAMFR script example [1]

#Before attempting to follow the following code, it is essential to check CAMFR manual on
#[http://camfr.sourceforge.net/].

```
##########################################################################
# Example python script for calculating the fiber coupling efficiency of a SOI          #
# waveguide grating coupler                                                              #
##########################################################################

from camfr import *
from numpy import *

# define parameters
set_lambda(1.55)   # wavelength
set_N(130)   #number of modes
set_polarisation(TE)
set_chunk_tracing(0)
set_degenerate(0)
set_orthogonal(False)

# define material
substrate=Material(1.444)
guiding=Material(3.4757)
nfib=1.46
iml=Material(nfib)
```

[1] The script presented here is a modification on the script presented in "Dirk Taillaert, 2005. grating couplers as interface between optical fibers and nanophotonic waveguides, Ph.D thesis, Gent University."

```
# define our own parameters
ff = 0.5
d = 7.0
pml = 0.4
set_lower_PML(-pml)
set_upper_PML(-pml)
guide_thickness = 0.26
dclad = 2.0
period = 0.55
groove_depth = 0.11

# period parametric sweep
for p in arange(0.75,1.05,0.05):
    period = p
    for f in arange(0.4,0.7,0.1):
        ff = f
        # create output file
        outfile = open("SOI_P="+str(period)+"_ff="+ str(ff)+"_depth="+str(groove_depth)+
                       ".txt",'w')

        # sweep the wavelength
        for L in arange(1500,1601,2):
            set_lambda(L/1000.0)

            # define slabs
            waveguide = Slab(guiding(d-dclad)+substrate(dclad)+guiding(guide_thickness)
                             +iml(d))
            etched = Slab(guiding(d-dclad)+substrate(dclad)+guiding(guide_thickness-
                             groove_depth)+iml(groove_depth+d))

            # define stack
            stack = Stack(waveguide(1.0) + 20*(etched(period*(1.0-ff))
                             + waveguide(period*ff)) + waveguide(2.0))

            # find the guided mode
            waveguide.calc()
            guided = 0
            niguided = 1
            for t in range(0,60):
                if abs(waveguide.mode(t).n_eff().imag) < niguided: guided = t
                    niguided = abs(waveguide.mode(t).n_eff().imag)

            # set input for calculating the fields
            inc = zeros(N())
            inc[guided] = 1
            stack.set_inc_field(inc)
```

```
    stack.calc()

    R = abs(stack.R12(guided,guided))
    T = abs(stack.T12(guided,guided))
    up = stack.lateral_S_flux(d+1.5)
    down = stack.lateral_S_flux(d-1.5)
    x = d+1.5

    #calculate the coupling efficiency to fibre
    powerup = 0.0 + 0.0*1j
    overlapint = zeros(100,complex) # 0 degrees
    soverlapint = zeros(100,complex) # 8 degrees
    align = zeros(100) # to find optimal fiber position
    pfib = 0.0

    #normalization Gaussian profile
    Zzero = 377
    nZ = nfib/Zzero
    for z in arange(-10.0,10.0,0.01): pfib+=0.01*exp(-((z/5.2)**2))*nZ*
                        exp(-((z/5.2)**2))

    #calculate different fibre position simultaneously
    for counter in range(100):
        align[counter]=-1.0-period*(counter/5)
    for z in arange(0.01, 23*period , 0.01):
        powerup+=(0.01*stack.field(Coord(x,0,z)).E2()*
                        conjugate(stack.field(Coord(x,0,z)).Hz()))
        overlapint+=(0.01*stack.field(Coord(x,0,z)).E2()*
                        nZ*exp(-(((align+z)/5.2)**2)))
        soverlapint+=(0.01*stack.field(Coord(x,0,z)).E2()*
                        nZ*exp(-(((align+z)/5.2)**2))*exp(0.85*1j*z))

    coupling = ((abs(overlapint))**2)/(pfib*powerup.real)
    scoupling = ((abs(soverlapint))**2)/(pfib*powerup.real)

    print » outfile, P,ff,period,R*R,T*T,powerup.real,powerup.real*scoupling[33]
    outfile.flush()
    print P, ff, period
    free_tmps()
outfile.close()
```

Appendix B

MATLAB® Code for Estimating Scattering Loss

The modified effective index method [157] has been used for calculating the scattering loss. The effective index method produces lower effective index than the actual numerical results. This is attributed to the fact of using the refractive index of the cladding regions of the corners in Fig. B.1 twice, once for each slab waveguide. The modified effective index method reduces the refractive index of the cladding in the second slab waveguide to compensate for this decrease. The modified cladding refractive index is given by

$$n_{new} = n_{eff1} \times \frac{n_{cladding}}{n_{core}} \tag{B.1}$$

where n_{eff1} is the first slab effective index.

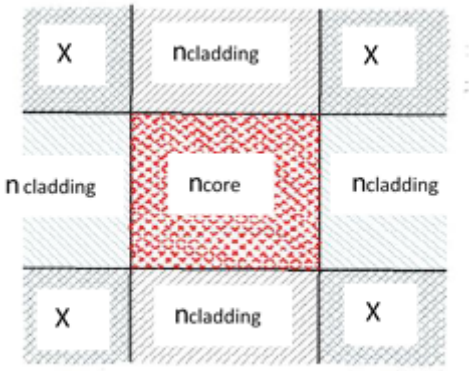

Fig. B.1 Schematic of refractive index distribution for the effective index method.

B.1 MATLAB® code

```
clear
clc
format long

%You only need to change the parameters in the input section according to your parameters

%inputs
h = 0.52; %waveguide half height in microns
w = 0.45; % waveguide half width in microns
n1 = 2.3855; %core refractive index
n2 = 1; %upper cladding refractive index
n3 = 1; %lower cladding refractive index
n4 = 1; %right cladding refractive index
n5 = 1; %left cladding refractive index
W_L = 1.55; %wavelength in microns

n_eff1 = 2.155; %horizontal slab waveguide effective index
n_eff = 2.039; %rectangular waveguide effective index

sigma_t = 0.002; %top surface RMS roughness in microns
sigma_b = 0.002; %bottom surface RMS roughness in microns
sigma_r = 0.002; %right surface RMS roughness in microns
sigma_l = 0.002; %left surface RMS roughness in microns

Lc_t = 0.5; %top surface correlation length in microns
Lc_b = 0.5; %bottom surface correlation length in microns
Lc_r = 0.5; %right surface correlation length in microns
Lc_l = 0.5; %left surface correlation length in microns

%universal variable
k_0 = 2*pi/W_L; %wavevector in free space

%modified effective index method parameters
n41 = neff1*n4/n1;
n51 = neff1*n5/n1;

%top surface variables
U_t = k_0*h*sqrt(n1^2-n_eff1^2);
V_t = k_0*h*sqrt(n1^2-n2^2);
W_t = k_0*h*sqrt(n_eff1^2-n2^2);
delta_t = (n1^2-n2^2)/(2*n1^2);
x_t = W_t*Lc_t/h;
gamma_t = n2*V_t/(n1*W_t*sqrt(delta_t));

gv_t = U_t^2*V_t^2/(1+W_t);
f_t = (x_t*sqrt(sqrt((1+x_t^2)^2+2*x_t^2*gamma_t^2)+1-x_t^2))/...
```

```
        sqrt((1+x_t^2)^2+2*x_t^2*gamma_t^2);

%losses from top surface
alpha_t = sigma_t^2/(sqrt(2)*k_0*h^4*n1)*gv_t*f_t*0.5;

%bottom surface variables
U_b = k_0*h*sqrt(n1^2-n_eff1^2);
V_b = k_0*h*sqrt(n1^2-n3^2);
W_b = k_0*h*sqrt(n_eff1^2-n3^2);
delta_b = (n1^2-n3^2)/(2*n1^2);
x_b = W_b*Lc_b/h;
gamma_b = n3*V_b/(n1*W_b*sqrt(delta_b));

gv_b = U_b^2*V_b^2/(1+W_b);

f_b = (x_b*sqrt(sqrt((1+x_b^2)^2+2*x_b^2*gamma_b^2)+1-x_b^2))/...
        sqrt((1+x_b^2)^2+2*x_b^2*gamma_b^2);

%losses from bottom surface
alpha_b = sigma_b^2/(sqrt(2)*k_0*h^4*n1)*gv_b*f_b*0.5;

%losses from horizontal slab
alpha_slab1 = abs(alpha_t) + abs(alpha_b);

%refractive index of vertical slab core
k = alpha_slab1*W_L/(4*pi); %extinction coefficient
N = n_eff1 + i*k; %complex refractive index

%right surface variables
U_r = k_0*w*sqrt(N^2-n_eff^2);
V_r = k_0*w*sqrt(N^2-n4^2);
W_r = k_0*w*sqrt(n_eff^2-n4^2);
delta_r = (N^2-n4^2)/(2*N^2);
x_r = W_r*Lc_r/w;
gamma_r = n4*V_r/(N*W_r*sqrt(delta_r));

gv_r = U_r^2*V_r^2/(1+W_r);
f_r = (x_r*sqrt(sqrt((1+x_r^2)^2+2*x_r^2*gamma_r^2)+1-x_r^2))/...
        sqrt((1+x_r^2)^2+2*x_r^2*gamma_r^2);

%losses from right surface
alpha_r = sigma_r^2/(sqrt(2)*k_0*w^4*N)*gv_r*f_r*0.5;

%left surface variables
U_l = k_0*w*sqrt(N^2-n_eff^2);
V_l = k_0*w*sqrt(N^2-n5^2);
W_l = k_0*w*sqrt(n_eff^2-n5^2);
delta_l = (N^2-n5^2)/(2*N^2);
```

```
x_l = W_l*Lc_l/w;
gamma_l = n5*V_l/(N*W_l*sqrt(delta_l));

gv_l = U_l^2*V_l^2/(1+W_l);
f_l = (x_l*sqrt(sqrt((1+x_l^2)^2+2*x_l^2*gamma_l^2)+1-x_l^2))/...
        sqrt((1+x_l^2)^2+2*x_l^2*gamma_l^2);

%losses from left surface
alpha_l = sigma_l^2/(sqrt(2)*k_0*w^4*N)*gv_l*f_l*0.5;

%losses for vertical slab
alpha_slab2 = abs(real(alpha_r)) + abs(real(alpha_l));

%total losses
alpha_total = alpha_slab1 + alpha_slab2
```

Appendix C

KOH Etching of Silicon

Silicon wet etching is a mature topic that is used in industry. Silicon wet etching is explained in details in several textbooks (e.g. [152]) and multiple publications (e.g. [146]). Here, we do not attempt to review or improve silicon wet etching techniques, but merely present our experience with masking materials.

C.1 Introduction

Silicon is formed of crystalline structures, and could be produced with certain crystal orientation. The three major crystal orientations are the <100>, <110> and <111> crystal planes. Silicon etch rate differs among the different crystal orientations. A good review of silicon etching is presented in [146]. Wet etching of silicon is a chemical reaction that depends on dissolving the silicon atoms and forming silicate compounds [X-SiO_3]. Mainly, base solutions are used for silicon etching as they produce hydroxide ions that react with the silicon atoms to form silicate ions, which in turn react with the cations in the solution to form silicate salt. Some of the chemicals used are the alkaline solutions of KOH (sodium hydroxide), NaOH (potassium hydroxide), and CsOH (caesium hydroxide), and the organic solutions of EDP (ethylenediamine-pyrocatechol-water), hydrazine-water, NH_4OH (ammonium hydroxide), and tetramethylammonium hydroxide (TMAH).

Anisotropic wet etching of silicon is well developed, were results using TMAH (e.g. [158]) and KOH with isopropanol (e.g. [159]) are widely available. The effect of crystal orientation and dopants on the anisotropic etching of silicon is documented in the reference papers ([160, 161]). As well as, the surface morphology of wet-etched silicon is also studied (e.g. [162]).

Conventionally etch masks for KOH etching were hard masks of silicon oxide or silicon nitride. The oxide mask is usually used for short etches, as it gets etched in KOH but at a much slower rate than silicon. While the nitride mask is used for long etches (up to several hours) as it has very low etch rate in KOH, and in some cases, it has zero etch rate [151]. Polymeric etch masks were not used as they either get etched in KOH or get peeled off. Recently, a polymeric etch mask has been proposed [163], which is claimed to have high resistance to KOH.

Table C.1 Brief experimental procedures of masking materials for KOH etching.

Mask material	cleaning	Mask deposition	KOH etch
Molybdenum	• 1 min acetone sonication • 1 min IPA sonication • DI rinse/N_2 blow dry • 2 min BOE dip • DI rinse/N_2 blow dry	• $\sim 90nm$ sputtered Mo with 150sccm Ar flow rate and 250W RF power	• Two separate tests using KOH and KOH -IPA solutions @ 65^oC with stirring.
AZ1505 +ve resist	• 1 min acetone sonication • 1 min IPA sonication • DI rinse/N_2 blow dry • 2 min BOE dip • DI rinse/N_2 blow dry	• Spin-coat resist @500rpm for 10 sec. • Second step @1000/4000 rpm for 50 sec. • Soft-bake (SB) @ 100^oC for 1 min • Bake @ 130^oC for 10 min	• Two separate tests using KOH and KOH -IPA solutions @ 65^oC with stirring.
AZ2020 -ve resist	• 1 min acetone sonication • 1 min IPA sonication • DI rinse/N_2 blow dry • 2 min BOE dip • DI rinse/N_2 blow dry	• Spin-coat resist @500rpm for 10 sec. • Second step @1000/4000 rpm for 50 sec. • SB @ 100^oC for 1 min • Expose with $> 400J/cm^2$ • PEB @ 105^oC for 1 min • Bake @130^oC for 10 min	• Two separate tests using KOH and KOH -IPA solutions @ 65^oC with stirring.
950PMMA A10	• 1 min acetone sonication • 1 min IPA sonication • DI rinse/N_2 blow dry • 2 min BOE dip • DI rinse/N_2 blow dry	• Spin-coat Surpass @3000rpm for 30 sec. • Spin-coat PMMA @ 500rpm for 10 sec. • Spin-coat PMMA @ 1000/4000rpm for 50 sec • Bake @ 210^oC for 15 min	• Two separate tests using KOH and KOH -IPA solutions @ 65^oC with stirring.
EPO-TEK® 301 epoxy	• 1 min acetone sonication • 1 min IPA sonication • DI rinse/N_2 blow dry • 2 min BOE dip • DI rinse/N_2 blow dry	• Spread the two-part mixture on substrates • Bond the silicon substrate to a glass slide for back protection • Protect edges using the epoxy mixture	• Two separate tests using KOH and KOH -IPA solutions @ 65^oC with stirring.

C.2 Experiment

$\sim 30\%$ KOH with isopropanol (IPA) solution was prepared from $> 85\%$ pure KOH pellets obtained from Fisher Scientific. $70g$ of KOH pellets were dissolved in $190ml$ water and $40ml$ IPA with stirring at a slightly elevated temperature ($\sim 40^oC$). A second batch was prepared from $70g$ KOH pellets and $230ml$ water without IPA.

For etching, the KOH solutions were heated on a hot plate at 65^oC, where the temperature was monitored using a thermocouple. The solutions were stirred using magnetic stirrer to ensure the removal of the formed salt off the surface of the substrates. <100> silicon thicknesses of up to $680\mu m$ were required to be etched, so long etches of several hours were needed. The problem was to find a mask that can withstand such long etches besides silicon nitride. Several options were considered. The different masking layers with their deposition parameters are reported in Table C.1. Before coating the samples, they were sonicated for 1 minute in acetone and 1 minute in IPA. They were then rinsed with DI water and blown dry using nitrogen gun. A quick two minutes dip in buffered-oxide-etchant (BOE) was conducted to remove the native oxide layer. After rinsing with DI water and drying with nitrogen, the deposition of the protective layer was conducted within 12 hours after the BOE dip to ensure no or minimal native oxide is formed on the silicon surface.

The first masking layer was a $90nm$ thick sputtered molybdenum (Mo) film. Mo was sputtered at a rate of 3 Å/sec in a Leybold UNIVEX 350 sputtering system with $150sccm$ Argon flow rate and $250W$ RF power. The second mask was the positive photoresist AZ1505 from MicroChem. Several samples were spun-coated with AZ1505, some at 4000rpm and other at 1000rpm. Then soft baked at 100^oC for 1 minute. After settling, the samples were hard baked at 130^oC for 10 minutes. The coated samples were divided into two sets, where one set was dipped in BOE for 30 minutes. Two sets of the negative photoresist AZ2020 from MicroChem were spun-coated at 4000rpm and 1000rpm. Then soft-baked at 100^oC for 1 minute. Flood exposure of the samples was conducted with $> 400J/cm^2$, which was followed by a post-exposure bake at 105^oC for 1 minute. After settling, the samples were hard baked at 130^oC for 10 minutes. Then, one set was dipped in BOE for 30 minutes. Poly(methyl methacrylate) (PMMA) was spun-coated on two sets of substrates, again at 4000rpm and 1000rpm and hard-baked at 210^oC. Each set was split into two subsets, one with Surpass 3000 'adhesion promoter' and one without. Lastly, EPO-TEK® 301 bonding epoxy was used to bond a glass substrate to the back-side of some silicon substrates and protect the edges. It was cured gradually in steps of two hours at room-temperature, 40^oC and 60^oC on a hotplate. Mask resistance to both KOH solutions was observed for the first 5-10 minutes, then at regular time intervals of one hour.

The main issue with polymeric protective coatings in KOH is that they get peeled off. A proposed method for improving the adhesion between polymeric coatings and substrates is by creating rough substrate surface [164]. We opted to coating the unpolished side of some silicon substrates to increase the adhesion of AZ1505 to them.

Also, etching silicon with $1.3\mu m$ thermal oxide mask was conducted to observe the nature of silicon etching in KOH solution with IPA. Etching time was kept at one hour to avoid the total removal of the oxide etch-mask, since KOH etches silicon oxide [151]. Etching <100> silicon using KOH-IPA solution can be both isotropic and anisotropic. The mask orientation is what determines the nature of the etch. To explore these cases, a ring shape was patterned in the thermal oxide layer grown on the <100> silicon substrate. The circular edges allow to simultaneously observe the different etch rates of the different planes' orientations.

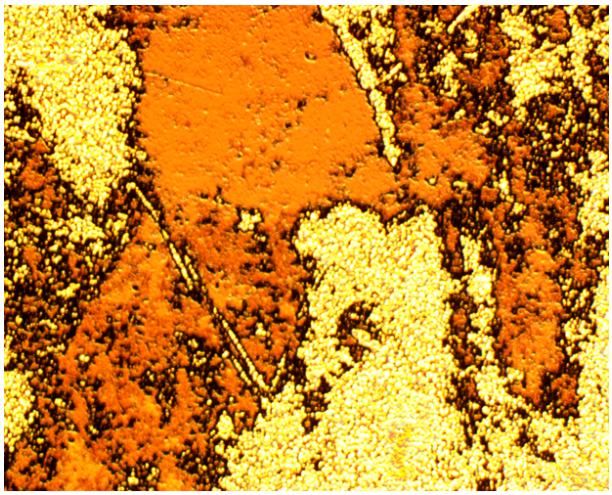

Fig. C.1 Molybdenum surface after KOH etching.

C.3 Results

C.3.1 Masks against KOH solution

The Mo mask seemed as if it reacts with the KOH solution. The reaction was vigorous, which resulted in the formation of a layer of dull appearance unlike the shiny Mo appearance. This reaction does not seem to affect the whole layer, and in some cases, it caused the peeling of Mo flakes of the surface. Fig. C.1 shows an optical image of the affected Mo film.

AZ1505 did not dissolve in the KOH solution, but it gets peeled off in few seconds. It was hard to study the nature by which the thin layer of AZ1505 peels off. The thicker the film the longer it takes to peel off, but still it takes less than 10 seconds for the two thicknesses ($600nm$ and $\sim 1\mu m$) used in this study. The same peeling effect was observed with the AZ2020 polymer. Using an 'adhesion promoter' (Surpass 3000) with both photoresists did not improve adhesion.

PMMA coatings suffer from poor adhesion when used in KOH solutions. When the 'adhesion promoter' was used, the protective PMMA film peeled of much slower than when no 'adhesion promoter' was used. But still it did not survive until the one-hour check. The KOH solution penetrates under the PMMA layer from the edges. And even when protecting the edges with PMMA, the KOH solution still goes underneath it. Surprisingly, the thin layer of the 'adhesion promoter' survived several hours as a protective coating against KOH etching. When applying only the 'adhesion promoter' without an over-layer of PMMA, it dissolves in the KOH solution in few second. We are unable to report the effectiveness of using the 'adhesion promoter' with PMMA over-layer as protective coating as it was not consistent from sample to another. Some samples survived in KOH solution for various times from 10 minutes to $\sim 3-4$ hours. While others, coated at the same time with the same parameters, did not survive.

The most resilient coating against KOH was EPO-TEK® 301 bonding epoxy. It does not get affected by the KOH solution. But at elevated temperature, it separates from the silicon substrates. We attributed this to the difference in the thermal expansion coefficient between the two materials (Si: $2.6\times10^{-6}/^{o}C$, Epoxy: $39\times10^{-6}/^{o}C$). We were able to etch $680\mu m$

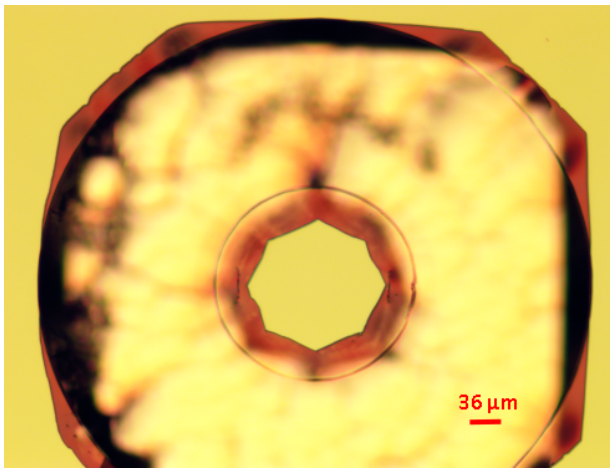

Fig. C.2 Optical image showing the isotropic and anisotropic etching behaviour of KOH-IPA solutions depending on the crystal lattice orientation of the etched wall.

thick silicon substrate using EPO-TEK® 301 protective coating. EPO-TEK® 301 survived for several days in KOH solutions heated to 65^oC without any noticeable effect on the film.

C.3.2 Masks against KOH-IPA solution

From experience, the anisotropicity of KOH solution is increased by adding moderate amounts of IPA to the solution. Also, IPA decreases the aggressiveness of the KOH solution, so protective coatings survive longer.

Mo reacted with the KOH-IPA solution, but less aggressively than in the case of KOH solution. It took several minutes (~ 20) to observe the change in the Mo layer. Films as shown in Fig. C.1 were observed for the KOH-IPA solution.

Photoresists (AZ1505 and AZ2020) were shown to be permeable to the KOH-IPA solution. But as the film thickness increases, the permeability decreases. For proper coating and exposure (in case of negative resist), spin-coating had to be conducted. So, films' thicknesses were maximum of ~ 1 micron for AZ1505 to few microns for AZ2020. The middle section of the films was permeable to KOH-IPA solution. This was confirmed by the formation of gas bubbles under the film, which is attributed to the generated hydrogen from the reaction between silicon and KOH solution. The film was not permeable to hydrogen gas, and the generated pressure from the enclosed gas worked on peeling the protective film inside-out towards the edges. On the other hand, the thick film at the edges, and mainly the corners, because of the edge beads was very resilient to KOH-IPA solution. Working with thicker films might provide resilient enough coatings.

The samples which went through BOE dip showed prolonged resistance against the KOH-IPA solution permeability. But eventually they were peeled off. Also, samples with rough surfaces showed better adhesion to the protective coating. But, the coatings on all samples were peeled off within few minutes at most.

PMMA films behaved similarly in KOH and KOH-IPA solutions. But no 'adhesion promoter' protection was observed with KOH-IPA solution. And again, EPO-TEK® 301 bonding epoxy showed superior protection properties.

C.3.3 Etching silicon

The silicon with oxide mask was etched in KOH-IPA solution at 65^oC for one hour. The etch depth was measured to be between $32-34\mu m$. The thickness variation is the resulting roughness after the etch, but it is within acceptable limits. The lateral etch was measured using an optical microscope. Fig. C.2 shows the obtained image, where the oxide mask is the circular outer periphery, and the silicon etch walls are the octagon outer periphery. Same behaviour is observed for the disc and octagon in the middle. The etch rate for the groove walls in the vertical direction (etch mask edge perpendicular to the wafer flat edge) have almost zero etch rate. While the groove walls at 45^o have lateral etch rate similar to the depth etch rate. It can be concluded that for rectangular etch mask, according to the orientation, either isotropic or anisotropic etching can be obtained using the same KOH-IPA solution.

C.4 Conclusion

Several KOH etch masks have been tried. Only EPO-TEK® 301 bonding epoxy showed good resistance to KOH solutions for prolonged periods (days). The AZ1505 and AZ202 photoresists are resilient to KOH-IPA solutions, but the adhesion between them and silicon substrates is not. It is expected for very thick films to withstand long etching periods. This assumption is based on the fact that thin photoresist films are permeable to KOH-IPA solution, and the peeling occurs because of the pressure due to the trapped hydrogen gas underneath.

KOH-IPA solutions can act as isotropic and anisotropic <100> silicon etchant. The nature of the etch is based on the etched wall crystal lattice orientation, which is determined by the mask alignment with respect to the flat edge of the wafer.